

UCLA

UCLA Electronic Theses and Dissertations

Title

Search for the Chiral Vortical Effect Using  $\Lambda$ -p Correlations at STAR

Permalink

<https://escholarship.org/uc/item/1s35d4tw>

Author

Chan, Brian Ki Hon

Publication Date

2023

Peer reviewed|Thesis/dissertation

UNIVERSITY OF CALIFORNIA  
Los Angeles

Search for the Chiral Vortical Effect  
Using  $\Lambda$ - $p$  Correlations  
at STAR

A dissertation submitted in partial satisfaction  
of the requirements for the degree  
Doctor of Philosophy in Physics

by

Brian Chan

2023

© Copyright by

Brian Chan

2023

# ABSTRACT OF THE DISSERTATION

Search for the Chiral Vortical Effect

Using  $\Lambda$ - $p$  Correlations

at STAR

by

Brian Chan

Doctor of Philosophy in Physics

University of California, Los Angeles, 2023

Professor Huan Z. Huang, Chair

The Quark Gluon Plasma (QGP), a state of matter in which deconfinement and chiral symmetry restoration occur, can be produced by ultra-relativistic heavy-ion collisions. This state of matter is of great interest because in QGP, the colored quarks and gluons, fundamental entities in matter whose interactions are governed by the Quantum ChromoDynamics (QCD), can exist as a fluid over an extended volume much larger than the size of nuclei. The Chiral Vortical Effect (CVE) is a QCD phenomenon related to the quark chirality arising from the topological sector of the QCD and the large vorticity of the QGP created. The search for quark chirality effects has been a major scientific objective at RHIC.

The Solenoid Tracker at RHIC (STAR) detector, located at the Relativistic Heavy-Ion Collider (RHIC) in the Brookhaven National Laboratory (BNL), provides the experimental capability needed to probe the QGP, with the particle tracking and identification abilities built into the different parts of the detector. This thesis focuses on the search for the CVE with STAR data from Au+Au collisions at  $\sqrt{s_{NN}} = 27$  GeV and 19.6 GeV, from Run 2018 and 2019, respectively.

In order to search for the CVE, measurements of the correlations of the azimuthal angles between baryons,  $\Lambda$  and protons, were made, in the form of observables  $\gamma_{112} \equiv \langle \cos(\phi_\alpha + \phi_\beta - 2\Psi_{RP}) \rangle$  and  $\gamma_{132} \equiv \langle \cos(\phi_\alpha - 3\phi_\beta + 2\Psi_{RP}) \rangle$ , in which mathematically the CVE effects would be made manifest.  $\alpha$  and  $\beta$  represent the charge of the correlated particles,

and to reduce the background, we take  $\Delta\gamma \equiv \gamma_{OS} - \gamma_{SS}$ , where we subtract the measurement of the correlation of pairs of same charge particles (SS) from that of opposite charge particles (OS). The KFParticle package was used for the reconstruction of the  $\Lambda$  particles. To have a better interpretation of the results, the observables  $\kappa_{112} \equiv \Delta\gamma_{112}/(v_2 \cdot \Delta\delta)$  and  $\kappa_{132} \equiv \Delta\gamma_{132}/(v_2 \cdot \Delta\delta)$  were computed that allows for comparison across different systems. Specifically, these observables were compared with data generated from the A Multi-Phase Transport Model (AMPT) simulations.

In addition, the flow-related background was also something that needed to be dealt with to get a clearer signal from the  $\Delta\gamma_{112}$  and  $\Delta\gamma_{132}$  observables. The Event Shape Selection method was applied in order to project the events to zero flow, attempting to reduce the flow-related background as much as possible. The Event Plane Detector (EPD) event plane was used as well to reduce the non-flow backgrounds.

Our search yielded no definitive observation of the proposed CVE signal. We obtained an upper limit on the CVE signal from Au+Au collisions at 19.6 GeV and 27 GeV energies. Because of large statistical errors due to limited number of  $\Lambda$  per event, the obtained upper limit is not very stringent. We will also discuss a possible effect due to the presence of baryon annihilations and the future direction of CVE searches. Large statistical data sets will be critical for those efforts.

The dissertation of Brian Chan is approved.

Gang Wang

Zhongbo Kang

Per J. Kraus

Graciela B. Gelmini

Huan Z. Huang, Committee Chair

University of California, Los Angeles

2023

*To God and my parents  
for always being there*

*To Jo  
for your love and support*

*To my church  
for carrying me all these years*

## TABLE OF CONTENTS

<b>1</b>	<b>Introduction</b>	<b>1</b>
1.1	Basic Parameters and Understanding of the Collisions	1
1.2	Quark Gluon Plasma	3
1.2.1	Predicted Signatures of the QGP	4
1.2.2	Experimental Probes of the QGP	13
<b>2</b>	<b>The Experimental Set-Up: RHIC &amp; STAR</b>	<b>19</b>
2.1	The Relativistic Heavy Ion Collider (RHIC)	19
2.2	Solenoid Tracker at RHIC (STAR)	23
2.2.1	Time Projection Chamber (TPC)	25
2.2.2	Time-of-Flight Detector (TOF)	31
2.2.3	Event Plane Detector (EPD)	33
<b>3</b>	<b>Introduction to the CME/ CVE</b>	<b>36</b>
3.1	Chiral Magnetic Effect	36
3.2	Chiral Vortical Effect	40
3.3	Studying CVE in Heavy-Ion Collisions	42
3.3.1	Vorticity in Heavy-Ion Collisions	42
3.3.2	Initial Conditions	43
3.3.3	CME in Heavy-Ion Collisions	43
3.3.4	CVE in Heavy-Ion Collisions	45
<b>4</b>	<b>Data Set and Reconstruction of Particles</b>	<b>47</b>
4.1	Information on Data Set	47

4.2	Run-by-Run Quality Checks . . . . .	47
4.3	Event Characterization and Selection . . . . .	50
4.3.1	Event Selection Criteria . . . . .	50
4.3.2	Centrality . . . . .	51
4.4	$\Lambda(\bar{\Lambda})$ Baryon Reconstruction . . . . .	57
4.4.1	Background Estimation . . . . .	59
4.4.2	KFParticle . . . . .	61
4.4.3	Background Estimation . . . . .	65
4.4.4	Efficiency Correction . . . . .	74
4.5	Primary Protons . . . . .	75
4.5.1	Selection Criteria . . . . .	75
4.5.2	Efficiency Correction . . . . .	76
4.6	Verification of Baryons with Elliptic Flow Comparisons . . . . .	78
4.7	A Multi-Phase Transport Model for Heavy Ion Collisions . . . . .	80
<b>5</b>	<b>Chiral Vortical Effect Analysis Results . . . . .</b>	<b>85</b>
5.1	$\gamma^{112}$ and $\gamma^{132}$ Correlators to search for the CVE . . . . .	85
5.1.1	Flow Normalized Correlator $\kappa_{112}$ and $\kappa_{132}$ . . . . .	87
5.2	Data Analysis Details . . . . .	89
5.2.1	Reaction Plane Reconstruction . . . . .	89
5.2.2	Detector Acceptance Correction . . . . .	94
5.2.3	Systematic Uncertainty Estimation . . . . .	100
5.3	Ensemble Results . . . . .	110
5.4	Event Shape Selection Method . . . . .	117
5.4.1	Application of ESE on $\Lambda$ - $p$ CVE Observables . . . . .	125

5.4.2	4 Approaches of ESE . . . . .	130
5.4.3	Methodology . . . . .	131
5.5	Summary of Results for the Search for the CVE . . . . .	139
<b>6</b>	<b>Conclusion and Future Perspectives . . . . .</b>	<b>150</b>
6.1	Baryon Annihilation Effect on $\Delta\gamma$ Correlation . . . . .	150
6.2	Conclusion . . . . .	152
<b>A</b>	<b>List of Bad Runs . . . . .</b>	<b>154</b>

## LIST OF FIGURES

1.1	This figure demonstrates a simplified picture of the two beams of nuclei colliding relativistically, with the nuclei being Lorentz-contracted into dishes in the center-of-mass frame. This is a central collision as the distance between the centers of the colliding beams of nuclei is close to 0, and the overlapping region is large [5].	2
1.2	A schematic light cone diagram of the evolution of a relativistic heavy-ion collision over time and space. $T_c$ represents the critical temperature, $T_{ch}$ the temperature at which the chemical freeze-out occurs, and $T_{fo}$ the temperature at which the kinetic freeze-out occurs [6]. . . . .	3
1.3	Phase diagram that illustrates the phase transitions between hadronic gas and the Quark Gluon Plasma. It also includes information about the different energies that are covered by the beam energy scan performed at RHIC and how it spans different parts of the phase diagram that includes the predicted critical point of the phase transitions [11]. . . . .	5
1.4	This figure shows the ratio between Stefan-Boltzmann pressure, $P_{SB}$ , and temperature, $T^4$ , as computed in LQCD with different number of degrees of freedom as a function of temperature. Specifically, the (2+1)-flavor corresponds to 2 light and 1 four-times-heavier strange quark mass. The arrows on the right indicate the corresponding Stefan-Boltzmann pressures for the various quark flavor assumptions [8]. . . . .	6
1.5	This figure shows the fit results for the screening mass $\mu(T)/T$ as a function of temperature; the dotted lines represent the lowest order perturbative QCD prediction, which is given by the equation $\mu(T) = A * m_e^0(T)$ [12]. . . . .	7

- 1.6 This figure shows the lattice QCD calculations for two dynamical quark flavors. It demonstrates the coincidence of the chiral symmetry restoration and deconfinement phase transitions with both plots being a function of the bare coupling strength  $\beta$  used in the computations. The left figure shows the deconfinement phase transitions, and the rapid decrease of chiral condensate ( $\bar{\Psi}\Psi$ ) in the right figure shows the signature of chiral symmetry restoration [8]. . . . . 8
- 1.7 This figure shows the time evolution of the spatial eccentricity  $\epsilon_x$  and the momentum anisotropy  $\epsilon_p$  for Au+Au collisions at RHIC with impact parameter (b) of 7fm - a non-central collision. The dashed curves are calculations based on computations of pressure as a function of energy density at vanishing net baryon density for the equation of state of an ideal gas of massless partons. The solid curves are ones based on computations that connect the equation of state of an ideal gas of massless partons, combined with a Hagedorn resonance gas, with a first-order phase transition at  $T_c = 164$  MeV, which is also what is used to model hydrodynamics calculations at RHIC. The time scale depicted on this figure is from initial attainment of local thermal equilibrium to the freezeout time in this calculation [16]. . . . . 10
- 1.8 These figures illustrate the excitation function of the elliptic flow coefficient  $v_2$ , the left vertical axis, and the radial flow  $\langle\langle v_\perp \rangle\rangle/c$ , the right vertical axis. The left figure is for Pb+Pb collisions with impact parameter (b) of 7fm, and the right figure is the side-on-side U+U collisions at  $b = 0$ fm. The solid curves correspond to the equation of state that is mentioned in Figure 1.7 for RHIC predictions, while the dashed curve is the second part (equation of state of a Hagedorn resonance gas) that is combined with the dashed curve in Figure 1.7 to give rise to the equation of state that the solid lines are based on. The soft phase transition stage in EOS Q leads to the dip in the elliptic flow [17]. The horizontal arrows at the bottom of the plots reflect early projections of particle multiplicities for the various facilities, but now it is shown that RHIC collisions produce multiplicities in the vicinity of the predicted dip [7]. . . . . 11

1.9	This figure illustrates ratios of $p_T$ -integrated yields for different hadron species measured in the central Au+Au collisions at $\sqrt{s_{NN}} = 200$ GeV at the STAR experiment. The horizontal bars represent the statistical model fits to the measured yield ratios [7]. . . . .	14
1.10	(a) This figure shows the STAR experimental results obtained from Au+Au collisions at $\sqrt{s_{NN}} = 200$ GeV of elliptic flow as a function of transverse momentum [23]. The dashed lines are hydrodynamics calculations [24], assuming early thermalization, ideal fluid expansion, an equation of state consistent with LQCD calculations that include a phase transition at $T_c = 165$ MeV, and a sharp kinetic freezeout at 130 MeV (EOS Q mentioned in Figure 1.8). (b) Similar calculations as those in (a), but now also with EOS H - equation of state for a hadron gas, and compared with STAR experimental results obtained from Au+Au collisions at $\sqrt{s_{NN}} = 130$ GeV [25]. This figure is taken from [7]. . . . .	15
1.11	The ratio of inclusive charged hadron yields in Au+Au and d+Au collisions to that of $p+p$ collisions from 4 different experiments [7]: (top left) BRAHMS [28], (top right) PHENIX [29], (bottom left) PHOBOS [30] and (bottom right) STAR [31]. . . . .	17
1.12	This figure shows the binary-scaled yield ratio $R_{CP}(p_T)$ of central (0-5%) to peripheral (40-60%, 60-80%) collisions for charged hadrons from Au+Au collisions at $\sqrt{s_{NN}} = 200$ GeV [34]. . . . .	18
2.1	A schematic drawing of the RHIC accelerator complex as shown on the official website. The important subsystems are labelled, and they are, respectively, (1) the Electron Beam Ion Source (EBIS), (2) the Linear Accelerator (Linac), (3) the Booster Synchrotron, (4) the Alternating Gradient Synchrotron (AGS), (5) the AGS-to-RHIC Beamline, and finally, (6) the RHIC magnetic rings [6]. . . . .	22
2.2	Layout of the STAR Detector as provided on the official STAR website [42] . . .	23
2.3	A schematic diagram of the STAR TPC [53] . . . . .	26

2.4	Schematic diagram of a full sector of the anode pad plane [53] . . . . .	28
2.5	The distribution of ionization energy loss of various particle species through the TPC as a function of their momenta [56]. . . . .	30
2.6	The cross section of the MRPC module of TOF, as well as a drawing of the readout pad array [56]. . . . .	32
2.7	TOF recorded values of $1/\beta$ of particles vs. their rigidity. The curves represent the expected mean values for the various particle species as labelled [60]. . . . .	33
2.8	An illustration of one of the two EPD wheels, which shows the 12 supersectors along with the 31 tiles on each of them, and the signal flow that proceeds from the tiles through the optical fibers into the STAR DAQ [51] . . . . .	34
3.1	An illustration of the gluon field, which is periodic in one direction and oscillator-like in all other directions in functional space. And the instanton is a large fluctuation that corresponds to quantum tunneling from one minimum to another in this gluon field, whereas the sphaleron is a solution that is static, unstable, and doesn't involve quantum tunneling [65]. One can picture it as the instanton being a transition that occurs from one valley to a neighboring one in the figure, passing through underneath the peak, whereas the sphaleron is a transition that goes from a valley to the neighboring peak, and back down to another valley. It is theorized that these vacuum transitions lead to the chirality imbalance that exists in the QGP, and that is then transferred to the quarks, which with chiral symmetry restoration have zero QCD mass, and hence sustains the chirality imbalance, a necessary condition for the CME. Figure is taken from [65]. . . . .	38
3.2	This figure demonstrates in a simple way what we have discussed in the text about how CME arises through the presence of a magnetic field, chirality imbalance, as well as chiral anomaly. [67] . . . . .	40

3.3	This figure demonstrates the CVE, in the specific case where there are more right-handed particles than left-handed ones (thus $\mu_5 > 0$ ), as well as more quarks than antiquarks ( $\mu > 0$ ). [67] . . . . .	42
3.4	Measurement of $\langle \sin(\phi - \Psi_{RP}) \rangle$ for Au+Au collisions at $\sqrt{s_{NN}} = 200$ GeV [71].	44
4.1	The nine criteria that were used in determination of the quality of the runs and whether or not they were included in this analysis. The red data points correspond to the runs that were removed (these runs are the same runs in all nine plots, not just the runs that were removed by the criterion that the plot represents). The black data points correspond to the runs that were ultimately included in the analysis and passed our quality checks. These plots correspond to the data collected by STAR in 2018, with Au+Au collisions at $\sqrt{s_{NN}} = 27$ GeV. . . . .	49
4.2	The transverse components and $z$ component of the primary vertex of the collision events to demonstrate the cuts that were applied on the event level. The top two plots are for Au+Au 19.6 GeV collisions, and the bottom two are for 27 GeV. .	51
4.3	This is a Glauber Monte Carlo event, simulated as a Au+Au collision at $\sqrt{s_{NN}} = 200$ GeV. The impact parameter ( $b$ ) of this simulated collision is 6 fm, a quantity that is randomly drawn from the distribution $d\sigma/db = 2\pi b$ . The left is a view in the transverse plane, and the right is a view from the beam pipe [73]. . . . .	52
4.4	A cartoon demonstration of how the multiplicity is related to Glauber model quantities like the impact parameter, $b$ , and the number of participants. Note that this is simply an illustration and does not show actual measurements [73]. .	54
4.5	Plot (a) shows the distribution of events across the centrality classes for 19.6 GeV Au+Au collisions, and Plot (b) is for 27 GeV Au+Au collisions. This is weighted by the event weight that is generated from the StRefMultCorr class. For reference, Table 4.3 shows the conversion between centrality classes and centrality bins used here. . . . .	56

4.6	This diagram demonstrates the topology of the decay of a general neutral particle into two daughters, and thus can be illustrative for our specific case of $\Lambda(\bar{\Lambda})$ Baryon particles decaying into $p\pi^-$ and $\bar{p}\pi^+$ . DCA is short-hand for Distance of Closest Approach, which is the closest distance of any two given points, or a track to a point, or any two tracks [75]. . . . .	58
4.7	An example distribution of $\Lambda$ Mass; The red line represents the polynomial fit to determine the background; the blue lines represent the mass cuts for optimal signal to background ratios while maintaining sufficient statistics. . . . .	60
4.8	The purity statistics of $\Lambda/\bar{\Lambda}$ particles for 27 GeV Au+Au collisions. The black data points represent $\Lambda$ and red data points represent $\bar{\Lambda}$ . . . . .	61
4.9	This is a block-diagram of the scheme used to reconstruct short-lived particles employed in the KF Particle Finder package [80]. The cuts on $\chi_{fit}^2$ and $\chi_{topo}^2$ are given in terms of the number of degrees of freedom. . . . .	64
4.10	Figures (a)-(h) are for 19.6 GeV Au+Au collisions, and Figures (i)-(p) are for 27 GeV Au+Au collisions. These figures are examples of the mass distribution of the reconstructed baryons for demonstration purposes. All these plots correspond to centrality bin 5, which is 20-30%, and for the event handle pair-pion $q_2^2$ between the values 0.9 and 1.0.  These plots are example plots for how the background estimation for the signals are done. The plots on the left column demonstrate how the signal was extracted (specifically the mass range that was selected for the signal), and the right column demonstrate the mass range for the background estimation of the signal. The red curve represents the estimation of the background under the signal curve, which is how we compute the percent purity for each of the centrality - pair-pion $q_2^2$ bins for background corrections in this analysis. . . . .	68

4.11	For 19.6 GeV Au+Au collisions, binned by pair-pion $q_2^2$ . The black data points correspond to $\Lambda$ purity statistics, whereas the red ones correspond to $\bar{\Lambda}$ particles. As can be seen from the plots, there is not a strong dependence on the event handler, and the purity is very good - over 90% of reconstructed baryons are estimated to be true baryons for all centralities and all event handler bins. . . .	70
4.12	For 27 GeV Au+Au collisions, binned by pair-pion $q_2^2$ . The black data points correspond to $\Lambda$ purity statistics, whereas the red ones correspond to $\bar{\Lambda}$ particles. As can be seen from the plots, there is not a strong dependence on the event handler, and the purity is very good - over 94% of reconstructed baryons are estimated to be true baryons for all centralities and all event handler bins. . . .	71
4.13	For 19.6 GeV Au+Au collisions, binned by single-pion $q_2^2$ . The black data points correspond to $\Lambda$ purity statistics, whereas the red ones correspond to $\bar{\Lambda}$ particles. As can be seen from the plots, there is not a strong dependence on the event handler, and the purity is very good - over 90% of reconstructed baryons are estimated to be true baryons for all centralities and all event handler bins. . . .	72
4.14	For 27 GeV Au+Au collisions, binned by single-pion $q_2^2$ . The black data points correspond to $\Lambda$ purity statistics, whereas the red ones correspond to $\bar{\Lambda}$ particles. As can be seen from the plots, there is not a strong dependence on the event handler, and the purity is very good - over 94% of reconstructed baryons are estimated to be true baryons for all centralities and all event handler bins. . . .	73
4.15	The left figures are the efficiency results for $\Lambda$ , and the right ones are for $\bar{\Lambda}$ . The first row corresponds to 19.6 GeV Au+Au collisions; the second row corresponds to 27 GeV Au+Au collisions. % Reconstructed refers to the reconstruction efficiency, which is calculated as ( $\#$ Reconstructed / $\#$ Total Embedded) for each $p_T$ bin. . . . .	75

4.16	The product of the efficiency of identification from the TPC and the efficiency of identification from TOF of protons and antiprotons across the nine centralities, as a function of their transverse momentum. (a) 19.6 GeV Au+Au; (b) 27 GeV Au+Au. . . . .	77
4.16	These figures compare the elliptic flow of $\Lambda$ particles from the data sets of interest in this analysis, with that of the study done in 2016 [82]. We see that in general the results agree with each other, sufficient to claim validity for the reconstruction and selection of these particles. . . . .	80
4.17	The left figure illustrates the scheme for the default AMPT model, and the right is that for the model with string melting. [114] . . . . .	82
5.1	These figures show the event plane resolutions calculated according to the sub event plane methods for TPC, 1 <sup>st</sup> and 2 <sup>nd</sup> order EPD event planes. Black - TPC; Blue - 1 <sup>st</sup> order EPD; Red - 2 <sup>nd</sup> order EPD. Unfortunately, with selections of events that have to have at least one baryon reconstructed, the more peripheral centralities are biased so that the EPD EP resolution is too low, also they have very few statistics, therefore the most peripheral centrality will be removed from the final results of this analysis (which is also why the 75% red data point is missing). (a) is 19.6 GeV Au+Au collisions, while (b) is 27 GeV Au+Au collisions.	93
5.2	These plots are examples of Event Planes that exhibit detector acceptance differences, thus leading to a non-uniform distribution. They are taken from Centrality 30-40%, with the top two being TPC event planes and bottom two are first order EPD event planes. . . . .	95
5.3	These six plots are examples of Event Planes based on TPC tracks. The first two rows correspond to the sub event plane method, and the last row corresponds to the full event plane method. . . . .	98
5.4	These plots are examples of Event Planes based on EPD tracks. They correspond to the 1 <sup>st</sup> order EPD event planes, and all of these are according to the sub event plane method. . . . .	99

5.5	These plots are examples of Event Planes based on EPD tracks. They correspond to the $2^{nd}$ order EPD event planes, and all of these are according to the sub event plane method. . . . .	100
5.6	Systematic Cut on the $z$ -component of the primary vertex of events. sys_1 - the events that fall on the left of 0; sys_5 - the events that fall on the right of 0. . .	103
5.7	Systematic Cut on nHitsFit of daughters of reconstructed baryons. sys_2 - the events that fall on the right of the red line. . . . .	104
5.8	Systematic Cut on nSigma of daughters of reconstructed baryons. sys_3 - the events that fall on the left of the red line. . . . .	105
5.9	Systematic Cut on distance of closest approach of daughters of reconstructed baryons. sys_4 and sys_5 - the events that fall on the right of the red line. (a) and (b) correspond to proton cuts; (c) and (d) correspond to pion cuts. . . . .	107
5.10	Systematic Cut on transverse momentum of daughters of reconstructed baryons. sys_6 - the events that fall on the right of the red line. . . . .	108
5.11	Systematic Cut on nSigma of primary protons. sys_7 - the events that fall on the left of the red line. . . . .	109
5.12	Ensemble results for $\Delta\gamma$ using $\Lambda$ - $p$ pairs. . . . .	112
5.13	AMPT results for $\Delta\gamma$ using $\Lambda$ - $p$ pairs. . . . .	113
5.14	Ensemble results for $\kappa$ using $\Lambda$ - $p$ pairs. . . . .	115
5.15	AMPT results for $\kappa$ using $\Lambda$ - $p$ pairs. . . . .	116
5.16	A schematic diagram of the event shape selection that attempts to project the entire event to spherical events. We see that this method is based on the particle emission pattern in the transverse plane, and therefore it could be possible that both $v_2$ and $q_2$ of the particles of interest fluctuate towards zero and yet there is a finite eccentricity in the overlapping region. . . . .	119

5.17	Top Panel: True $v_2$ of particles of interest in sub-event A. Bottom Panel: Reaction plane calculated from sub-event B, used to correct results from sub-event A, to avoid self-correlation. $x$ -axis is the variable proposed, $v_{2,ebye}^{observe}$ that describes the ellipticity of the event. As seen in this figure, unfortunately such an event does not truly describe the ellipticity of the particles of interest, and especially even when it is required to be 0, it does not coincide with the particles of interest exhibiting a spherical nature. The correlation between $R^B$ and the event handle is also troubling. This plot is taken from [139]. . . . .	120
5.18	In the bottom panel, it is clear that the true elliptic flow $v_2^A$ and the corrected elliptic flow $v_2^{observe}$ as functions of $q$ are in a higher level of agreement. This plot is taken from Ref. [139]. . . . .	121
5.19	In the bottom panel, it is clear that the true elliptic flow $v_2^A$ and the corrected elliptic flow $v_2^{observe}$ as functions of $q$ are in a higher level of agreement. This plot is taken from Ref. [139]. . . . .	122
5.20	This figure shows in (a) $N_{part} \times \gamma^{112}$ and (b) $N_{part} \Delta\gamma^{112}$ as a function of $q^2$ . The full symbols represent results obtained with the true reaction plane, whereas the open symbols are for the reconstructed event plane corrected for the event plane resolution. In the lower panel, the solid line is a second-order polynomial fit of the full data points, and the dashed line is for the open data points. This plot is taken from Ref. [139]. . . . .	124
5.21	Distribution of $\Lambda/p$ Multiplicities for Au+Au 19.6 GeV. . . . .	127
5.22	Distribution of $\Lambda/p$ Multiplicities for Au+Au 27 GeV. . . . .	129
5.23	Correlators of interest, $\gamma^{112}$ and $\gamma^{132}$ , binned by the event shape handlers used to control the flow background. . . . .	132
5.24	$v_2$ binned by the event shape handlers. . . . .	134

5.25	Event Plane resolutions binned by event shape handler. The red line depicts the range of the event shape handler considered in the ESE approach, but the fit values were not used. The specific binned values were used in the event plane resolution correction. . . . .	135
5.26	$\Delta\gamma^{112}$ and $\gamma^{132}$ event shape selection method for the 4 recipes, projecting to zero flow, based on the first order EPD event plane. . . . .	137
5.27	$\Delta\gamma^{112}$ and $\gamma^{132}$ event shape selection method for the 4 recipes, projecting to zero flow, based on the second order EPD event plane. . . . .	139
5.28	$\Delta\gamma^{112}$ and $\Delta\gamma^{132}$ for $\Lambda$ - $p$ Correlations for Au+Au 19.6 GeV collisions. . . . .	143
5.29	$\Delta\gamma^{112}$ and $\Delta\gamma^{132}$ for $\Lambda$ - $p$ Correlations for Au+Au 27 GeV collisions. . . . .	147
5.30	Summary results for $\Delta\gamma^{112}$ and $\Delta\gamma^{132}$ for $\sqrt{s_{NN}} = 19.6$ GeV and 27 GeV for 1 <sup>st</sup> and 2 <sup>nd</sup> order EPD event plane. . . . .	148
6.1	Distribution of the ratio of number of $\Lambda$ - $p$ pairs in same event data to mixed event data as a function of $\Delta q$ , the invariant vector used here to measure how close these tracks are in the kinematic phase space. This is data from the 2018 27 GeV Au+Au data set. . . . .	151

## LIST OF TABLES

4.1	Triggers Used in Analysis . . . . .	47
4.2	$N_{\text{part}}$ of Centrality Classes . . . . .	55
4.3	Centrality Classes and Centrality Bins . . . . .	57
4.4	Track Quality Cuts for Daughter Tracks for $\Lambda \rightarrow p\pi^- / \bar{\Lambda} \rightarrow \bar{p}\pi^+$ . . . . .	59
4.5	Centrality-Dependent Topology Cuts for $\Lambda \rightarrow p\pi^- / \bar{\Lambda} \rightarrow \bar{p}\pi^+$ . . . . .	59
4.6	Track Quality Cuts for Identifying Primary $p/\bar{p}$ Tracks . . . . .	76
5.1	Systematic Uncertainty Estimation . . . . .	102
5.2	Upper Bound of CVE Signal As Represented By $N_{\text{part}}\Delta\gamma^{112}$ . . . . .	148
6.1	Upper Bound of CVE Signal As Represented By $N_{\text{part}}\Delta\gamma_{112}$ . . . . .	153

## ACKNOWLEDGMENTS

As I look back to the past seven years, I can't help but recognize that there are so many people in my life that I must thank for the completion of this dissertation.

I would like to first thank my advisor, Professor Huan Zhong Huang, for the opportunity to pursue this study, for introducing me to this topic of interest, for being a constant source of knowledge, and for the support and guidance shown me all these years. Thank you also for showing us care through the ups and downs, especially with COVID as well as my following transition. I genuinely am extremely grateful for that.

I would also like to thank my doctoral committee members, Professor Zhongbo Kang, Professor Per Kraus, Professor Graciela Gelmini and Professor Gang Wang for their time and critical feedback. I am also very thankful for the time they took, even during COVID and the days with Zoom, to be a part of my committee, both for my advancement to candidacy as well as my thesis defense.

I am also very thankful for all the members of the Nuclear Physics Group at UCLA, specifically to Dylan Neff for going through the past seven years together, to Zhiwan Xu for all the analysis help I received from her, and to everyone else for the many discussions we've had regarding Physics and everything else. I would also specifically like to thank Gang for all the ways he guided me through my research analysis, gave me insights and inspired me with ideas, and in general always being there for me to turn to when I hit obstacles along the way. Thank you so much for being so responsive over emails, and always so patient with me!

Thank you to all the members of the STAR Collaboration that made studying these topics possible. It would not have been remotely probable for me to pursue this dissertation without the hard work of every one of the members that allowed this experiment to go on for so many years, yielding fruitful results.

And of course I would like to thank my family. Thank you to Mom and Dad for always supporting me, for your unconditional love towards me, and all the help, from physical, to emotional, to even financial, that you have given me despite the difficulties over all these

years that allowed me to complete this dissertation. Thank you to my lovely Jo, who has been a constant source of support and love as well the past few years, crucial to me being able to cross the finishing line now.

I would also like to thank God, who through the church, showed me so much support through the past years. From the fellowship that we had, to the ministry that kept me sober, to all the relationships that have become a lifeline for me. I am so thankful!

I am so utterly grateful to all, because I know for a fact that I would not have been able to do this without all these people in my life, whom I definitely do not deserve to have.

Praise the Lord!

## VITA

- 2012 – 2016 Bachelor of Arts in Physics and Mathematics,  
University of California, Berkeley, California, United States
- 2016 – 2018 Teaching Assistant,  
Department of Physics and Astronomy,  
University of California, Los Angeles
- 2018 – Graduate Student Researcher,  
Nuclear QCD group  
Department of Physics and Astronomy,  
University of California, Los Angeles

# CHAPTER 1

## Introduction

In the 1970s, T.D. Lee and G.C. Wick proposed the possibility of creating new physical systems, one of which is the Quark Gluon Plasma (QGP), through heavy-ions collisions [1]. Since then, there have been different efforts to pursue this goal, starting from the Lawrence Berkeley National Lab (LBNL) in the late 1970s and 1980s [2], to the present day heavy-ion colliders, such as the Relativistic Heavy-Ion Collider (RHIC) at the Brookhaven National Laboratory (BNL) that runs with beam energy spanning from a few GeV to 200 GeV [3], and the Large Hadron Collider (LHC) at the European Organization for Nuclear Research (CERN) that reaches the energy of 14 TeV [4]. There are a lot of topics of high interest associated with the Quark Gluon Plasma, which is why there has been much effort poured into creating this physical system. However, before diving into the specifics of the interest associated with the QGP, we will first take a look at the details about these heavy-ion collisions, from what they are, to how they are capable of creating the QGP that we are interested in.

### 1.1 Basic Parameters and Understanding of the Collisions

The main characteristics that define the initial state of heavy-ion collisions are: the beam energy, the heavy ion species used, and the impact parameter,  $b$ , which is the distance between the centers of the colliding beams of nuclei. In relativistic heavy-ion collisions, the colliding nuclei are Lorentz-contracted into dishes in the center-of-mass frame, and the impact parameter determines how much overlap there is between the two beams (see Figure 1.1 for a simplified example of what the collision could look like). The nucleons in the region where

the two beams overlap are named participant nucleons, as they are the ones that interact with each other, whereas those that are outside of the overlapping region are called spectator nucleons. Figure 1.1 portrays a central collision, which is characterized by a small impact parameter, and therefore a large overlapping area relative to the non-overlapping area. When the impact parameter is large with respect to the radius of the nuclei, then there are much fewer participant nucleons compared with spectator ones, and thus the collision is regarded as a peripheral collision, in contrast to the central ones. However, the impact parameter is not a direct observable in heavy-ion collision experiments. Instead, because the number of produced particles is correlated to the number of participant nucleons, we are able to use the number of produced particles, or what is called multiplicity, to determine how central the collisions are.

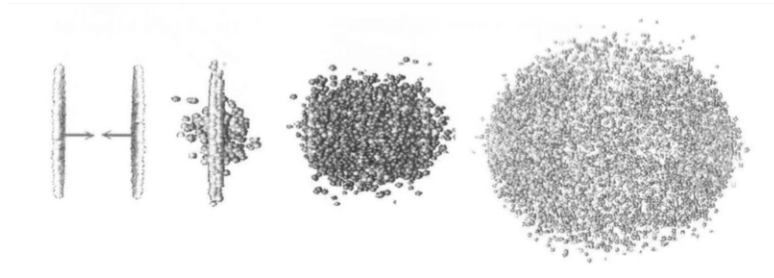


Figure 1.1: This figure demonstrates a simplified picture of the two beams of nuclei colliding relativistically, with the nuclei being Lorentz-contracted into dishes in the center-of-mass frame. This is a central collision as the distance between the centers of the colliding beams of nuclei is close to 0, and the overlapping region is large [5].

In collisions that are more central, a fireball is created from the participant nucleons, and the energy density can be so high that the fire ball reaches a (locally) thermalized equilibrium phase with partonic degrees of freedom and high temperature, and this material would be what we theorize to be the Quark Gluon Plasma that we had set out to create with these heavy-ion collisions. After it is created, it would expand rapidly and thus the temperature would decrease, and the medium becomes a mixed phase of partonic and hadronic matter after the temperature decreases past the critical temperature. As the temperature continues to decrease, chemical freeze-out happens, and the hadron species are fixed. The next stage is

then kinematic freeze-out as temperature continues to drop, and the hadrons stop interacting elastically with each other. Figure 1.2 shows the evolution over time and space of a relativistic heavy-ion collision [6].

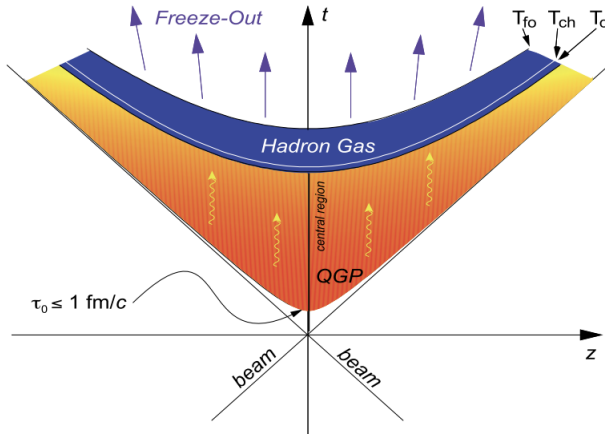


Figure 1.2: A schematic light cone diagram of the evolution of a relativistic heavy-ion collision over time and space.  $T_c$  represents the critical temperature,  $T_{ch}$  the temperature at which the chemical freeze-out occurs, and  $T_{fo}$  the temperature at which the kinetic freeze-out occurs [6].

## 1.2 Quark Gluon Plasma

Equipped with an overview of relativistic heavy-ion collisions, we can look more into the fireball as mentioned in the end of the previous section - the Quark Gluon Plasma. As mentioned in a STAR review paper [7], it is important to define what the Quark Gluon Plasma is in order to decipher whether or not it is actually formed in the heavy-ion collisions. After taking over 20 years of understanding into account, the paper decides on the following definition of the Quark Gluon Plasma that we will also use here on out: “we take the QGP to be a (locally) thermally equilibrated state of matter in which quarks and gluons are deconfined from hadrons, so that color degrees of freedom become manifest over nuclear, rather than merely nucleonic, volumes.” This definition is significant, because according to the theory of QCD, the confining properties manifests itself as heavy quark potential that

increases linearly with distance, forcing quarks and gluons to be confined to a hadronic bag, which is also the reason for observations of only color-less states [8]. The QGP is therefore a state of matter at which the temperature is so high that such confining properties break down, and the matter exists in a deconfined state. It is expected that with sufficiently high temperature, as well as high density in nuclear matter, a transition will occur from excited hadronic matter to Quark Gluon Plasma. The QGP is believed to have existed in the first few microseconds after the Big Bang, and it could also exist in the cores of neutron stars [9]. The production and detection of the Quark Gluon Plasma itself would be an accomplishment, but in addition to that, it will allow one to study fundamental aspects of Quantum Chromodynamics (QCD) and confinement that are not possible in few-hadron experiments - by making it possible to study QCD over large distance scales [7].

### 1.2.1 Predicted Signatures of the QGP

As it is impossible to directly detect the creation of the QGP, we have to find signatures of it through measurements of physical quantities of the final state particles produced from the heavy-ion collisions. However, given the complexity of heavy-ion collisions and hadron formation, it is very difficult to have quantitative measurements that can unambiguously point to the presence of the QGP within the system. Therefore, in order to point to the existence of the QGP within the collisions detected by STAR, the collaboration had to identify the most striking qualitative predictions of the theory that yielded results that were quantitatively significant, and by making multiple of such observations, we are able to arrive at a conclusion that unambiguously point to the existence of the QGP despite the complexity of the system. Here will be a short summary of the various theoretical predictions as well as RHIC experimental results that show support for them, and therefore the production of the QGP within these heavy-ion collisions.

The theoretical understanding of the phase diagram related to the QGP (Figure 1.3) would begin with QCD's description of bulk thermally equilibrated strongly interacting matter. If we take the limit where the deconfined quarks and gluons are non-interacting and that the quarks are massless, then the Stefan-Boltzmann pressure,  $P_{SB}$ , as a function of temperature

$T$  at zero chemical potential would be determined by the following equation that is dictated by the degrees of freedom [10]:

$$\frac{P_{SB}}{T^4} = [2(N_c^2 - 1) + \frac{7}{2}N_c N_f] \frac{\pi^2}{90} \quad (1.1)$$

where  $N_c$  is the number of colors,  $N_f$  is the number of quark flavors. However, in order to model a more realistic situation, for example to incorporate effects of color interactions among the constituents, or having non-zero quark masses and chemical potential, or to model the transitions from hadrons to partons, we would need to make QCD calculations on a space-time lattice, what is known as LQCD.

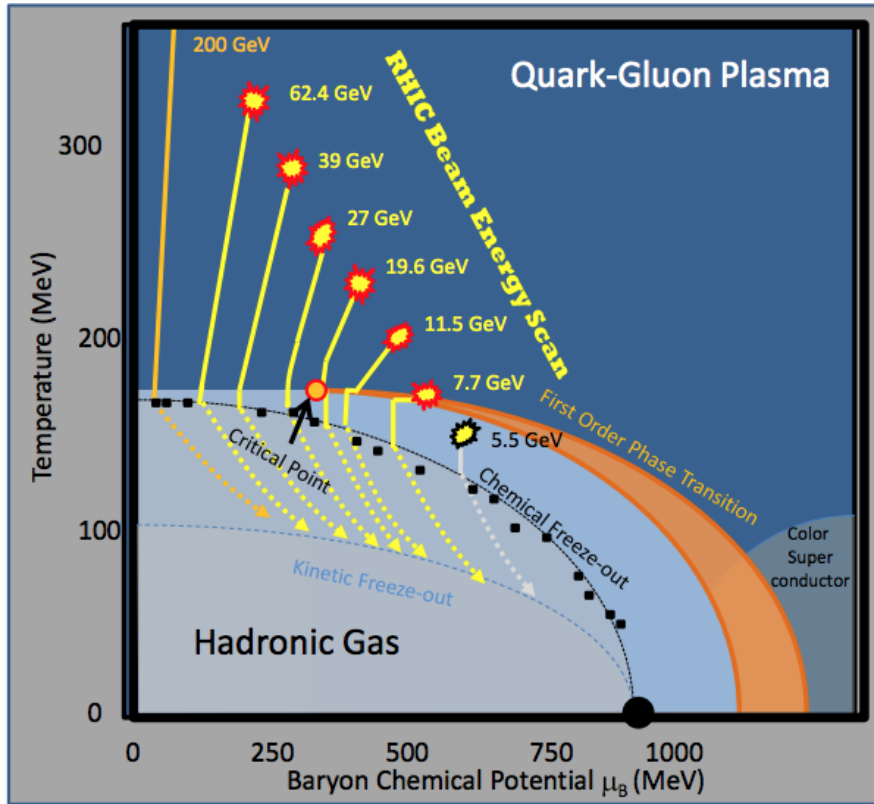


Figure 1.3: Phase diagram that illustrates the phase transitions between hadronic gas and the Quark Gluon Plasma. It also includes information about the different energies that are covered by the beam energy scan performed at RHIC and how it spans different parts of the phase diagram that includes the predicted critical point of the phase transitions [11].

Within the technical limits of this calculation to model reality, a few important predictions were made that would prove important to detecting signatures of the QGP creation in heavy-ion collisions. First, there is a predicted transition between a hadronic and QGP phase, occurring at a temperature around 160 MeV for zero chemical potential. Second, as seen in Figure 1.4, the ratio between the pressure and  $T^4$  saturates at values substantially below the Stefan-Boltzmann limit, which indicates substantial remaining interactions among the quarks and gluons in the QGP phase. Third, there is a screening mass that arises from the effective potential between a heavy quark-antiquark pair and deviates from the expectations from perturbative QCD, as seen in Figure 1.5. This increasing screening mass leads to a predicted suppression of charmonium production in relation to open charm.

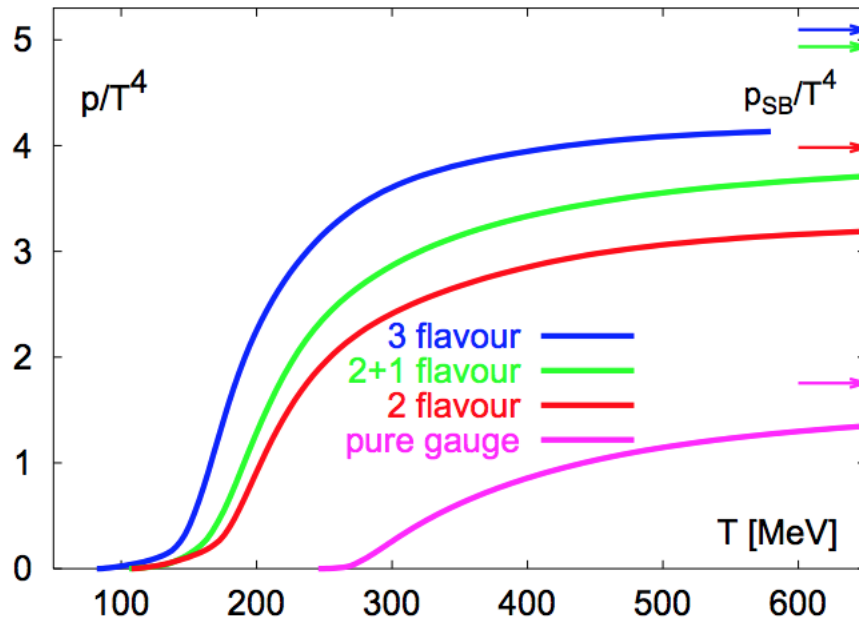


Figure 1.4: This figure shows the ratio between Stefan-Boltzmann pressure,  $P_{SB}$ , and temperature,  $T^4$ , as computed in LQCD with different number of degrees of freedom as a function of temperature. Specifically, the (2+1)-flavor corresponds to 2 light and 1 four-times-heavier strange quark mass. The arrows on the right indicate the corresponding Stefan-Boltzmann pressures for the various quark flavor assumptions [8].

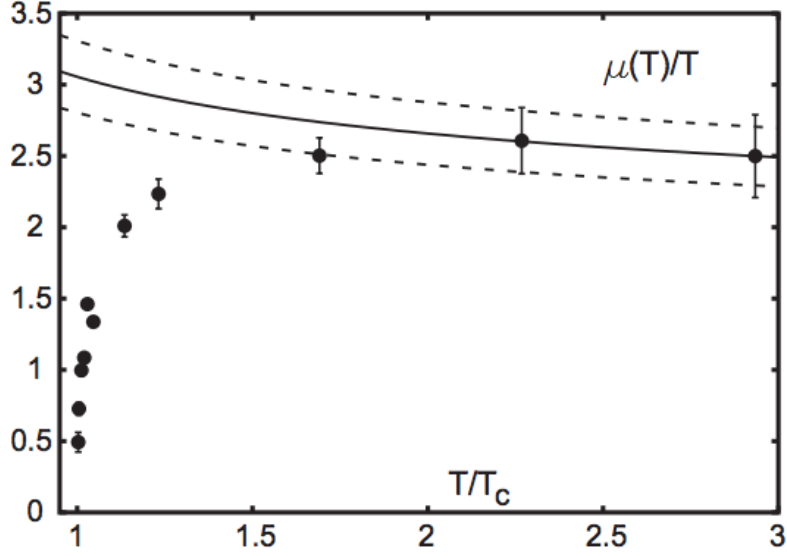


Figure 1.5: This figure shows the fit results for the screening mass  $\mu(T)/T$  as a function of temperature; the dotted lines represent the lowest order perturbative QCD prediction, which is given by the equation  $\mu(T) = A * m_e^0(T)$  [12].

Fourth, the calculations at non-zero chemical potential also predicts the existence of a critical point, which corresponds to the one seen in Figure 1.3. Fifth, this deconfinement transition is also often accompanied by a chiral symmetry restoration transition (see Figure 1.6), which is very important to the main analysis of this thesis as it is part of the fundamental physics processes that give rise to the Chiral Magnetic Effect and the Chiral Vortical Effect. At normal temperatures, the theory of QCD theorizes there to be an explicit symmetry breaking due to quantum corrections in the QCD partition function, the axial anomaly, and that dictates that the QCD mass for quarks stay nonzero as long as this chiral symmetry is broken [8]. However, when temperatures rise above the critical temperature, then chiral symmetry is restored, and the QCD mass of the quarks no longer have to be nonzero, which is a huge contributing factor to the CME/CVE that we have set out to measure in this analysis. Other than that, the reduction in the chiral condensate led to by this chiral symmetry restoration also leads to variations in in-medium meson masses.

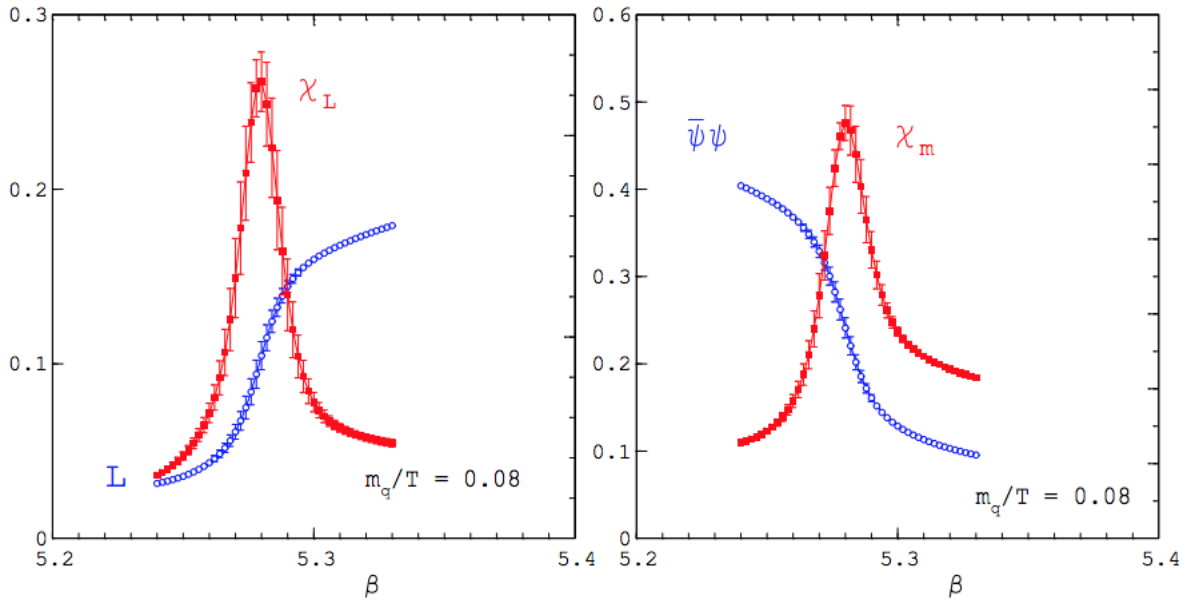


Figure 1.6: This figure shows the lattice QCD calculations for two dynamical quark flavors. It demonstrates the coincidence of the chiral symmetry restoration and deconfinement phase transitions with both plots being a function of the bare coupling strength  $\beta$  used in the computations. The left figure shows the deconfinement phase transitions, and the rapid decrease of chiral condensate ( $\bar{\Psi}\Psi$ ) in the right figure shows the signature of chiral symmetry restoration [8].

Another set of signatures that was predicted to be observed from the QGP comes from the application of relativistic hydrodynamics for the description of the hadronic fireballs that are created in the heavy-ion collisions. The hydrodynamic evolution of the fireball is sensitive to the equation of state of the flowing matter, which makes it sensitive to the possible crossing of a phase or crossover transition during the system expansion and cooling. Therefore, the hydrodynamic evolution would provide information on the material that is created by the collisions. By measuring the momenta of the produced particles at the final state and the correlations of such particles, we are able to make measurements on the transverse flows to compare with model predictions in studying the equation of state of the potential QGP that was formed in the collisions. In non-central collisions, there are azimuthally anisotropic

pressure gradients due to the shape of the reaction zone, and that leads to a nontrivial elliptic flow pattern that has to be measured using a Fourier decomposition of momentum spectra relative to the event-by-event reaction plane. Now the azimuthal distribution of the produced particles can be expanded with a Fourier series:

$$\frac{dN}{d\phi} = 1 + 2v_1 \cos(\phi - \Psi) + 2v_2 \cos(2(\phi - \Psi)) + \dots \quad (1.2)$$

with  $\phi$  being the azimuthal angle of the produced particle and  $\Psi$  as the reaction plane angle; the second Fourier coefficient,  $v_2 = \langle \cos(2(\phi - \Psi)) \rangle$ , is the elliptic flow mentioned above, which is the most significant term in representing the azimuthal anisotropy of hadrons in momentum space [13]. The reaction plane is defined by the beam direction and the impact parameter for that specific event. The important feature of elliptic flow is that it is “self-quenching” - the pressure-driven expansion tends to reduce the spatial anisotropy that gives rise to the azimuthally anisotropic pressure gradient that leads to elliptic flow [14, 15]. This can be seen in the hydrodynamic calculations illustrated in Figure 1.7. The increase in the momentum anisotropy led to by the gradual decline in spatial eccentricity by the pressure gradients demonstrate the self-quenching aspect of elliptic flow. This makes the elliptic flow particularly sensitive to earlier collision stages, when the spatial anisotropy and pressure gradient are the greatest. What this seems to illustrate is that when the fireball transitions from the QGP to hadronic matter, the buildup of momentum anisotropy in the flowing matter is stalled. This is more pronounced when we look at the computations of  $p_T$ -integrated elliptic flow as a function of produced hadron multiplicity shown in Figure 1.8. There is a dip under conditions where the phase transition occupies most of the early collision stages. One thing to note is that these calculations are based on a fixed impact parameter. Therefore, to confirm these predictions, measurements are made as a function of collision energy.

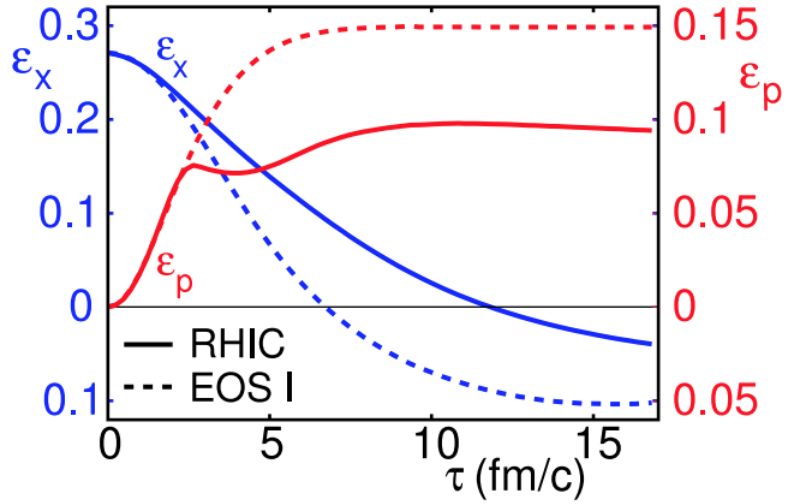


Figure 1.7: This figure shows the time evolution of the spatial eccentricity  $\epsilon_x$  and the momentum anisotropy  $\epsilon_p$  for Au+Au collisions at RHIC with impact parameter ( $b$ ) of 7fm - a non-central collision. The dashed curves are calculations based on computations of pressure as a function of energy density at vanishing net baryon density for the equation of state of an ideal gas of massless partons. The solid curves are ones based on computations that connect the equation of state of an ideal gas of massless partons, combined with a Hagedorn resonance gas, with a first-order phase transition at  $T_c = 164$  MeV, which is also what is used to model hydrodynamics calculations at RHIC. The time scale depicted on this figure is from initial attainment of local thermal equilibrium to the freezeout time in this calculation [16].

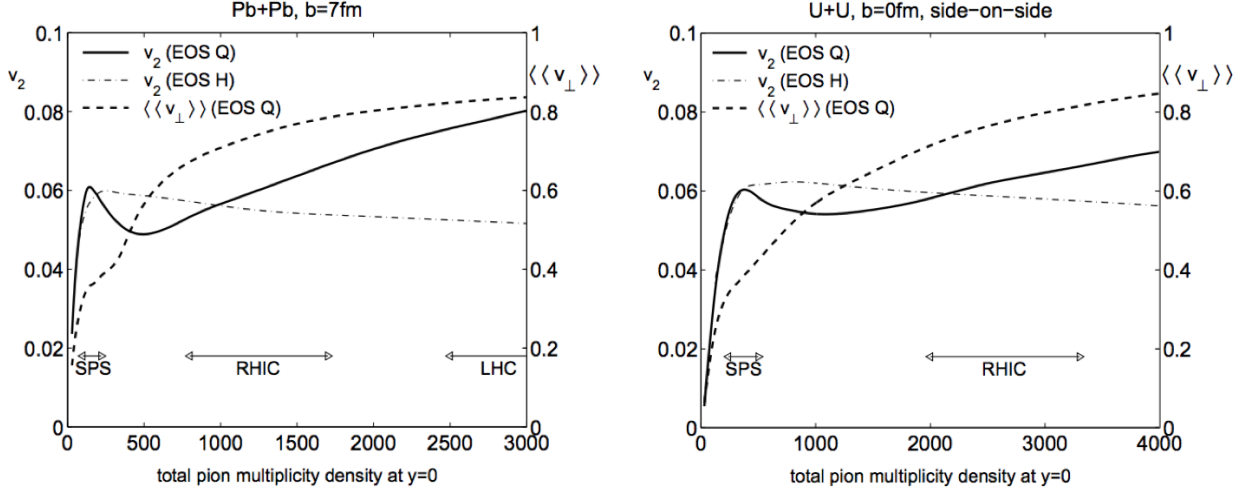


Figure 1.8: These figures illustrate the excitation function of the elliptic flow coefficient  $v_2$ , the left vertical axis, and the radial flow  $\langle\langle v_{\perp} \rangle\rangle/c$ , the right vertical axis. The left figure is for Pb+Pb collisions with impact parameter ( $b$ ) of 7fm, and the right figure is the side-on-side U+U collisions at  $b = 0$ fm. The solid curves correspond to the equation of state that is mentioned in Figure 1.7 for RHIC predictions, while the dashed curve is the second part (equation of state of a Hagedorn resonance gas) that is combined with the dashed curve in Figure 1.7 to give rise to the equation of state that the solid lines are based on. The soft phase transition stage in EOS Q leads to the dip in the elliptic flow [17]. The horizontal arrows at the bottom of the plots reflect early projections of particle multiplicities for the various facilities, but now it is shown that RHIC collisions produce multiplicities in the vicinity of the predicted dip [7].

Another signature is jet quenching and parton energy loss. In heavy-ion collisions, the colliding nuclei undergo hard-scattering, and partons from them could serve as colored probes for the colored bulk matter that forms after the collision. These partons that travel through bulk partonic matter could undergo significant energy loss, and this can be observed through the parton's subsequent fragmentation into hadrons, and these are what we call jets. Bjorken first suggested that this could be due to elastic parton scattering, and while recent theoretical studies have demonstrated that this contribution is likely to be quite small, gluon

radiation by passage through the matter could be sizable, and that could lead to energy loss and a manifestation in the parton's fragmentation into hadrons [18]. Specifically, these jets would be softened and broadened if they are results of partons that travelled through substantial lengths of matter containing a high density of partons. And this is what we call jet quenching. It is important however to distinguish between parton energy loss through the QGP from other possible sources of jet softening and broadening. There are various theoretical evaluations of the non-Abelian radiative energy loss of partons in dense but finite QCD matter, and they give approximately consistent results with some non-intuitive predictions. The energy loss computed from these predictions are then embedded in a perturbative QCD treatment of the hard parton scattering. There are effects here that could also lead to the softening and broadening of final-state jets that we are looking for as a signature, but in principle they could be calibrated by complementing RHIC A+A collision studies with  $p$ +A or  $d$ +A collisions in which we do not predict to have QGP formation. While there are certainly insufficiencies with these models, for example, the fact that they assume vacuum fragmentation of the degraded parton and its spawned gluons that is questionable for the soft radiated gluons and over the leading-parton momentum ranges which is what this assumption is applied for in RHIC collisions, and with that also the implications of neglecting final-state interaction effects for the hadronic fragmentation products that is assumed with this vacuum fragmentation assumption, the basic qualitative prediction that substantial jet quenching is a necessary result of QGP formation is most likely without question (even if the quantitative calculations might not be the case). Therefore, the problem lies in determining whether or not jet quenching is a sufficient quality for demonstrating the production of the QGP. Now with the models we have, it seems like we can only indirectly infer the role of the QGP from the magnitude of the gluon density needed to reproduce jet quenching in RHIC collision matter, and therefore, what we have to examine is whether or not the extracted gluon density is consistent with what one might expect for a QGP formed from RHIC collisions. With the assumption that QGP formation in a RHIC collision being dominated by gluon-gluon interactions in the saturation regime, saturation models have been developed to predict the density of gluons. With experimental data of outgoing hadron multiplicities from

RHIC collisions, these models will be able to predict the dependence of hadron multiplicity on collision energy, rapidity, centrality and mass number. Then this information can be used to compare with the jet quenching information that we mentioned previously, as well as the information from measuring elliptic flow to give us information about the QGP that potentially is created within the RHIC collisions.

The last signature to be discussed is related to quark recombination, which suggests a mechanism that allows quarks produced through different processes, specifically processes that differ in their energy level and therefore on a certain level speed, to combine with each other [19]. However, for QGP formation in RHIC, the expected recombination might be of a different kind, where there is coalescence of abundant thermal partons that provide another hadron production mechanism that is active over a wide range of rapidity and transverse momentum [20]. And if in our experimental data it shows the need for a substantial of recombination of this kind in order to explain the hadron yields and flow, it might be taken as a signature of QGP formation [21].

### **1.2.2 Experimental Probes of the QGP**

Equipped with this overview of predicted signatures of QGP formation in RHIC heavy-ion collisions, we will briefly summarize the different experimental observations made over years of collecting data from the fireball generated by the heavy-ion collisions at RHIC that that points to the formation of the QGP.

There are two main categories of results that will be discussed, the first category being particles generated at a lower transverse momenta that reflect the properties of the bulk of the matter produced in the collision, and the second being energetic particles that are generated through hard scattering processes.

With regards to the first category of particles that reflect the bulk properties, we analyze the hadron yields and spectra, which provide us with insight with regards to the bulk properties of the matter created in the collisions. The reason for this is that after the chemical freeze-out, particles only interact elastically, and the hadron species is fixed, so the information of the system at chemical freeze-out can be obtained from the integrated yields of the different

particle species within the framework of statistical thermal models. After the kinetic freeze-out, the particles stop interacting elastically and so the spectra will remain the same, and thus reflecting the properties of the medium at kinetic freeze-out. There are two contributions to the transverse momentum distributions of the particles. One of them is random and can be identified with the temperature of the system at kinetic freeze-out. The other contribution is collective that comes from the matter density gradient from the center to the boundary of the fireball created in heavy-ion collisions, and it is sensitive to the strength of the interactions amongst the particles in the collisions. At RHIC energies, this is expected to come from the pre-hadronic phase. There are three features that were observed in Au+Au collisions at STAR that point to the creation of the QGP in these collisions at RHIC. The first is that the hadron yields suggest chemical equilibration across the  $u$ ,  $d$  and  $s$  quark sectors. The second and third have to do with the elliptic flow, where it seems that it attained the strength expected for an ideal relativistic fluid thermalized very shortly after the collision, and at intermediate  $p_T$  the elliptic flow appears to arise from the flow of quarks in a pre-hadronic stage of the matter.

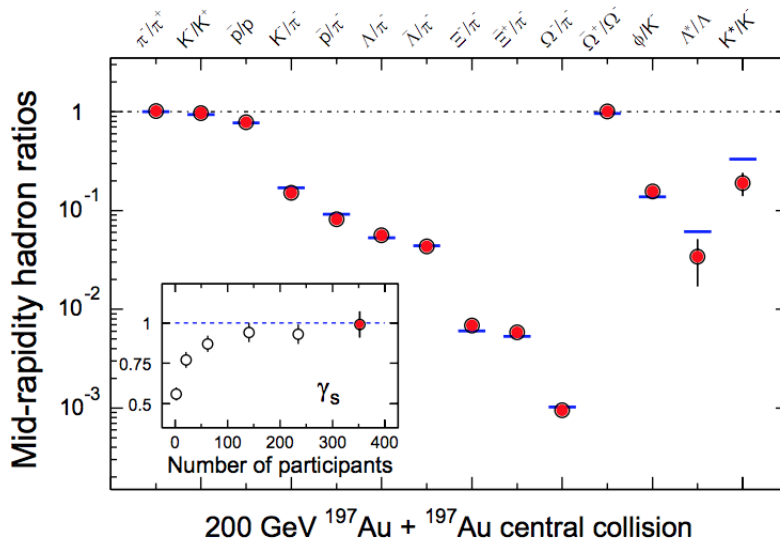


Figure 1.9: This figure illustrates ratios of  $p_T$ -integrated yields for different hadron species measured in the central Au+Au collisions at  $\sqrt{s_{\text{NN}}} = 200$  GeV at the STAR experiment. The horizontal bars represent the statistical model fits to the measured yield ratios [7].

As seen in Figure 1.9, which compares STAR measurements to statistical model fits, the fit to the ratio is excellent, which seems to suggest that the light flavors,  $u$ ,  $d$  and  $s$ , have reached chemical equilibrium at chemical freezeout, as the statistical models assume that the system is in thermal and chemical equilibrium at that stage [22].

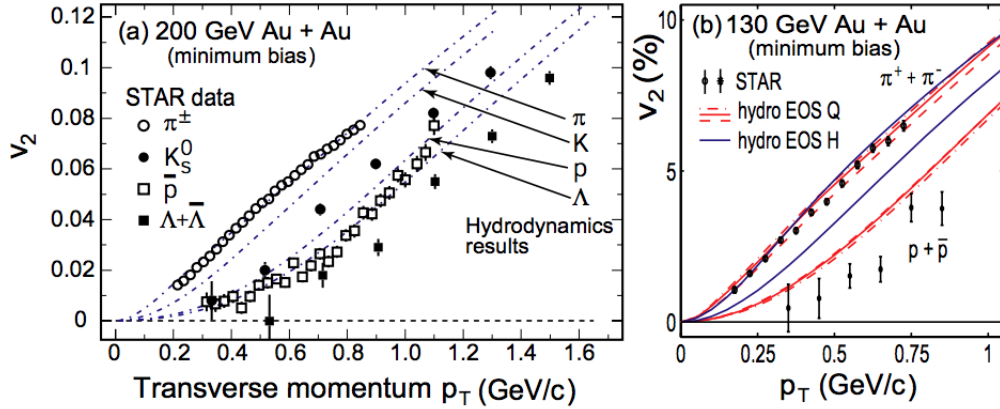


Figure 1.10: (a) This figure shows the STAR experimental results obtained from Au+Au collisions at  $\sqrt{s_{NN}} = 200$  GeV of elliptic flow as a function of transverse momentum [23]. The dashed lines are hydrodynamics calculations [24], assuming early thermalization, ideal fluid expansion, an equation of state consistent with LQCD calculations that include a phase transition at  $T_c = 165$  MeV, and a sharp kinetic freezeout at 130 MeV (EOS Q mentioned in Figure 1.8). (b) Similar calculations as those in (a), but now also with EOS H - equation of state for a hadron gas, and compared with STAR experimental results obtained from Au+Au collisions at  $\sqrt{s_{NN}} = 130$  GeV [25]. This figure is taken from [7].

Figure 1.10 shows that the elliptic flow measured from STAR demonstrates a strong mass dependence, and that the hydrodynamics calculations, also shown in the same figure, seem to reproduce this mass dependence, as well as the absolute magnitude of the elliptic flow, reasonably well -  $\pm 30\%$ . Given that the parameters of the hydrodynamic calculations are tuned for zero impact parameter, and that they assume ideal relativistic fluid flow, this suggests that the elliptic flow measured from STAR does in fact attain the strength that is expected for an ideal relativistic fluid. On top of that, the agreement seems to be optimized when it assumes that the matter reaches local thermal equilibrium very early, seen also in

Figure 1.10. Also, when the expanding matter is treated as a pure hadron gas - thus EOS H in Figure 1.10, the mass-dependence of the elliptic flow is significantly underpredicted. This implies that there is early thermalization, and it suggests that a “perfect liquid” [26] - very strongly interacting matter with very short constituent mean free paths - dominate the early stages of the collision. One possible interpretation of this observation is that thermalized, strongly interacting QGP is what dominates in that region.

The second category of results has to do with energetic particles that are produced through hard scattering processes. The interaction of these particles with the medium provides us with a class of unique, penetrating probes that could reveal the properties of the matter that is created in these heavy-ion collisions. Specifically, we will look at hadrons with transverse momentum that is greater than 5 GeV/c, as they exhibit the power-law falloff in cross section with increasing  $p_T$  that is characteristic of perturbative QCD hard-scattering processes [27], which shows that these hadrons are penetrating through the created matter. Figure 1.11 shows the ratio of inclusive charged hadron yields in Au+Au and d+Au collisions to that of  $p+p$  collisions, corrected for trivial geometric effects by scaling according to  $\langle N_{bin} \rangle$ . This ratio,  $R_{AB}(p_T)$  is defined as follow:

$$R_{AB}(p_T) = \frac{dN_{AB}/d\eta d^2p_T}{T_{AB} d\sigma_{NN}/d\eta d^2p_T} \quad (1.3)$$

where the overlap integral  $T_{AB} = \langle N_{bin} \rangle / \sigma_{inelastic}^{pp}$ . The surprising observation is that at large  $p_T$ , there is a suppression by a factor of around 5 relative to binary scaling expectations, and this is not something that conventional nuclear effects could account for. The fact that this suppression is not seen in d+Au collisions and only in Au+Au collisions also shows that this suppression is not from nuclear effects in the initial state, but rather it is hard scattered partons or their fragmentation interacting with the dense medium generated in Au+Au collisions [28, 29, 30, 31].

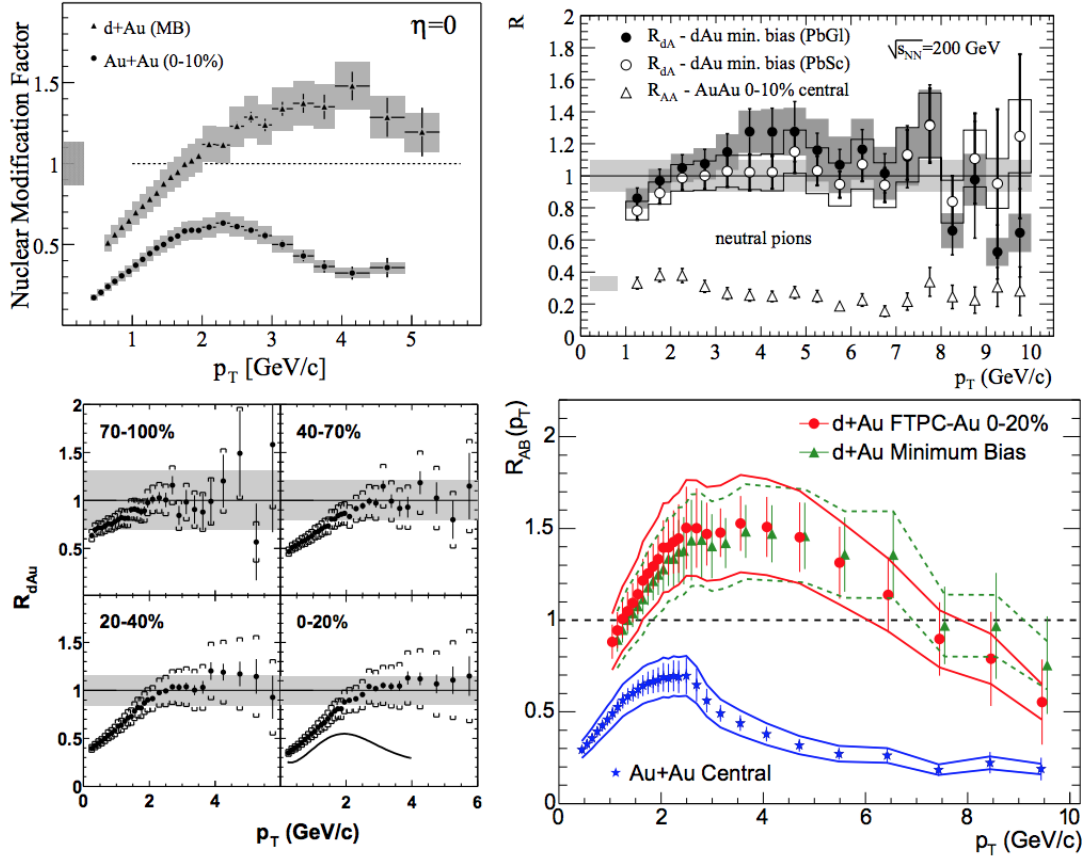


Figure 1.11: The ratio of inclusive charged hadron yields in Au+Au and d+Au collisions to that of  $p+p$  collisions from 4 different experiments [7]: (top left) BRAHMS [28], (top right) PHENIX [29], (bottom left) PHOBOS [30] and (bottom right) STAR [31].

Another ratio that provides insight towards the existence of the QGP is the binary scaled ratio of yields from central collisions relative to peripheral collisions,  $R_{CP}(p_T)$ . This ratio is shown in Figure 1.12, and it can be seen that the suppression for central collisions is similar to the previous ratio, around 5 times relative to the most peripheral collisions. Theoretical calculations based on perturbative QCD that incorporates partonic energy loss in dense matter as well as gluon saturation effects that suppress high  $p_T$  yield are also shown in the same figure. In order to describe this suppression, these models require an initial gluon density that is around 50 times that of cold nuclear matter [32, 33]. This order of magnitude of gluon density falls well into the regime that lattice QCD calculations predictions fall with

regards to the QGP phase.

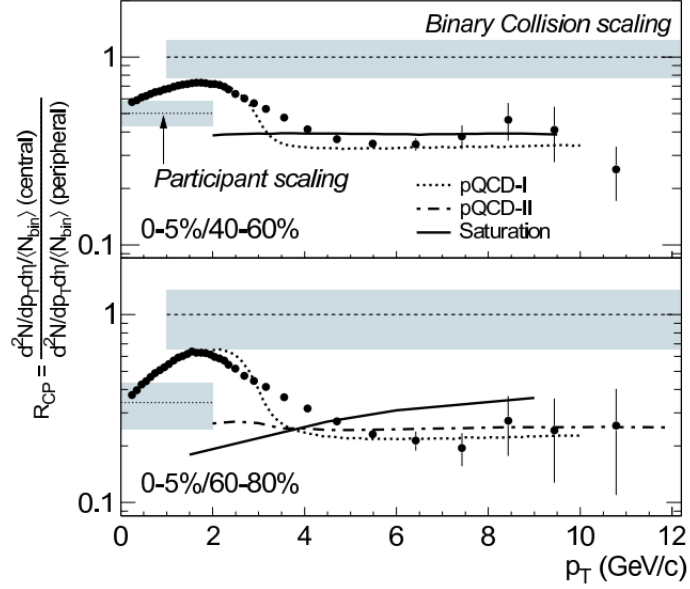


Figure 1.12: This figure shows the binary-scaled yield ratio  $R_{CP}(p_T)$  of central (0-5%) to peripheral (40-60%, 60-80%) collisions for charged hadrons from Au+Au collisions at  $\sqrt{s_{NN}} = 200$  GeV [34].

This short overview merely highlights a few of the observations that have been made over the years that point to the formation of the QGP at these heavy-ion collisions at RHIC that were detected by various experiments, and it is by no means a complete description of all that has been measured in effort to search for signatures of the existence of the QGP. However, it does show a very good set of evidence that points to the existence of the QGP, which is the medium in which many interesting topics of physics is based on, including the analyses covered in this thesis. However, before moving onto the analyses, we will first turn to looking at the STAR detector that was built to make all these observations possible in the first place.

## CHAPTER 2

### The Experimental Set-Up: RHIC & STAR

#### 2.1 The Relativistic Heavy Ion Collider (RHIC)

The Relativistic Heavy Ion Collider, known also as RHIC, located at the Brookhaven National Laboratory in Upton, New York, is the world's first accelerator facility that has the ability to collide heavy and light ions, including polarized protons, deuterons, copper and gold, at relativistic energies, varying from 7.7 to 200 GeV in the center-of-mass frame of the colliding nucleon pairs. The collider needs to operate over long periods of time while holding the beams at relativistic energies in order to accomplish this feat of colliding these species of particles at these energy levels. However, to achieve this in an accelerator of limited physical size means that we would need very strong magnetic fields, which essentially requires RHIC to use superconducting technology for its magnets, allowing for a minimizing of power consumption while allowing a much higher level of magnetic fields required to maintain the energy levels of the colliding nuclei beams. Also, a unique part of the physics research planned to be done at RHIC is to collide beams of different ion species at the same energy per nucleon, which means that the beam rigidities would have to be different. This implies that RHIC would need two separate rings operating at two different magnetic fields to maintain the energies desires.

To describe the details of RHIC, we will follow the journey of the heavy ions from the beginning of its acceleration to its end in collision through the different subsystems within the RHIC complex (Figure 2.1) [35] [36]:

1. The Electron Beam Ion Source (EBIS): This is a new pre-injector system that was developed and put into use since 2012. Its predecessor were two Tandem van de

Graaff accelerators, and it has a much better performance than them. It is capable of producing any type of ions, from deuterons to uranium, even including noble gases such as helium and argon, with much lower operating costs; it is also easy to switch between species, even pulse-to-pulse, when feeding the trap by injecting ions with unit charge from external sources. There is also a precise control over the charge state produced, which makes it possible to produce a distribution that peaks at intermediate charge states with ions that have not been completely stripped of their electrons. There is also good control over the pulse width on top of these controls, and the source is more reliable [37]. The EBIS consists of an electron beam ionization source that is followed by a radiofrequency quadrupole linac and an interdigital-H linac. It first starts with an injection of ions of unit positive charge into the EBIS trap, and from there the EBIS acts as a charge state multiplier, and produces the desired ions with desired charge to the Booster Synchrotron.

2. The Linear Accelerator (Linac): This is specifically for experiments colliding beams of protons as it is a 200-MeV Linac that supplies energetic protons that get transferred to the Booster Synchrotron.
3. The Booster Synchrotron: After the heavy ions and protons are accelerated by linear accelerators, they get sent to the Booster Synchrotron, which is a powerful circular accelerator that provides the ions with more energy. The way that it accomplishes this is by synchronizing the accelerating voltage with the circulation period of the particles that are being accelerated. This subsystem pre-accelerates particles before they enter the Alternating Gradient Synchrotron, which is done with its superior vacuum that makes it possible to accelerate heavy ions, even uranium.
4. The Alternating Gradient Synchrotron (AGS): When the ions enter this subsystem from the Booster, they are typically travelling at around 37% of the speed of light, and they are accelerated as they circle around the AGS until they are travelling at around 0.997 the speed of light. This corresponds to having gold ions that are accelerated to 100 MeV per nucleon with a charge of +77 coming in from the Booster Synchrotron,

to leaving the AGS with 8.86 GeV per nucleon with the same charge. The mechanism of the AGS comes from the concept of alternating gradient focusing. The accelerator's 240 magnets' field gradients are successively alternated inward and outward, and so the particles are focused in both the horizontal and vertical plane at the same time.

5. The AGS-to-RHIC Beamline: This beam line, as described by its name, takes the ion beam from the AGS to the RHIC rings when the ion beam reaches its top speed. The important aspect of this is that there is a fork in the road at the end of the line: a switching magnet sends the ion bunches down one of the two beam lines, corresponding to one of the two RHIC rings, as mentioned previously. This is also where the gold ions are fully stripped of their electrons, to reach an electric charge of +79.
6. The RHIC magnetic rings: The rings are 2.4 miles long, and they have six interaction points (where the two rings of the accelerating magnets cross, allowing the nucleons to collide), which is also where the STAR detector - the detector that this analysis obtained its data from - resides.

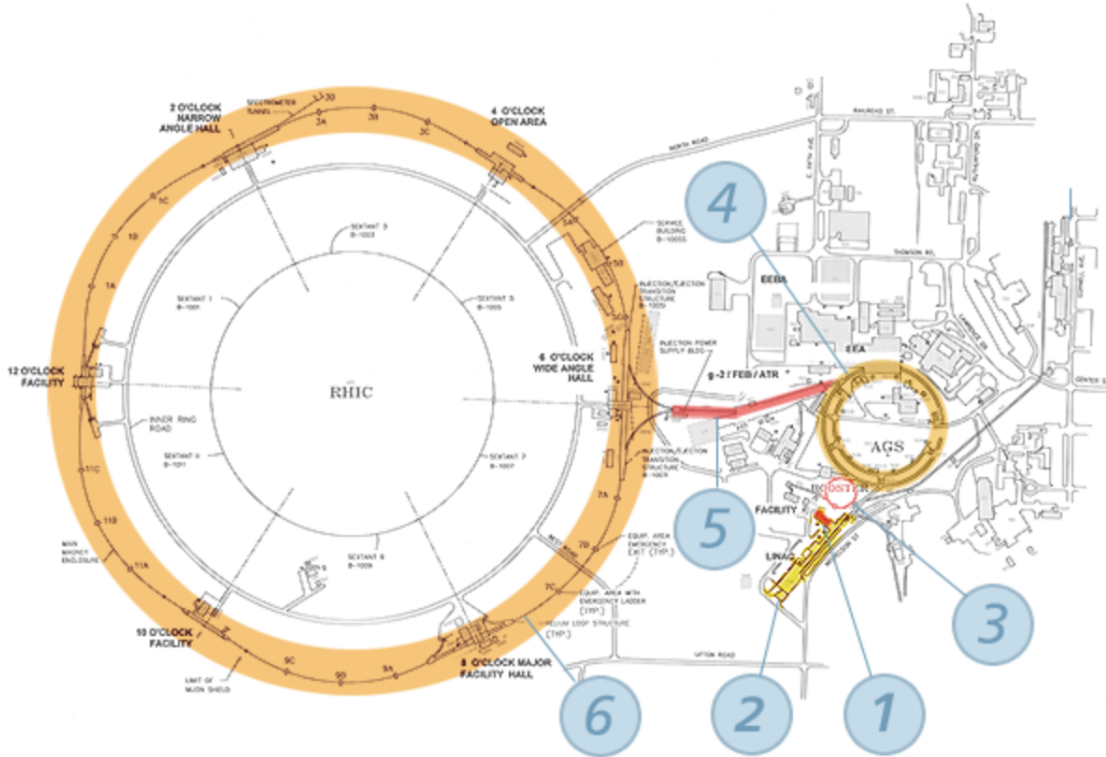


Figure 2.1: A schematic drawing of the RHIC accelerator complex as shown on the official website. The important subsystems are labelled, and they are, respectively, (1) the Electron Beam Ion Source (EBIS), (2) the Linear Accelerator (Linac), (3) the Booster Synchrotron, (4) the Alternating Gradient Synchrotron (AGS), (5) the AGS-to-RHIC Beamline, and finally, (6) the RHIC magnetic rings [6].

There were originally 4 experimental detectors located at one of the six interaction points of RHIC: PHENIX, PHOBOS, BRAHMS and STAR. PHOBOS, decommissioned in 2015, had the largest pseudo-rapidity coverage, and was specialized in measuring bulk particle multiplicities [38]. BRAHMS, decommissioned in 2006, aimed to study small- $x$  physics using momentum spectroscopy [39]. PHENIX, which remained operational until recently in 2016, used a partial coverage detector system in an axial magnetic field that was generated using superconductive technology to measure the direct probes of the collision [40]. Recently, sPHENIX sprung up to become a new project at RHIC, which radically improved the PHENIX detectors to bring them back into commission, and this new experiment is very

close to getting off the ground and collecting data, and having the opportunity to investigate exciting new physics. But until then, STAR remains to be the only active experimental detector at RHIC. It specializes in tracking and identification of charged hadrons over a large solid angle at mid-rapidity in a solenoidal magnetic field, hence the name Solenoid Tracker at RHIC (STAR) [41]. Since this is the detector where the data that this analysis is based on, we will explore it in a little more detail in the next section.

## 2.2 Solenoid Tracker at RHIC (STAR)

The Solenoid Tracker at RHIC (STAR) was constructed with the goal of finding signatures of the QGP and to study its properties in relativistic heavy-ion collisions, and since such collisions result in a large number of particles with very high momentum, STAR is designed to measure hadron production across a large solid angle to have the ability of tracking the large number of charged particles produced in these relativistic collisions. Figure 2.2 shows a schematic side view of the STAR detector as provided by the official STAR website.

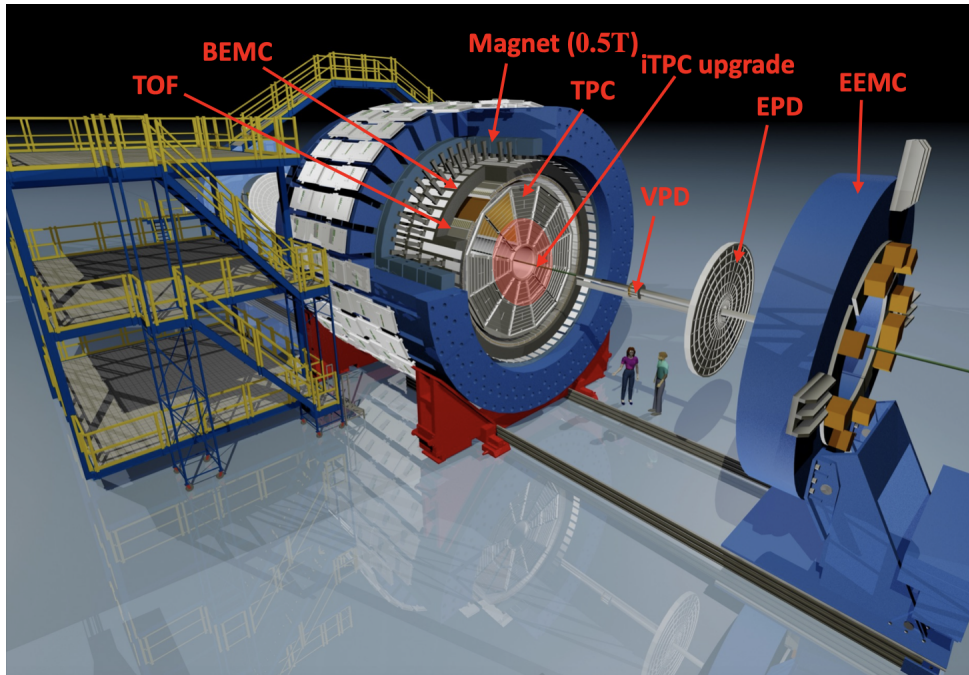


Figure 2.2: Layout of the STAR Detector as provided on the official STAR website [42]

The central subsystem of this STAR detector is the Time Projection Chamber (TPC) [43]. This instrument is a cylindrical detector that tracks and identifies particles through their ionization energy loss as they pass through it. As mentioned previously, STAR is located at one of the interaction points where the two beams meet, and so the beam crossing point is at the center of the TPC, and the coordinate system that is used here has the direction of the beam being the  $z$ -direction (STAR uses a right-handed Cartesian system as its coordination system; the  $y$  axis is perpendicular to the axis of the solenoid with positive  $y$  in the opposite direction of gravity, as much as that is possible) [44]. Surrounding the TPC is the Time-of-Flight detector, which allows particle identification at STAR to go above 1 GeV/ $c$ , which is the limit on the momentum of particles that could be identified by the TPC [45]. Surrounding the TOF detector is STAR's E-M Calorimeter, which includes the Barrel Electromagnetic Calorimeter (BEMC), the Barrel Shower Maximum Detector (BSMD) [46], and the End-cap Electromagnetic Calorimeter (EEMC), which is located only on one side of STAR [47]. This system can measure the transverse momentum of photons, electrons and electro-magnetically decaying hadrons. The BEMC is in turn surrounded by the STAR magnet coils that provides a uniform magnetic field of 0.5T along the beam line [48].

Other than these larger sub-systems, there are a few others that aid in beam monitoring and triggering. The first of such sub-systems is the Beam Beam Counters (BBC) that are located around 3.5m away from the center of STAR on both sides and monitor event rates in  $p+p$  collisions by providing triggers, monitoring overall luminosity as well as measuring the relative luminosity for different proton spin orientations [49]. The second of these sub-systems is a pair of Zero Degree Calorimeter (ZDC) detectors that are located along the beam pipe on both sides of STAR, with the functionality of monitoring small-angle scattering of neutral particles, for example spectator neutrons [50]. Thirdly, there is the Vertex Position Detectors (VPD) that are located at 5.6m on both sides of the center of the solenoid, and they provide the start time of the collisions, which is essential for Time-of-Flight measurements [45]. Last but definitely not least, a relatively new detector, the Event Plane Detector was added in 2018 [51] to measure the forward-going charged particles generated in heavy-ion collisions, which would in turn allow us to extract information about the event plane of the

collision.

Because the TPC, TOF and EPD detectors are specifically important for particle tracking and identification as well as event plane reconstructions, which are crucial parts of the analysis in this thesis, we will go into a little more detail about these detectors in the following subsections.

### 2.2.1 Time Projection Chamber (TPC)

RHIC accelerates heavy ions up to a very high energy, with massive heavy ions like Au+Au collisions, and so each collision could produce many primary particles. On top of that, these primary particles decay and scatter, which leads to a high flux of secondary particles. All these particles, as much as possible, would need to be tracked in order to accomplish the physics goals of STAR. The Time Projection Chamber, being STAR's primary tracking device [52], is a very important detector that needs to have capabilities to track all these particles that are generated through various mechanisms from the heavy-ion collisions that occur in RHIC. The primary functionalities of the TPC include recording the tracks of particles, measuring their momenta, and identifying the particles by measuring their ionization energy loss ( $dE/dx$ ). The acceptance of the TPC covers  $[-1.5, 1.5]$  units of pseudo-rapidity through the full azimuthal angle over the full range of multiplicities. The limit of the momentum of particles that can be identified is  $[100 \text{ MeV}/c, 1 \text{ GeV}/c]$ , and the momentum of particles that can be measured goes up to  $30 \text{ GeV}/c$ .

Figure 2.3 is a schematic diagram of the TPC. It is an empty volume of gas in a well defined, uniform, electric field of around  $135 \text{ V}/\text{cm}$ . The volume of gas is filled with P10gas (10% methane, 90% argon) kept at 2 mbar above atmospheric pressure. The reason for using this particular type of gas is that it has a fast drift velocity that peaks at a low electric field. This is important because it is best to operate on the peak of the velocity curve, as that allows the drift velocity to be stable - relatively insensitive to small variations in temperature and pressure. So by having a gas in which the drift velocity peaks at a low electric field, that allows for a simpler field cage design.

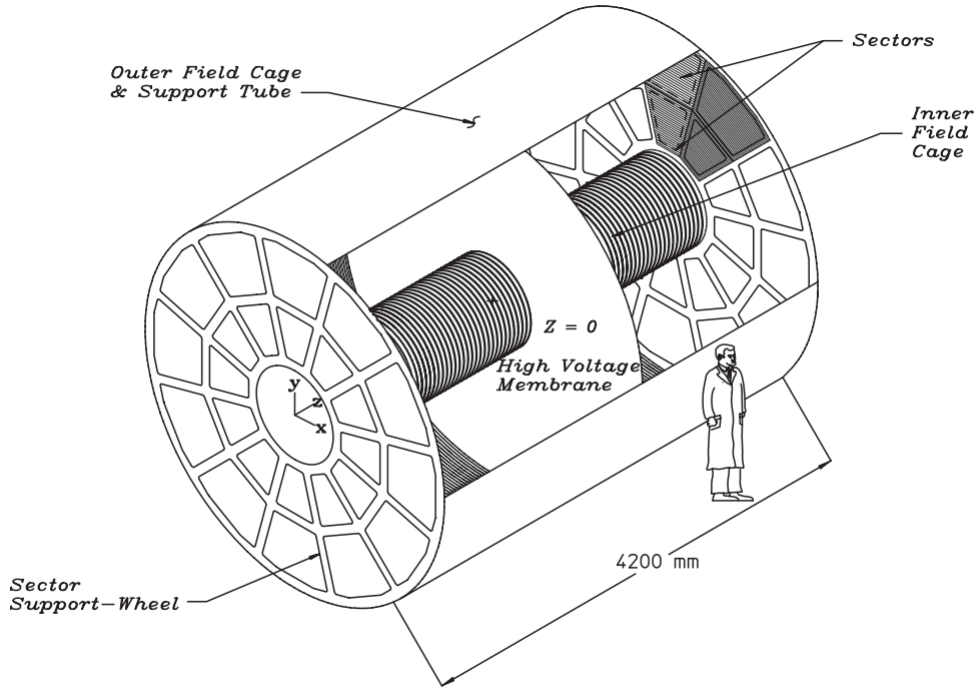


Figure 2.3: A schematic diagram of the STAR TPC [53]

As the primary ionizing particles traverse through the gas volume, they generate electrons from the gas, which then, because of the electric field present, drift to the readout end caps at the ends of the TPC. With the information from these secondary electrons, we are able to reconstruct the trajectories of these primary ionizing particles. The uniform electric field which is required to drift the electrons is defined by a thin conductive Central Membrane at the center of the TPC. It is very important for the electric field to be uniform because track reconstruction precision is sub-millimeter and electron drift paths are up to 2.1m (half the length of the TPC).

So how is this uniform and stable electric field established in the TPC? It is defined by establishing the correct boundary conditions with the parallel disks of the central membrane, the end-caps and the concentric field cage cylinders. The central membrane is operated at 28kV and the end caps are grounded. The field cage cylinders provide a series of equipotential rings that divide the space between the central membrane and the anode planes into

182 equally spaced segments. The rings are biased by resistor chains of 183 precision  $2M\Omega$  resistors that provide a uniform gradient between the central membrane and the grounded end caps.

The readout system is based on Multi-Wire Proportional Chambers (MWPC) with readout pads. The original design of the read out planes is as follows: modular units are arranged in a circular manner with 12 sectors, and they are mounted on aluminum support wheels. Each of these sectors consists of four components: a pad plane and three wire planes. Because of the different needs when comparing the inner radius and the outer, these sectors are further divided into the outer and inner radius sub-sectors (see Figure 2.4 for a schematic diagram of one full sector broken down into the outer and inner sub-sectors). The outer radius sub-sectors have continuous pad coverage to optimize the  $dE/dx$  resolution, so that the full track ionization signal can be collected, which will then improve statistics on the  $dE/dx$  measurement. It also improves tracking resolution because of anti-correlation of errors between pad rows. On the outer radius sub-sectors, the pads are arranged on a rectangular grid that is phased with the anode wires so that a wire lies over the center of the pads. It is designed in such a way that places most of the signal on 3 pads which gives good centroid determination at minimum gas gain, and that allows for a good signal to noise ratio while not seriously compromising two-track resolution. The inner sub-sectors are in the region where the track density is highest, and so they needed to be optimized for good two-hit resolution. Therefore, the inner sub-sectors use smaller pads, and the induced surface charge width is also reduced to less than the electron cloud diffusion. The shorter pad length is the most important improvement in two track resolution because it is important for lower momentum tracks which cross the pad row at angles far from perpendicular as well as for the tracks that have a large dip angle, as the shorter pads give shorter projective widths in both the direction along the pad row and the drift direction. However, because of the smaller pads used, there is a compromise in continuous pad coverage.

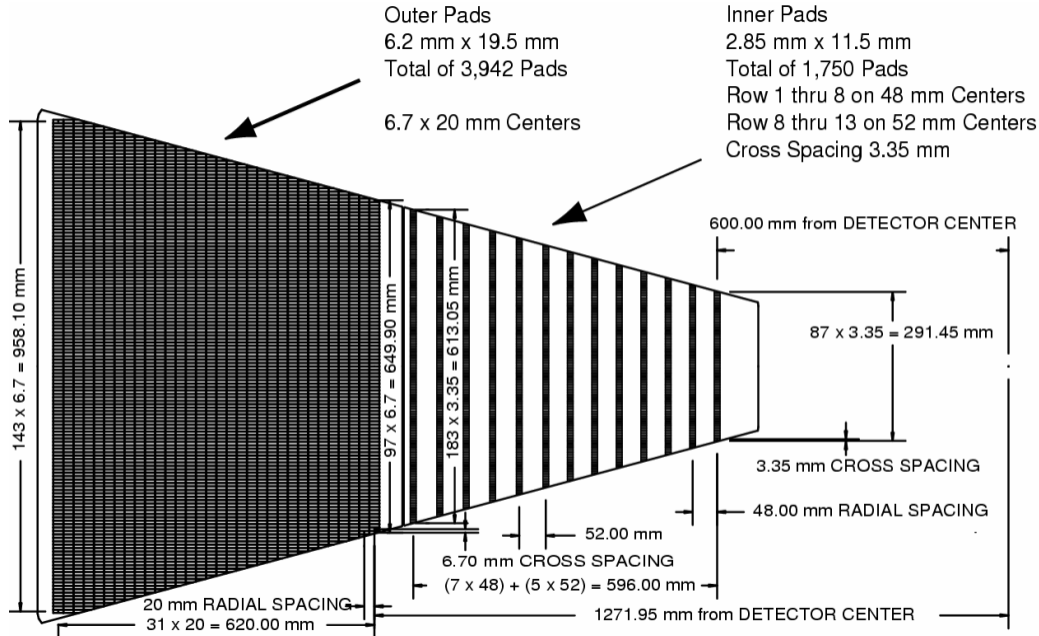


Figure 2.4: Schematic diagram of a full sector of the anode pad plane [53]

However, there have been upgrades to the TPC over the years, and the most significant one being the upgrade to the inner sectors of the TPC that was implemented for data taking starting from 2019. This upgrade replaced all 24 inner sectors in the STAR TPC with sectors with 40 pad-row readouts, a significant increase from the 13 pad-row readouts of the sectors that are being replaced [54]. This increases the number of pads from 1750 to 3440, and the sizes of each pad is also increased, helping to cover a much larger portion of area compared to the 20% that was achieved previously. With this level of increase in detectors, an upgrade to the electronics was also necessary, from the preamp, to the digitizer ASIC, front end electronic cards, readout boards, and finally the data acquisition system [54]. All these upgrades lead to better momentum resolution - from the previous lower limit of 150 MeV/c to the current 60 MeV/c, better  $dE/dx$  resolution, as well as increasing the acceptance of the TPC from the old  $[-1.0, 1.0]$  units of pseudo-rapidity to  $[-1.5, 1.5]$  [55].

Now that we have discussed the different components that play a part in forming the overall functionality of the TPC, we can look into how the TPC actually tracks particles. The trajectories of the particles passing through the TPC is reconstructed by finding ionization

clusters along the track, and they are found separately in  $x$ ,  $y$  and  $z$  space. The  $x$  and  $y$  coordinates of a cluster are determined by the charge measured on adjacent pads in a single pad row. In order to do this, it is assumed that the signal distribution on the pads - the pad response function - is Gaussian, and then the signal is fitted to find the coordinate. However, there are some limitations. First, this Gaussian approximation doesn't quite match the tails of the true pad response function, so there would be an  $x$ -dependant bias. Second, the accuracy of this algorithm decreases at large crossing angles. The  $z$  coordinate of a point inside the TPC is determined by measuring the time of drift of a cluster of secondary electrons from the point of origin to the anodes on the endcap and dividing that time by the average drift velocity.

The tracking software performs two tasks - The first one is to associate space points to form tracks, and the other being fitting the points on a track with a track-model to extract information about the track, such as the momentum of the particle. The model is a helix to the first order, while taking into account second order effects such as the energy lost in the gas which causes the particle to traverse through a trajectory slightly off of the helix. In order to measure the transverse momentum of a track, the track is fitted with a circle through the  $x$  and  $y$  coordinates of the vertex and the points along the track; the total momentum is calculated using this radius of curvature and the angle between the track and the  $z$  axis of the TPC.

Another important feature of tracking is to determine the primary vertex of an event, which can help to improve the momentum resolution of the tracks, and also to separate the secondary particles from primary ones - something that is very important in the process of identifying strange particles produced in heavy ion collisions. The method to determine the primary vertex is by considering all the tracks reconstructed in the TPC, and then extrapolating them back to the origin, averaging those positions and we get the primary vertex position. A resolution of  $350\mu\text{m}$  is achieved when there are more than 1000 tracks.

Particle identification is also very important to the analyses done at STAR, and energy lost in the TPC gas is a valuable tool for accomplishing this. It is much easier to do so for low momentum particles, but as particle energy rises, then the energy loss becomes less

mass-dependent as thus not as useful for particle identification. The limit is at velocities around  $0.7c$ , above which it becomes difficult to determine the particle species. The ionization energy loss ( $dE/dx$ ) for the tracks is extracted from the energy loss measured from the maximum of 45 pad rows. Because of the short length over which the particle energy loss is measured, the most probable energy is measured by calculating the truncated mean of 70% of the clusters, rather than the average value [56]. Figure 2.5 shows a typical plot of measured  $dE/dx$  as a function of track momentum, with the solid lines being predictions from the Bischel function for different particle species [57]. The typical resolution of  $dE/dx$  in Au+Au collisions is 8%.

The tracking efficiency depends on the acceptance of the detector (for TPC it is 94%), the detection efficiency of the electrons (which is essentially 100% except for rare dead channels), as well as the two-hit separation capability of the system, which is difficult to do a simple calculation to estimate effects on the data, though simulations are possible.

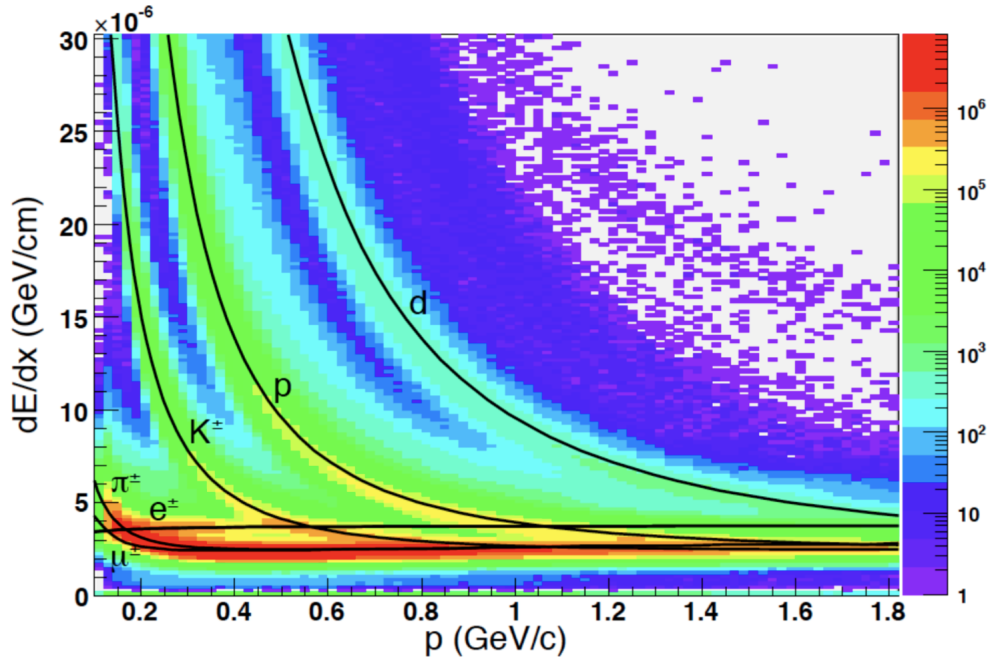


Figure 2.5: The distribution of ionization energy loss of various particle species through the TPC as a function of their momenta [56].

### 2.2.2 Time-of-Flight Detector (TOF)

As mentioned in the TPC section, the TPC is well suited for identifying particles with low momenta, but not so much for high-momentum particles because of the poorer correlation between energy loss and mass. So in order to improve this aspect of STAR, a small-acceptance Time-Of-Flight (TOF) system was added. This detector has a highly-segmented cylindrical detector that surrounds the TPC and it consists of an arrangement of 120 trays, each of them is 2.4m long, 21.3cm wide, and 8.5cm deep. The TOF detector has 32 Multigap Resistive Plate Chamber (MRPC) modules along the  $z$  direction, which was inspired by a similar system built for the ALICE experiment at CERN [58] [45]. These modules essentially are stacks of resistive plates arranged in parallel, and these plates are used to quench the streamers so that they do not initiate a spark breakdown, and the intermediate plates create a series of gas gaps. The outermost glass plate is then connected to HV. With a gas mixture containing a certain quantity of freon, the chamber works in avalanche mode - when a charged particle passes through these gaps, the initial ionization processes are amplified under the high electric field across the gaps and these electrical signals are captured by the electrodes. Since the resistive plates are semiconductors that are not electrically grounded, they have zero inner electric field and are transparent to induced signals. The signals that are collected on the electrodes are the analogue sum of the induced signals by each of the gas gaps. Then using the energy deposited into the glass plates, the TOF detector is able to record the time when the particle reached it, and by matching that information about the particle track with a TPC-recorded track, the velocity of the particle can be inferred. This allows the TOF detector to identify the species of the particles that have higher momentum than the upper limit of the capabilities of the TPC detector. This is better than the previous technology that used shaped scintillators coupling to fast photon multiplier tubes (PMTs) because of the high cost of the PMT-solution (it would require around 25000 fast PMTs and they would have to be insensitive to magnetic fields) [59].

The TOF detector is made up of 2 subsystems, one being the Vertex Position Detector (VPD) - the “start” detector - and the other the 32 Time-Of-Flight Multigap Resistive Plate Chamber (MRPC) modules, the “stop” detector. The MRPC modules are stacks of resistive

plates with gas gaps in between, allowing charged particles to induce avalanches as they pass through. These subsystems are based on conventional scintillator/phototube technology and includes custom high-performance front end electronics and common digitization in CAMAC. Shown in Figure 2.6, it is the cross section view of the MRPC as well as the readout pad array. With the VPD detecting the common start of the event, and the MRPC modules detecting the time that the track hits the TOF detector, then the time of flight (hence the name) of the track can be computed, and matching it with the TPC recorded track hits, we are able to identify the particle species of a given track.

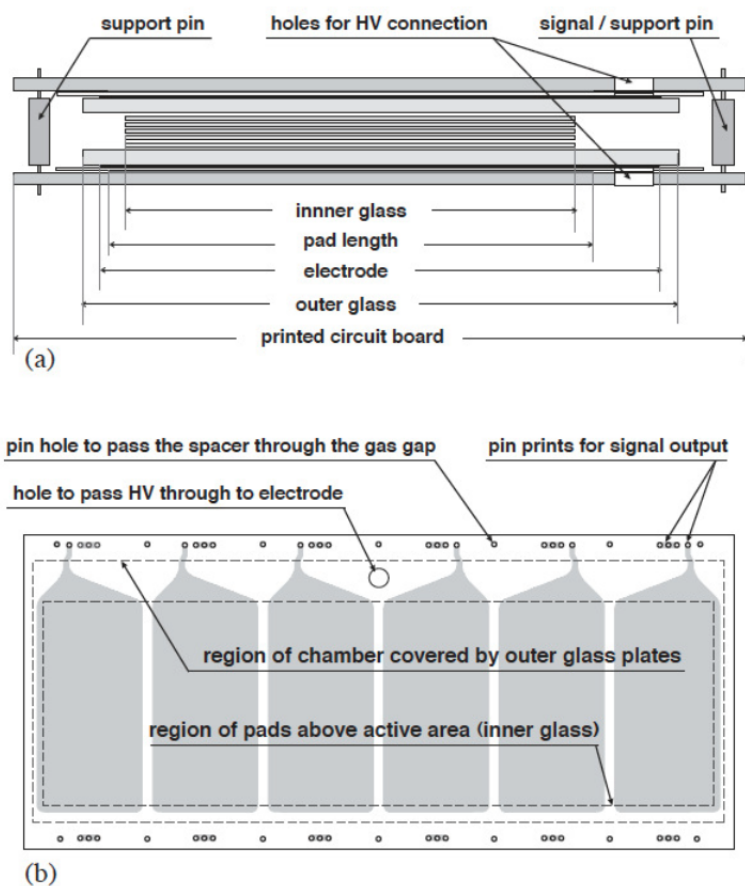


Figure 2.6: The cross section of the MRPC module of TOF, as well as a drawing of the readout pad array [56].

Figure 2.7 shows the detection of particles by the TOF detector, showing the inverse velocity of the particles and its relation to the rigidity of the particles - the ratio between momentum

and charge of the particles.

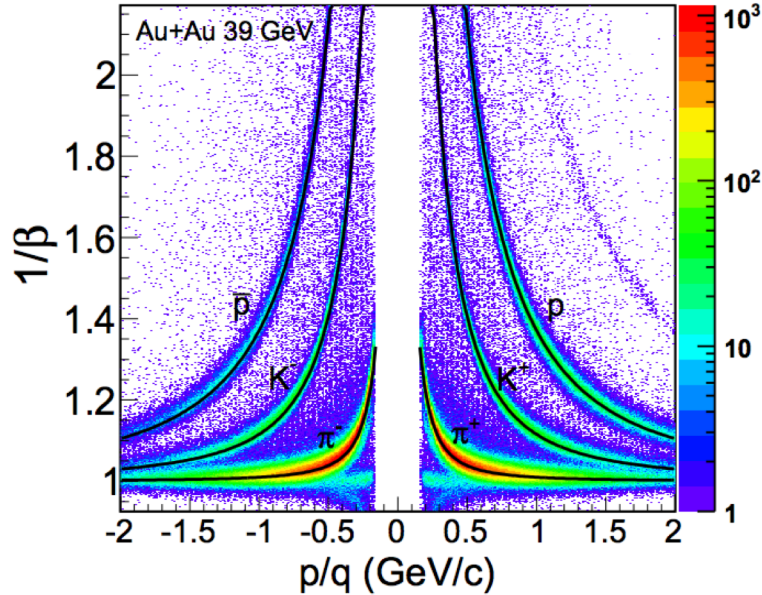


Figure 2.7: TOF recorded values of  $1/\beta$  of particles vs. their rigidity. The curves represent the expected mean values for the various particle species as labelled [60].

### 2.2.3 Event Plane Detector (EPD)

With these heavy-ion collisions, one very crucial component to our analysis is the understanding of the initial geometry of each of the collision, or event, as that allows us to map out the particles of interest with respect to all other particles within the event. This information is often extracted by calculating the “event planes” - an estimation of the true reaction plane of the collision event - through information about the azimuthal angles and transverse momenta of the primordial particles involved in that event [13]. The Event Plane Detector (EPD) is a detector that was added with the purpose of measuring the forward-going charged particles emitted in a heavy-ion collision event, which would provide us with information to extract the event plane from these particles [51]. It measures them at angles  $0.7^\circ < \theta < 13.5^\circ$ , or in pseudorapidity,  $\eta \equiv -\ln[\tan(\theta/2)]$ ,  $2.14 < |\eta| < 5.09$ , relative to the initial directions of the beams. The EPD detector consists of two wheels, and each wheel has 12 “supersectors” which covers  $30^\circ$  in the azimuth. Each of these supersectors is then divided into 31 tiles that

send signals through optical fibers to silicon photomultipliers (SiPMs). After that, these signals are amplified and sent to the STAR digitizing and acquisition system (DAQ) [61]. An illustration of one of the two wheels can be seen in Figure 2.8.

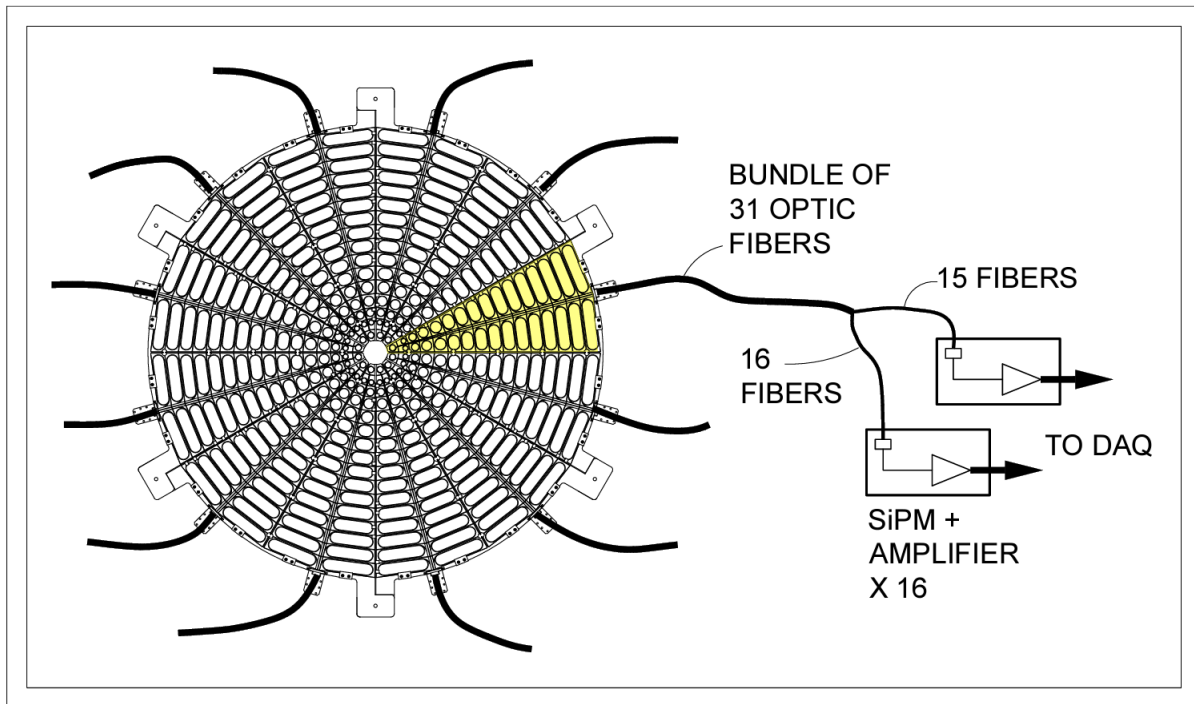


Figure 2.8: An illustration of one of the two EPD wheels, which shows the 12 supersectors along with the 31 tiles on each of them, and the signal flow that proceeds from the tiles through the optical fibers into the STAR DAQ [51]

As this detector was built for the very specific reason of measuring the event plane, it leads to specific characteristics of the detection of particles that differ from the previous detectors mentioned. First, since it is not necessary to know the particle species in order to use the particle in event plane reconstruction, there is no particle identification capabilities built into this detector. Second, simulations from the EPD working group showed that the magnetic field bending of particle tracks does not affect the determination of the event plane significantly, therefore, the EPD also does not have tracking abilities, but simply records one hit for each particle. Third, since event planes are determined by Fourier decomposition of the azimuthal dependence of particle yields [13], the EPD was designed to be azimuthally

symmetric.

With this detector upgrade, it allows us to have more information in extracting the event plane in our analysis, and we will be using information from the EPD in order to extract the event plane in the analysis described in this thesis.

## CHAPTER 3

### Introduction to the CME/ CVE

#### 3.1 Chiral Magnetic Effect

In QCD, the confinement of color, which implies that colored particles cannot be observed in isolation, is not included in the perturbation theory, therefore it is theorized that the mechanism has to be from non-perturbative dynamics, which many believe to originate in the topological sector of QCD.

Therefore, in order to find observable manifestations of the topological structure of the theory, one direction has been to investigate the Chiral Magnetic Effect (CME). To discuss CME, we will first set the stage by considering the quark-gluon plasma (QGP) with restored chiral symmetry for light quarks. With chiral symmetry restored, the quarks essentially become massless, which also means that any chirality these quarks possess will be sustained rather than fluctuate like they would if chiral symmetry was broken. For each specific flavor of these chiral fermions, one can introduce the corresponding vector current  $J_\mu$  and axial current  $J_5^\mu$ :

$$J_\mu = \langle \bar{\Psi} \gamma^\mu \Psi \rangle, J_5^\mu = \langle \bar{\Psi} \gamma^\mu \gamma^5 \Psi \rangle \quad (3.1)$$

The thermodynamics states of this QGP can then be specified with the vector chemical potential  $\mu$  (related to the vector number density  $J^0$ ) as well as the axial chemical potential  $\mu_5$  (for the axial number density  $J_5^0$ ), on top of temperature  $T$ . The quantity  $\mu_5$  characterizes the imbalance of right-handed and left-handed fermions in the system, and the QGP with nonzero  $\mu_5$  is a chiral medium, which may be created locally in heavy-ion collisions.

One way that we have used to probe properties of matter has been to apply external electromagnetic fields and examine how the matter responds to it. One example of that is to

see how an electric current can be generated in the presence of an external electric field for a conductor through Ohm's law:

$$\vec{J} = \sigma \vec{E} \tag{3.2}$$

with  $\sigma$  being the electric conductivity characterizing the vector charge transport property of matter. However, this is not very interesting because QGP has electrically charged quarks freely flowing in the medium and therefore it obviously is a conductor. The interesting question therefore becomes: Can a vector current be generated that is similar to that in the electric field case if we use an external magnetic field to probe QGP instead? Normally this is not possible because of symmetry:  $\vec{J}$  is parity odd and  $\vec{B}$  is parity even. However, the symmetry argument breaks down if the medium, and in this case, the QGP, itself is chiral, an example being a chiral QGP with nonzero  $\mu_5$  whose parity mirror image has an opposite  $\mu_5$ , which is what we just discussed above. And if this is the case, CME will then predict the generation of a vector current analogous to Eq.(3.2), with  $\vec{J} = \sigma_5 \vec{B}$ , where  $\sigma_5 = \frac{Qe}{2\pi^2} \mu_5$  is a chiral magnetic conductivity.

This generation of a vector current in the presence of chirality imbalance was first discussed by Vilenkin [62]. One important feature that is theorized regarding the QGP is that axial symmetry is broken, and therefore the chiral charge is not conserved, what is called chiral anomaly, which gives rise to a chirality imbalance within the QGP. With gauge theories, gauge fields have topologically non-trivial configurations. Associated with these configurations of gauge fields are tunneling between different states that are related by topologically non-trivial gauge transformations [63]. These different states are characterized by the Chern-Simons topological charge [64], and the transition between these different states is what induces the anomalous processes, like the parity symmetry breaking processes that lead to chiral anomaly. In large energy density substances, like the QGP, vacuum transitions arise between these states, and gives rise to chirality imbalance. This imbalance is then transferred to the quarks, leading to an imbalance of right-handed and left-handed quarks, which is represented by the Chern-Simons topological charge [65]. Along with chiral symmetry restoration that the QGP reaches since the material reaches above the temperature that QCD predicts the restoration to happen, this allows for a sustained imbalance in chirality.

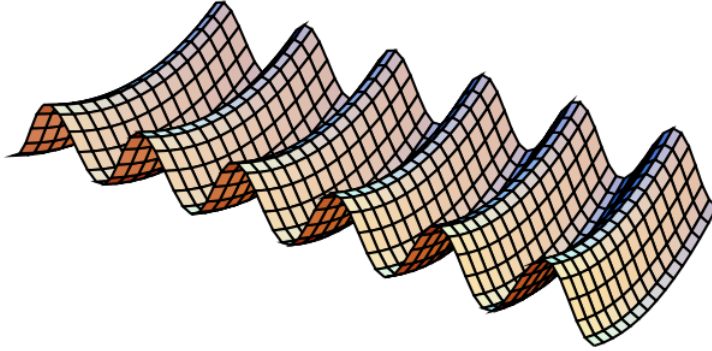


Figure 3.1: An illustration of the gluon field, which is periodic in one direction and oscillator-like in all other directions in functional space. And the instanton is a large fluctuation that corresponds to quantum tunneling from one minimum to another in this gluon field, whereas the sphaleron is a solution that is static, unstable, and doesn't involve quantum tunneling [65]. One can picture it as the instanton being a transition that occurs from one valley to a neighboring one in the figure, passing through underneath the peak, whereas the sphaleron is a transition that goes from a valley to the neighboring peak, and back down to another valley. It is theorized that these vacuum transitions lead to the chirality imbalance that exists in the QGP, and that is then transferred to the quarks, which with chiral symmetry restoration have zero QCD mass, and hence sustains the chirality imbalance, a necessary condition for the CME. Figure is taken from [65].

Another important feature of the QGP is that it reaches above the temperature, seemingly coincidentally, similar to the temperature at which chiral symmetry restoration happens, deconfinement of color charge also is predicted to occur. The quark chirality may be maintained in the QGP phase with restored chiral symmetry, and that is how we reach the current that the CME effect induces in the QGP [63].

There is yet another way to have an intuitive understanding of the Chiral Magnetic Effect. Suppose a magnetic field is applied to the QGP, then a spin polarization effect arises, which is that the quarks' spins prefer to be aligned along the magnetic field's direction. The momentum of the quarks will be correlated with the orientation of their spin - for

right-handed quarks, their momentum will be parallel to their spin direction, whereas for left-handed quarks, it would be anti-parallel. Therefore, if there is chirality imbalance, that would mean that there is a net correlation between spin and momentum (suppose we have more right-handed quarks, then the momentum of the system would preferably be parallel to the direction of spin).

Therefore, with the spin polarization effect, we have:

$$\langle \vec{s} \rangle \propto Qe\vec{B} \quad (3.3)$$

And then, since there is a net correlation between spin and momentum if there is chirality imbalance (which means  $\mu_5 \neq 0$ ):

$$\langle \vec{p} \rangle \propto \mu_5 \langle \vec{s} \rangle \propto \mu_5 Qe\vec{B} \quad (3.4)$$

And therefore, with that net momentum of quarks, we get a vector current:

$$\langle \vec{J} \rangle \propto \langle \vec{p} \rangle \propto \mu_5 Qe\vec{B} \quad (3.5)$$

However, even though we are able to show that there is a current that arises from this chirality imbalance within a magnetic field, it is actually, as mentioned previously, still not sufficient for fully explaining and accounting for the CME. One way to see the impact of chiral anomaly is through the following derivation. Suppose we assume a CME-induced electric current:

$$\vec{J} = Qe\sigma_5\vec{B} \quad (3.6)$$

And we use an arbitrarily small auxiliary electric field that is parallel to the magnetic field in order to probe the existence of such a current by examining the energy changing rate of the system. The usual way to compute with electrodynamics would be to compute the power that's done by this electric field (work per unit time):

$$P = \int_{\vec{x}} \vec{J} \cdot \vec{E} = \int_{\vec{x}} Qe\sigma_5\vec{B} \cdot \vec{E} \quad (3.7)$$

A different way to do this for a system of chiral fermions would be to use the implication of chiral anomaly to see that there is a generation of axial charge with a rate of

$$\frac{dQ_5}{dt} = \int_{\vec{x}} C_A \vec{E} \cdot \vec{B}, C_A = \frac{(Qe)^2}{2\pi^2} \quad (3.8)$$

So with a nonzero axial chemical potential, it implies that there is an energy cost for creating each unit of axial charge, so the energy changing rate through anomaly counting would be  $\mu_5 dQ_5/dt$ . So with equations 3.7 and 3.8, we get

$$\int_{\vec{x}} Q_e \sigma_5 \vec{B} \cdot \vec{E} = \int_{\vec{x}} \mu_5 C_A \vec{E} \cdot \vec{B} \quad (3.9)$$

which means  $\sigma_5 = \frac{\mu_5 C_A}{Q_e} = \frac{\mu_5 Q_e}{2\pi^2}$ , and so it becomes fixed by the chiral anomaly. Therefore, these anomaly-induced currents, which are protected by topology, are currents that are non-dissipative [66], which is what allows for the CME currents to be sustained. That wraps up the necessary and sufficient conditions for the CME. This is also the reason for the interest in searching for the CME in QGP, as that will allow us to gain a deeper understanding of properties of the QGP related to intrinsic nature of the QCD.

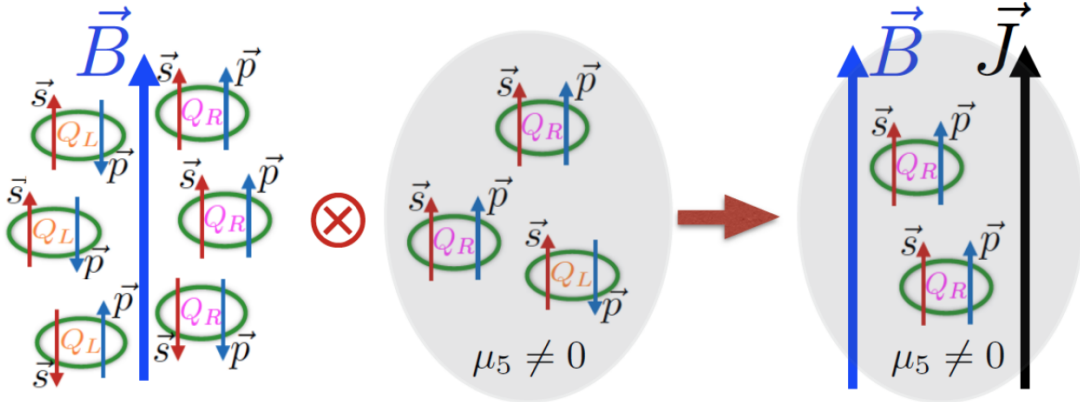


Figure 3.2: This figure demonstrates in a simple way what we have discussed in the text about how CME arises through the presence of a magnetic field, chirality imbalance, as well as chiral anomaly. [67]

### 3.2 Chiral Vortical Effect

A similar effect, called the Chiral Vortical Effect (CVE), can take place in a drop of chiral fermions that is rotating as a whole, and that rotation can be quantified by the quantity vorticity, defined as  $\omega = \frac{1}{2} \vec{\Delta} \times \vec{v}$ , where  $\vec{v}$  is the flow velocity field. With this kind of system,

we can draw an analogy with the CME, which is what we call the CVE: with the flow velocity being analogous to the magnetic vector potential, which leads to vorticity being analogous to the magnetic field as  $\vec{B} = \vec{\Delta} \times \vec{A}$ .

One way that we can see the legitimacy of this analogy is by considering this example: Suppose a charge particle moves in a circle perpendicular to a constant magnetic field. Then what that leads to, quantum mechanically speaking, is that it will pick up a phase factor  $e^{iQe\Phi_B/\hbar}$ , where  $\Phi_B$  is the magnetic flux through the area enclosed by the circular path. Now if that charge particle instead moves in the same circle, but perpendicular to a constant vorticity field  $\omega$  instead, it then picks up a phase factor of  $e^{iL/\hbar}$ , where  $L$  is the corresponding angular momentum. Therefore, we can see that the two cases parallel each other quite well, and it has been hypothesized that a similar effect to the CME could arise in a vorticity field. And so, suppose we have a chiral medium with nonzero  $\mu_5$ , and it has a vorticity field  $\vec{\omega}$ , then it could generate a vector current that is driven by  $\mu\vec{\omega}$ :

$$\vec{J} = \frac{1}{\pi} \mu_5 \mu \vec{\omega} \quad (3.10)$$

One way to picture this effect (see Figure 3.3) is by imagining the follow scenario. Suppose we have a global rotation, then the fermions would experience an effective interaction of the form  $\sim \vec{\omega} \cdot \vec{S}$  in their local rest frame, with  $\vec{S}$  being the spin of the fermions. And so, just like in the CME, the quarks' spins would prefer to be aligned along the magnetic field's direction, here we have a spin polarization effect where the spin of the fermions would prefer to be aligned with the vorticity's direction; however, unlike the CME, this effect is not affected by the charge of the fermions. So if then we also have chirality imbalance and chiral anomaly, a.k.a.  $\mu_5$  and  $\mu$  are both nonzero, we will have a vector current that is proportional to  $(\mu_5 \mu) \vec{\omega}$ , with the sign being dependent on whether  $\mu_5$  and  $\mu$  are positive or negative.

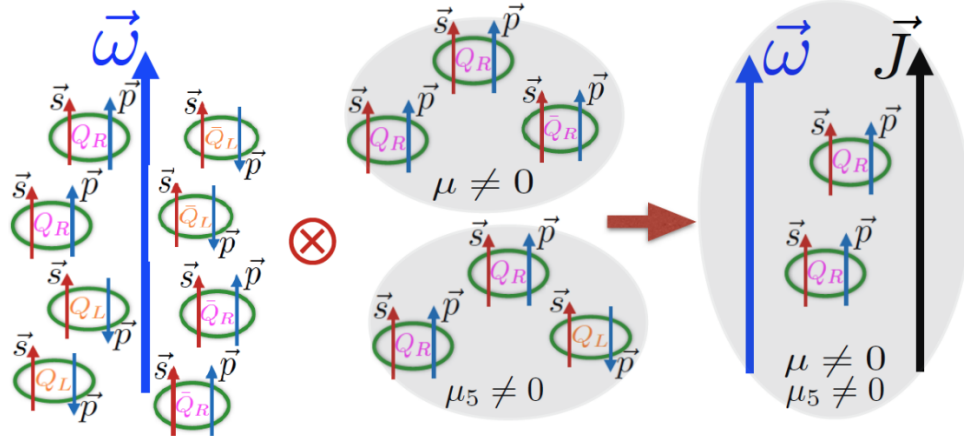


Figure 3.3: This figure demonstrates the CVE, in the specific case where there are more right-handed particles than left-handed ones (thus  $\mu_5 > 0$ ), as well as more quarks than antiquarks ( $\mu > 0$ ). [67]

### 3.3 Studying CVE in Heavy-Ion Collisions

#### 3.3.1 Vorticity in Heavy-Ion Collisions

Specifically, in this analysis, what we are concerned with is investigating the Chiral Vortical Effect (CVE) in heavy-ion collisions that take place at the Relativistic Heavy Ion Collider (RHIC). In order for this effect to take place, it requires global rotation of the Quark Gluon Plasma (QGP) in the heavy-ion collisions to create the vorticity. Now in a general non-central collision, where the two bunches of ions collide only partially, there would be a nonzero global angular momentum [68]. Even though the majority of the angular momentum is carried away by the spectator nucleons, recent simulations [69] show that a considerable fraction of the angular momentum that remains in the QGP in the collisions and is more or less conserved as time goes on, which means that the vortical effects from this global angular momentum could last for a while, advantageous for studying the CVE in heavy-ion collisions. This angular momentum that is studied in the simulations also points approximately in the out-of-plane direction, and that is important because if we then have a signal from this vortical effect -

such as a CVE induced current, it would also be along this direction, which could be picked up by the detectors that are placed coaxially around the ion beams.

### 3.3.2 Initial Conditions

Other than vorticity, the other important elements to give rise to the CVE would be the presence of nonzero initial vector and axial charge densities. Fortunately, in heavy-ion collisions, these initial charge densities naturally arise from fluctuations.

The axial charge density could be generated from: the topological fluctuations of the gluonic sector (via instanton and sphaleron transitions), the chromomagnetic flux tubes with nonzero local  $\vec{E} \cdot \vec{B}$  in the initial glasma, as well as simple fluctuations in the quark sector. The vector charge density could arise from “deposition” in the collision zone by the initial colliding nuclei which possess large baryonic, electric, and isospin charges [67].

### 3.3.3 CME in Heavy-Ion Collisions

Given the magnetic field,  $\vec{B}$ , and the initial axial charge,  $\mu_5$ , there will be an induced CME current along the direction of the magnetic field, and the sign will be dependent on the axial charge. This current will then transport the positive and negative charges to opposite ends of the Quark Gluon Plasma fireball, and that will form a dipole moment that depends on the non-uniform charge distribution in the QGP.

This can be included into the hadron production at freeze-out through a nontrivial electric charge potential of the form  $\sim \mu_e \sin(\phi_s - \Psi_{RP})$ , with  $\phi_s$  being the spatial azimuthal angle, and  $\Psi_{RP}$  being the reaction plane angle. This effect can be shown through the Cooper-Frye procedure for the produced final hadron’s spectra:

$$\frac{dN_{\pm}}{d\phi} \propto \int_{source} e^{-p^{\mu} u_{\mu}} e^{\pm(\mu_e/T_f) \sin(\phi_s - \Psi_{RP})} \quad (3.11)$$

Here we suppressed other kinetic variables and focused on the azimuthal angle distribution, and for simplicity we have chosen to use the Boltzmann approximation with the freeze-out temperature  $T_f$ . The strong radial flow (hidden in the flow velocity field  $u_{\mu}$ ) will collimate the azimuthal angle of the emitted hadron’s momentum with the spatial angle of the local

emission cell in the source, and so the out-of-plane dipole in the chemical potential will “translate” into a charge-dependent dipole term in the emitted hadron distributions. Using the parametrization of the particle azimuthal distribution in a form [70]:

$$\begin{aligned} \frac{dN_{\pm}}{d\phi} \propto & 1 + 2v_{\pm,1} \cos(\phi - \Psi_{RP}) + 2v_{\pm,2} \cos[2(\phi - \Psi_{RP})] + \dots \\ & + 2a_{\pm,1} \sin(\phi - \Psi_{RP}) + 2a_{\pm,2} \sin[2(\phi - \Psi_{RP})] + \dots \end{aligned} \quad (3.12)$$

where the coefficients  $v$  account for flow harmonics, specifically  $v_1$  accounts for directed flow and  $v_2$  accounts for elliptic flow; the coefficients  $a$  account for the charge separation effect, as we see that  $a_+ = -a_- \propto \mu_5 |\vec{B}|$ . Though this seems to lend itself to an easy way to investigate the charge separation effect, one thing that we need to note is that  $\mu_5$  arises from fluctuations and take on different signs for different events, and actually it is equally probable for it to be positive or negative, which means that directly measuring this observable would only lead to a result of 0 as it averages itself out over a large number of events. And that is what STAR has observed as seen in Figure 3.4, that there is no significant charge dependence across the centrality intervals [71].

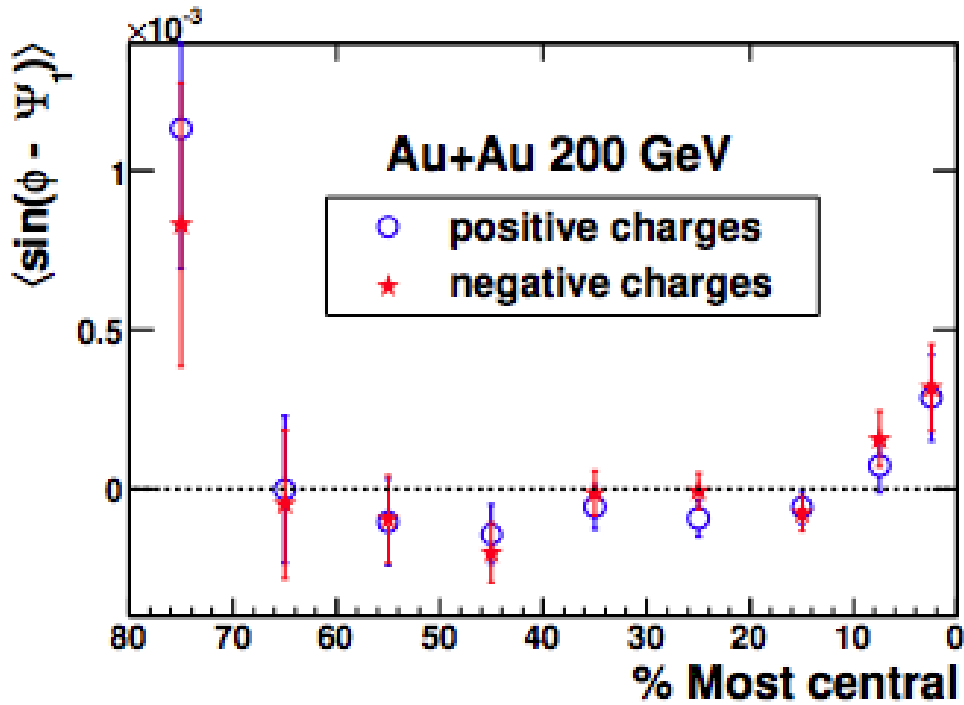


Figure 3.4: Measurement of  $\langle \sin(\phi - \Psi_{RP}) \rangle$  for Au+Au collisions at  $\sqrt{s_{NN}} = 200$  GeV [71].

One way to deal with this issue is by making it into a parity even observable, so that it would not average out to zero across the events, by measuring  $\langle a_{1,\alpha} a_{1,\beta} \rangle$ , with  $\alpha$  and  $\beta$  representing electric charges - positive or negative. The con of doing this is that this observable is vulnerable to background effects that could potentially dominate the measurement. Voloshin proposed a method to suppress these background effects by subtracting the desired out-of-plane correlation from the in-plane correlation [70], and it is the  $\gamma^{112}$  correlator:

$$\begin{aligned}
\gamma^{112} &\equiv \langle \cos(\phi_\alpha + \phi_\beta - 2\Psi_{RP}) \rangle \\
&= \langle \cos(\phi_\alpha - \Psi_{RP}) \cos(\phi_\beta - \Psi_{RP}) \rangle - \langle \sin(\phi_\alpha - \Psi_{RP}) \sin(\phi_\beta - \Psi_{RP}) \rangle \quad (3.13) \\
&= [\langle v_{1,\alpha} v_{1,\beta} \rangle + B_{IN}] - [\langle a_{1,\alpha} a_{1,\beta} \rangle + B_{OUT}]
\end{aligned}$$

With this correlator, we first note that the signal,  $\langle a_{1,\alpha} a_{1,\beta} \rangle$ , is now a parity even observable that does not average out to zero. Then, with  $\langle v_{1,\alpha} v_{1,\beta} \rangle$ , we have a reference to the directed flow, which we expect to be theoretically the same for same-charge ( $\alpha = \beta$ ) and opposite-charge ( $\alpha = -\beta$ ) particle correlations. This is the opposite for  $\langle a_{1,\alpha} a_{1,\beta} \rangle$ , where it is expected to be positive for same-charge correlation and negative for opposite-charge correlation. Therefore, if we subtract the opposite-charge  $\gamma$  correlator by the same-charge one, then the directed flow term would mostly vanish, while the charge separation effect remains, along with the background influences that is expected to cancel out to a large extent. The other interesting thing to note with regards to this background is its correlation with elliptic flow, that calculations from [70] and [67] have demonstrated. That will be a key piece of information for one of the methods developed and used in this analysis, called the event shape selection method that will be introduced later in this thesis.

### 3.3.4 CVE in Heavy-Ion Collisions

As mentioned before, the CVE is very similar to the CME. With nonzero average rotation  $\vec{\omega}$  of the QGP, and nonzero background vector charge density, specifically for this analysis a nonzero baryon density, the CVE current can be generated by the initial axial charge, and that leads to a separation of quarks and anti-quarks across the reaction plane, thus resulting in baryonic charge separation, analogous to the electric charge separation of the

CME. While the similarity in the two effects is very helpful in understanding the effects, it leads to complications because the two effects could simultaneously exist and difficult to separate out. Therefore, in order to ensure that we are investigating the CVE in this study, we specifically chose  $\Lambda/\bar{\Lambda}$  as it has baryonic charge while no electric charge.

One advantage of studying CVE is that it has been found that the vorticity of QGP is sustained [72], and that makes it theoretically easier to detect effects that arise from the vorticity of the fireball.

# CHAPTER 4

## Data Set and Reconstruction of Particles

### 4.1 Information on Data Set

This analysis focuses on the search for the CVE through investigating the correlation among the azimuthal angles of  $\Lambda/\bar{\Lambda}$  particles,  $p/\bar{p}$  and the event plane angle. This investigation was carried out using the minimum bias triggered data collected by STAR in 2018, with Au+Au collisions at  $\sqrt{s_{NN}} = 27$  GeV, as well as in 2019 Au+Au collisions at  $\sqrt{s_{NN}} = 19.6$  GeV. The trigger ID set is listed in Table 4.1.

Table 4.1: Triggers Used in Analysis

(a) $\sqrt{s_{NN}} = 27$ GeV		(b) $\sqrt{s_{NN}} = 19.6$ GeV	
Trigger Label	Offline Trigger ID	Trigger Label	Offline Trigger ID
minbias	610001	minbias	640001
minbias	610011	minbias	640011
minbias	610021	minbias	640021
minbias	610031	minbias	640031
minbias	610041	minbias	640041
minbias	610051	minbias	640051

### 4.2 Run-by-Run Quality Checks

In the data collection system of STAR, we call each collision as an event, and with a period of time collecting these events, we call them runs. While the most optimal would be that the

system does not change from event to event, from run to run, that clearly is not possible in the actual data taking process, and the machine and environment changes as time progresses. Therefore, it is necessary for us to do some quality assurance checks on these runs and events in order to make sure that the analysis that is performed is not influenced by the changes in environment. In this section we will discuss the criteria that we used in this analysis to check the runs. The committee that is responsible for determining the criteria for computations of the centrality of collisions also provides a bad run list with their own criteria, but we look at some further checks to make sure that the runs we ultimately include in the analysis satisfy our standards. There are nine criteria that we looked at in order to determine whether each run is usable - whether or not a run falls within reasonable conditions and thus can be used in our analysis. For each of these criteria, we looked at the runs and compared them with their neighboring runs and determined whether or not that they were outliers, see Figure 4.1. It is important to not look at outliers as a whole because sometimes there are systematic shifts in the environment, that actually is acceptable and the data do not need to be thrown out, one example being the reference multiplicity distribution that we see in the top right of Figure 4.1, where after a certain run the entire distribution shifted upwards because of changes in the system. The data points that are colored red represent the runs that were marked as bad runs and removed from the analysis.

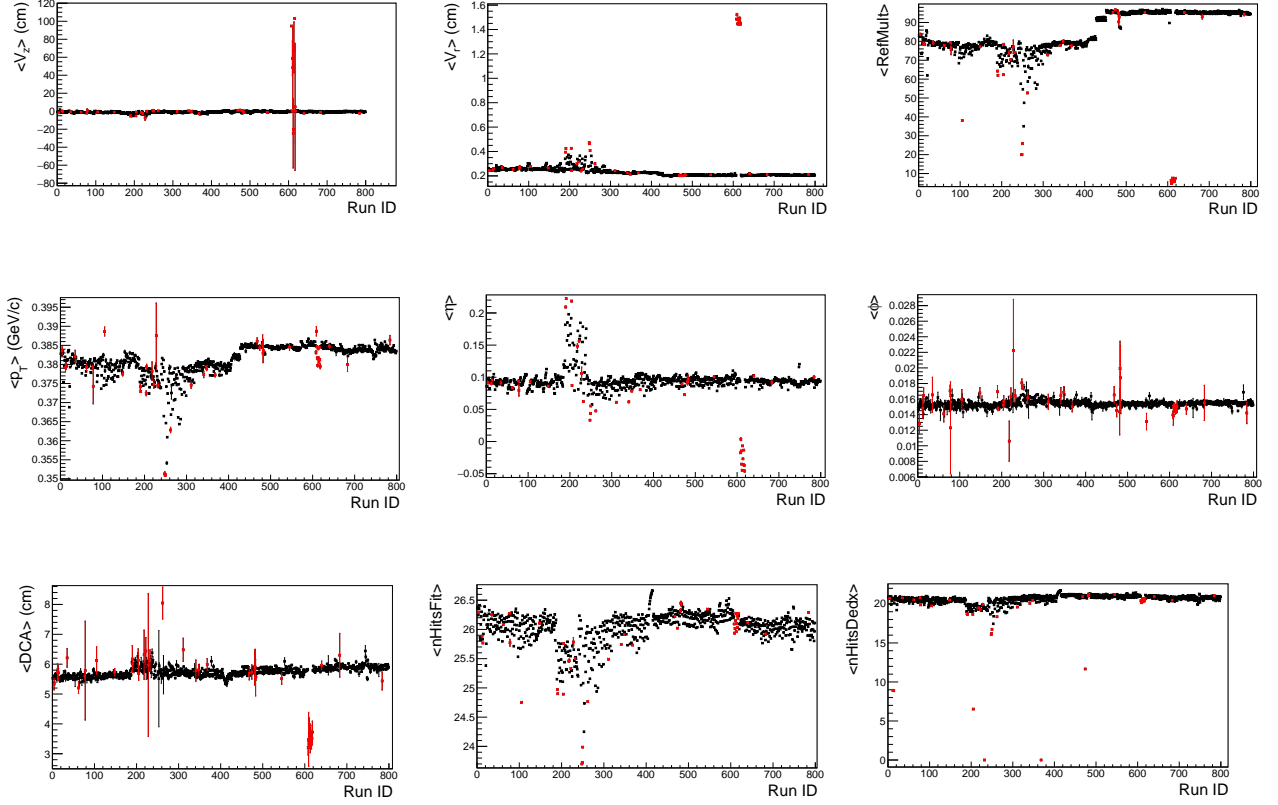


Figure 4.1: The nine criteria that were used in determination of the quality of the runs and whether or not they were included in this analysis. The red data points correspond to the runs that were removed (these runs are the same runs in all nine plots, not just the runs that were removed by the criterion that the plot represents). The black data points correspond to the runs that were ultimately included in the analysis and passed our quality checks. These plots correspond to the data collected by STAR in 2018, with Au+Au collisions at  $\sqrt{s_{NN}} = 27$  GeV.

Figure 4.1 corresponds to the data collected by STAR in 2018, with Au+Au collisions at  $\sqrt{s_{NN}} = 27$  GeV, and a similar procedure was performed to the data collected in 2019 Au+Au collisions at  $\sqrt{s_{NN}} = 19.6$  GeV to determine the bad runs for that data set. The full list of runs that were marked as “bad” and removed from the analysis can be found in Appendix A.

## 4.3 Event Characterization and Selection

### 4.3.1 Event Selection Criteria

There are also various criteria to eliminate events that were created in less than ideal scenarios. The first criterion is a selection in the  $x$ - $y$  plane, to lower the chances that collisions between a projectile ion and the wall of the beam pipe, or with residual gas in the vacuum would make it into the analysis. Therefore, a cut on the radial component of the primary vertex,  $v_r$ , is applied, requiring it to be less than or equal to 2cm. Also, in order to have reasonably consistent detector acceptance for the event sample, due to finite length of the detectors, for this data set there is a cut on the  $z$  component of the primary vertex,  $v_z$ , requiring it to be within the range of -70 to 70cm. See Figure 4.2 for plots demonstrating the distribution of the vertices of the events used in the analysis. These cuts are the same for both the 27 GeV and 19.6 GeV data sets. After these event-level cuts, there are approximately  $4.12 \times 10^8$  events for 19.6 GeV Au+Au collisions, and  $5.16 \times 10^8$  events for 27 GeV.

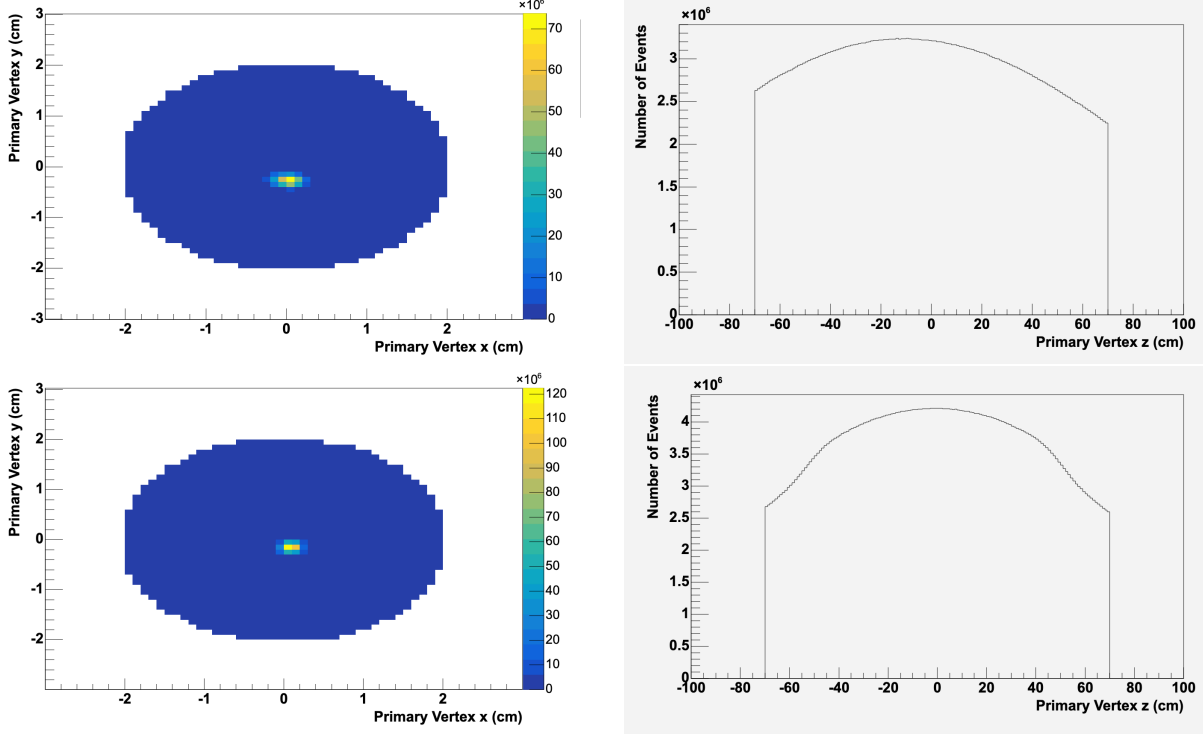


Figure 4.2: The transverse components and  $z$  component of the primary vertex of the collision events to demonstrate the cuts that were applied on the event level. The top two plots are for Au+Au 19.6 GeV collisions, and the bottom two are for 27 GeV.

### 4.3.2 Centrality

Centrality is a crucial characteristic used to classify events in nuclear collisions. It represents the degree of overlap between the two colliding beams in a particle accelerator. The significance of centrality arises from the substantial differences that can be observed in the nuclear matter produced during heavy ion collisions, depending on whether the collisions are central or peripheral. Hence, it is essential to differentiate between measurements based on these distinct collision types. Since the STAR detector, along with other detectors at RHIC, cannot directly observe the microscopic geometry of each collision event, the Glauber model [73] was developed. This model utilizes Monte Carlo simulations to indirectly extract information about the collision geometry from the data collected by our detectors.

The Glauber model is based on the concept of representing the nucleus as an assembly

of uncorrelated nucleons, sampled from experimentally derived density distributions. This approach simplifies the scenario by eliminating potential complexities arising from correlations. In this model, two nuclei undergo collisions with random impact parameters ( $b$ ), drawn from the distribution  $d\sigma/db = 2\pi b$ , and the collision outcomes are projected onto the  $x$ - $y$  plane. The simplification arises from the treatment of nucleus-nucleus collisions as a sequence of independent binary nucleon-nucleon collisions. This means that nucleons move along straight-line trajectories, and the inelastic nucleon-nucleon cross-section is assumed to be independent of the number of collisions a nucleon has experienced prior. The determination of whether a collision occurs is based on comparing the distance between nucleons to various functions. The choice of function depends on the specific version of the Glauber model employed and can be related to either the inelastic collision cross-section or the Gaussian overlap function. An example of this, colored to represent nucleons that are and are not part of the simulated collisions, is shown in Figure 4.3.

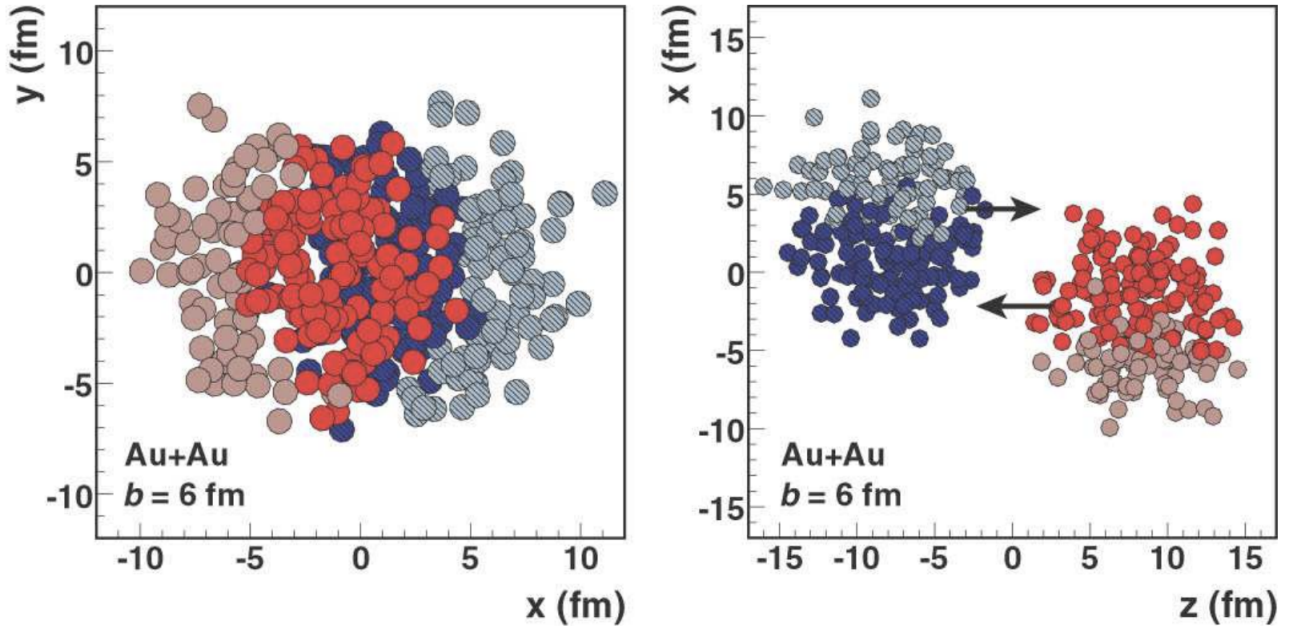


Figure 4.3: This is a Glauber Monte Carlo event, simulated as a Au+Au collision at  $\sqrt{s_{NN}} = 200$  GeV. The impact parameter ( $b$ ) of this simulated collision is 6 fm, a quantity that is randomly drawn from the distribution  $d\sigma/db = 2\pi b$ . The left is a view in the transverse plane, and the right is a view from the beam pipe [73].

However, the Glauber model, because it depends on the nucleon-nucleon inelastic cross section and the geometry of the interacting nuclei, it will depend on the number of participant and number of collisions. However, these numbers are not directly measurable from RHIC heavy-ion collisions. This means that the Glauber model would have to map a measured distribution to the corresponding distribution obtained from phenomenological Glauber calculations by connecting the mean values from the same centrality class in these two distributions. This mapping will be heavily dependant on the specifics of the experiment as well as the collision system. Therefore, each year, for each type of collision system at STAR, there is a Centrality Group that focuses on defining the proper definitions for the Centrality classes, and that is also what is referenced in the analysis in this thesis as the results are shown split by centrality. Figure 4.4 demonstrates the basic assumption of this split in centrality bins - that the impact parameter is monotonically related to particle multiplicity, in both the mid and forward rapidity. This means for peripheral events, where the impact parameter is large, we expect low multiplicity at mid-rapidity and a high number of spectator nucleons, whereas for central events, with small impact parameters, we would see large multiplicities in the mid-rapidity and a small number of spectator nucleons.

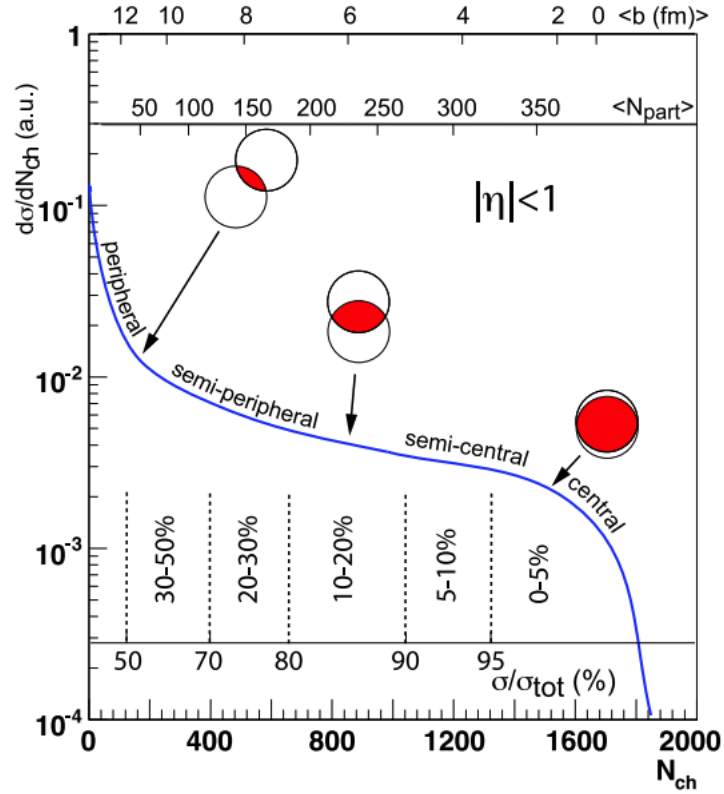


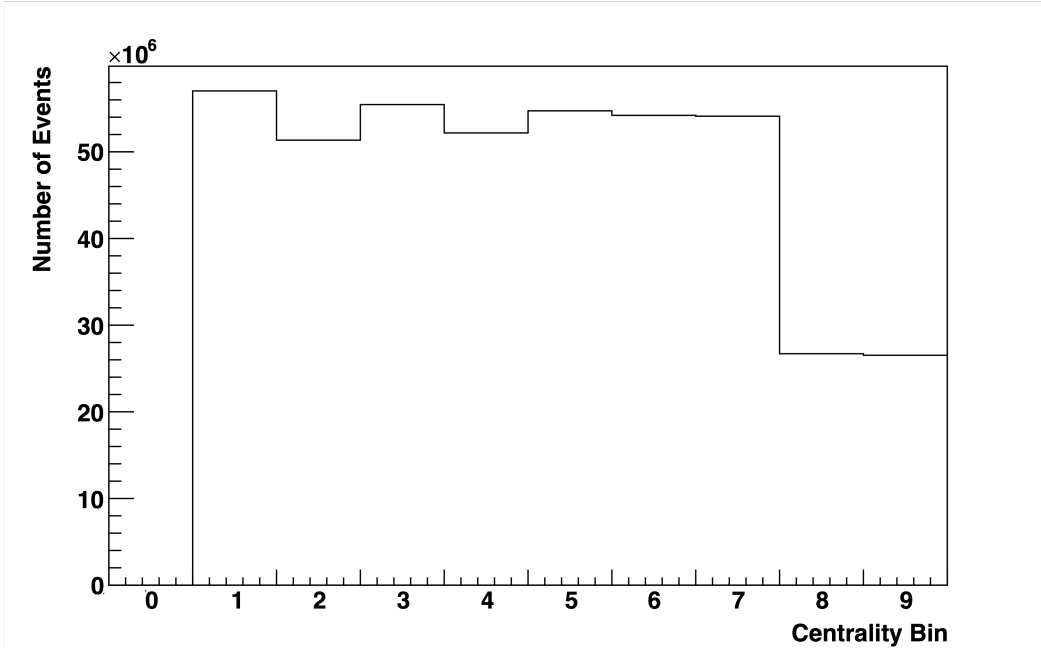
Figure 4.4: A cartoon demonstration of how the multiplicity is related to Glauber model quantities like the impact parameter,  $b$ , and the number of participants. Note that this is simply an illustration and does not show actual measurements [73].

For this specific analysis, the collision systems of interest are the 27 GeV Au+Au collisions and the 19.6 GeV Au+Au collisions. The Centrality classes are provided as a software package class named `StRefMultCorr`, and is used in this analysis. The computed values of the number of participants,  $N_{\text{part}}$ , can be found in Table 4.2, and these values will be used to better visualize the results of this thesis' analysis later.

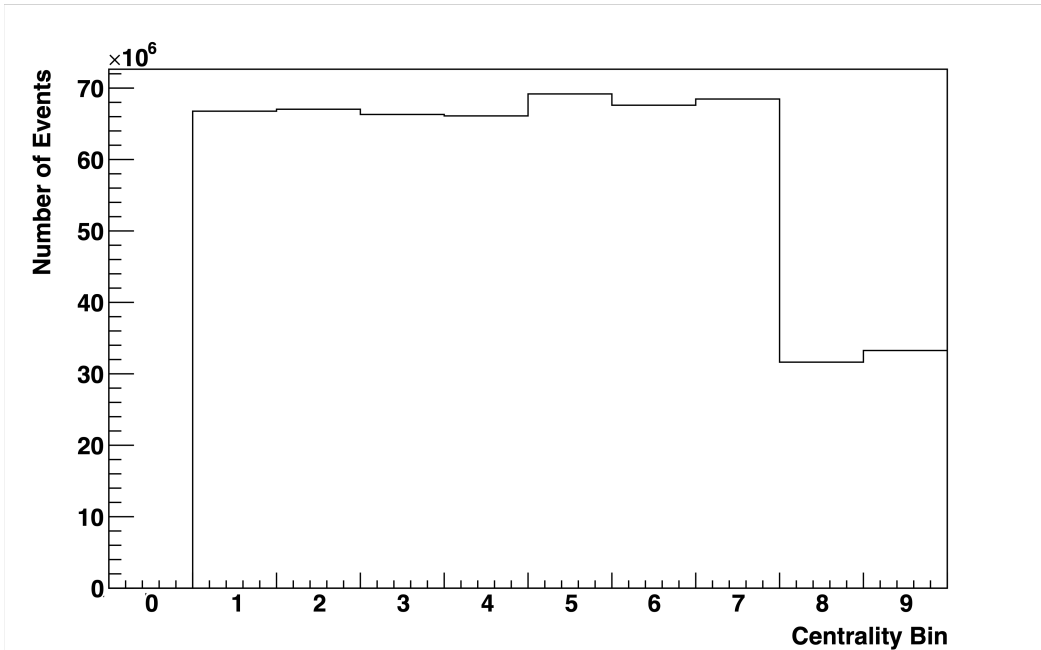
Table 4.2:  $N_{\text{part}}$  of Centrality Classes

(a) $\sqrt{s_{\text{NN}}} = 27 \text{ GeV}$			(b) $\sqrt{s_{\text{NN}}} = 19.6 \text{ GeV}$		
Centrality	$N_{\text{part}}$	systematic error	Centrality	$N_{\text{part}}$	systematic error
0-5%	343.3	2.01	0-5%	338.0	2.29
5-10%	299.3	6.19	5-10%	289.2	6.00
10-20%	233.6	8.98	10-20%	224.9	8.62
20-30%	165.5	10.71	20-30%	158.1	10.48
30-40%	114.0	11.28	30-40%	108.0	10.64
40-50%	75.0	10.33	40-50%	70.85	10.09
50-60%	46.7	9.19	50-60%	43.88	8.71
60-70%	26.8	7.76	60-70%	25.46	6.78
70-80%	13.8	5.83	70-80%	13.84	4.99

With the definition of the centrality classes with the aforementioned software package class named StRefMultCorr developed by STAR, and the centrality definitions generated according to the Glauber model for each collision energy and type, the following figure shows the distribution of events across the centralities for the two collisions that are of interest in this thesis:



(a)



(b)

Figure 4.5: Plot (a) shows the distribution of events across the centrality classes for 19.6 GeV Au+Au collisions, and Plot (b) is for 27 GeV Au+Au collisions. This is weighted by the event weight that is generated from the StRefMultCorr class. For reference, Table 4.3 shows the conversion between centrality classes and centrality bins used here.

For some of the plots later in this thesis, as well as the figures above, instead of using the centrality classes for label, we also use the centrality bin interchangeably as sometimes that is an easier depiction. So for reference the following is a conversion between the centrality class and centrality bin, Table 4.3:

Table 4.3: Centrality Classes and Centrality Bins

Centrality	Centrality Bin
0-5%	9
5-10%	8
10-20%	7
20-30%	6
30-40%	5
40-50%	4
50-60%	3
60-70%	2
70-80%	1

#### 4.4 $\Lambda(\bar{\Lambda})$ Baryon Reconstruction

Since the decay length of  $\Lambda(\bar{\Lambda})$  Baryon particles ( $m = 1115.683 \pm 0.006$  MeV,  $\tau = 2.632 \pm 0.020 \times 10^{-10}$ s [74]) is short, and they do not have electrical charge, it is difficult to directly detect them in STAR. However, it is possible to choose the decay channel where they decay into charged particles with longer half-lives to reconstruct them. The decay channel that was chosen is:

$$\Lambda \rightarrow p\pi^- \quad (4.1)$$

$$\bar{\Lambda} \rightarrow \bar{p}\pi^+ \quad (4.2)$$

with a branching ratio of  $63.9 \pm 0.5\%$  [74]. These particles will be reconstructed by the Time Projection Chamber (TPC), and thus possible to be used to reconstruct the  $\Lambda(\bar{\Lambda})$  Baryon

particles of interest. The method to choose the proper daughter particles to reconstruct the parent particles includes basic quality cuts on each of the tracks, and then using what we understand about the decay topology (see Figure 4.6) to determine topological cuts to ensure that the daughter particles' tracks coincided with one another, thus having the possibility of being the decay daughters of the  $\Lambda(\bar{\Lambda})$  Baryon particles of interest. See Table 4.4 for a summary of the track quality cuts, and Table 4.5 for the centrality-dependent topological cuts.

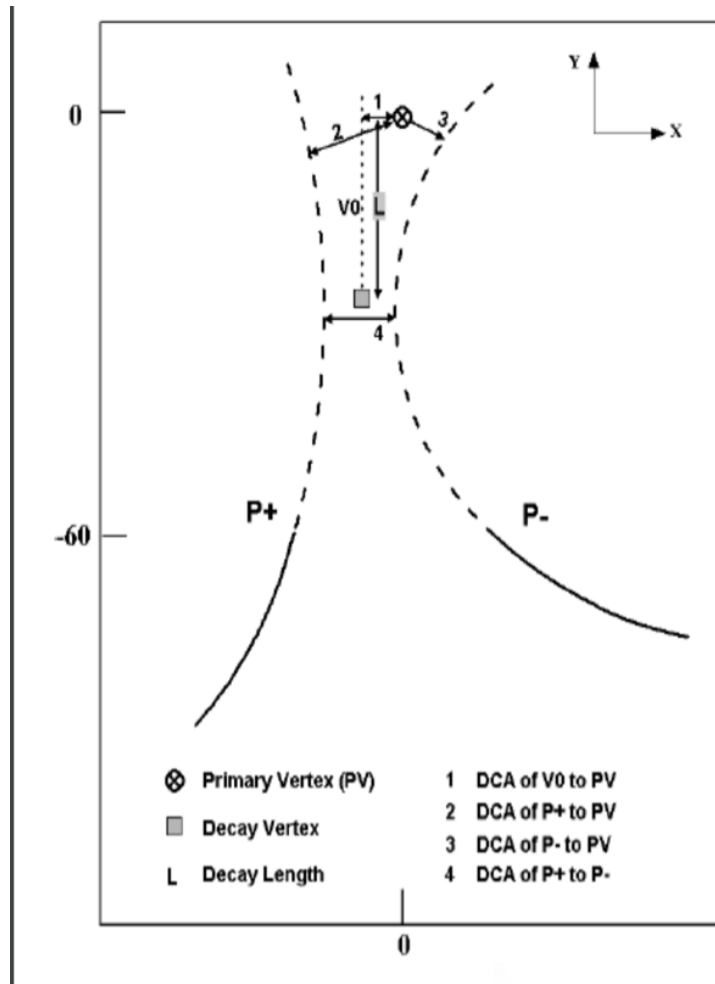


Figure 4.6: This diagram demonstrates the topology of the decay of a general neutral particle into two daughters, and thus can be illustrative for our specific case of  $\Lambda(\bar{\Lambda})$  Baryon particles decaying into  $p\pi^-$  and  $\bar{p}\pi^+$ . DCA is short-hand for Distance of Closest Approach, which is the closest distance of any two given points, or a track to a point, or any two tracks [75].

Table 4.4: Track Quality Cuts for Daughter Tracks for  $\Lambda \rightarrow p\pi^- / \bar{\Lambda} \rightarrow \bar{p}\pi^+$

Track Cuts	Values
# of TPC Hits Used in Fit/ Max. # of Possible TPC Hits	$\geq 0.52$
# of TPC Hits Used in Fit	$>15$
$ N\sigma $ for $p/\bar{p}$	$<4.0$
$ N\sigma $ for $\pi^-/\pi^+$	$<4.0$
$p_T$ of $\pi^-/\pi^+$	$>0.15$ GeV/c
$p_T$ of $p/\bar{p}$	$>0.2$ GeV/c , $<2.0$ GeV/c

Table 4.5: Centrality-Dependent Topology Cuts for  $\Lambda \rightarrow p\pi^- / \bar{\Lambda} \rightarrow \bar{p}\pi^+$

Centrality	DCA from $p/\bar{p}$ to Primary Vertex	DCA from $\pi^-/\pi^+$ to Primary Vertex	DCA from $p/\bar{p}$ to $\pi^-/\pi^+$	Decay Length of $\Lambda/\bar{\Lambda}$
0-20%	$>0.4$ cm	$>1.5$ cm	$<0.9$ cm	$>4.0$ cm
20-40%	$>0.3$ cm	$>1.3$ cm	$<1.0$ cm	$>3.5$ cm
40-60%	$>0.2$ cm	$>1.0$ cm	$<1.1$ cm	$>3.0$ cm
60-80%	$>0.1$ cm	$>0.8$ cm	$<1.2$ cm	$>2.5$ cm

#### 4.4.1 Background Estimation

Even with these cuts there will be background to this reconstruction. Therefore, it is important to find a way to model the background and to estimate the background contribution. The method that we use in this analysis is by creating fake  $\Lambda(\bar{\Lambda})$  baryons by rotating the  $\pi^+/\pi^-$  track by  $180^\circ$ . Basically, by identifying a  $\pi^+/\pi^-$  track using the same criteria, then rotating the track by  $180^\circ$ , and then matching this rotated track with a  $p/\bar{p}$  track and select based on the same topological criteria, we would reconstruct  $\Lambda(\bar{\Lambda})$  baryons that are certainly not real. Then, by looking at the invariant mass distribution of these baryons, it would help

model the background of the reconstructed baryons.

What we can understand for the invariant mass distribution of the rotated backgrounds is that it is a smooth distribution without any peaks, especially under the peak of the invariant mass distribution of the reconstructed baryons. This piece of information is important because that allows us to model the background of the reconstructed baryons with a polynomial function. Hence we have the models, with an example in Figure 4.7, where the red line represents the polynomial fit to identify the background underneath the signal peak. Then we varied the mass cuts, represented by the blue vertical lines, a little to try to get the best ratio between real signal to background, and settled on a mass cut of  $(1.113 \leq m \leq 1.119) \text{ GeV}/c^2$ .

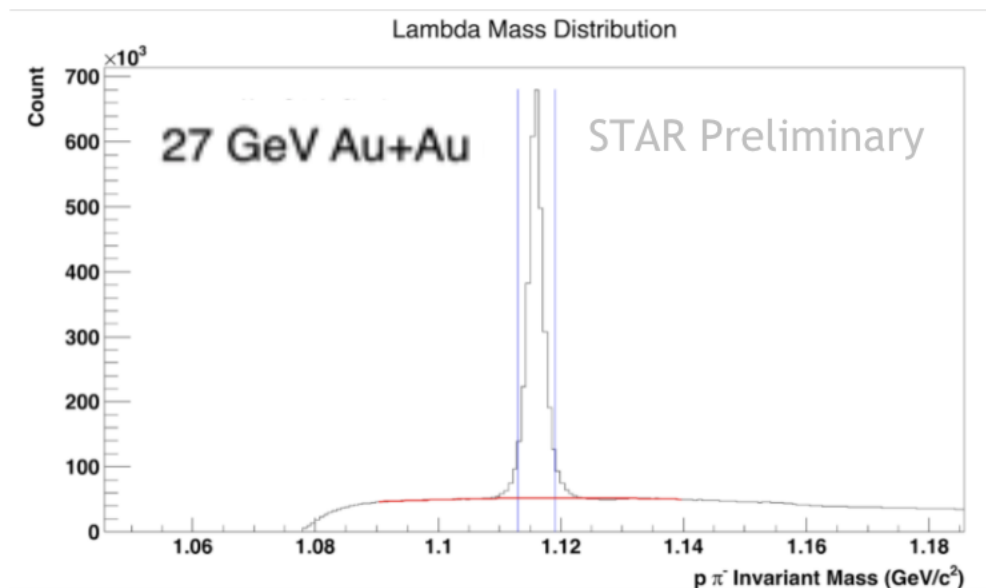


Figure 4.7: An example distribution of  $\Lambda$  Mass; The red line represents the polynomial fit to determine the background; the blue lines represent the mass cuts for optimal signal to background ratios while maintaining sufficient statistics.

With this mass cut, then the purity statistics (the signal to total statistics ratios) were computed, and are used in the analysis to correct the background effects. Figure 4.8 shows the purity statistics of  $\Lambda/\bar{\Lambda}$  particles for 27 GeV Au+Au collisions.

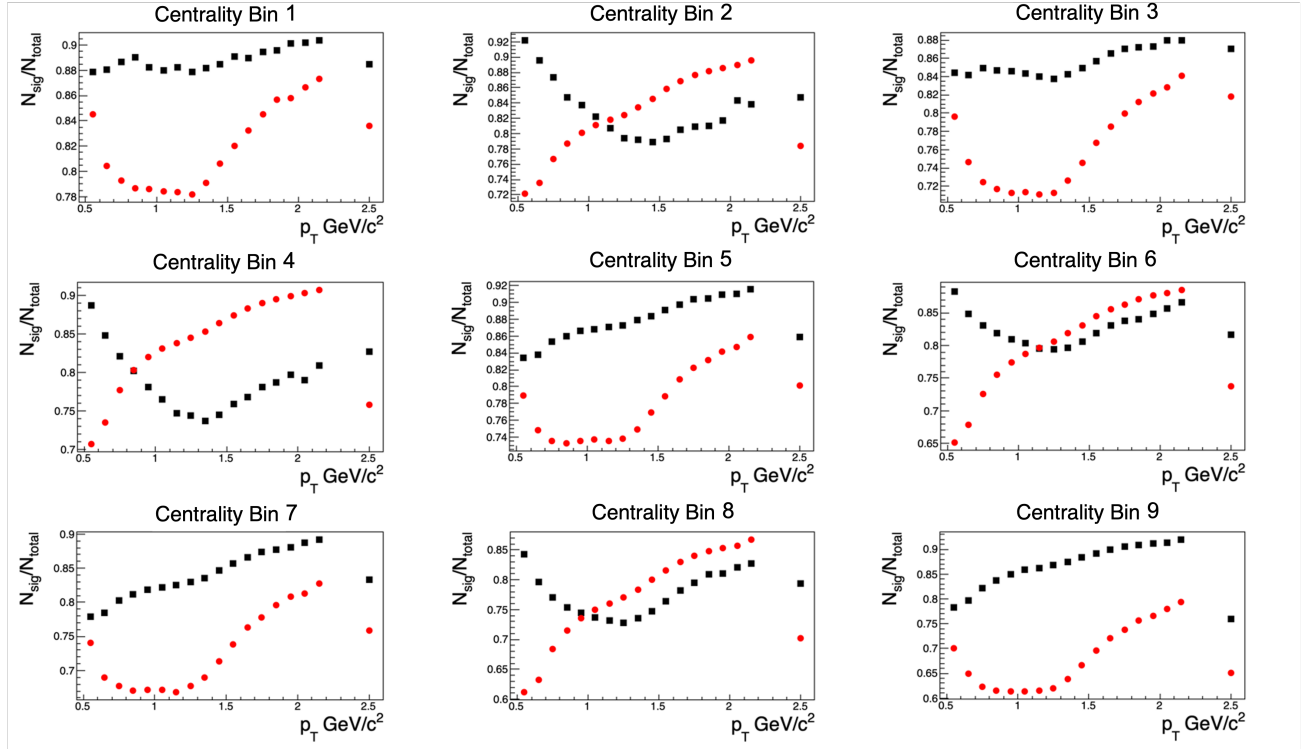


Figure 4.8: The purity statistics of  $\Lambda/\bar{\Lambda}$  particles for 27 GeV Au+Au collisions. The black data points represent  $\Lambda$  and red data points represent  $\bar{\Lambda}$ .

#### 4.4.2 KFParticle

The traditional method to reconstruct particles have some serious shortcomings. First, the information about the errors of daughter particle trajectories is not taken into account, and that could affect the reconstruction accuracy of the mother particle. For example, for this analysis, it would mean that the error information of the daughter  $p$  and  $\pi$  tracks was not taken into account in the reconstruction of the  $\Lambda$  particle. Second, the method that involves finding a point of closest approach in a nonhomogeneous magnetic field is not time efficient. Third, even though there are other methods that reconstruct these short-lived particles, such as the secondary vertex, or the point at which the particle decayed, by fitting with the Kalman filter method [76][77], these methods all have their own downsides that would be great to be addressed for future methods to reconstruct short-lived particles. And that is what the KF Particle package has been developed for [78][79].

The KF Particle package is based on the Kalman filter mathematics, with the state vector of the particle that includes eight parameters: the three coordinates of the particle, three components of its momentum, its energy, and when its production point is known, the time between production and decay points measured in a distance normalized by the momentum of the particle [80]. The daughter and mother particles are described with the same set of parameters and are treated in exactly the same way. The daughter particles are added to the mother particle in a way that allows the addition to be absolutely independent. The package itself is geometry independent and allows reconstruction of decay chains. It is implemented in single precision and is fully SIMDized [80].

With this information, the KF Particle Package is able to fully reconstruct a particle's decay vertex, momentum and energy. On top of that, the covariance matrix is estimated together with the state vector, so that not only the parameters are obtained but also their accuracy and the quality of reconstruction based on  $\chi^2$ . The package also allows for the users to set constraints on the particle state vector, specifically on the mass and production point of the particle. This is significant because the mass constraints allow for improvements in the information of the mass and momentum of the found particle. The production point constraints could help with identifying the point from which the particle is coming, for example a collision point. These pieces of information are very important for decay chain reconstructions [80]. The package also sophisticated methods to compute the point of closest approach between a particle and a vertex, as well as between two particles, as well as methods to apply nonlinear mass constraints to decay reconstruction trees to improve on the resolution of the mass of the reconstructed particles.

One way that the  $\chi^2$  criteria are used in order to improve the final reconstruction results is the distinguishing between secondary and primary particles. Primary particles are those that were produced directly in the heavy-ion collisions, when the nuclei collide. Secondary particles are the decay products of short-live particles that were produced from the collisions. Therefore, it is quite important to properly distinguish between primary and secondary tracks when going through this reconstruction process.  $\chi^2$  criterion is used here to place a constraint on the distance of the closest approach between the track examined and a primary vertex,

normalized on their total error. It defines the probability that this particular track intersects the primary vertex within the errors, with the assumption that parameters of the track are distributed according to the Gaussian distribution, while  $\chi^2$  is distributed according to the  $\chi^2$ -distribution with two degrees of freedom. And this is true for when the Kalman filter is used, and all the tracks are extrapolated to the primary vertex point in order to compute the  $\chi^2$  criterion.

After these tracks are sorted into primary and secondary tracks, as well as positively and negatively charged tracks, the reconstruction of the short-lived mother particles can begin. The scheme is outlined in the block-diagram shown in Figure 4.9. The short-lived particles that have a lifetime large enough to be separated from the primary vertex are reconstructed from one positive and one negative secondary track, and the  $\Lambda/\bar{\Lambda}$  particles that are of interest in this analysis are created through that scheme. The positive and negative secondary tracks are combined according to their PID hypothesis into the particle candidates decaying by the corresponding channels. However, there are combinations of these tracks that produce a candidate that are simply not real particles, and those are the backgrounds to our physical signals. Various cuts based on fit quality and decay topology are employed in order to suppress this background. The first cut is one on the  $\chi^2_{fit}/\text{NDF}$  criterion that is calculated by the KF Particle mathematics in the candidate fit. This criterion essentially shows whether or not the pair of secondary tracks currently used to combine into the particle candidate have trajectories that intersect within their errors. A second cut is on the  $\chi^2_{topo}/\text{NDF}$  criterion. This cut constrains the production point of the candidate reconstructed to be near the primary vertex region. The third cut is on the distance from the decay point of the candidate to the primary vertex normalized on the error. However, because strange particles and hypernuclei have a larger lifetime and that separates them from the primary vertex, only the first and third cuts are applied, selecting the candidates that are constructed more than several  $\sigma$  away from the primary vertex region. These cuts are optimized with respect to the signal to background ratio [81]. The reconstructed candidates that pass these cuts are then the ones that are used in the analysis.

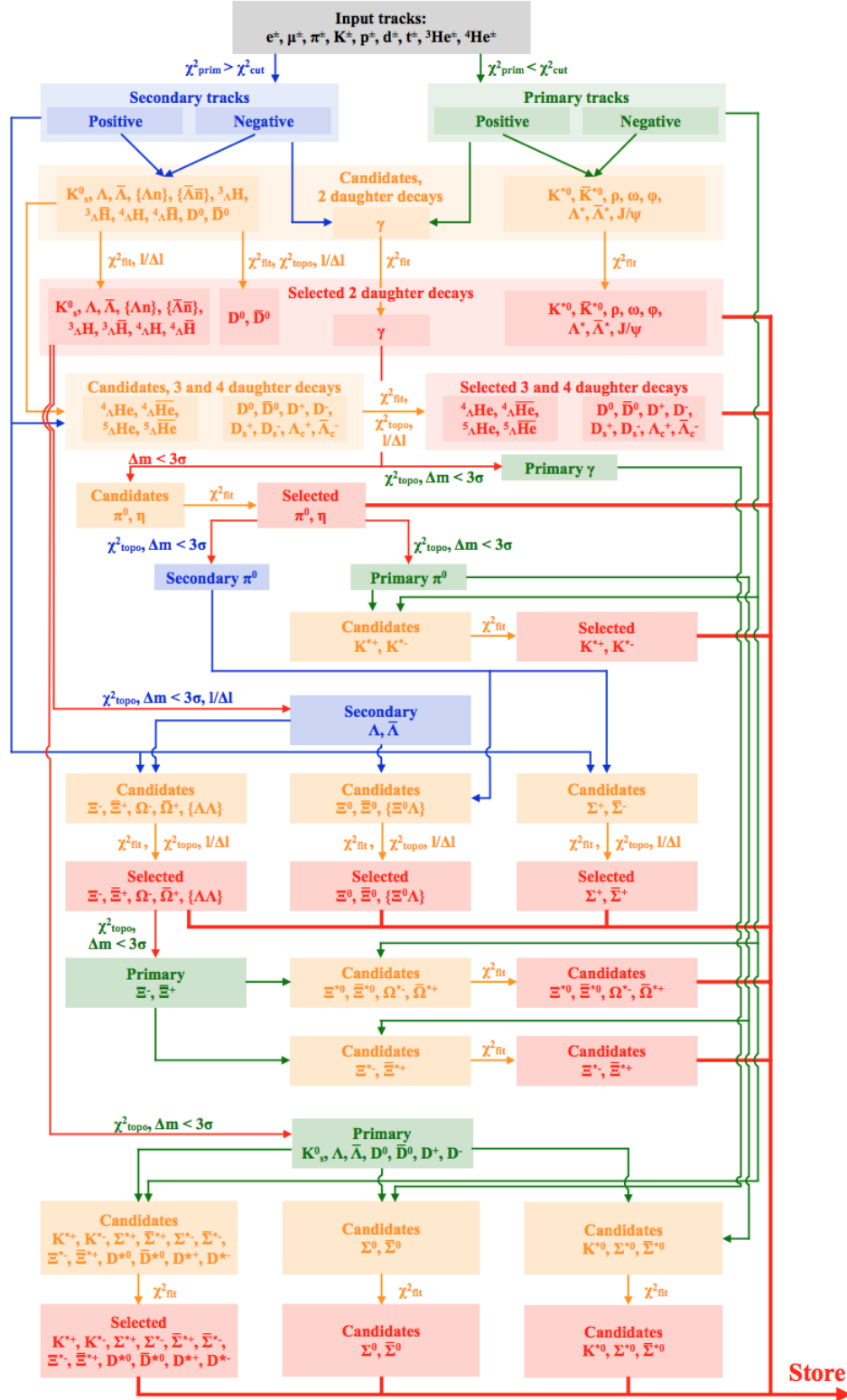
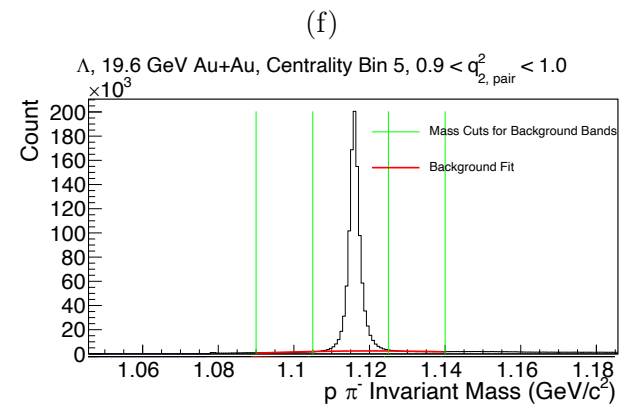
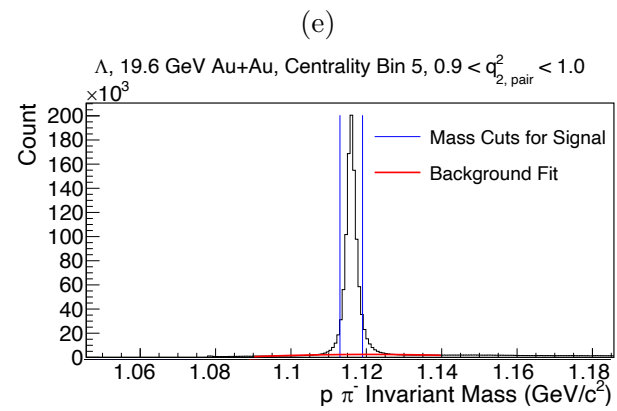
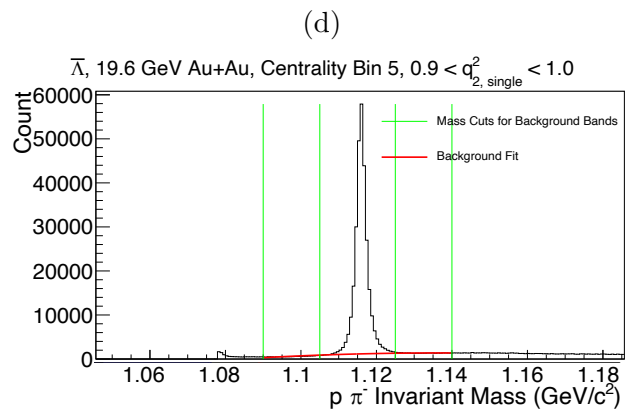
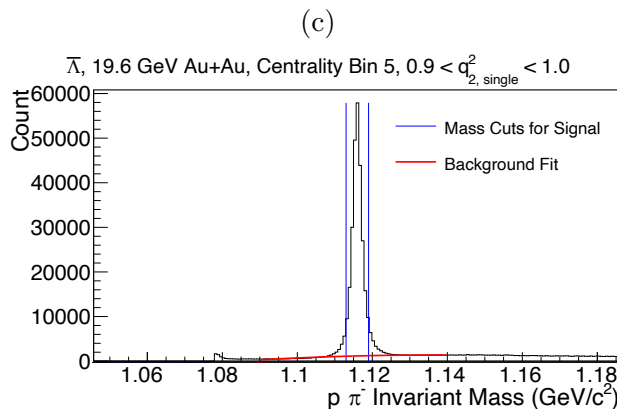
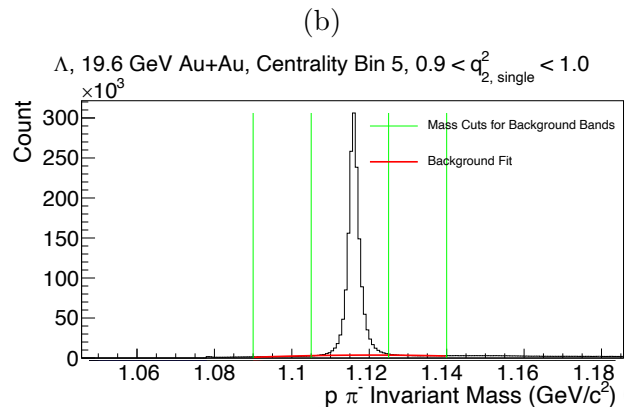
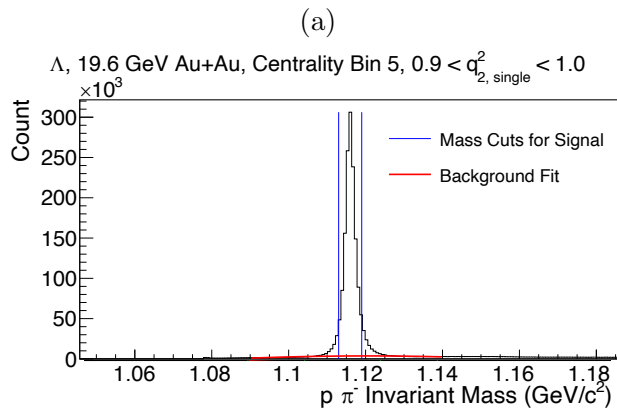
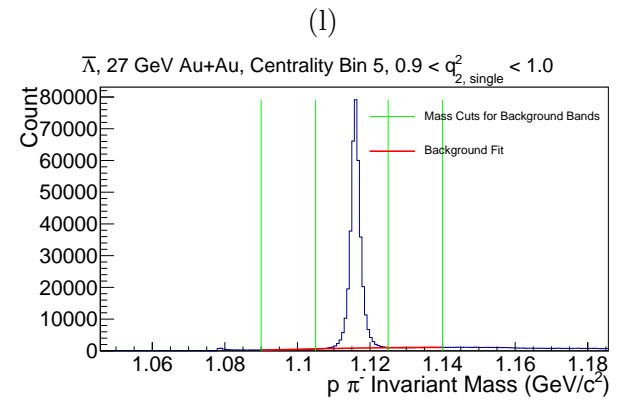
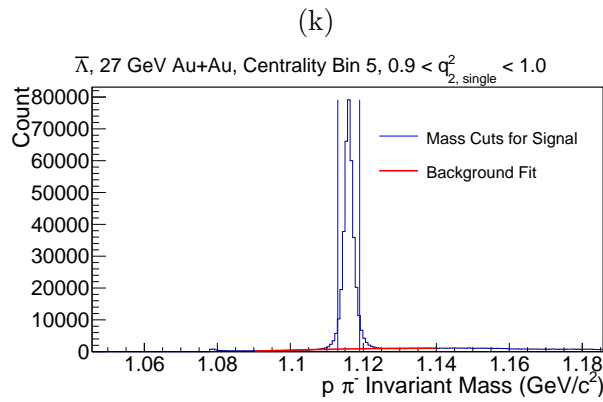
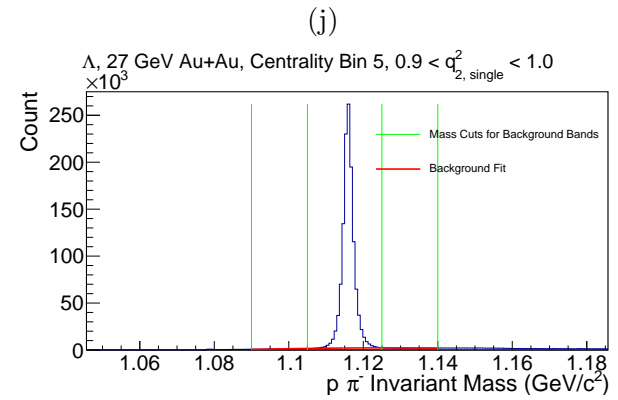
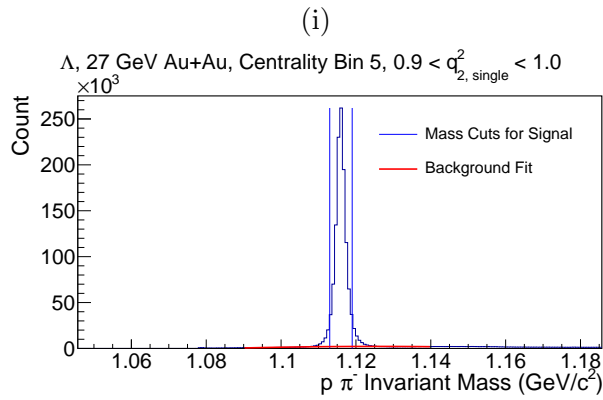
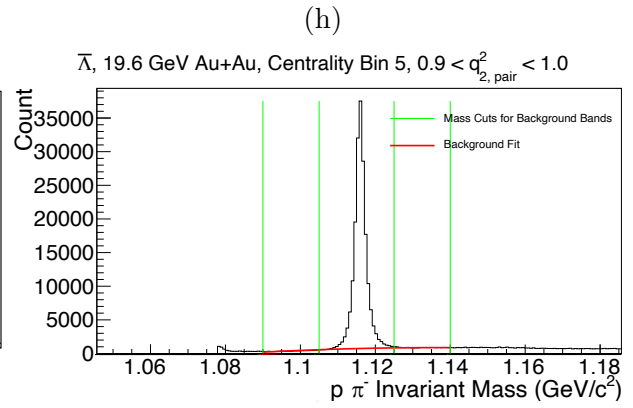
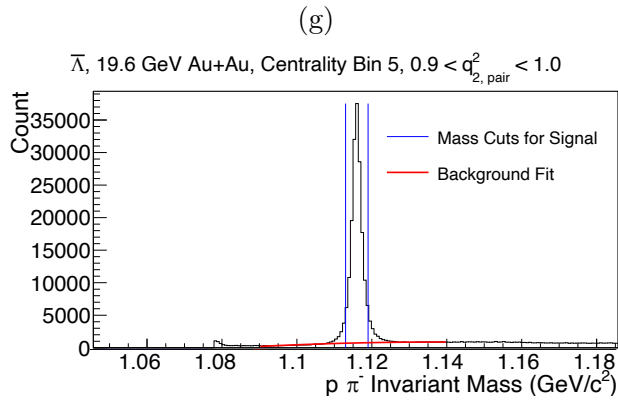


Figure 4.9: This is a block-diagram of the scheme used to reconstruct short-lived particles employed in the KF Particle Finder package [80]. The cuts on  $\chi^2_{\text{fit}}$  and  $\chi^2_{\text{topo}}$  are given in terms of the number of degrees of freedom.

### 4.4.3 Background Estimation

With the better reconstruction algorithm of KFParticle, we are able to reconstruct  $\Lambda/\bar{\Lambda}$  particles with a much higher purity. Figure 4.10 shows examples of the new distributions for these baryons. Because of the event shape engineering method that we will use as described later in this thesis, and that we'll be using the event handle pair-pion  $q_2^2$ , where  $q$  is the flow vector as defined by Eq. 5.36, 5.37 and 5.38 for all pion pairs, we'll divide the baryon distributions based on binning on this event handle as well.





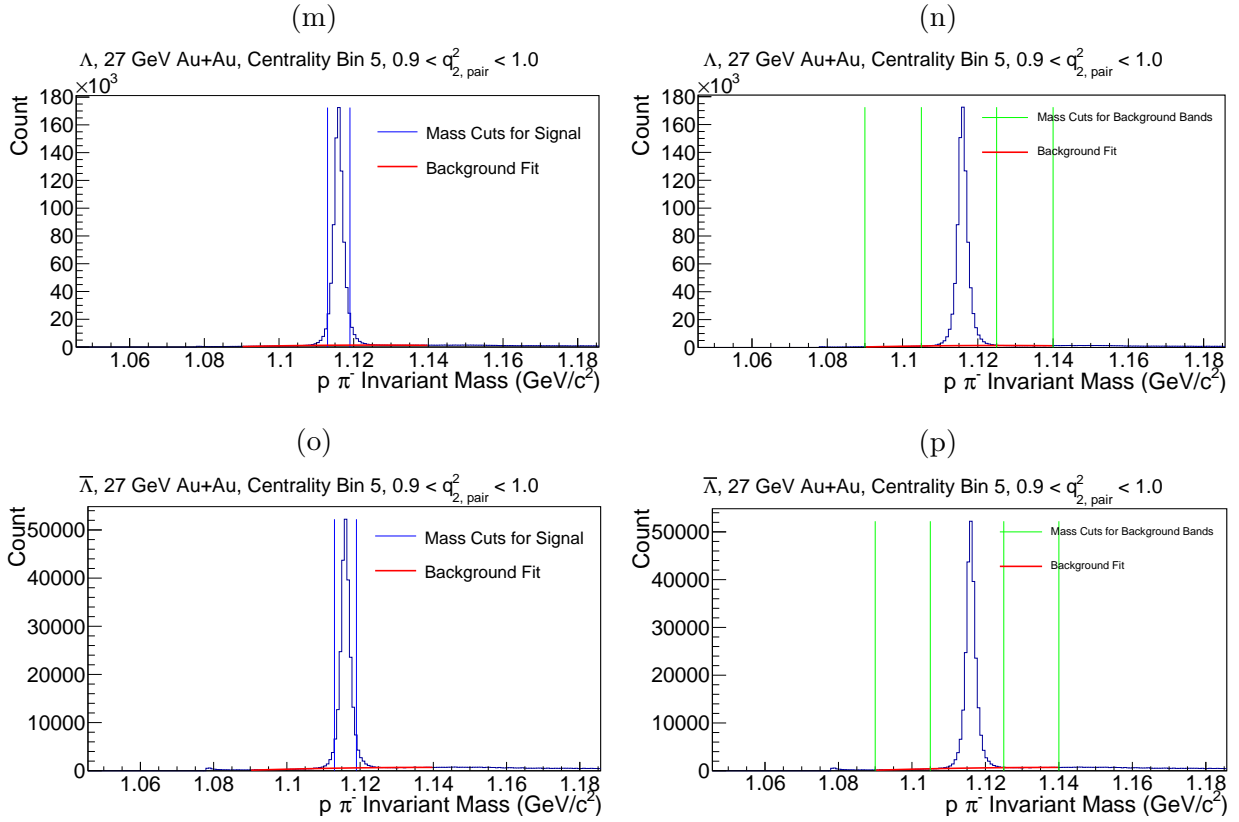


Figure 4.10: Figures (a)-(h) are for 19.6 GeV Au+Au collisions, and Figures (i)-(p) are for 27 GeV Au+Au collisions. These figures are examples of the mass distribution of the reconstructed baryons for demonstration purposes. All these plots correspond to centrality bin 5, which is 20-30%, and for the event handle pair-pion  $q_2^2$  between the values 0.9 and 1.0. These plots are example plots for how the background estimation for the signals are done. The plots on the left column demonstrate how the signal was extracted (specifically the mass range that was selected for the signal), and the right column demonstrate the mass range for the background estimation of the signal. The red curve represents the estimation of the background under the signal curve, which is how we compute the percent purity for each of the centrality - pair-pion  $q_2^2$  bins for background corrections in this analysis.

As we see in Figure 4.10, as compared with Figure 4.7 using the topological reconstruction method, the KFPparticle algorithm does a much better job of eliminating background and keeping the sample pure, while also maintaining a good number of signal. As for how this

information is used, we see in Figure 4.10, the left column corresponds to the selection of the baryons that are used in our signal calculation. This sample includes a certain number of falsely-reconstructed baryons, which are represented under the red curve. The estimate how the percent of the signal that is from actual baryons compared to the total number of baryons reconstructed is what we call purity. Having this information, along with what we get in the right column, which represent the mass ranges that we used in order to select for baryons that were reconstructed that we know are not real baryons, but we use those to compute our observable as well, in order to have an estimate on the background for our observable. So with our  $\text{signal}_{\text{measured}}$ , purity, and  $\text{signal}_{\text{background}}$ , we can arrive at the following relation in order to extract the real signal,  $\text{signal}_{\text{real}}$ :

$$\text{signal}_{\text{measured}} = \text{purity} * \text{signal}_{\text{real}} + (1 - \text{purity}) * \text{signal}_{\text{background}} \quad (4.3)$$

$$\text{signal}_{\text{real}} = (\text{signal}_{\text{measured}} - (1 - \text{purity}) * \text{signal}_{\text{background}}) / \text{purity} \quad (4.4)$$

Therefore, we compute our purity statistics in order to help us make this estimated correction for falsely reconstructed baryons that are under the signal curve. Figures 4.11 and 4.12 show the purity statistics as a function of our event handle pair-pion  $q_2^2$  bins, and Figures 4.13 and 4.14 show the statistics as a function of event handle single-pion  $q_2^2$  bins.

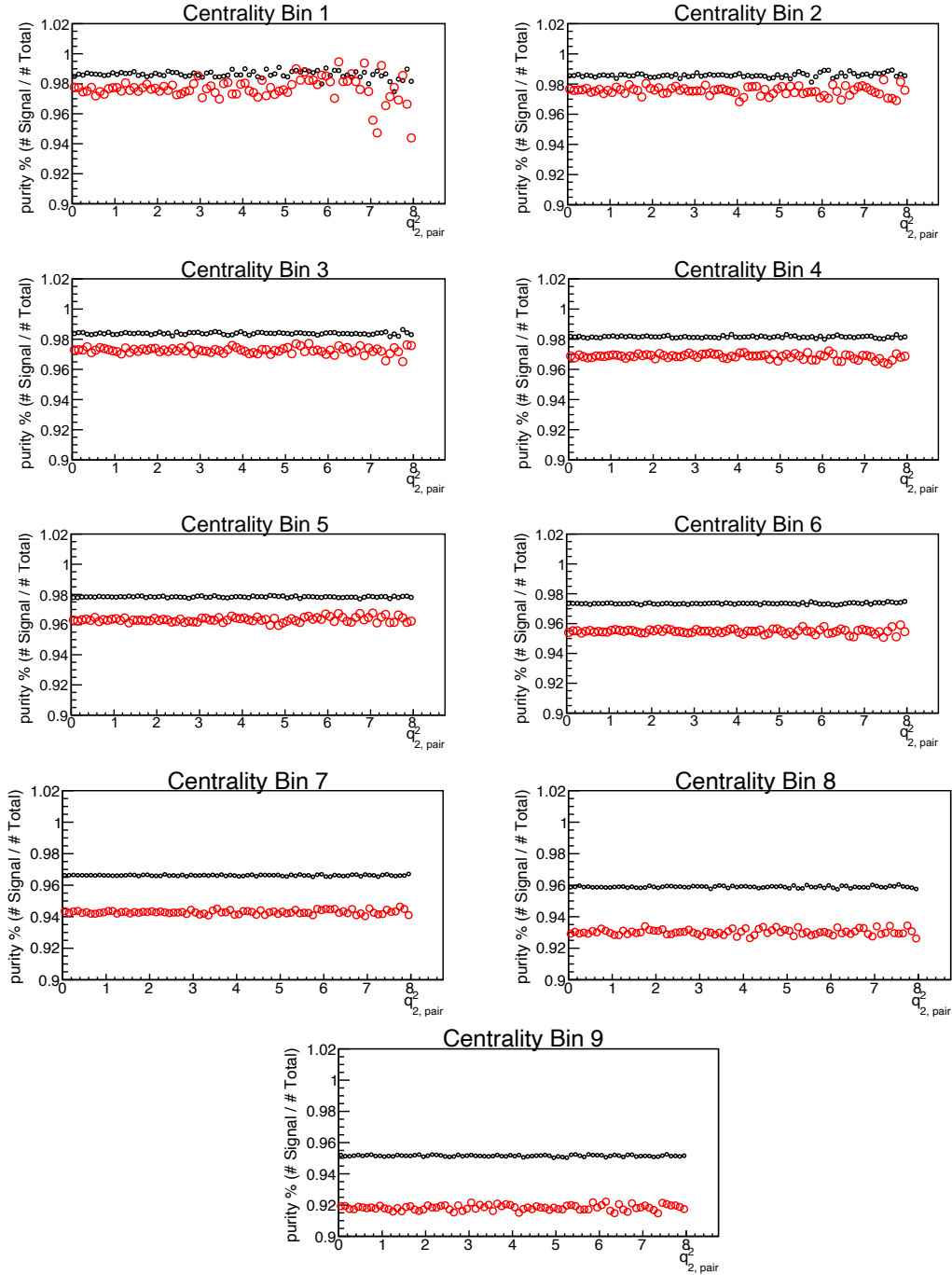


Figure 4.11: For 19.6 GeV Au+Au collisions, binned by pair-pion  $q_2^2$ . The black data points correspond to  $\Lambda$  purity statistics, whereas the red ones correspond to  $\bar{\Lambda}$  particles. As can be seen from the plots, there is not a strong dependence on the event handler, and the purity is very good - over 90% of reconstructed baryons are estimated to be true baryons for all centralities and all event handler bins.

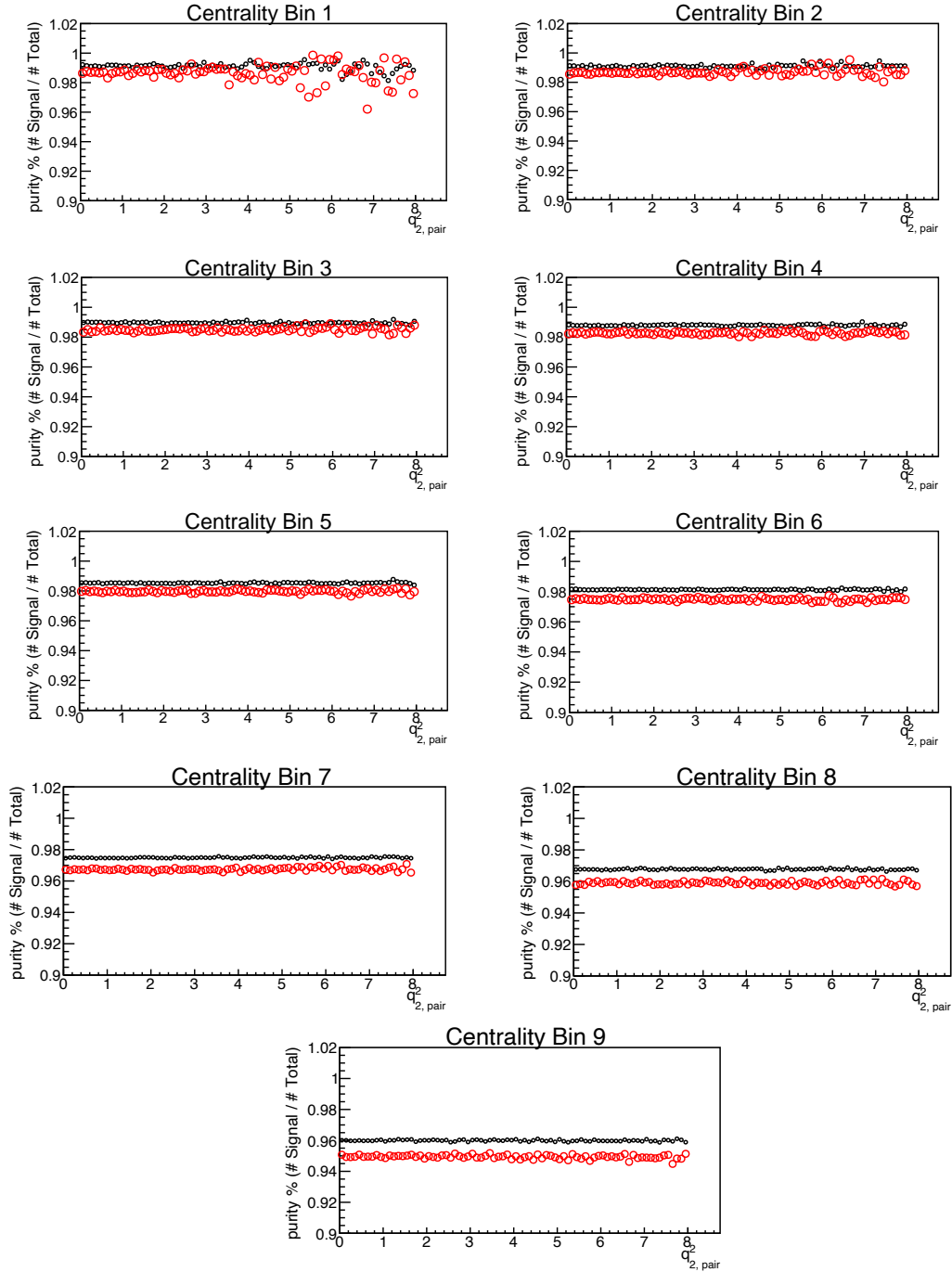


Figure 4.12: For 27 GeV Au+Au collisions, binned by pair-pion  $q_2^2$ . The black data points correspond to  $\Lambda$  purity statistics, whereas the red ones correspond to  $\bar{\Lambda}$  particles. As can be seen from the plots, there is not a strong dependence on the event handler, and the purity is very good - over 94% of reconstructed baryons are estimated to be true baryons for all centralities and all event handler bins.

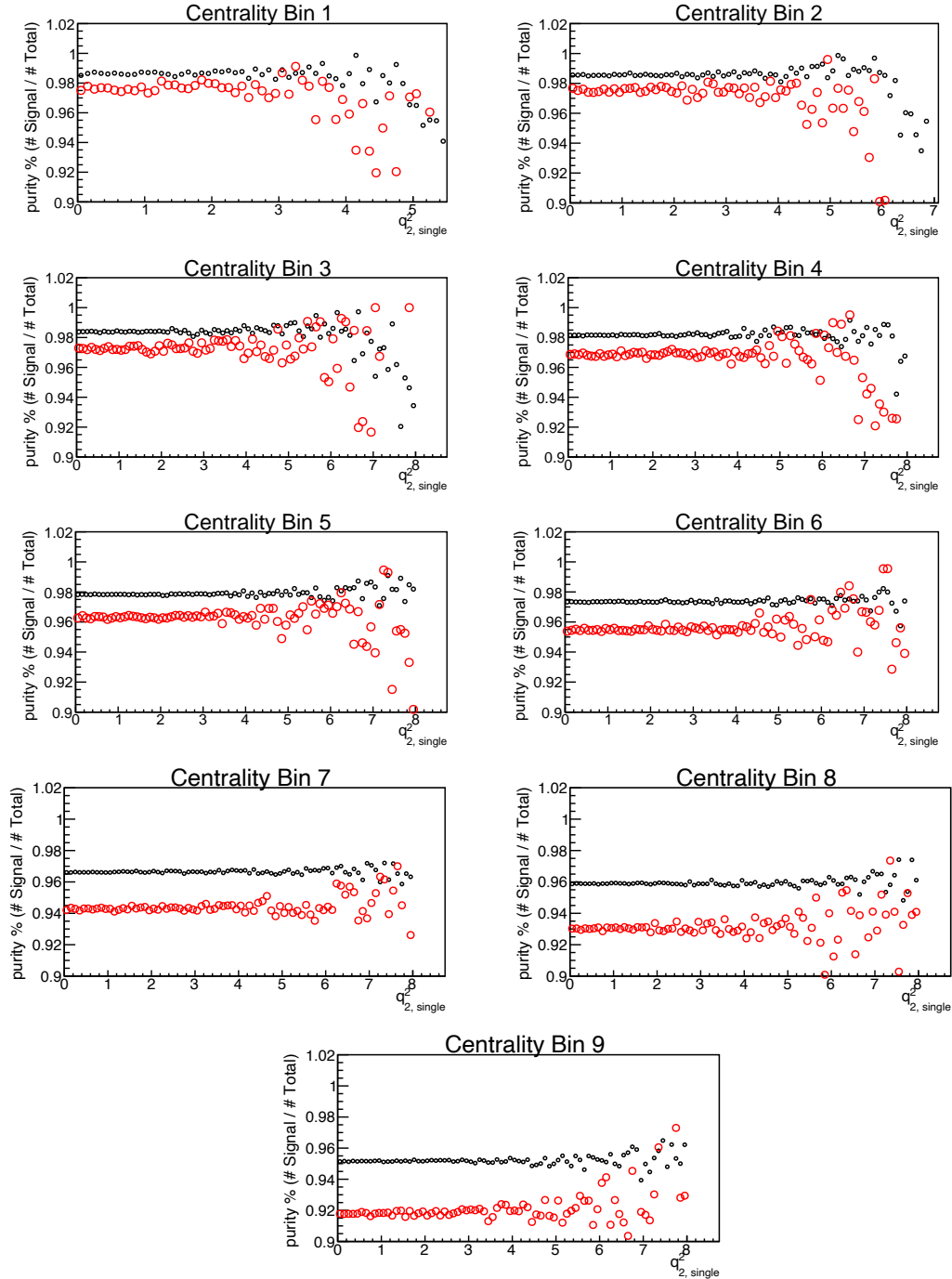


Figure 4.13: For 19.6 GeV Au+Au collisions, binned by single-pion  $q_2^2$ . The black data points correspond to  $\Lambda$  purity statistics, whereas the red ones correspond to  $\bar{\Lambda}$  particles. As can be seen from the plots, there is not a strong dependence on the event handler, and the purity is very good - over 90% of reconstructed baryons are estimated to be true baryons for all centralities and all event handler bins.

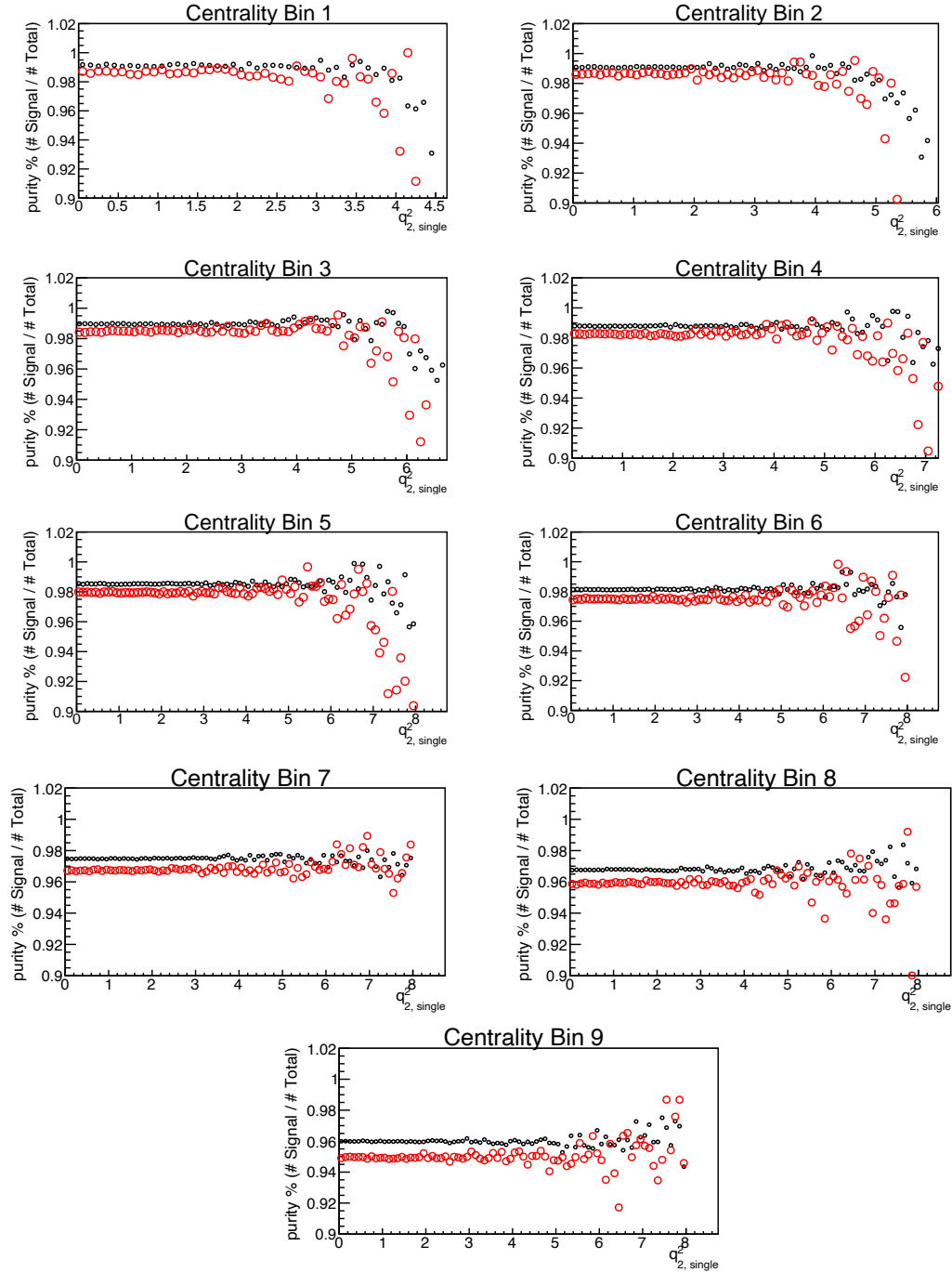


Figure 4.14: For 27 GeV Au+Au collisions, binned by single-pion  $q_2^2$ . The black data points correspond to  $\Lambda$  purity statistics, whereas the red ones correspond to  $\bar{\Lambda}$  particles. As can be seen from the plots, there is not a strong dependence on the event handler, and the purity is very good - over 94% of reconstructed baryons are estimated to be true baryons for all centralities and all event handler bins.

#### 4.4.4 Efficiency Correction

The previous section takes care of the false positives - cases in which the tracks passed through the reconstruction cuts to reconstruct a particle that is not a real  $\Lambda/\bar{\Lambda}$ . However, there are also cases in which a real  $\Lambda/\bar{\Lambda}$  does not get reconstructed because the cuts removed their daughter particles from consideration. This section will be interested in addressing this false negative case. The detectors that are employed in STAR have sensitivities that depend on the momentum of the particles that are being detected. Because of this, we are interested in understanding how the efficiency of reconstructing  $\Lambda/\bar{\Lambda}$  depends on its transverse momentum.

In order to do this, we need to rely on simulations. We use a data set with real data collected, and then embed randomly generated  $\Lambda/\bar{\Lambda}$  tracks into the data along with the decay products of these generated baryon particles, and then we feed this data through the reconstruction algorithm and see how many of these embedded tracks are actually reconstructed for each transverse momentum bin. The results are seen in Figure 4.15. These statistics will be included in the final analysis to correct the results of interest.

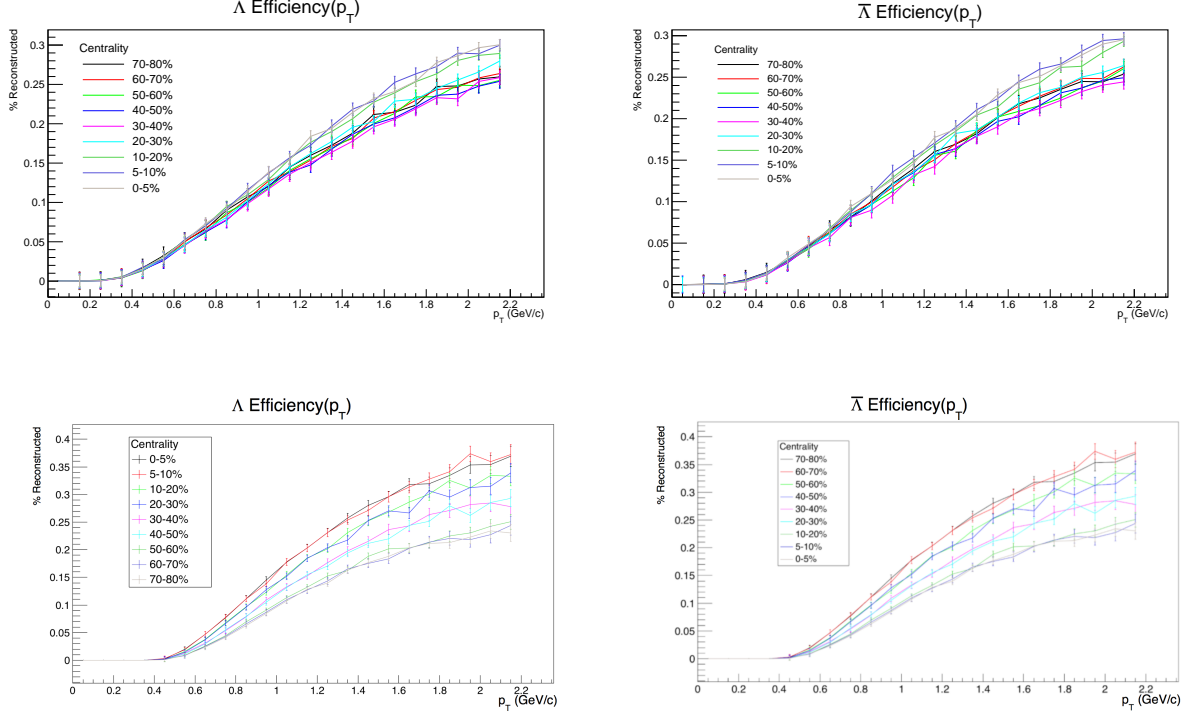


Figure 4.15: The left figures are the efficiency results for  $\Lambda$ , and the right ones are for  $\bar{\Lambda}$ . The first row corresponds to 19.6 GeV Au+Au collisions; the second row corresponds to 27 GeV Au+Au collisions. % Reconstructed refers to the reconstruction efficiency, which is calculated as  $(\# \text{ Reconstructed} / \# \text{ Total Embedded})$  for each  $p_T$  bin.

## 4.5 Primary Protons

In this section we will discuss the selection criteria used for identifying primary  $p/\bar{p}$  tracks, as well as the efficiency corrections for the cuts used in this analysis.

### 4.5.1 Selection Criteria

Table 4.6 lists the selection criteria used for identifying these tracks that will be used in the correlations with the  $\Lambda/\bar{\Lambda}$  particles to search for the CVE.

Table 4.6: Track Quality Cuts for Identifying Primary  $p/\bar{p}$  Tracks

Track Cuts	Values
TPC Hits Used in Fit/ Max. Possible TPC Hits	$\geq 0.52$
TPC Hits Used in Fit	$>15$
TPC Hits Used in $dE/dx$ Measurements	$>15$
$ N\sigma_{\text{proton}} $	$<2.0$
$p_T$	$>0.4 \text{ GeV}/c$
$ \vec{p} $	$<2.0 \text{ GeV}/c$
Mass <sup>2</sup>	$>0.8 (\text{GeV}/c^2)^2, <1.0 (\text{GeV}/c^2)^2$
Require TOF Hit	True
TOF y Local	$<1.8\text{cm}$
DCA from Primary Vertex	$<1\text{cm}$

#### 4.5.2 Efficiency Correction

For the primary  $p/\bar{p}$  particles, there are two efficiencies that are important: the efficiency of reconstruction from TPC, as well as that from TOF. The idea behind computing the estimate of the efficiency of reconstruction from TPC is similar to that of the computation of efficiency of reconstruction of  $\Lambda/\bar{\Lambda}$  particles that was described above: the STAR collaboration produces a data set that includes embedded Monte Carlo tracks of  $p/\bar{p}$  particles, so by using that data set, feeding through the algorithm that selects the primary protons that are used in this analysis, we can calculate the percentage of particles that are identified compared with the total number that was embedded. The efficiency determination for TOF is a little trickier as there is not direct way of estimating, as there is no particle identification built into TOF. Therefore, an estimate is used by comparing the number of particles that passed all the TPC cuts and enters the TOF cuts, with the number of particles that pass the TOF cuts, and that is used as an estimate for the efficiency of TOF identification of the  $p/\bar{p}$  particles. These two efficiencies are both computed as a function of the transverse

momentum of the  $p/\bar{p}$  particles, and their effects are combined as a product into one function that is depicted in Figure 4.16. As can be seen, there is not a very strong dependence on transverse momentum in the range that was selected for this analysis, but the statistics will still be used in correcting the final result for the observables.

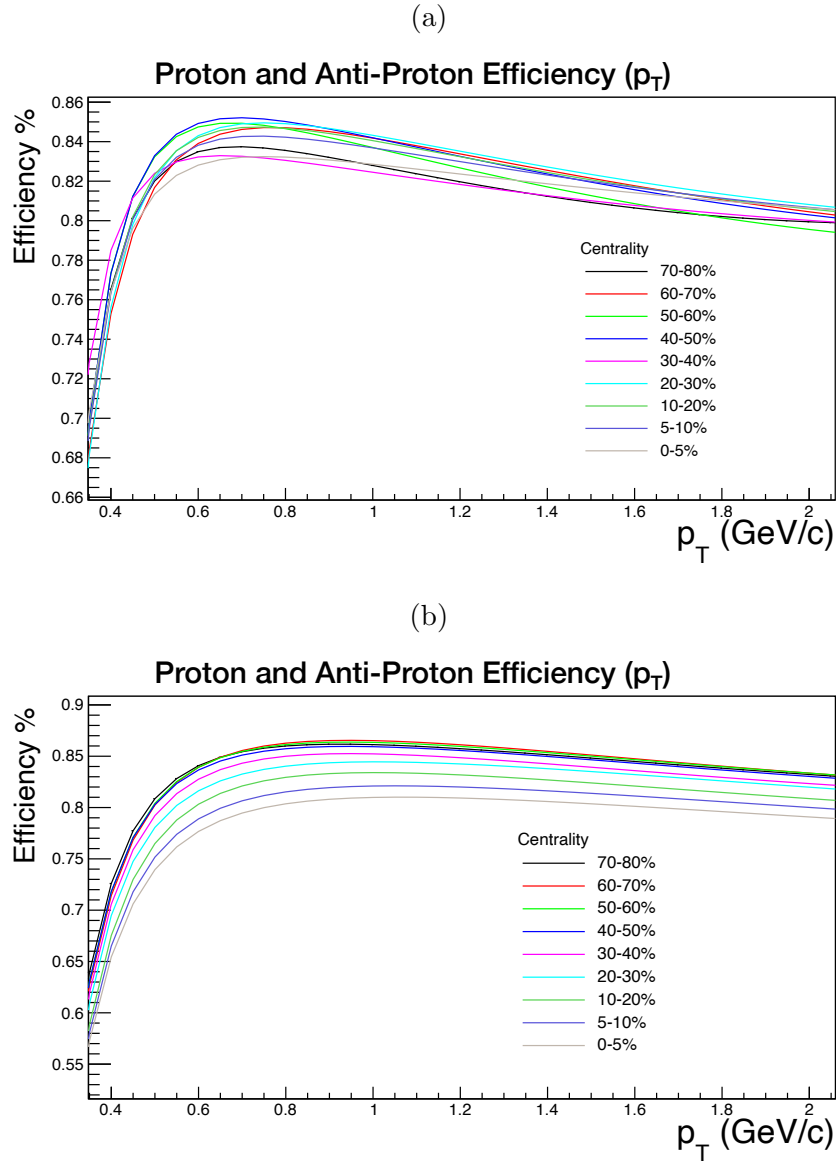
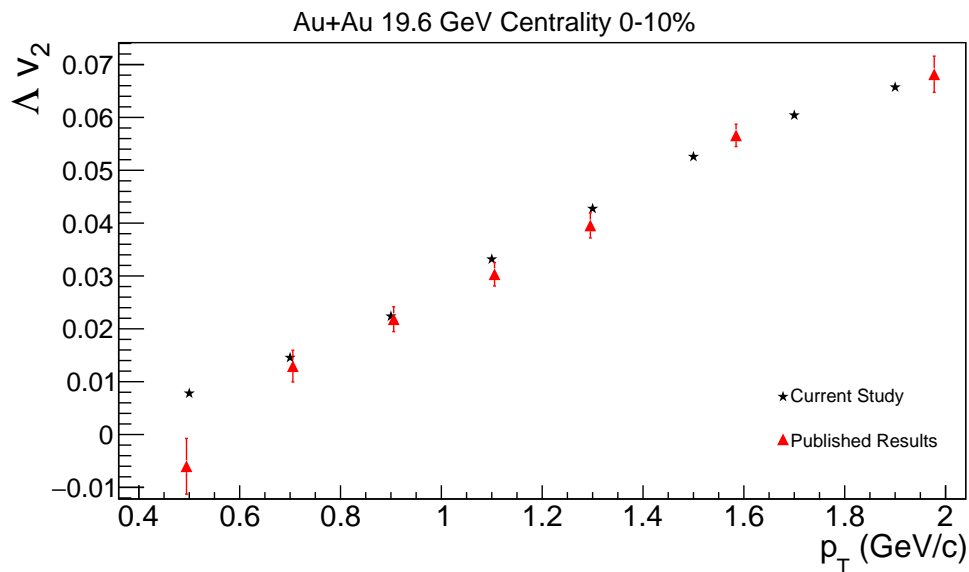


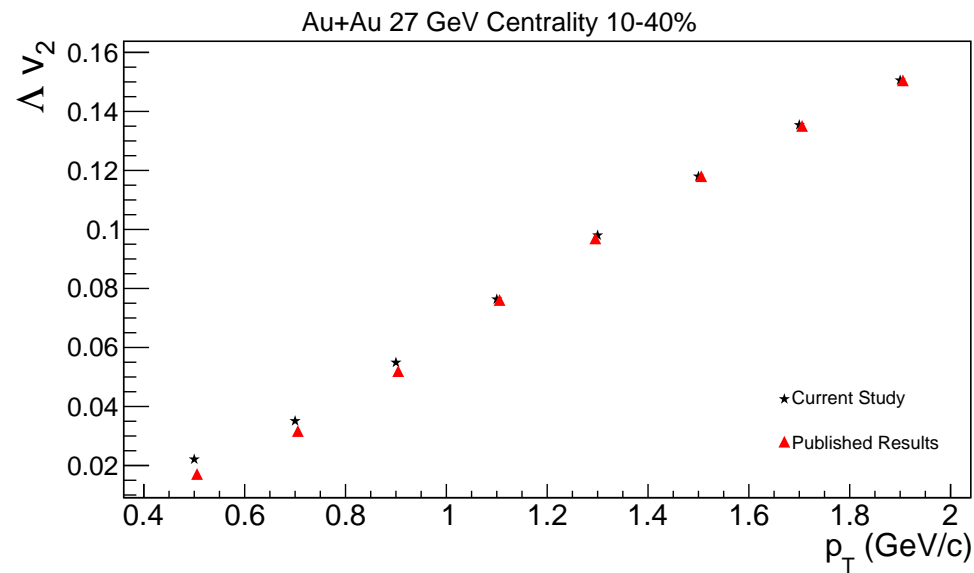
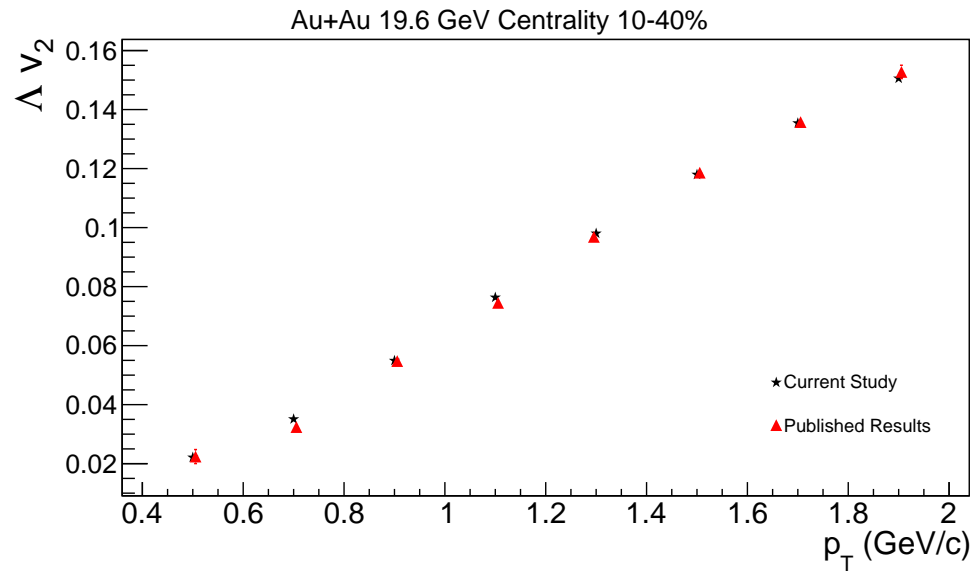
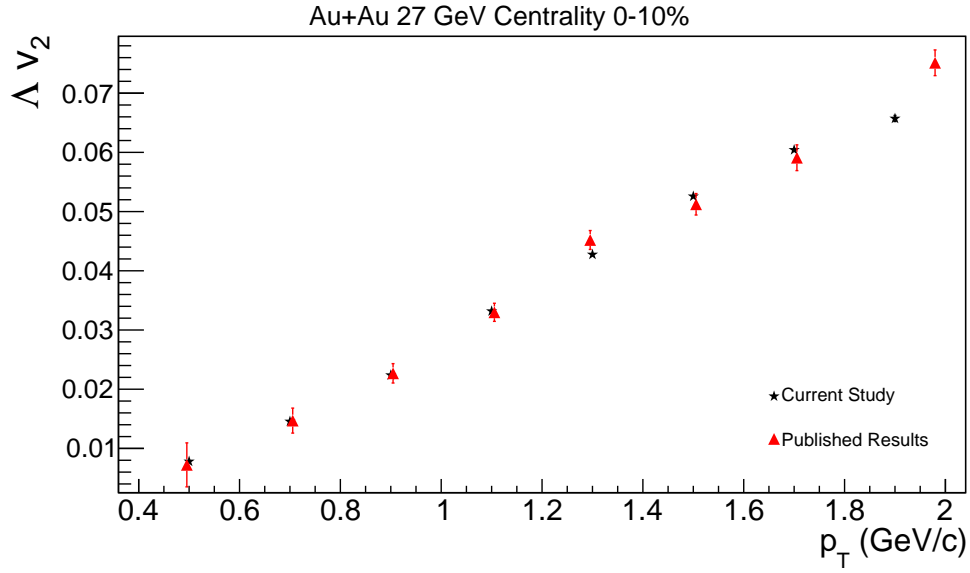
Figure 4.16: The product of the efficiency of identification from the TPC and the efficiency of identification from TOF of protons and antiprotons across the nine centralities, as a function of their transverse momentum. (a) 19.6 GeV Au+Au; (b) 27 GeV Au+Au.

## 4.6 Verification of Baryons with Elliptic Flow Comparisons

In order to have an understanding of the validity of the reconstructed  $\Lambda$ , we decided to compute the elliptic flow of these particles and compare that with the published results from STAR in 2016 [82]. There are definitely differences between the methods of reconstruction and criteria for selection, for example, the use of KFParticle to reconstruct the  $\Lambda$  baryons and the difference in the event plane reconstruction (different sizes of  $\eta$  gaps). However, despite the differences, we expect the elliptic flow of these particles to be roughly the same, and if that is what we see in our calculations, it gives us more confidence on the reconstruction and selection procedures.

And indeed that is what we see: we see that though there are some differences, the elliptic flow between the particles reconstructed in this set of data to be roughly the same as the beam energy scan I data that the analysis of [82] was performed on. The results can be seen in the following figures:





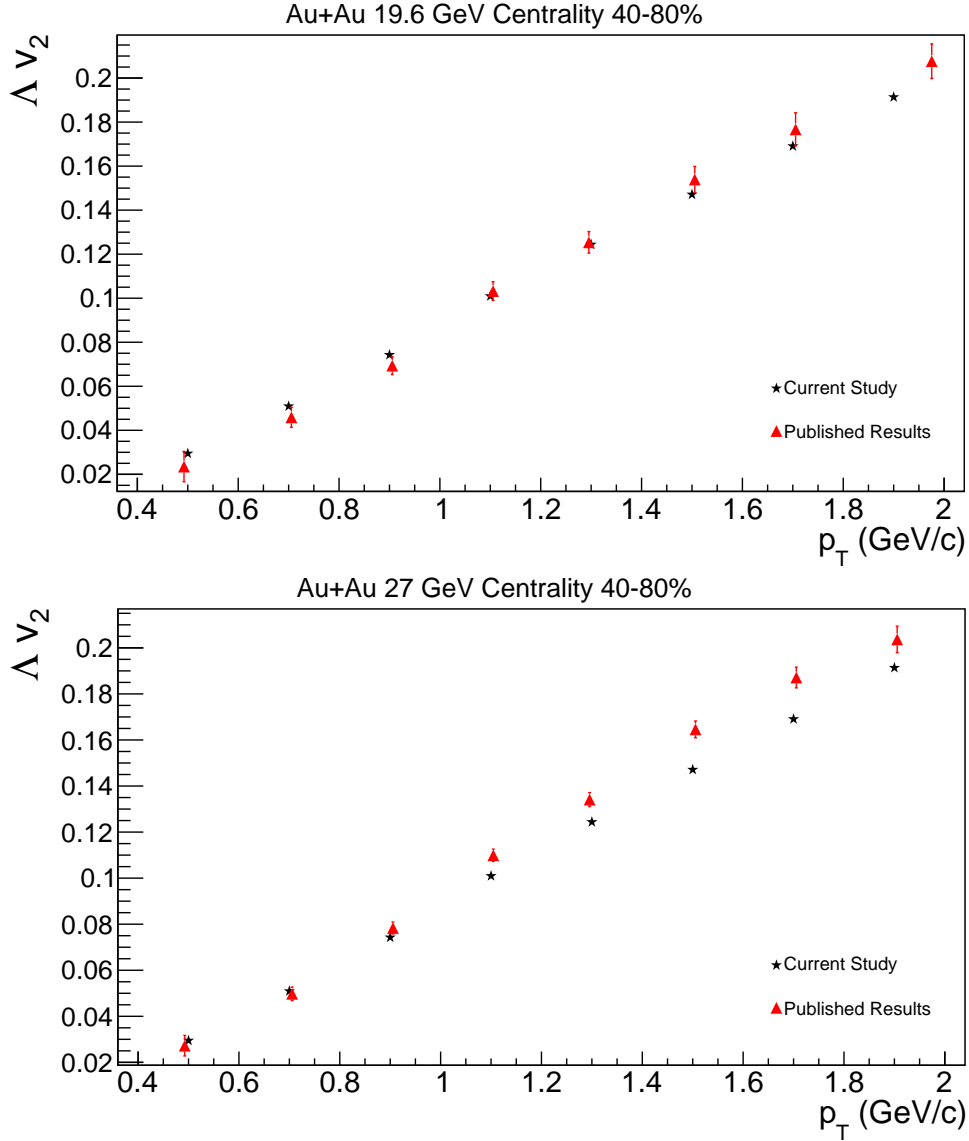


Figure 4.16: These figures compare the elliptic flow of  $\Lambda$  particles from the data sets of interest in this analysis, with that of the study done in 2016 [82]. We see that in general the results agree with each other, sufficient to claim validity for the reconstruction and selection of these particles.

## 4.7 A Multi-Phase Transport Model for Heavy Ion Collisions

Many models have been developed in order to understand the experimental results that we have been able to obtain from RHIC. A Multi-Phase Transport Model (AMPT) is a sophis-

ticated one that combines many previously developed ones to try to accurately describe the evolution of the heavy-ion collisions at RHIC, and is one of the models used in this analysis to compare results in order to better understand the potential Chiral Vortical Effects that may or may not be present in the collision.

There are thermal models that were developed in the past that are based on the assumption of global thermal and chemical equilibrium [83][84][85][86]. There are also hydrodynamic models that are based only on the assumption of local thermal equilibrium [87, 88, 89, 90, 24, 91, 92]; these models are useful for understanding the collective behavior of low transverse momentum particles, such as elliptic flow  $v_2$ . There are also transport models [93, 94, 95, 96, 97, 98, 99, 100, 101] that treat non-equilibrium dynamics explicitly, and they have been very successful in accounting for the yield of various particles and their ratios. Because these transport models treat chemical and thermal freeze-out dynamically, they are also useful for studying the Hanbury-Brown-Twiss interferometry of hadrons. Approaches based on the perturbative quantum chromodynamics (pQCD) using parton distribution functions in the colliding nuclei have been used to model hard processes that involve large momentum transfer [102][103]. The classical Yang-Mills theory has been developed in order to address the evolution of parton distribution functions in nuclei at ultra-relativistic energies [104][105][106] as well as to study the hadron rapidity distribution and its centrality dependence at RHIC [107][108][109]. These different scenarios and conditions have also been studied in the pQCD based final-state saturation model [110][111][112].

There have been studies that show that thermalization could be achieved if we have collisions of very large nuclei or if the collisions occur at extremely high energy, even though the initial distribution of these gluons is very far from thermal equilibrium, and that the strong coupling constant decreases at high energies and at the saturation scale is asymptotically small [113]. However, the Quark Gluon Plasma that is created in the heavy ion collisions at RHIC, because of finite volume and energy, may not achieve full thermal or chemical equilibrium. Therefore, in order to address this kind of non-equilibrium, many-body dynamics, the model, A Multi-Phase Transport (AMPT) model [114], was developed to include both initial partonic and hadronic interactions, as well as the transition between these two phases

of matter [115, 116, 117, 118, 119, 120, 121, 122, 123]. The AMPT model is constructed to describe nuclear collisions ranging from  $p + A$  to  $A + A$  systems at center-of-mass energies from about  $\sqrt{s_{NN}} = 5$  GeV up to 5500 GeV at LHC, where strings and minijets dominate the initial energy production and effects from final-state interactions are important.

The following figures (Fig. 4.17) show the two different modes of the AMPT model, as well as the key components that are necessary in order to model what was previously mentioned, and will be described in more details:

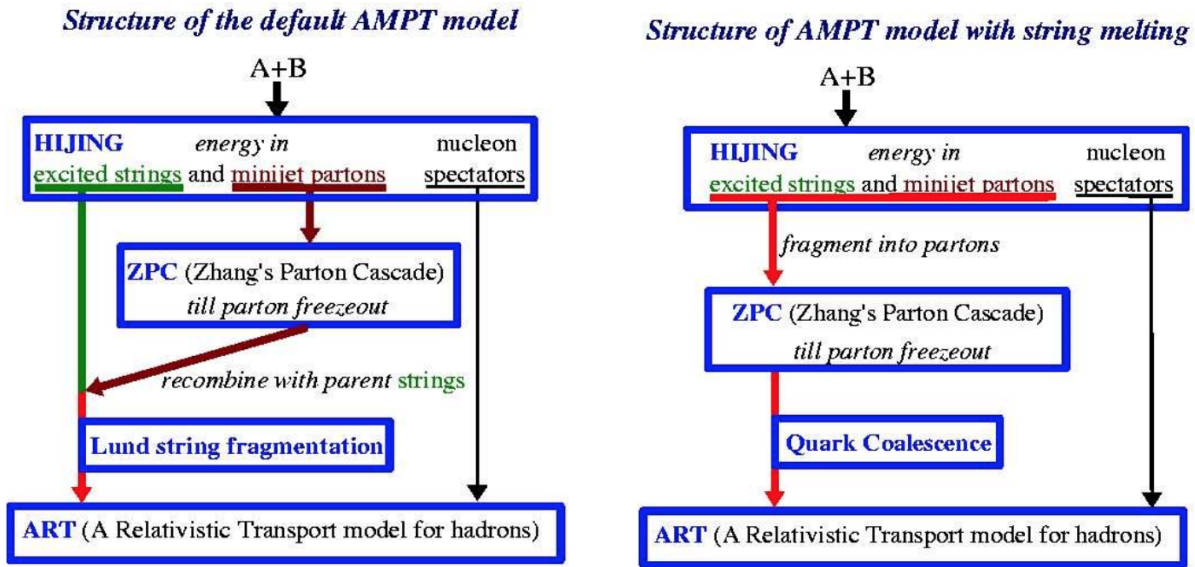


Figure 4.17: The left figure illustrates the scheme for the default AMPT model, and the right is that for the model with string melting. [114]

The AMPT model obtain information from the HIJING model for the determination of the initial conditions. These include the spatial and momentum distribution of minijet partons and soft string excitations [124, 125, 126, 127]. The HIJING model models the radial density profiles of the two colliding nuclei as having Woods-Saxon shapes, while the multiple scatterings among incoming nucleons are treated in the eikonal formalism. There are two components then that factor into particle production from the colliding nucleons, a hard and a soft one. The determination of this characterization is based on a momentum transfer threshold, above which is taken care of by the hard component, and below being taken care

of by the soft one. The hard component evaluates these processes with the pQCD using the parton distribution function in a nucleus, and these processes lead to the production of energetic minijet partons that are treated with the PYTHIA program. On the other hand, the processes that have a lower momentum transfer are treated by taking into account non-perturbative processes, and modeled by the formation of strings, which are then assumed to decay independently according to the Lund JETSET fragmentation model [114]. Now even though the partonic part in the default AMPT model only includes minijets from the HIJING model, its energy density can be very high in the heavy ion collisions at RHIC. So if the excited strings were just kept in the high energy density region [128], that would underestimate the partonic effect in these collisions. This is the reason for having the string melting mode of the AMPT model, as this extends the AMPT model to include the string melting mechanism and models this effect in the high energy density regions. This string melting mechanism [120][121][123] essentially has all the excited strings (but not projectile and target nucleons without any interactions) be converted into partons according to the flavor and spin structures of their valence quarks.

In the transport approach, interactions among partons are described by equations of motion for their Wigner distribution functions, which describe semi-classically their density distributions in phase space. These equations can be approximately written as Boltzmann equations. Zhang's parton cascade (ZPC) is then used to describe scatterings among partons to solve the Boltzmann equations [96]. This model includes only two-body scatterings with cross sections obtained from the pQCD with screening masses. There are then two modes of the AMPT model that combine partons into hadrons. With the default AMPT model [115, 116, 117, 118, 122], partons are recombined with their parent strings when they stop interacting because minijets are allowed to coexist with the remaining part of their parent nucleons, and then the resulting strings are converted to hadrons using the Lund string fragmentation model [129][130][131]. The second mode is the AMPT model with string melting [120][121][123]. This model uses a quark coalescence model (similar to the ALCOR model [132]) to combine partons into hadrons by converting the hadrons into their valence quarks and antiquarks. Then the hadronization is modelled by combining the two nearest partons

into a meson and three nearest quarks (antiquarks) into a baryon (antibaryon). However, because the invariant mass of combined partons forms a continuous spectrum instead of a discrete one, it is generally impossible to conserve 4-momentum when partons are coalesced into a hadron. Therefore, the current model chooses to conserve the three-momentum during coalescence and determine the hadron species according to the flavor and invariant mass of coalescing partons [114]. The resulting hadrons are given an additional formation time of  $0.7\text{fm}/c$  in their rest frame before they are allowed to scatter with other hadrons during the hadron cascade. Therefore, because partons freeze out dynamically at different times in the parton cascade, they coalesce and form hadrons at different times as well, which can lead to the appearance of a phase during hadronization where partons and hadrons coexist.

Scatterings among the resulting hadrons are described by the ART hadronic transport model [100][101], a hadronic cascade model. This relativistic transport model was originally developed for heavy ion collisions at Alternating Gradient Synchrotron (AGS) energies, and includes baryon-baryon, baryon-meson, and meson-meson elastic and inelastic scatterings. It treats the isospin degrees of freedom for most particle species and their interactions explicitly, so it is suitable for studying those effects in heavy ion collisions [133], and it also includes mean-field potentials for nucleons and kaons, and therefore used for studying the effect due to the hadronic equation of state. However, for high energy heavy ion collisions at RHIC, the potentials are turned off because their effects are much less important. The ART model was extended in AMPT to include additional reaction channels that are important at high energies, like the formation and decay of  $K^*$  resonance and antibaryon resonances, and baryon-antibaryon production from mesons and their inverse reactions of annihilation. With parameters, such as those in the string fragmentation, fixed by the experimental data from heavy ion collisions at the CERN Super Proton Synchrotron (SPS), the AMPT model has been able to describe reasonably many of the experimental observations at RHIC.

The final results from the AMPT model are obtained after the hadronic interactions are terminated at a cutoff time,  $t_{cut}$ . This cutoff time is determined to be the point at which the observables of interest are considered stable, in other words, that further hadronic interactions afterwards would not significantly affect them [114].

# CHAPTER 5

## Chiral Vortical Effect Analysis Results

### 5.1 $\gamma^{112}$ and $\gamma^{132}$ Correlators to search for the CVE

As mentioned in Section 4, we will be using the  $\gamma^{112}$  Correlator (Eq. 5.1) to extract the CVE signal from  $\Lambda/\bar{\Lambda} - p/\bar{p}$  Correlations. The following is the definition of the  $\gamma^{112}$  Correlator.

$$\begin{aligned}\gamma^{112} &\equiv \langle \cos(\phi_\alpha + \phi_\beta - 2\Psi_{RP}) \rangle \\ &= \langle \cos(\phi_\alpha - \Psi_{RP}) \cos(\phi_\beta - \Psi_{RP}) \rangle - \langle \sin(\phi_\alpha - \Psi_{RP}) \sin(\phi_\beta - \Psi_{RP}) \rangle \quad (5.1) \\ &= [\langle v_{1,\alpha} v_{1,\beta} \rangle + B_{IN}] - [\langle a_{1,\alpha} a_{1,\beta} \rangle + B_{OUT}]\end{aligned}$$

As seen in the definition, there are background effects,  $B_{IN}$  and  $B_{OUT}$ , that exist in this correlator, as we try to build an observable for CME/ CVE signals that do not simply vanish because of the isotropically distributed reaction plane. In order to attempt to remove these, we recognize that we can take the difference between  $\gamma_{112,OS}$  and  $\gamma_{112,SS}$ , which corresponds to the correlators calculated with opposite sign particles and with same sign particles, and here the sign could represent electric charge - for CME - or baryonic charge - for CVE, which is what is done in this analysis. This is because from our theoretical understanding, we would cancel out most of the background and simply be left with information about  $\langle a_{1,\alpha} a_{1,\beta} \rangle$  because this is the term whose sign is flipped when comparing opposite and same Baryonic-charge results. However, experimentally, it is not as simple due to more complicated background effects to this observable that are not strictly constant between the opposite sign

observable and same sign one. More realistically, what we get is the following:

$$\begin{aligned}
\Delta\gamma^{112} &\equiv \gamma_{112}^{OS} - \gamma_{112}^{SS} \\
&= (a_{1,+}^2 + a_{1,-}^2)/2 - a_{1,+}a_{1,-} + BG \\
&= 2a_1^2 + BG
\end{aligned} \tag{5.2}$$

where  $2a_1^2$  is the shorthand for the CME/CVE signal, and BG represents the background contributions that we still have to take care of. That will be a main challenge that we are trying to address both in the analysis of this thesis, but also looking towards the future of our search for CME and CVE signals in QGP.

One way that we have developed to have an estimate on the background effects is by using another correlator to do so, namely the  $\gamma^{132}$  Correlator. The definition of the correlator is as follows:

$$\gamma^{132} \equiv \langle \cos(\phi_\alpha - 3\phi_\beta + 2\Psi_{RP}) \rangle \tag{5.3}$$

In order to understand how this correlator can model the background for  $\gamma^{112}$ , we can expand them into their cumulants, which can demonstrate the true correlation between two quantities, as it removes the trivial mean quantities from the correlation [134]. The cumulant is defined as follows:

$$\langle\langle a \cdot b \rangle\rangle = \langle a \cdot b \rangle - \langle a \rangle \cdot \langle b \rangle \tag{5.4}$$

If we were to expand these two correlators into cumulants, what we get are:

$$\begin{aligned}
\gamma^{112} &\equiv \langle \cos(\phi_\alpha + \phi_\beta - 2\Psi_{RP}) \rangle = \langle \cos(\phi_\beta - \phi_\alpha - 2\phi_\beta + 2\Psi_{RP}) \rangle \\
&= \langle \cos(\phi_\beta - \phi_\alpha) \cos(2\phi_\beta - 2\Psi_{RP}) \rangle \\
&\quad + \langle \sin(\phi_\beta - \phi_\alpha) \sin(2\phi_\beta - 2\Psi_{RP}) \rangle \\
&= \langle\langle \cos(\phi_\beta - \phi_\alpha) \cos(2\phi_\beta - 2\Psi_{RP}) \rangle\rangle \\
&\quad + \langle \cos(\phi_\beta - \phi_\alpha) \rangle \langle \cos(2\phi_\beta - 2\Psi_{RP}) \rangle \\
&\quad + \langle\langle \sin(\phi_\beta - \phi_\alpha) \sin(2\phi_\beta - 2\Psi_{RP}) \rangle\rangle \\
&\quad + \langle \sin(\phi_\beta - \phi_\alpha) \rangle \langle \sin(2\phi_\beta - 2\Psi_{RP}) \rangle
\end{aligned} \tag{5.5}$$

$$\begin{aligned}
&= \delta \cdot v_2 \\
&\quad + \langle \langle \cos(\phi_\beta - \phi_\alpha) \cos(2\phi_\beta - 2\Psi_{RP}) \rangle \rangle \\
&\quad + \langle \langle \sin(\phi_\beta - \phi_\alpha) \sin(2\phi_\beta - 2\Psi_{RP}) \rangle \rangle
\end{aligned} \tag{5.6}$$

From Eq. 5.5 to Eq. 5.6, we used the cumulants Eq. 5.4, as well as the definitions for  $\delta = \langle \cos(\phi_\beta - \phi_\alpha) \rangle$  and  $v_2 = \langle \cos(2\phi_\beta - 2\Psi_{RP}) \rangle$ . It is then similar for  $\gamma^{132}$ :

$$\begin{aligned}
\gamma^{132} &\equiv \langle \cos(\phi_\alpha - 3\phi_\beta + 2\Psi_{RP}) \rangle = \langle \cos(\phi_\beta - \phi_\alpha + 2\phi_\beta - 2\Psi_{RP}) \rangle \\
&= \langle \cos(\phi_\beta - \phi_\alpha) \cos(2\phi_\beta - 2\Psi_{RP}) \rangle \\
&\quad - \langle \sin(\phi_\beta - \phi_\alpha) \sin(2\phi_\beta - 2\Psi_{RP}) \rangle \\
&= \langle \langle \cos(\phi_\beta - \phi_\alpha) \cos(2\phi_\beta - 2\Psi_{RP}) \rangle \rangle \\
&\quad + \langle \cos(\phi_\beta - \phi_\alpha) \rangle \langle \cos(2\phi_\beta - 2\Psi_{RP}) \rangle \\
&\quad - \langle \langle \sin(\phi_\beta - \phi_\alpha) \sin(2\phi_\beta - 2\Psi_{RP}) \rangle \rangle \\
&\quad - \langle \sin(\phi_\beta - \phi_\alpha) \rangle \langle \sin(2\phi_\beta - 2\Psi_{RP}) \rangle
\end{aligned} \tag{5.7}$$

$$\begin{aligned}
&= \delta \cdot v_2 \\
&\quad + \langle \langle \cos(\phi_\beta - \phi_\alpha) \cos(2\phi_\beta - 2\Psi_{RP}) \rangle \rangle \\
&\quad - \langle \langle \sin(\phi_\beta - \phi_\alpha) \sin(2\phi_\beta - 2\Psi_{RP}) \rangle \rangle
\end{aligned} \tag{5.8}$$

We see here that the only difference between the correlators when we expand them by their cumulants is that for  $\gamma^{112}$ , the two cumulants are added together whereas for  $\gamma^{132}$ , they are canceled out by one another. so if  $\kappa_{132} \equiv \Delta\gamma^{132}/(\Delta\delta \cdot v_2) \approx 1$ , then we see that those two terms essentially cancel each other out for  $\gamma^{132}$ , while it is not the case for  $\gamma^{112}$ . And since  $\delta \cdot v_2$  does not include CVE effects, we see that  $\gamma^{132}$  can serve as some kind of baseline model for the background of  $\gamma^{112}$  (though still it does not completely model it).

### 5.1.1 Flow Normalized Correlator $\kappa_{112}$ and $\kappa_{132}$

Since there is significant flow-related background that contributes to the  $\gamma^{112}$  correlator, and that is system dependent, in order to compare our observable between different systems, say data collected from RHIC by STAR and simulation data from the AMPT model, we need

to have a correlator that is normalized with respect to flow. That is what the  $\kappa$  correlators are.

One way to decompose the  $\gamma$  correlators into flow-related background and the rest of the signal has been to introduce a pure signal correlator  $H$  and using the two particle correlator  $\delta \equiv \langle \cos(\phi_a - \phi_b) \rangle$ , and we get the following, if we subtract the same-sign correlator from the opposite-sign one [135]:

$$\Delta\gamma^{112} \equiv \langle \cos(\phi_a + \phi_b - 2\Psi_2) \rangle_{OS-SS} = \kappa_{112}v_2\Delta F - \Delta H \quad (5.9)$$

$$\Delta\delta \equiv \langle \cos(\phi_a - \phi_b) \rangle_{OS-SS} = \Delta F + \Delta H \quad (5.10)$$

where  $F$  represents the strength of various flow-dependent effects, for example the transverse momentum conservation and the local charge conservation effects, which are flow-dependent;  $H$  represents the strength of flow-independent effects, most notably the CME/CVE effects that are of interest.  $\Delta F$  and  $\Delta H$  simply refer to the strengths of the same-charge pairs being subtracted from the opposite-charge pairs. Note that although Eq. 5.9 is specifically for  $\Delta\gamma^{112}$ , the same decomposition can be done for  $\Delta\gamma^{132}$  and we would get a relationship between  $\Delta\gamma^{132}$  and  $\kappa_{132}$ . The same holds true for the following as well.

So with Eq. 5.9 and 5.10, we can obtain the following:

$$\kappa_{112} = \frac{\Delta\gamma^{112} + \Delta H}{v_2(\Delta\delta - \Delta H)} \quad (5.11)$$

and if we take the pure background scenario, which means that  $\Delta H$  is 0, then we get our new observable:

$$\kappa_{112} = \frac{\Delta\gamma^{112}}{v_2\Delta\delta} \quad (5.12)$$

Since this correlator is normalized with respect to the flow-related effects in the system, we can compare this correlator across multiple systems to get a better understanding of the signal effects in our data from the Au+Au heavy-ion collisions system.

## 5.2 Data Analysis Details

### 5.2.1 Reaction Plane Reconstruction

As seen in the previous section, it is extremely important to have an understanding of the reaction plane of the heavy-ion collision event because the hypothesis is that there should be charge separation with respect to the reaction plane. However, as one could imagine, this is not something that we could detect with our detectors, but instead, we detect the final particles and use them to reconstruct the reaction plane, and measure, what we call, the event plane, which is a best-estimation for the actual reaction plane of the event.

The method that we have adopted for this analysis is from [13], where the main idea is to use the elliptic flow that is significantly present in Au+Au collisions to estimate the event plane. Here we have the event flow vector  $Q_n$  and the event plane angle  $\Psi_n$ , which correspond to the n-th harmonic of the distribution, defined as follows:

$$Q_n \cos(n\Psi_n) = X_n = \sum_i w_i \cos(n\phi_i) \quad (5.13)$$

$$Q_n \sin(n\Psi_n) = Y_n = \sum_i w_i \sin(n\phi_i) \quad (5.14)$$

$$\Psi_n = (\arctan \frac{\sum_i w_i \sin(n\phi_i)}{\sum_i w_i \cos(n\phi_i)})/n \quad (5.15)$$

where in these equations, the sums are over the  $i$  particles that are used in the event plane determination, and the  $w_i$  are weights, and in this particular analysis the weights are the transverse momentum of the particles that are used.

When choosing the particles to reconstruct the event plane, it is very important to choose particles that are not the ones that have been used for the analysis itself, if not it will lead to self-correlations that will lead to an exaggeration of the observable being measured. Therefore, if we use the particle tracks from the TPC, it is very important to exclude the particles that were used to reconstruct the  $\Lambda/\bar{\Lambda}$  particles, or the primary  $p/\bar{p}$  particles used for correlations. This effect is taken care of more easily with the change to using EPD for reconstruction of the event plane, because it records a different set of particles that are not used in the analysis. Therefore, for the final results of this analysis, we use both the first

order and second order event planes reconstructed from the EPD recorded tracks, which corresponds to  $n = 1$  and  $2$  in the above equations.

Now with this understanding, we need to modify our expression for  $\gamma^{112}$  (and by extension,  $\gamma^{132}$ ) because we do not know the actual reaction plane, and only have our first and second order event planes to best estimate the actual reaction plane. We will use the azimuthal angle correlation between two particles, a and b, since it uses the second order event plane, rather than the true reaction plane:

$$\begin{aligned}
\langle \cos(\phi_a + \phi_b - \Psi_2) \rangle &= \langle \cos(\phi_a + \phi_b - 2\Psi_{RP} + 2\Psi_{RP} - \Psi_2) \rangle \\
&= \langle \cos(\phi_a - \Psi_{RP}) \cos(\phi_b - \Psi_{RP}) - \sin(\phi_a - \Psi_{RP}) \sin(\phi_b - \Psi_{RP}) \rangle \\
&\quad (\langle \cos(2\Psi_{RP} - 2\Psi_2) \rangle - \langle \sin(2\Psi_{RP} - 2\Psi_2) \rangle) \\
&= (\langle \cos(\phi_a - \Psi_{RP}) \rangle \langle \cos(\phi_b - \Psi_{RP}) \rangle \\
&\quad - \langle \sin(\phi_a - \Psi_{RP}) \rangle \langle \sin(\phi_b - \Psi_{RP}) \rangle) \times \langle \cos(2\Psi_{RP} - 2\Psi_2) \rangle \\
&= (v_{1,a}v_{1,b} - a_{1,a}a_{1,b}) \langle \cos(2\Psi_{RP} - 2\Psi_2) \rangle
\end{aligned} \tag{5.16}$$

where in the first step we used a simple mathematical trick, the second step is based on trigonometric identities, the third step is the approximation with distributing the averages, as well as realizing that the  $\sin()$  term averages out to zero because it is an odd function averaged over isotropic angles, and finally we invoke the definitions of  $v_1$  and  $a_1$  in the last step. Given this, and given that we had already discussed previously that

$$\gamma^{112} \approx (v_{1,a}v_{1,b} - a_{1,a}a_{1,b}) \tag{5.17}$$

then now we have a new relationship, with

$$\gamma^{112} \approx \frac{\langle \cos(\phi_a + \phi_b - \Psi_2) \rangle}{\langle \cos(2\Psi_{RP} - 2\Psi_2) \rangle} \tag{5.18}$$

where  $\langle \cos(2\Psi_{RP} - 2\Psi_2) \rangle$  is essentially a representation of the resolution of the event plane that we have computed to estimate the reaction plane - this being that the closer the second order event plane is to the reaction plane, the closer this quantity would be to 1, acting as an estimation of the spread of the reconstructed event plane.

According to [13], it is possible to compute the event plane resolution, as we call it here, analytically. To begin, we start with the distribution of  $m(\Psi_m - \Psi_{RP})$ :

$$\frac{dP}{d(m(\Psi_m - \Psi_{RP}))} = \int \frac{v'_m dv'_m}{2\pi\sigma^2} \exp\left(-\frac{v_m^2 + v_m'^2 - 2v_m v'_m \cos(m(\Psi_m - \Psi_{RP}))}{2\sigma^2}\right) \quad (5.19)$$

where the parameter  $\sigma$  to second order in flow is common for all  $m$ , has the relationship of  $\sigma^2 = \frac{1}{2N} \frac{\langle w^2 \rangle}{\langle w \rangle^2}$ . Then, if we evaluate Eq. 5.19 analytically according to [136][137], and define  $\chi_m \equiv \frac{v_m}{\sigma} = v_m \sqrt{2N}$ , the event plane resolution can be expressed as

$$\langle \cos(km(\Psi_m - \Psi_r)) \rangle = \frac{\sqrt{\pi}}{2\sqrt{2}} \chi_m \exp\left(-\frac{\chi_m^2}{4}\right) [I_{\frac{k-1}{2}}\left(\frac{\chi_m^2}{4}\right) + I_{\frac{k+1}{2}}\left(\frac{\chi_m^2}{4}\right)] \quad (5.20)$$

with  $I_v$  being the modified Bessel function of order  $v$ .

To make use of this, there are two ways: one way is through numerical approximations that will allow us to compute the event plane resolution - which is what we call computing the full event plane resolution, or another way would be slightly simpler, using event planes of two different windows, or sub-events, which we call the sub event plane resolution.

For the numerical solution to the equation as an approximation, we are able to get the following for the most needed cases of  $k = 1, 2$ :

$$\langle \cos(m(\Psi_m - \Psi_{RP})) \rangle = 0.626657\chi_m - 0.09694\chi_m^3 + 0.02754\chi_m^4 - 0.002283\chi_m^5 \quad (5.21)$$

$$\langle \cos(2m(\Psi_m - \Psi_{RP})) \rangle = 0.25\chi_m - 0.011414\chi_m^3 - 0.034726\chi_m^4 + 0.006815\chi_m^5 \quad (5.22)$$

For the sub event plane resolution method, we first recognize that the correlation between flow angles of independent set of particles, say set (a) and set (b), has the following relation:

$$\langle \cos(n(\Psi_n^a - \Psi_n^b)) \rangle = \langle \cos(n(\Psi_n^a - \Psi_{RP})) \rangle \langle \cos(n(\Psi_n^b - \Psi_{RP})) \rangle \quad (5.23)$$

with the assumption that there are no other correlations other than the ones that are from flow (or that the other correlations can be neglected). Therefore, with this relation, we are able to conclude that if we know the correlation between two equal multiplicity sub-events, thus we can expect the resolution of each of the sub-events are roughly the same, then the resolution would be:

$$\langle \cos(n(\Psi_m^a - \Psi_{RP})) \rangle = \sqrt{\langle \cos(n(\Psi_m^a - \Psi_m^b)) \rangle} \quad (5.24)$$

Now if we would like to use all the particles to construct the event plane using this sub event plane method, then we can note that because  $\chi_m = \frac{v_m}{\sigma}$  being proportional to  $\sqrt{N}$ , we can reduce the relationship to:

$$\langle \cos(n(\Psi_m - \Psi_{RP})) \rangle = \sqrt{2} \langle \cos(n(\Psi_m^a - \Psi_{RP})) \rangle \quad (5.25)$$

We will be mainly using the sub event plane method for our event plane calculations, using the EPD recorded track information, however, there will also be full event plane resolution calculations used to verify results.

The following figures show the event plane resolution that was calculated according to the sub event plane method, for the TPC, 1st and 2nd order EPD event planes.

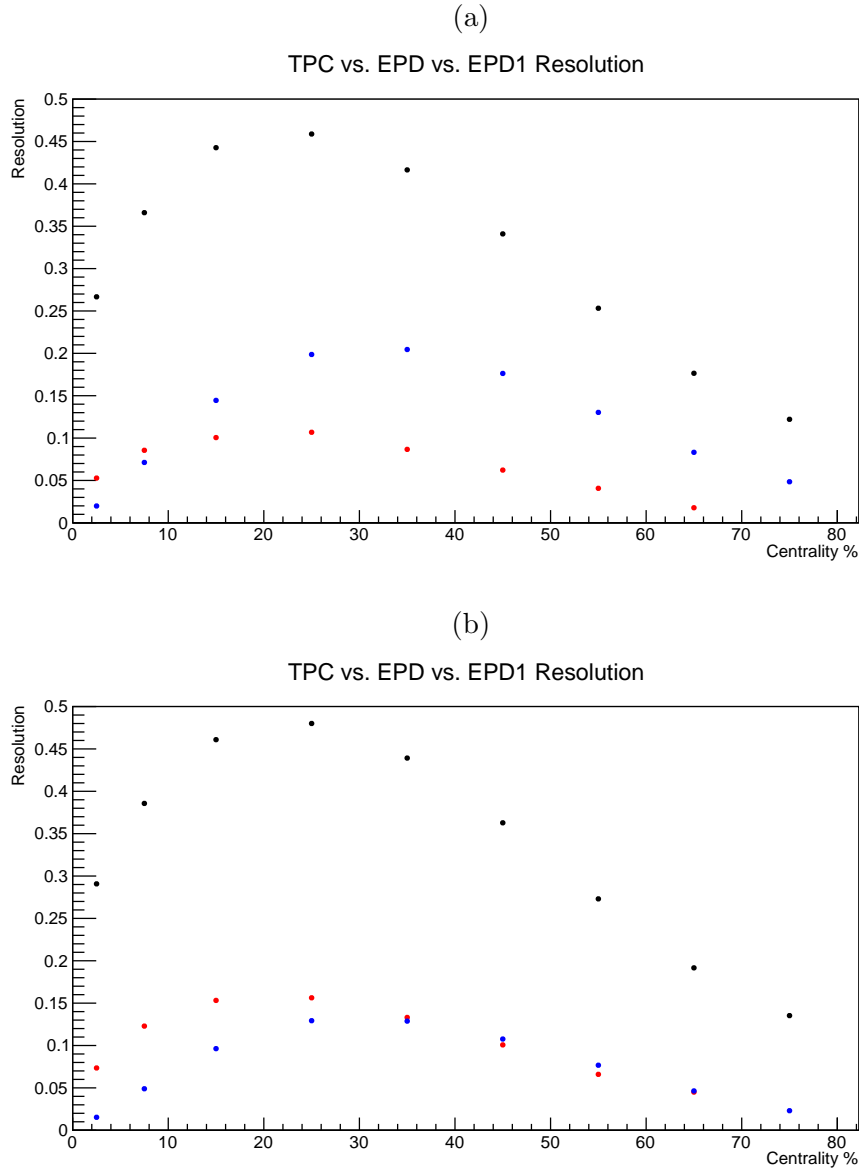


Figure 5.1: These figures show the event plane resolutions calculated according to the sub event plane methods for TPC, 1<sup>st</sup> and 2<sup>nd</sup> order EPD event planes. Black - TPC; Blue - 1<sup>st</sup> order EPD; Red - 2<sup>nd</sup> order EPD. Unfortunately, with selections of events that have to have at least one baryon reconstructed, the more peripheral centralities are biased so that the EPD EP resolution is too low, also they have very few statistics, therefore the most peripheral centrality will be removed from the final results of this analysis (which is also why the 75% red data point is missing). (a) is 19.6 GeV Au+Au collisions, while (b) is 27 GeV Au+Au collisions.

### 5.2.2 Detector Acceptance Correction

Another important factor to take into consideration is that there is a finite acceptance of the detector system due to various imperfections in the detectors. What this means is that while the reaction plane in heavy-ion collisions should be randomly distributed, that is not the case in terms of the recorded reaction plane - there will be differences of acceptance because of the detector imperfections, leading to non-uniform distributions across the event plane angles, as well as other azimuthal angles that we record for different particle tracks. Figure 5.2 shows some examples of this.

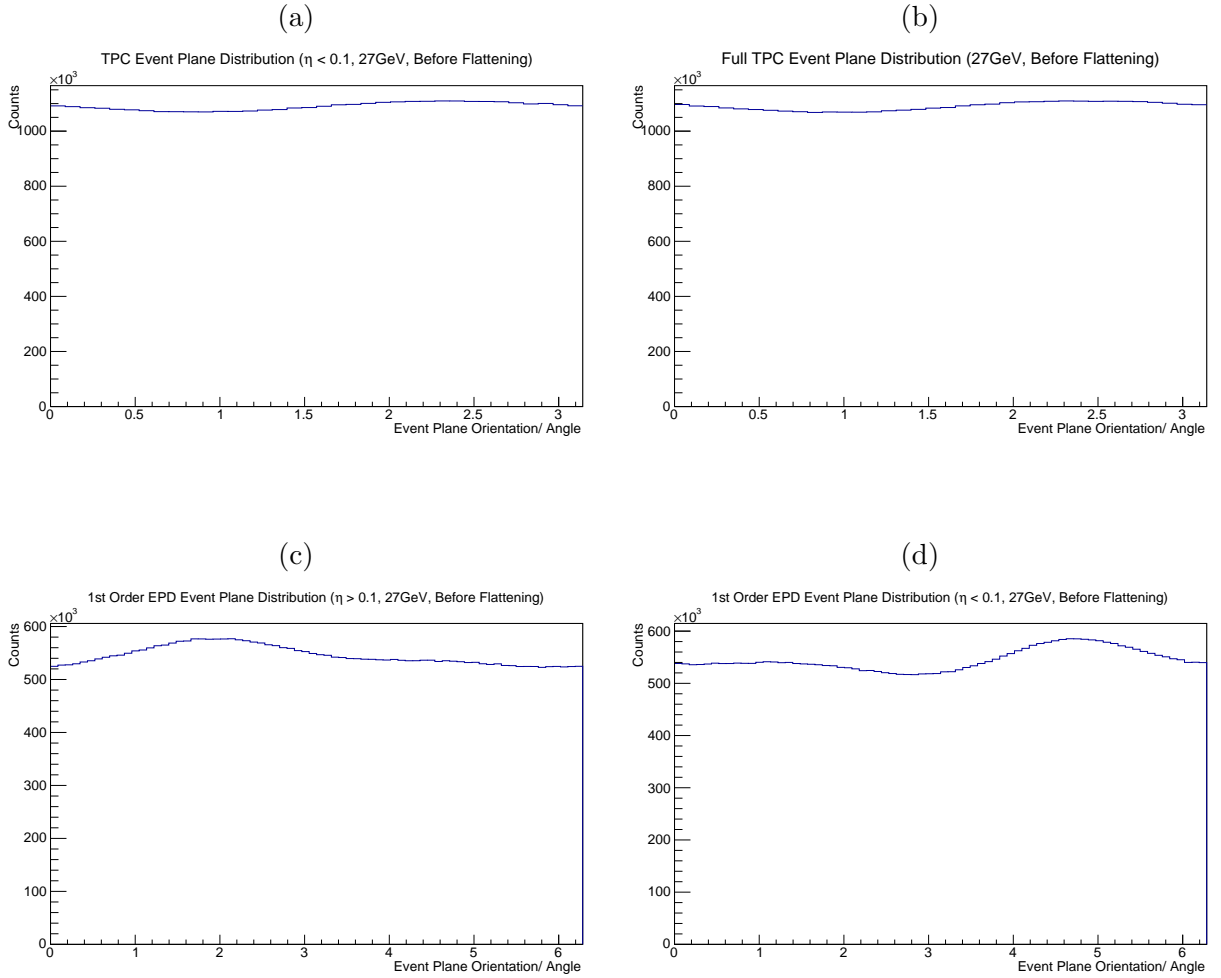


Figure 5.2: These plots are examples of Event Planes that exhibit detector acceptance differences, thus leading to a non-uniform distribution. They are taken from Centrality 30-40%, with the top two being TPC event planes and bottom two are first order EPD event planes.

One way to deal with this is by making corrections to the event plane angle itself, and flattening the event plane distribution [138]. Starting with the raw event plane distribution,  $\frac{dN}{d\psi}$ , we can expand it in a Fourier series:

$$\frac{dN}{d\psi} = \frac{a_0}{2} + \sum_n (a_n \cos n\psi + b_n \sin n\psi) \quad (5.26)$$

where the coefficients are defined as:

$$\begin{aligned} a_n &= \frac{1}{\pi} \int_{-\pi}^{\pi} \frac{dN}{d\psi} \cos(n\psi) d\psi, \quad n = 0, 1, 2, \dots \\ b_n &= \frac{1}{\pi} \int_{-\pi}^{\pi} \frac{dN}{d\psi} \sin(n\psi) d\psi, \quad n = 1, 2, 3, \dots \end{aligned} \quad (5.27)$$

Now in order to flatten the event plane distribution, what we want is to shift the raw event plane angles  $\psi$  to flattened event plane angles  $\psi'$ , that will lead to a uniform distribution of event plane angles:

$$\frac{dN}{d\psi'} = \frac{dN}{d\psi} \frac{d\psi}{d\psi'} = \frac{N}{2\pi} = \frac{a_0}{2} \quad (5.28)$$

We can achieve this by generating the flattened event plane angles by adding a correction term  $\Delta\psi$  to it, and thus we get:

$$\psi' = \psi + \Delta\psi = \psi + \sum_n (A_n \cos n\psi + B_n \sin n\psi) \quad (5.29)$$

$$\frac{d\psi'}{d\psi} = 1 + \sum_n (-nA_n \cos n\psi + nB_n \sin n\psi) \quad (5.30)$$

Then from Eq. 5.28 and 5.30, we get

$$\frac{dN}{d\psi} = \frac{dN}{d\psi'} \frac{d\psi'}{d\psi} = \frac{a_0}{2} \left( 1 + \sum_n (-nA_n \cos n\psi + nB_n \sin n\psi) \right) \quad (5.31)$$

Comparing Eq. 5.26 and Eq. 5.31, we see that the coefficients are

$$\begin{aligned} A_n &= -\frac{2 b_n}{n a_0} = -\frac{2}{n} \langle \sin n\psi \rangle \\ B_n &= -\frac{2 a_n}{n a_0} = -\frac{2}{n} \langle \cos n\psi \rangle \end{aligned} \quad (5.32)$$

which means that our final flattened event plane angles are

$$\psi' = \psi + \sum_n \frac{2}{n} (-\langle \sin n\psi \rangle \cos n\psi + \langle \cos n\psi \rangle \sin n\psi) \quad (5.33)$$

n here would be what we refer to the order to which we correct the event plane to. For this specific analysis, we correct the event plane, as well as the azimuthal angles of the particles of interest,  $\Lambda/\bar{\Lambda}$  and  $p/\bar{p}$ , up to the 10th order, and we see that the angles are flattened after this correction.

The following figure demonstrates the results of this flattening on the event planes of interest in this analysis. We see that each of them are flattened to very close to being uniform distributions, and the detector effects are sufficiently wiped out.

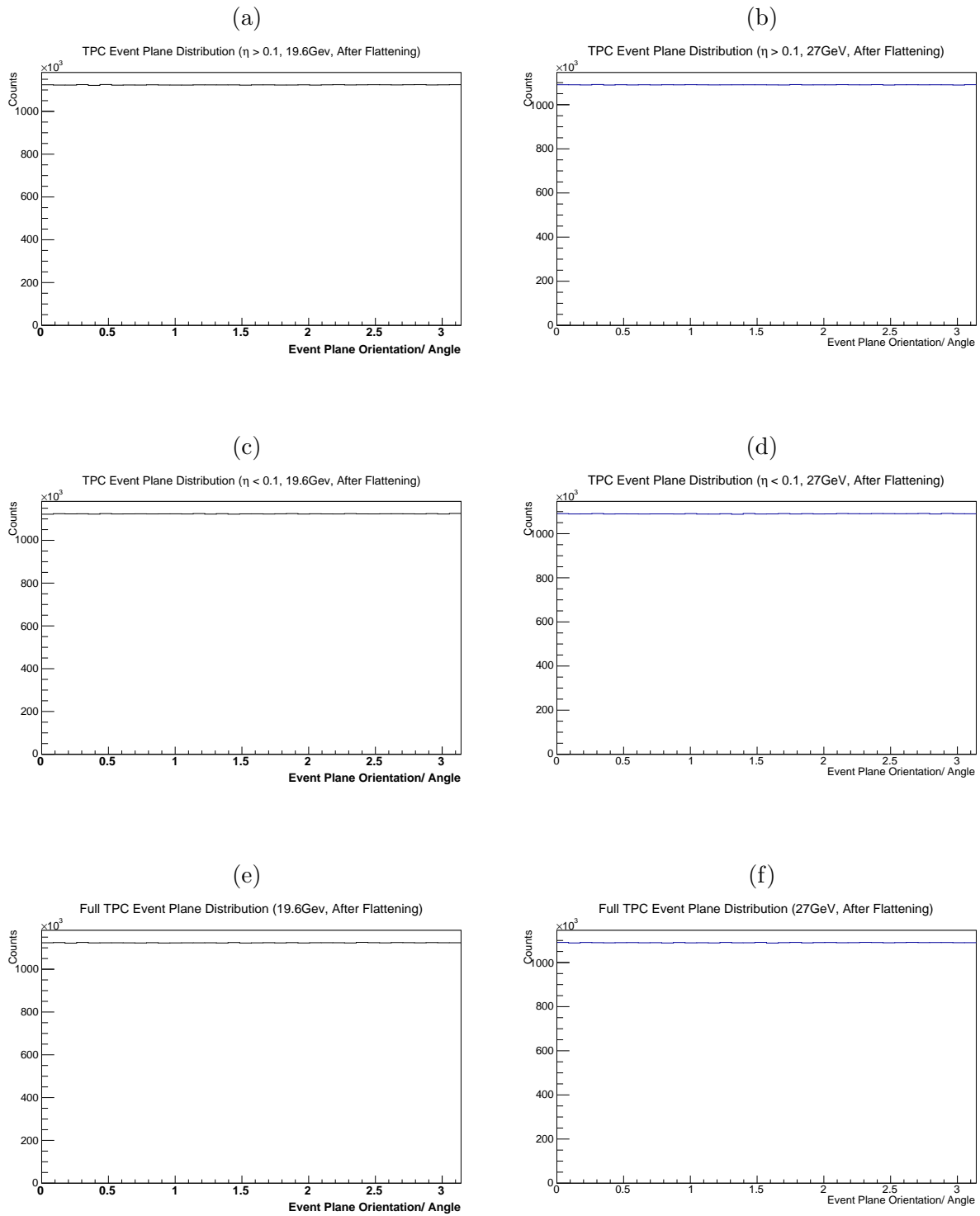


Figure 5.3: These six plots are examples of Event Planes based on TPC tracks. The first two rows correspond to the sub event plane method, and the last row corresponds to the full event plane method.

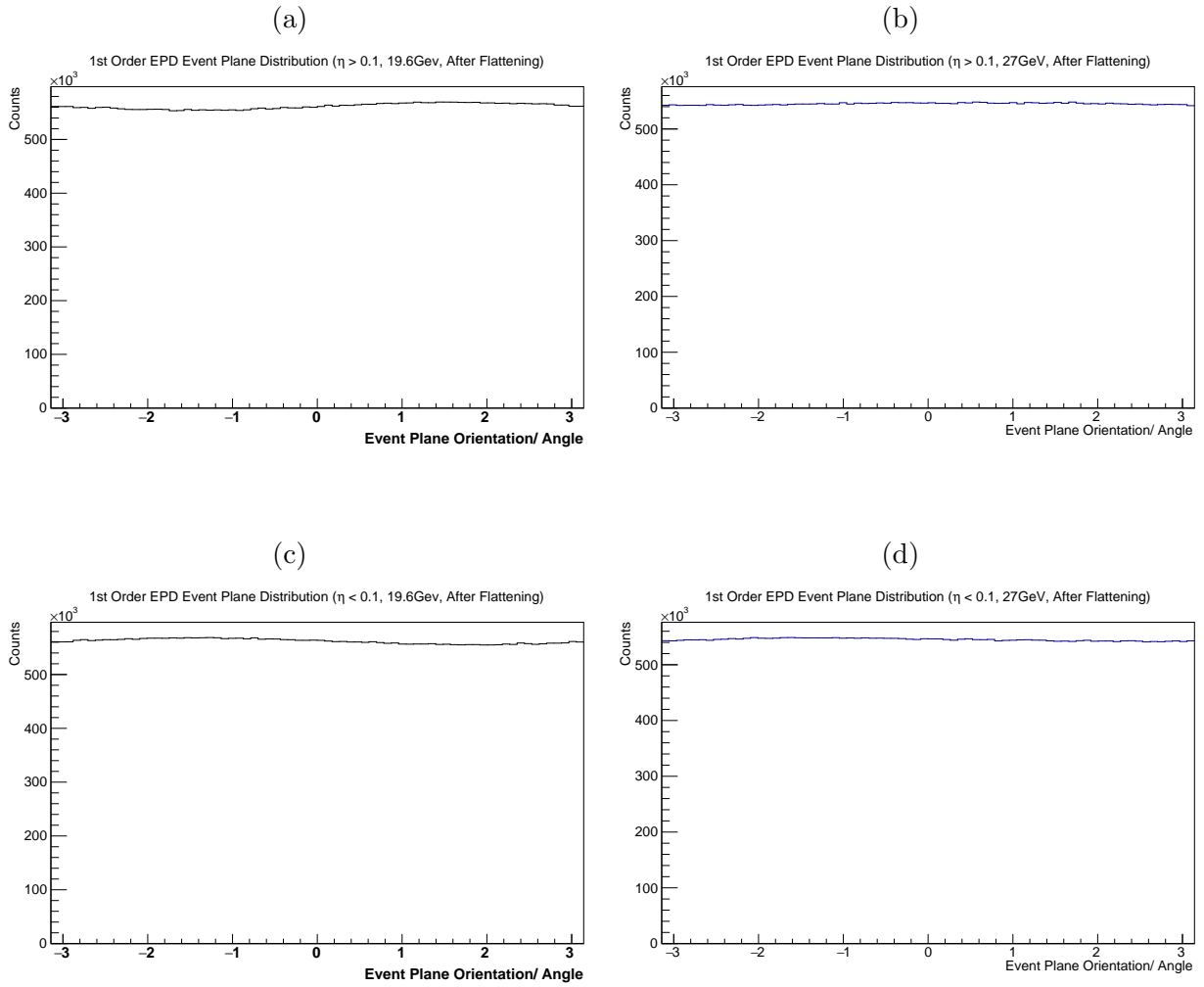


Figure 5.4: These plots are examples of Event Planes based on EPD tracks. They correspond to the 1<sup>st</sup> order EPD event planes, and all of these are according to the sub event plane method.

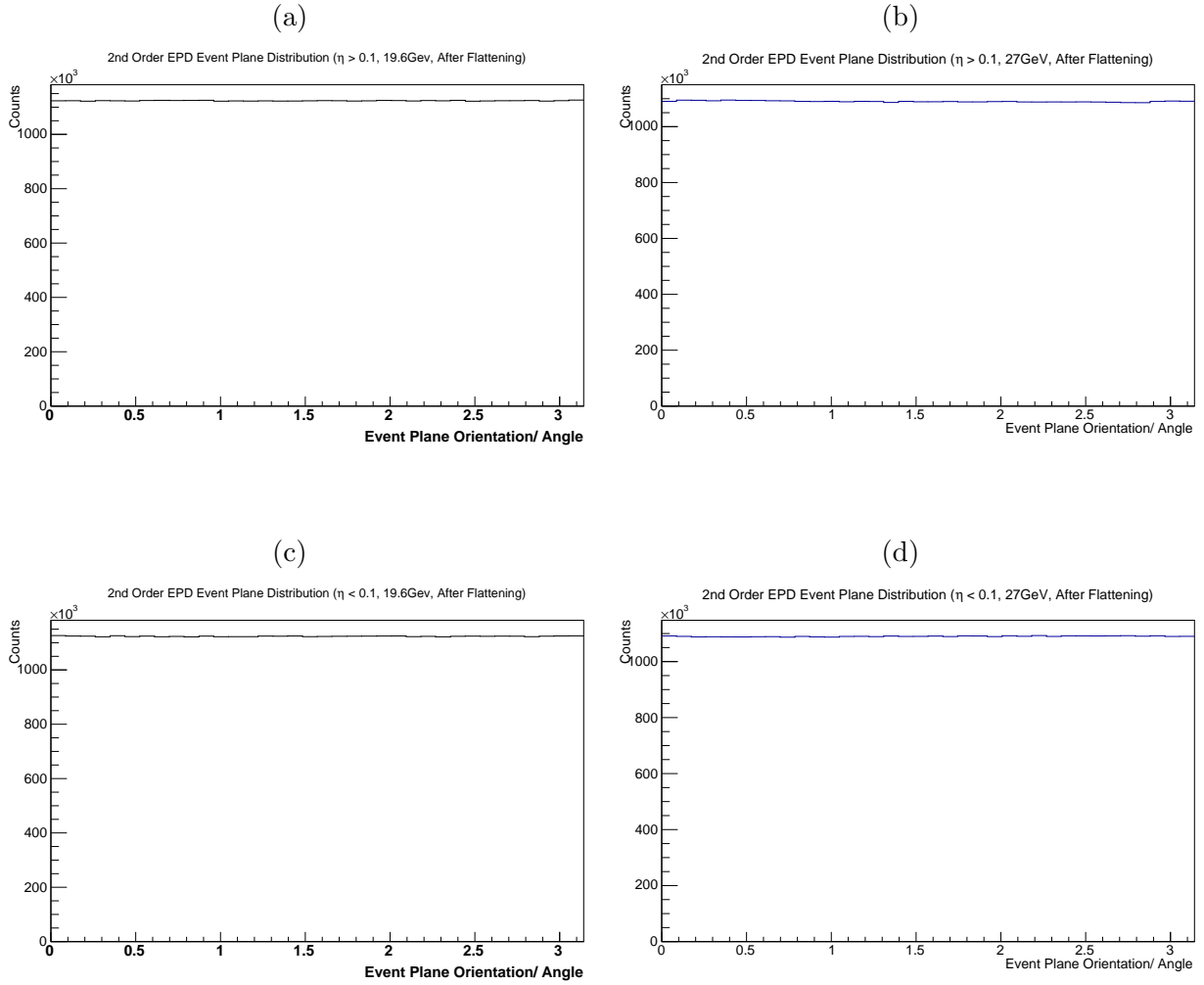


Figure 5.5: These plots are examples of Event Planes based on EPD tracks. They correspond to the  $2^{nd}$  order EPD event planes, and all of these are according to the sub event plane method.

### 5.2.3 Systematic Uncertainty Estimation

There are different sources that can contribute to systematic uncertainties in the determination of the final results of this analysis, and this section will demonstrate how we attempted to address and estimate those uncertainties. These effects range from event level cuts to reconstruction variations to particle identification.

Because of the obvious limitation to the detector having finite length in the  $z$ -direction, for events with primary vertices that happen too far from the center of the detector, it is difficult to have a high level of confidence of the resulting tracks being properly recorded. Therefore, there is a cut on the  $z$  distance from the center of the STAR detector in place, however, that could potentially introduce arbitrary effects for our final measurements. Therefore, the first systematic cut would be to vary the original  $z$ -component of the primary vertex cut, changing it from  $-70\text{cm} \leq V_z \leq 70\text{cm}$  to  $-70\text{cm} \leq V_z \leq 0\text{cm}$ . Another effect related to limitations of detection of particles has to do with the fact that the more hits that a particles has on the TPC affects the confidence of the determination of the particle information, for example, the momentum and the particle identification. Therefore we have a cut on the quantity nHitsFit that represents our confidence on the identification of the particle, however, such a cut is also subjective and based on wisdom passed down, and could potentially lead to biases as well. Therefore another systematic cut would be to tighten such a cut for the daughter particles identified to reconstruct the  $\Lambda/\bar{\Lambda}$  particles to see the effect on the final observable.

The other set of systematic cuts have mostly to do with how pure we want to be able to reconstruct the  $\Lambda/\bar{\Lambda}$  particles as well as identifying the primary protons for the correlations to obtain the  $\gamma^{112}$  and  $\gamma^{132}$  observables. For this set of cuts, we restrict the confidence of the particle identification to a higher level: for the daughters, we now reject everything that is less than  $3\sigma$  confidence, while for the primary proton we reject everything that is less than  $1.5\sigma$  confidence. Another set of cuts have to do with the distance of closest approach (DCA) of these particles from the primary vertex. We increase the strictness of the daughters of the baryons, for the proton to reject all protons within 1.0cm, and for all pions within 2.0cm, and for the reconstructed baryons we reject all that are 2.0cm away from the primary vertex. Last but not least, we increase the cut on the lower bound on the transverse momentum of the primary proton used for the correlations to 0.5 GeV/c.

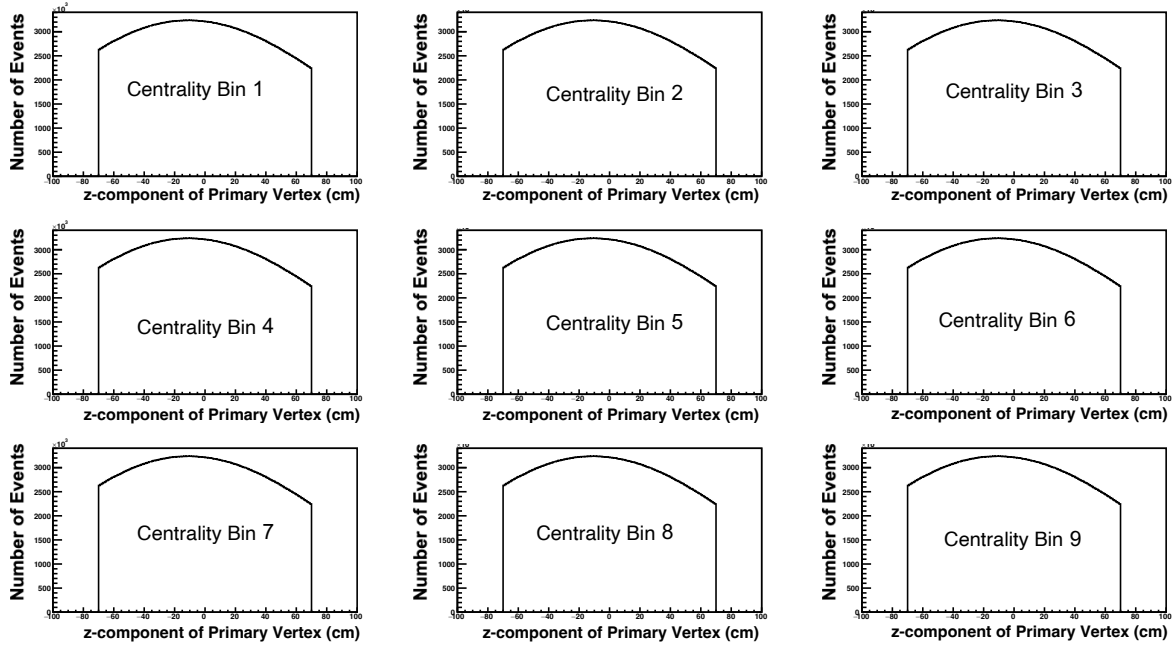
The following table summarizes these cuts, as well as the label of the systematic uncertainty estimator that will be used to reference these cuts later.

Table 5.1: Systematic Uncertainty Estimation

Label	Systematic Cut
sys_1	$-70 \leq z\text{-component of Primary Vertex} \leq 0$
sys_2	nHitsFit of Daughters $> 20$
sys_3	nSigma of Daughters $\leq 2$
sys_4	DCA of Daughters - protons $> 1.0\text{cm}$ ; pions $> 2.0\text{cm}$
sys_5	$0 \leq z\text{-component of Primary Vertex} \leq 70$
sys_6	$p_T$ of primary proton $> 0.5\text{GeV}/c$
sys_7	nSigma of primary proton $< 1.0$

The following plots demonstrate the distribution of the baseline cuts for these different quantities, as well as red lines to demonstrate the systematic cut.

(a) 19.6 GeV



(b) 27 GeV

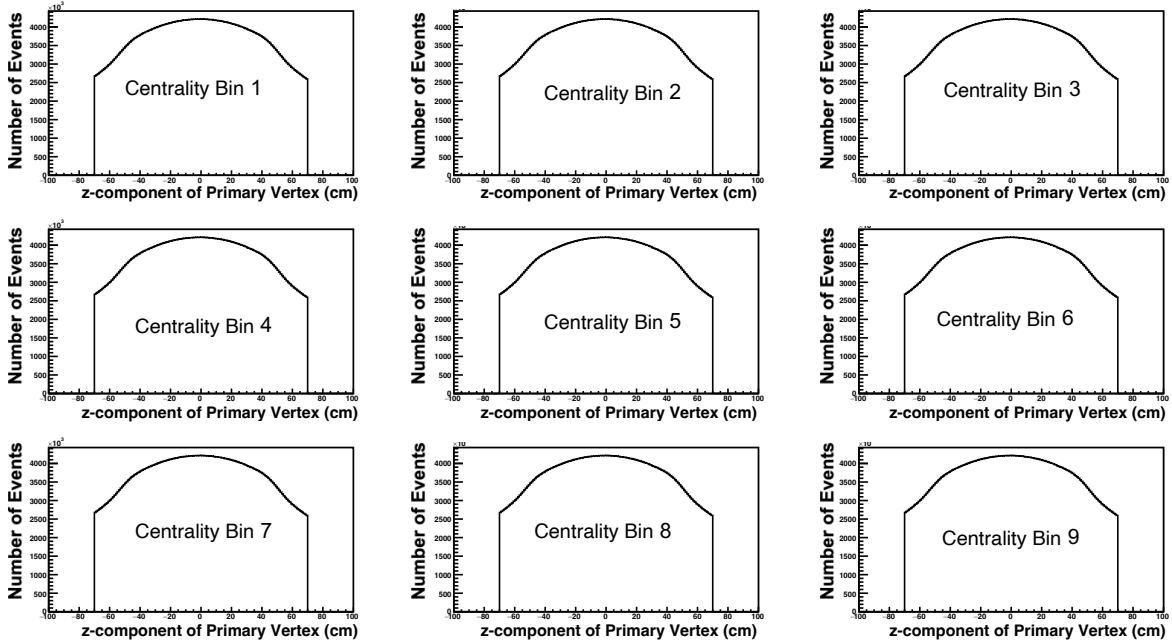
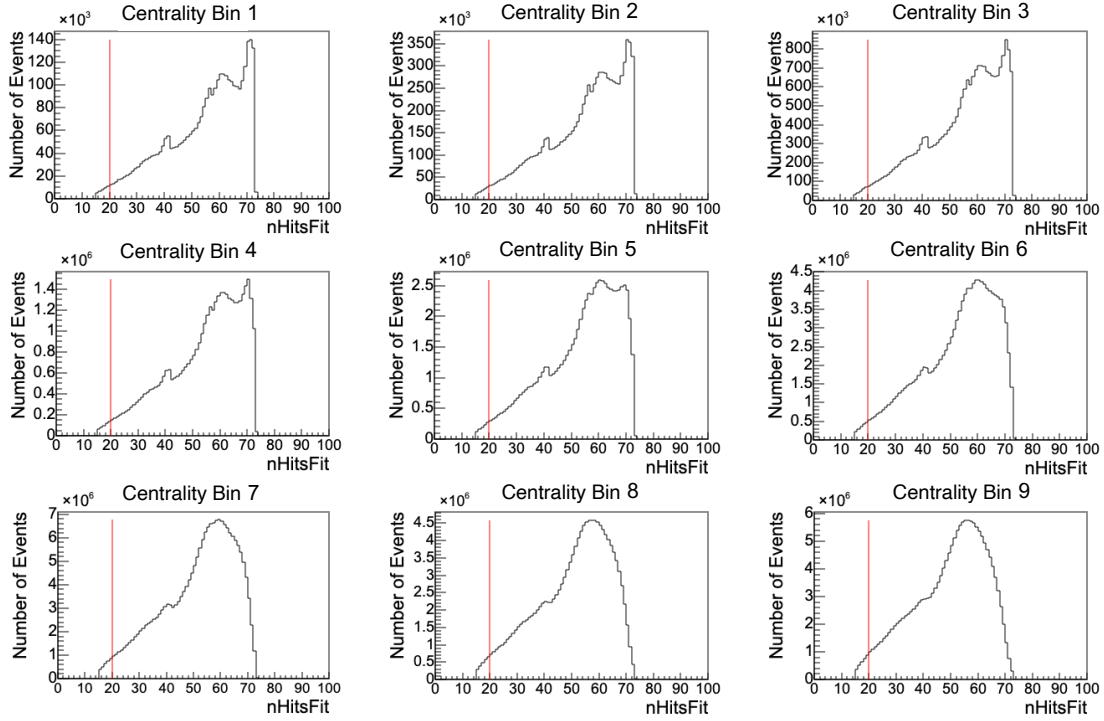


Figure 5.6: Systematic Cut on the  $z$ -component of the primary vertex of events. `sys.1` - the events that fall on the left of 0; `sys.5` - the events that fall on the right of 0.

(a) 19.6 GeV



(b) 27 GeV

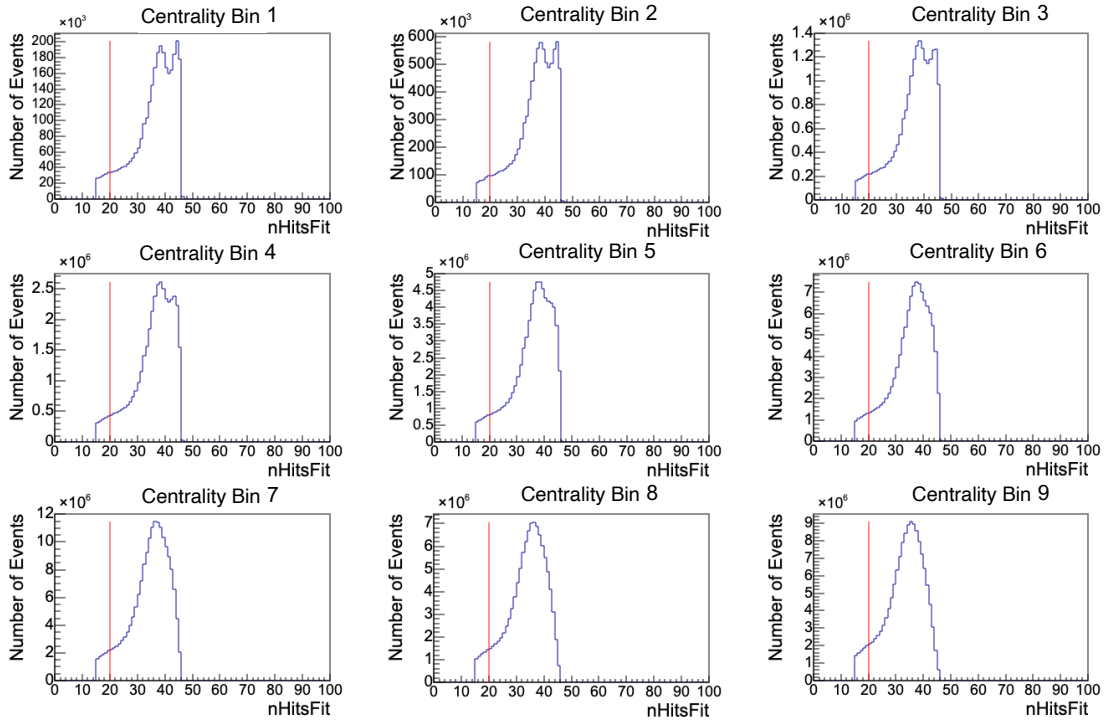
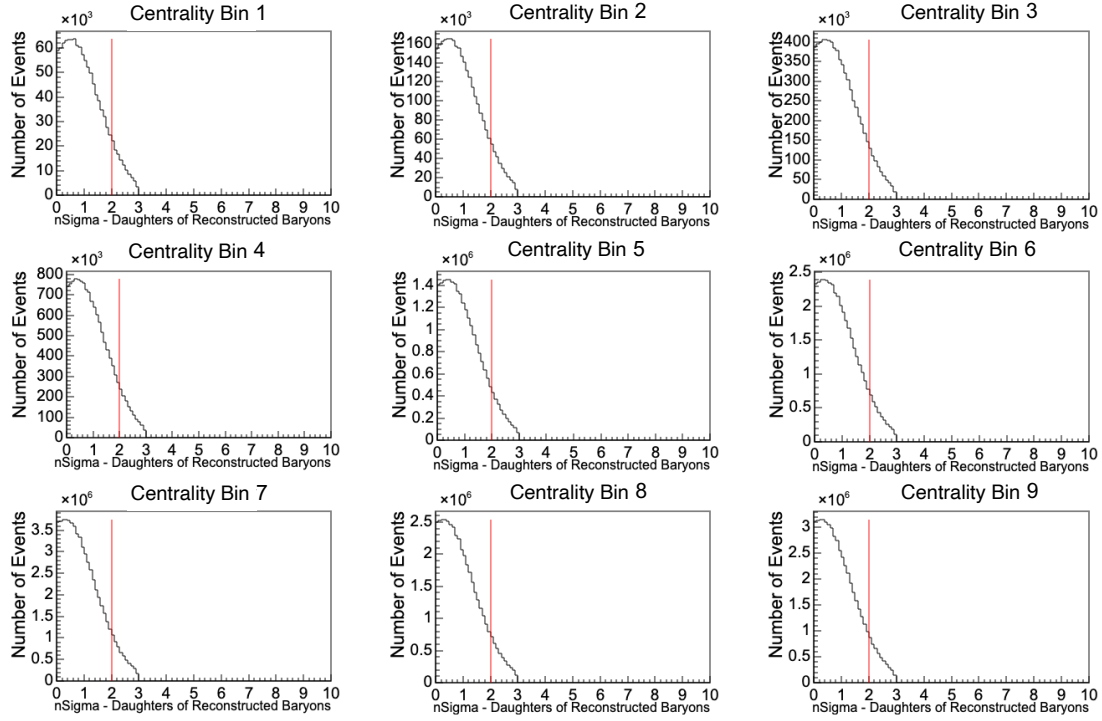


Figure 5.7: Systematic Cut on  $n_{\text{HitsFit}}$  of daughters of reconstructed baryons. sys\_2 - the events that fall on the right of the red line.

(a) 19.6 GeV



(b) 27 GeV

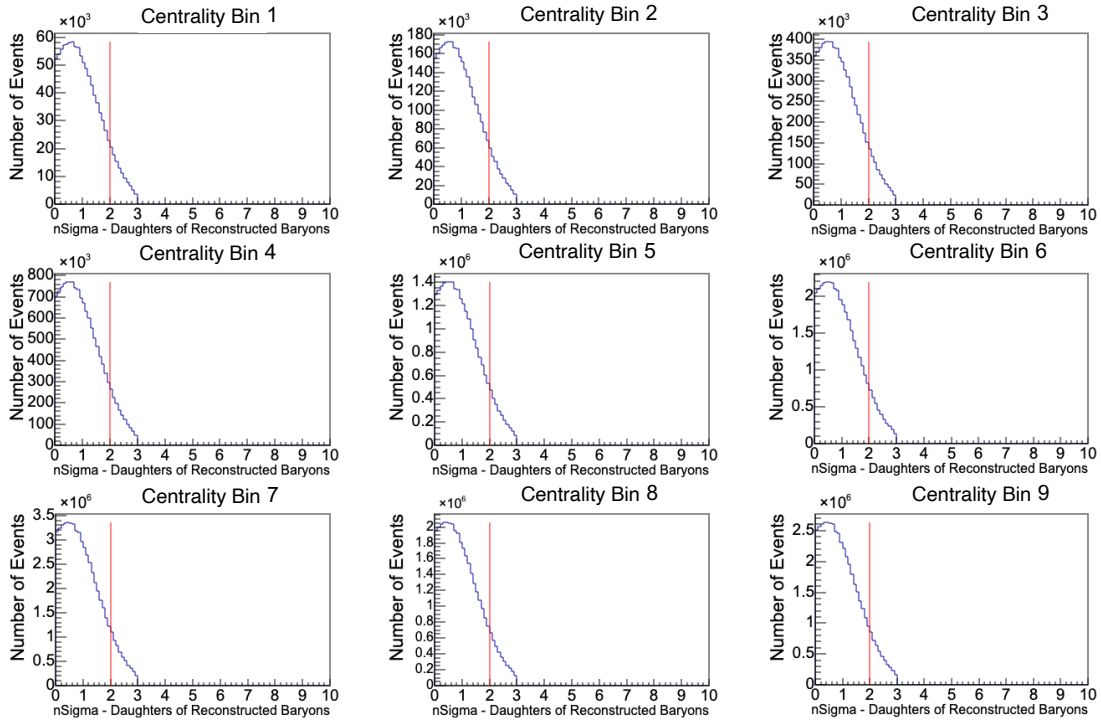
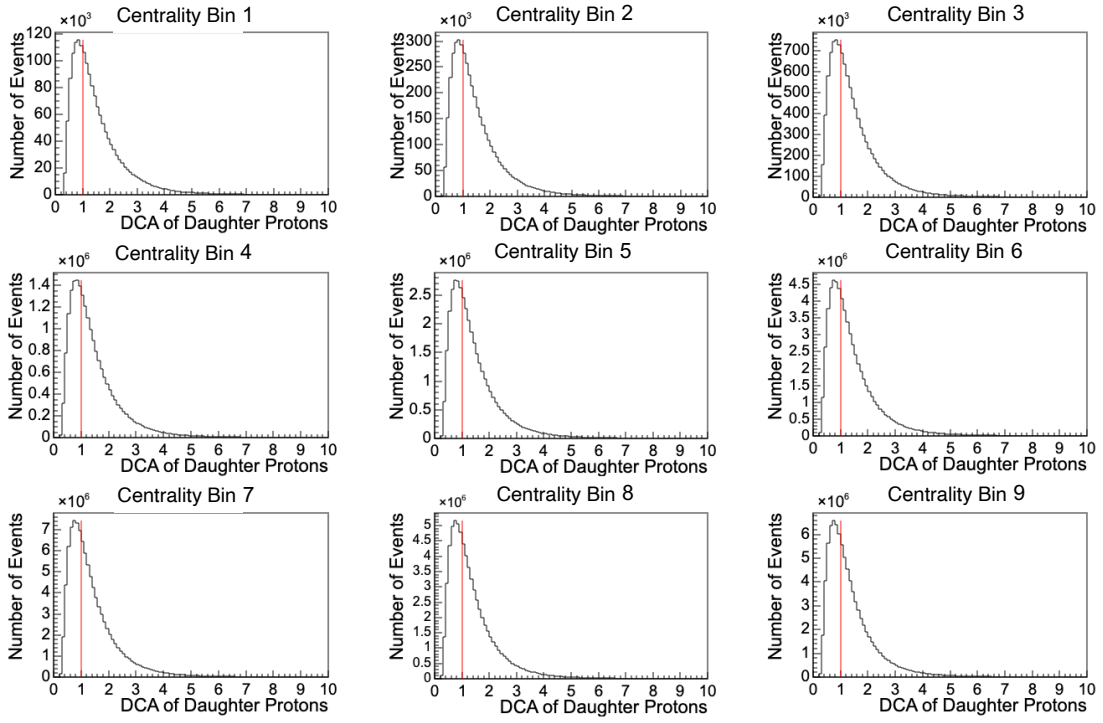
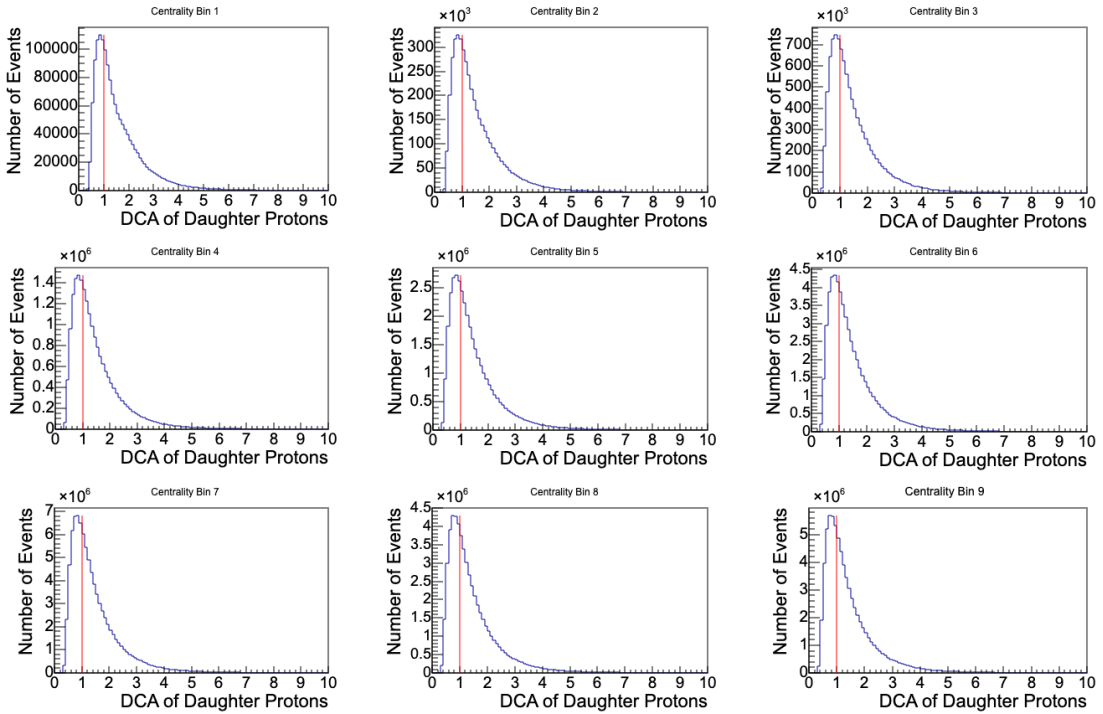


Figure 5.8: Systematic Cut on nSigma of daughters of reconstructed baryons. sys\_3 - the events that fall on the left of the red line.

(a) 19.6 GeV



(b) 27 GeV



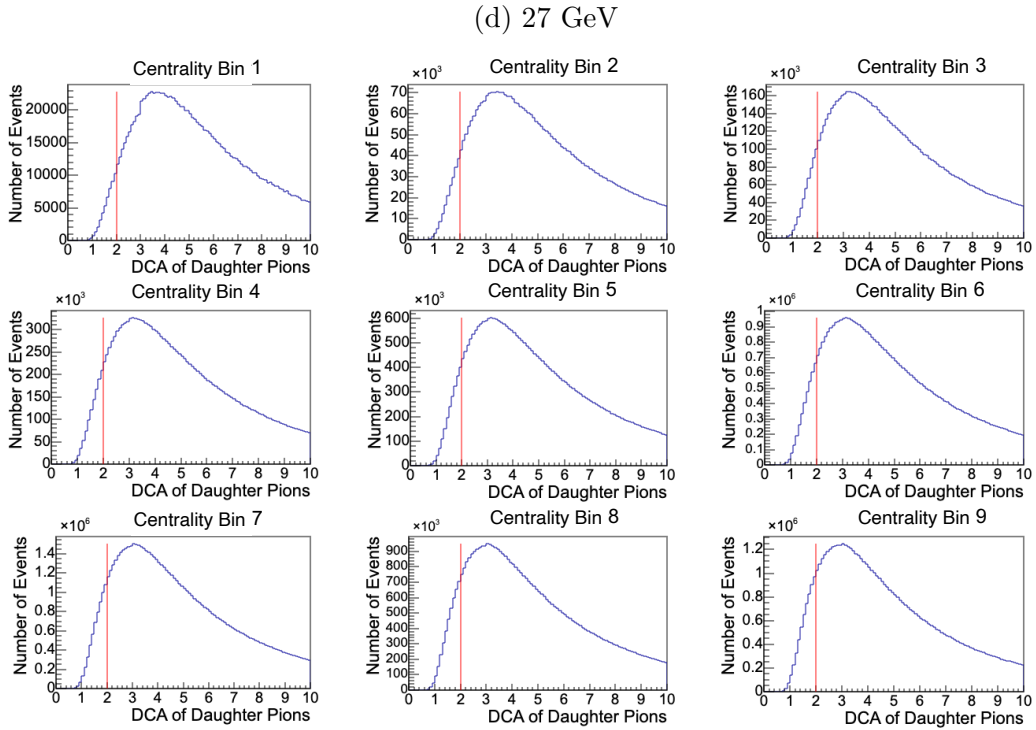
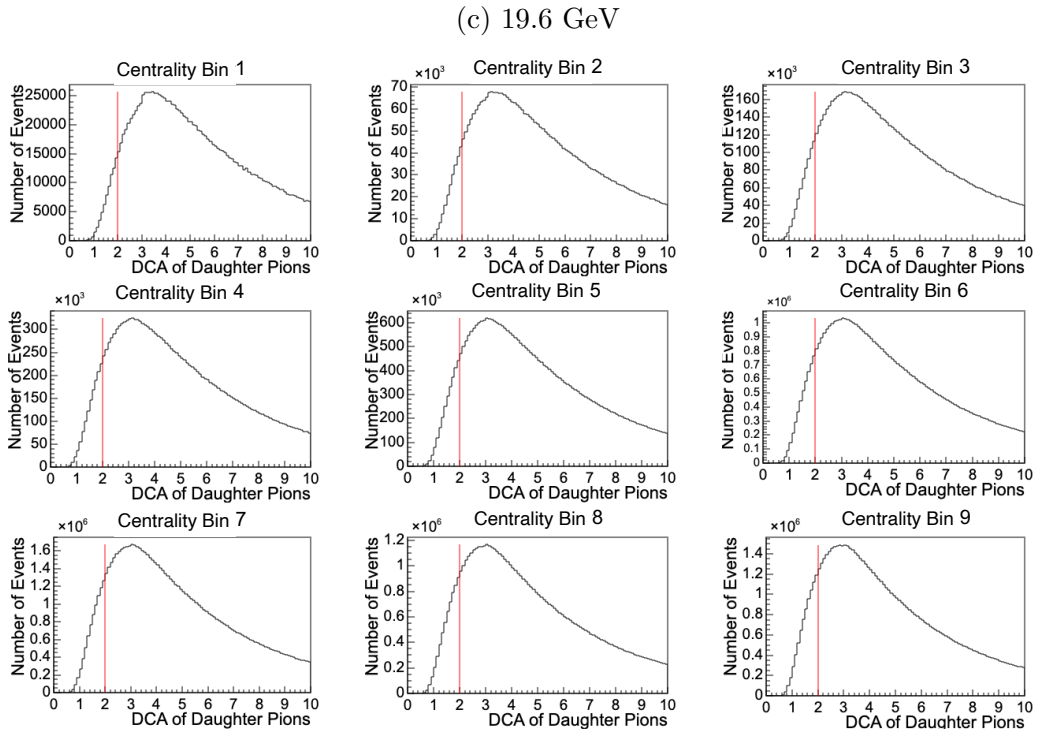
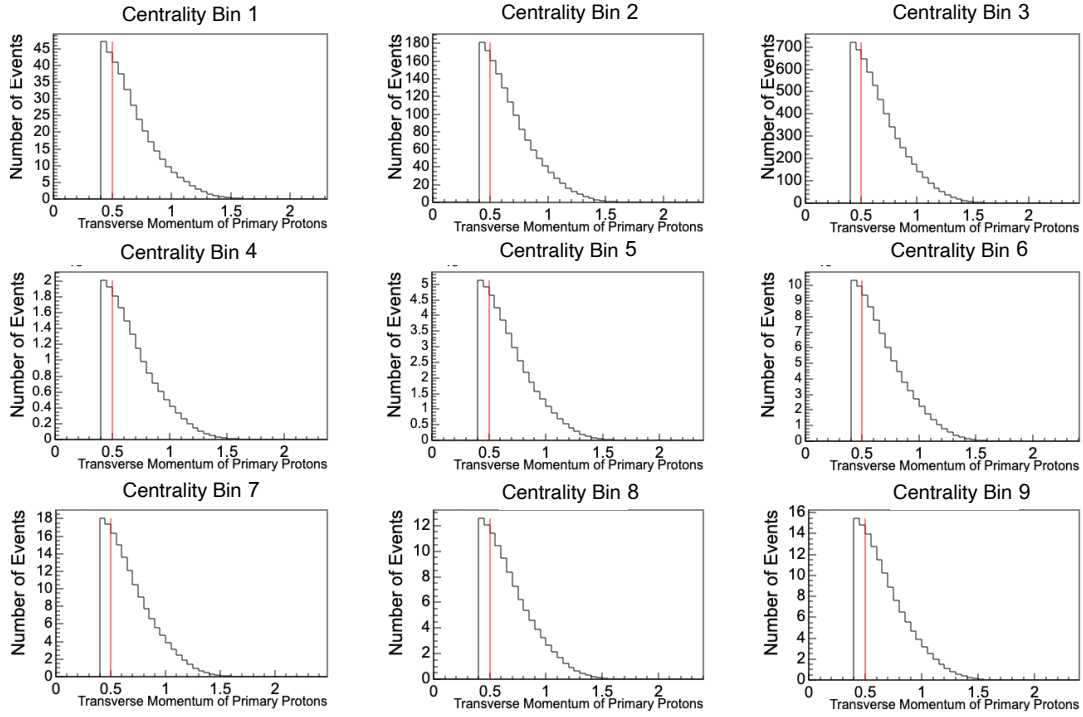


Figure 5.9: Systematic Cut on distance of closest approach of daughters of reconstructed baryons. `sys_4` and `sys_5` - the events that fall on the right of the red line. (a) and (b) correspond to proton cuts; (c) and (d) correspond to pion cuts.

(a) 19.6 GeV



(b) 27 GeV

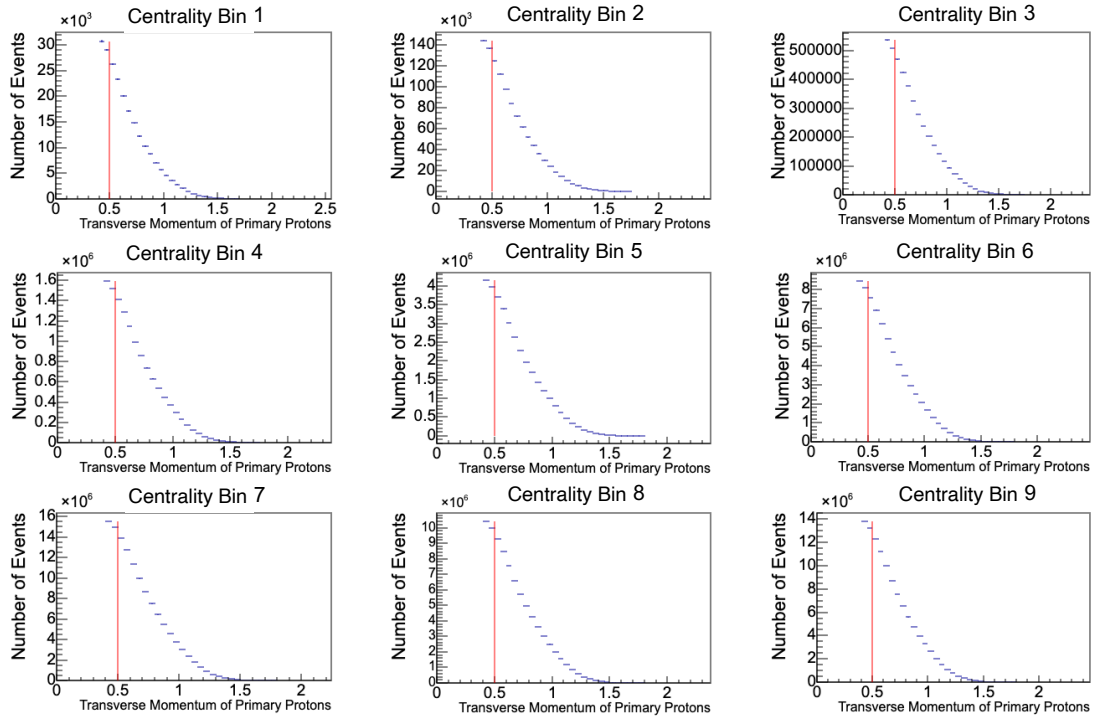
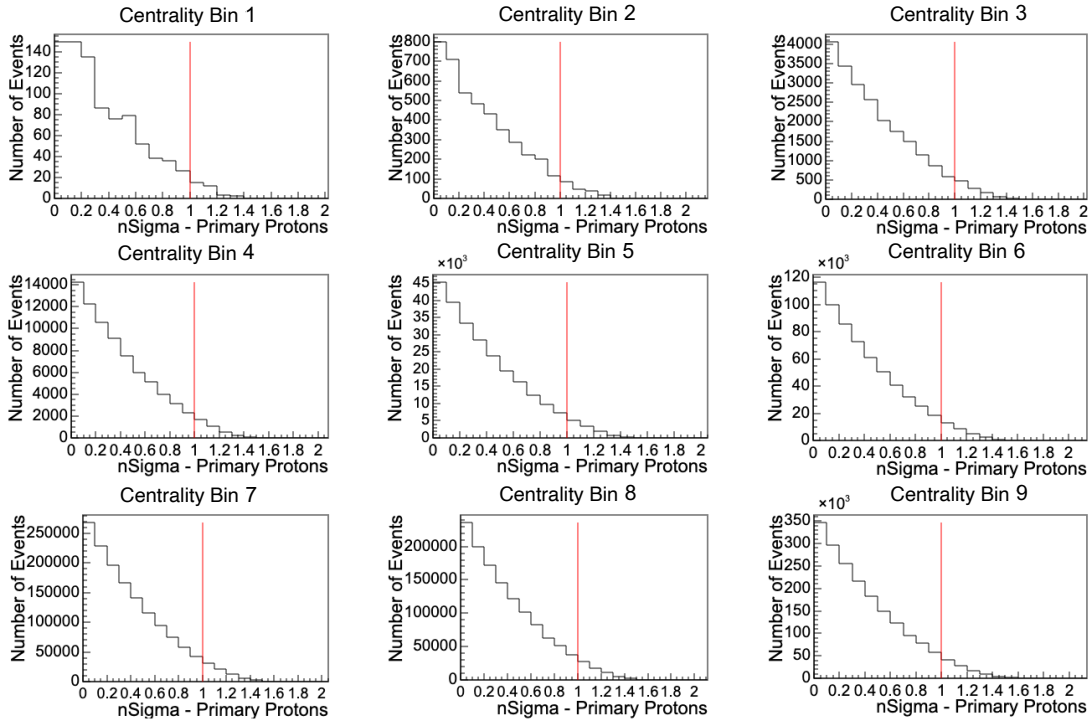


Figure 5.10: Systematic Cut on transverse momentum of daughters of reconstructed baryons. sys\_6 - the events that fall on the right of the red line.

(a) 19.6 GeV



(b) 27 GeV

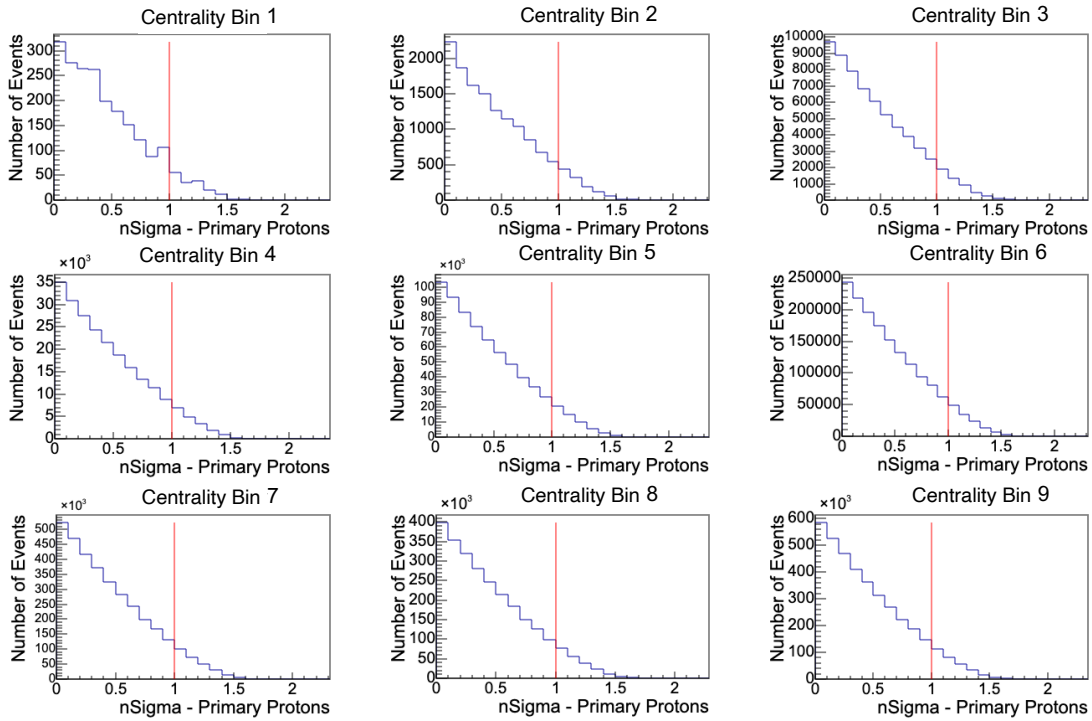


Figure 5.11: Systematic Cut on  $n\text{Sigma}$  of primary protons. `sys_7` - the events that fall on the left of the red line.

With these cuts, we perform the analysis and measure our observables the exact same way as we do the default values, with the exception of this extra systematic cut. Then, we compute the systematic error by using the following equation:

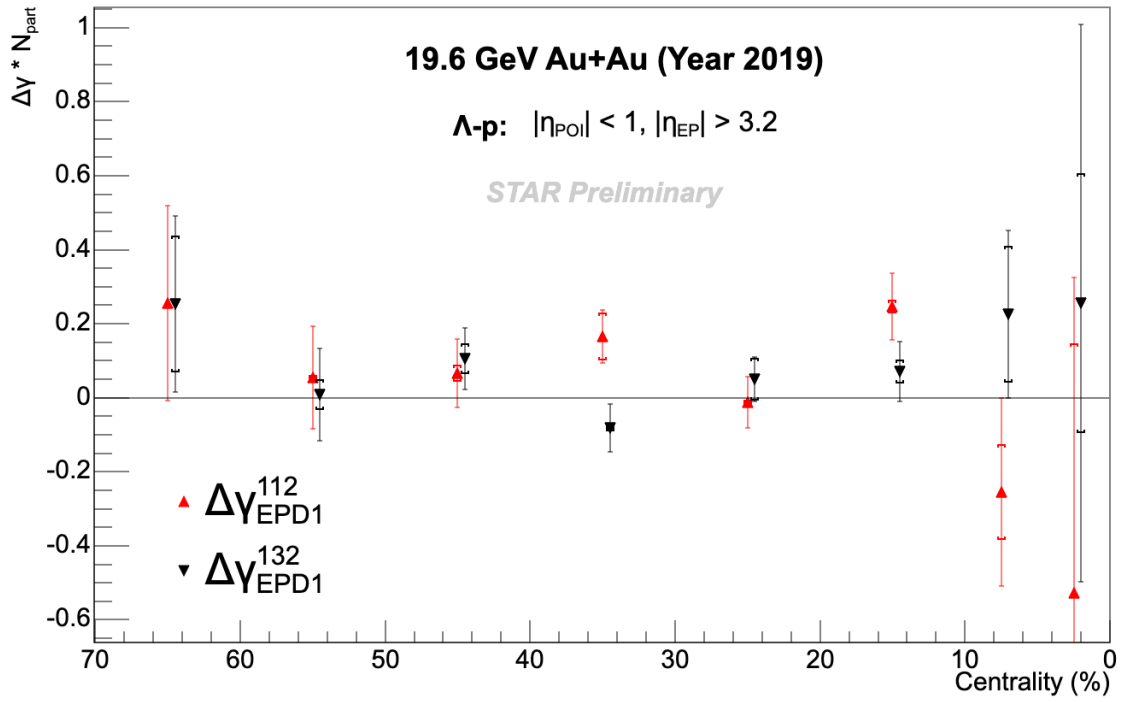
$$\text{SystematicUncertainty} = \sqrt{\sum_{i=1}^7 \left( \frac{\sqrt{(O_d - O_i)^2 - |e_d^2 - e_i^2|}}{\sqrt{12}} \right)^2} \quad (5.34)$$

with  $O_d$  and  $e_d$  being the default value for the observable and the error on that value respectively, and  $O_i$  and  $e_i$  being the value and error of the observable with the systematic cut  $i$  in place.  $i$  ranges from 1 to 7, corresponding to the 7 different systematic cut values. For each of the systematic cuts, one standard deviation of the systematic uncertainty is computed as the value within the summation. Then, they are all added together in quadrature. This will be the method through which we compute the systematic uncertainty of the observables.

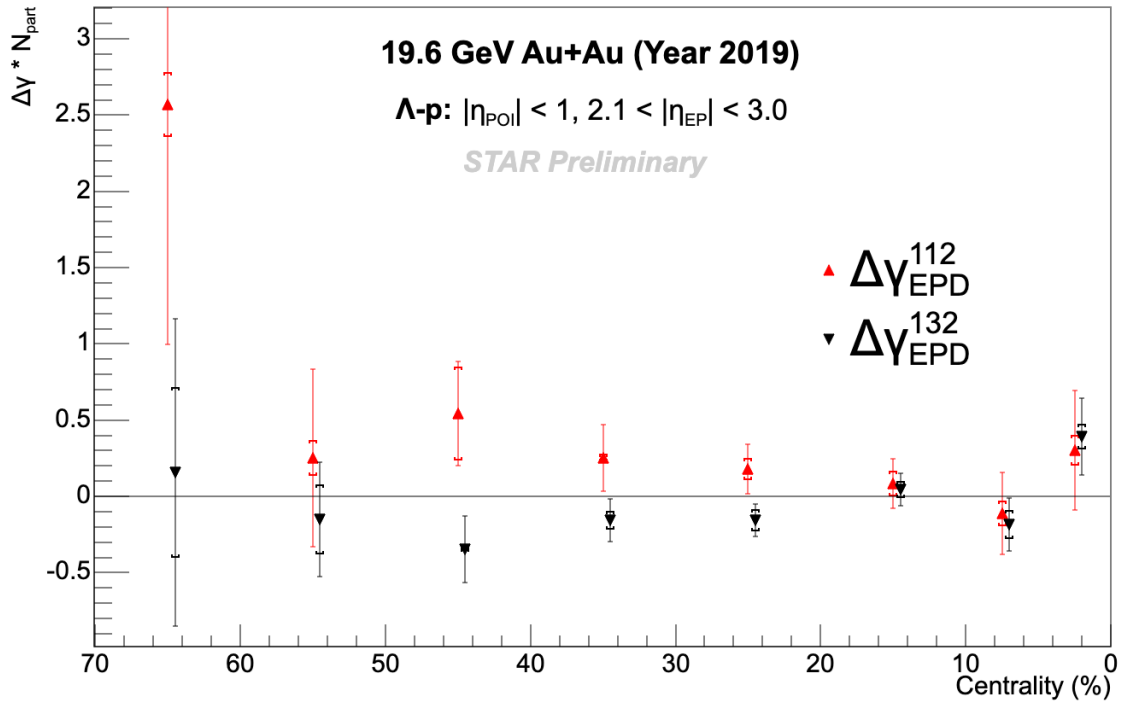
### 5.3 Ensemble Results

In this section, we will present the results of the correlators mentioned previously in this thesis for the search for CVE through  $\Lambda$ - $p$  azimuthal angle correlations. The following are the  $\Delta\gamma^{112}$  and  $\Delta\gamma^{132}$  results for 19.6 GeV and 27 GeV Au+Au collisions:

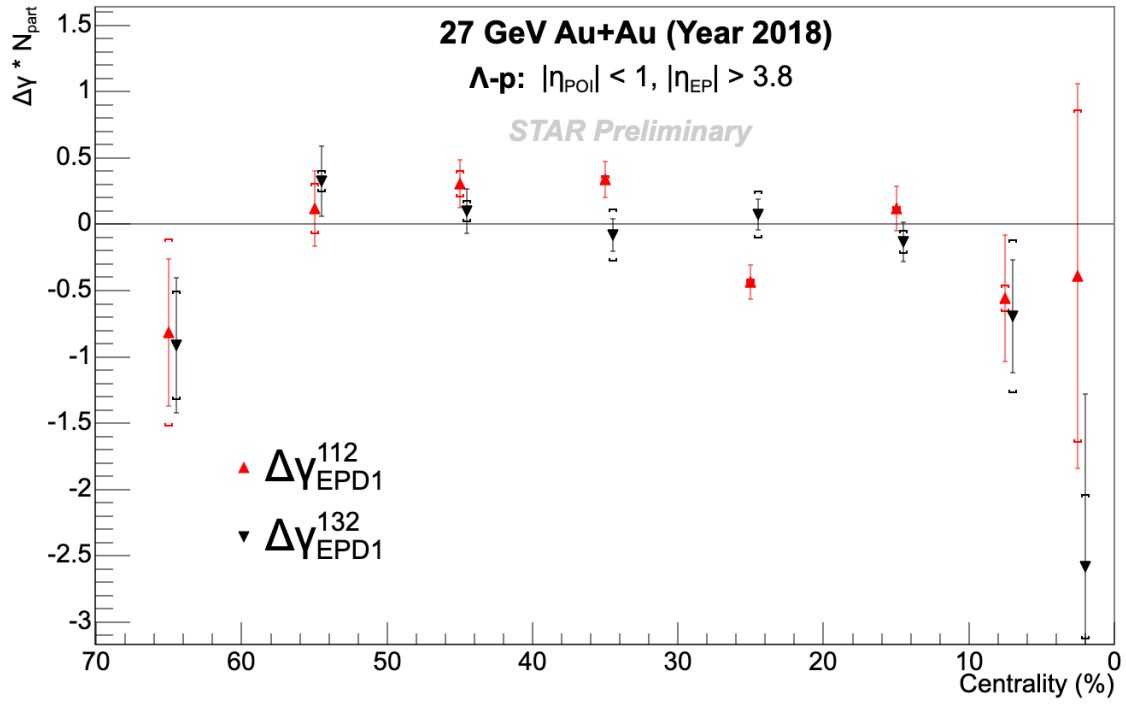
(a) 19.6 GeV Au+Au Collisions  $\Delta\gamma$  with 1<sup>st</sup> order EPD event plane



(b) 19.6 GeV Au+Au Collisions  $\Delta\gamma$  with 2<sup>nd</sup> order EPD event plane



(c) 27 GeV Au+Au Collisions  $\Delta\gamma$  with 1<sup>st</sup> order EPD event plane



(d) 27 GeV Au+Au Collisions  $\Delta\gamma$  with 2<sup>nd</sup> order EPD event plane

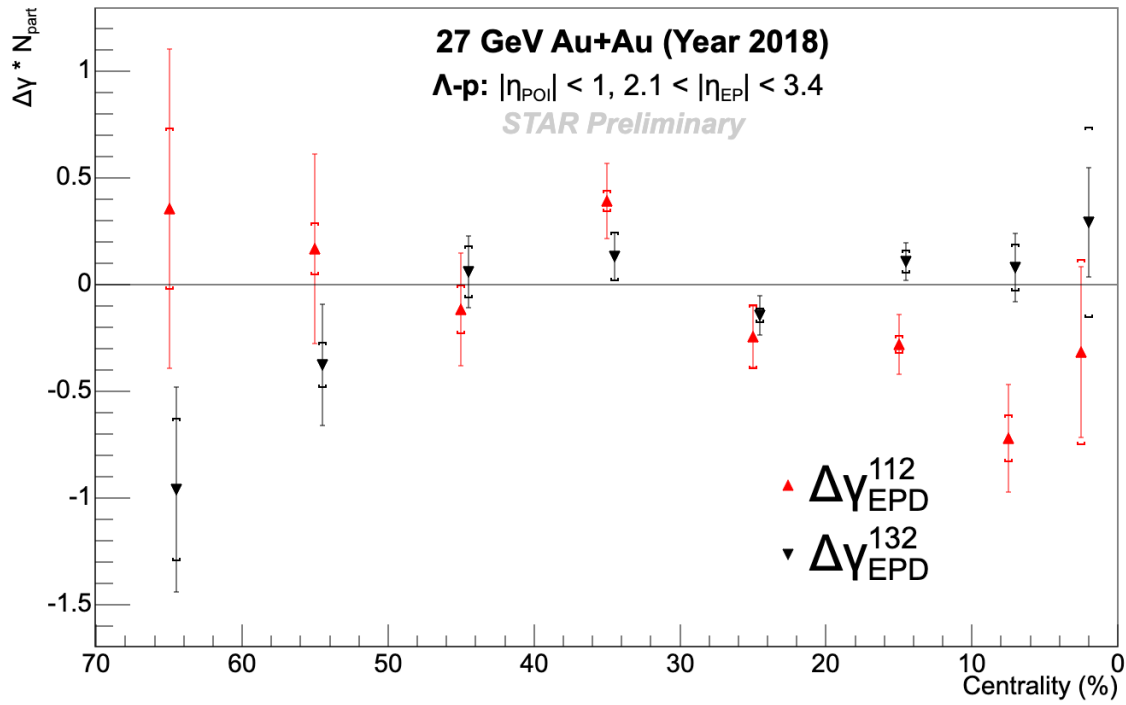
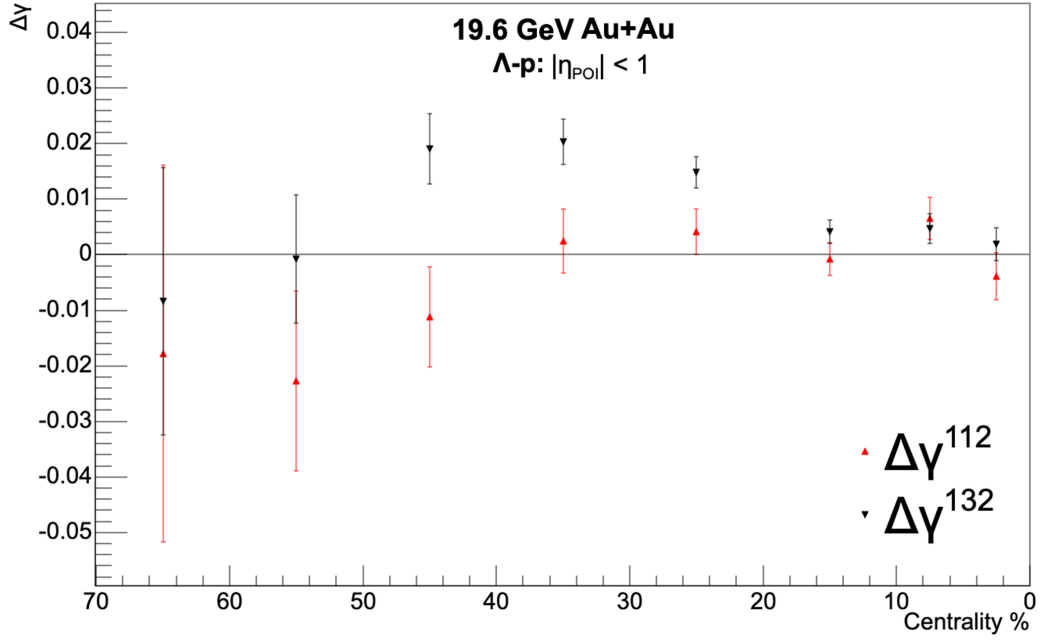


Figure 5.12: Ensemble results for  $\Delta\gamma$  using  $\Lambda$ - $p$  pairs.

These are the  $\Delta\gamma^{112}$  and  $\Delta\gamma^{132}$  results from AMPT for the two energies:

(a) AMPT 19.6 GeV Au+Au Collisions  $\Delta\gamma$



(b) AMPT 27 GeV Au+Au Collisions  $\Delta\gamma$

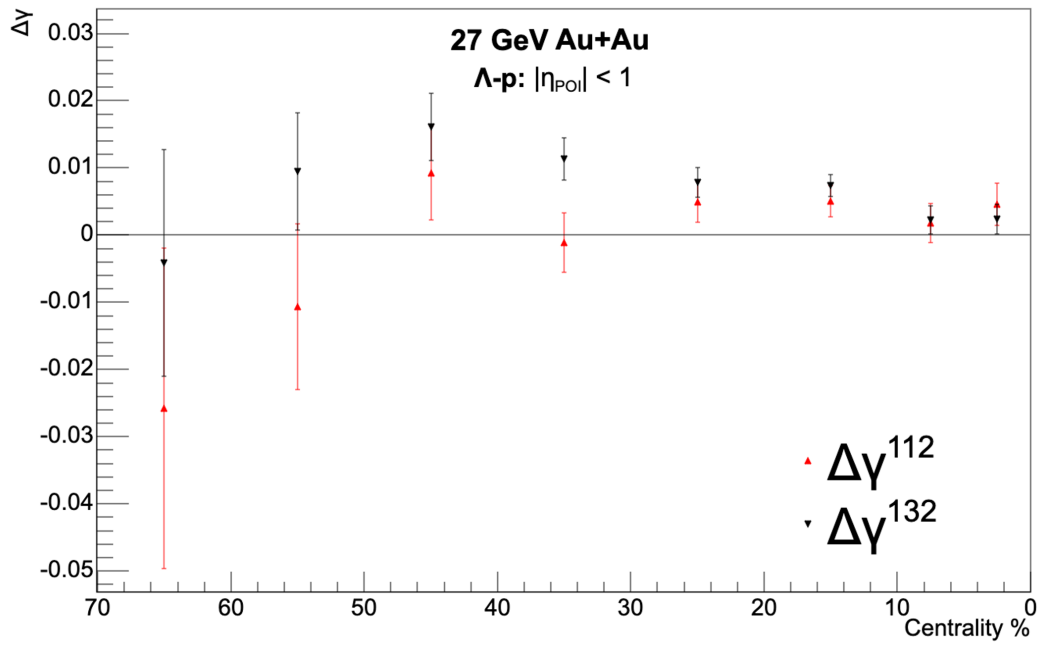
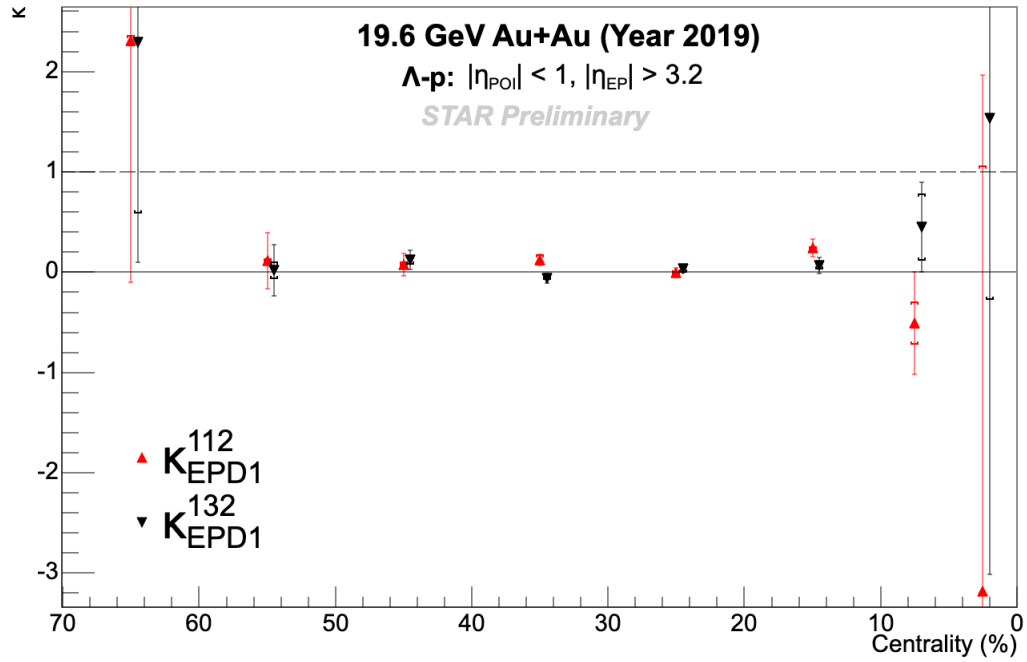


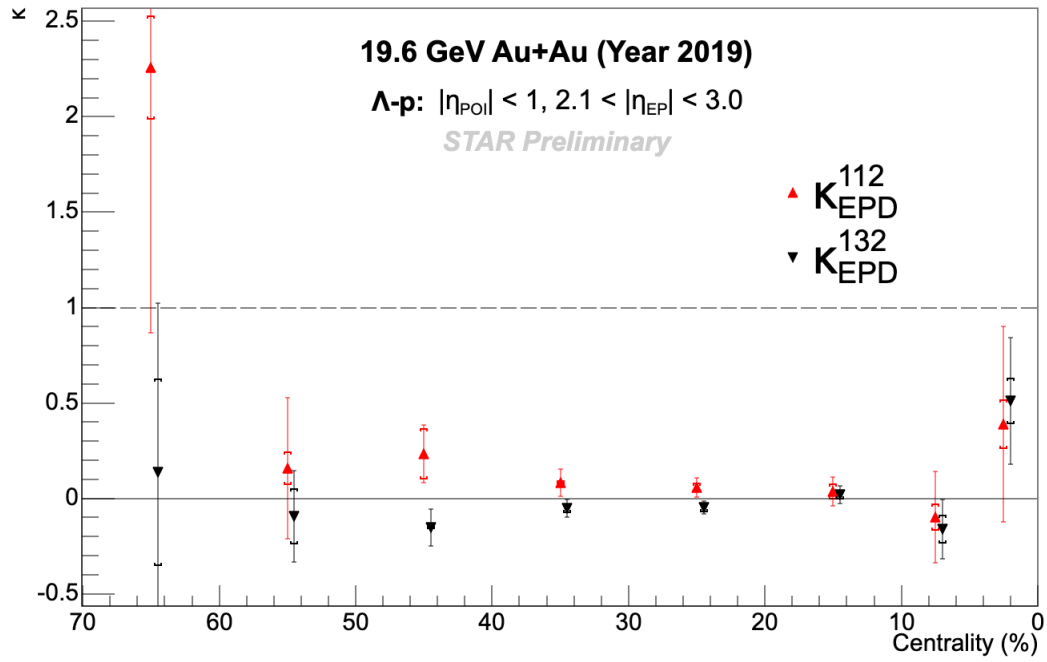
Figure 5.13: AMPT results for  $\Delta\gamma$  using  $\Lambda$ - $p$  pairs.

These are the  $\kappa_{112}$  and  $\kappa_{132}$  results, comparing collected data with AMPT data:

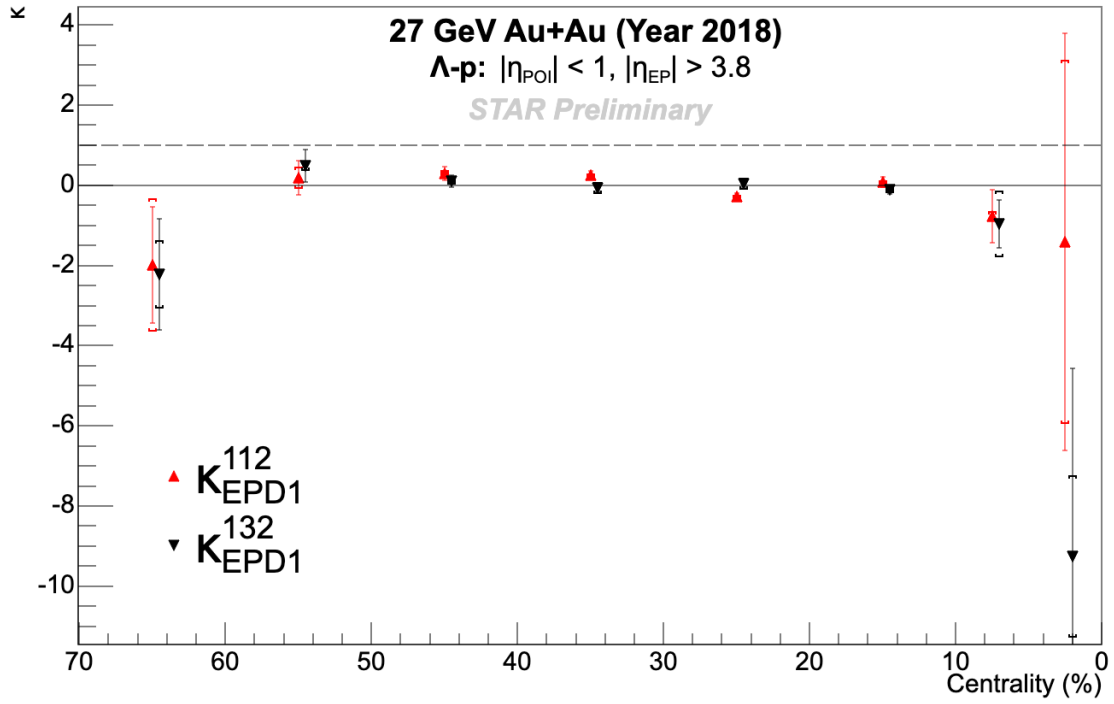
(a) 19.6 GeV Au+Au Collisions  $\kappa$  with 1<sup>st</sup> order EPD event plane



(b) 19.6 GeV Au+Au Collisions  $\kappa$  with 2<sup>nd</sup> order EPD event plane



(c) 27 GeV Au+Au Collisions  $\kappa$  with 1<sup>st</sup> order EPD event plane



(d) 27 GeV Au+Au Collisions  $\kappa$  with 2<sup>nd</sup> order EPD event plane

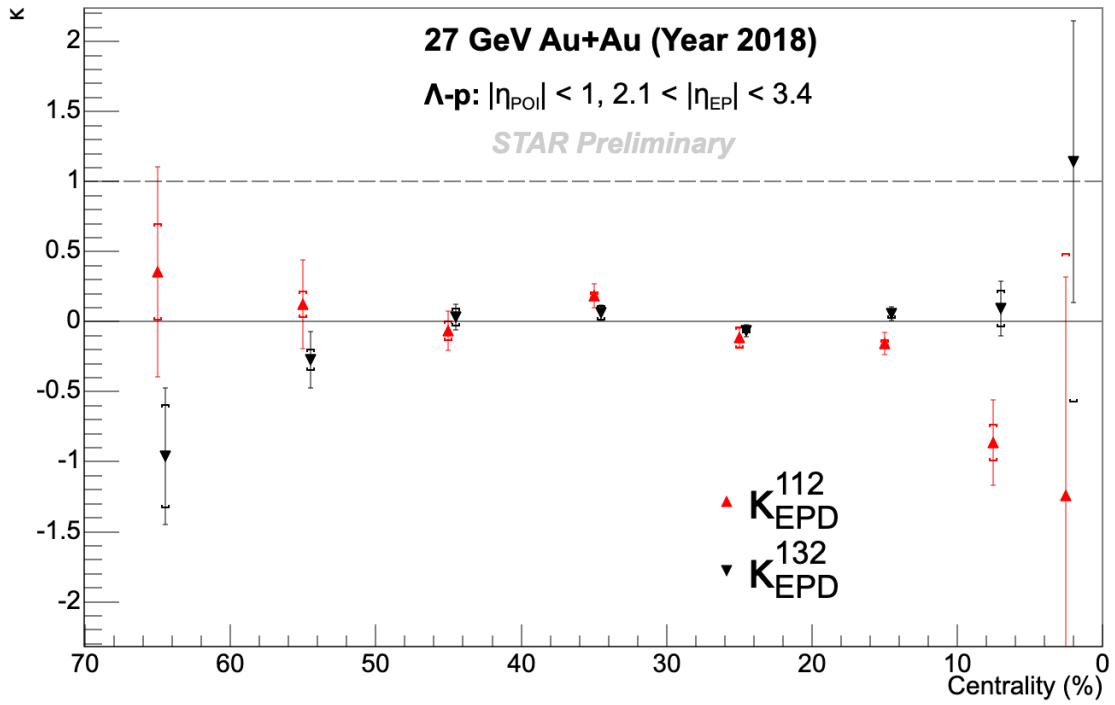
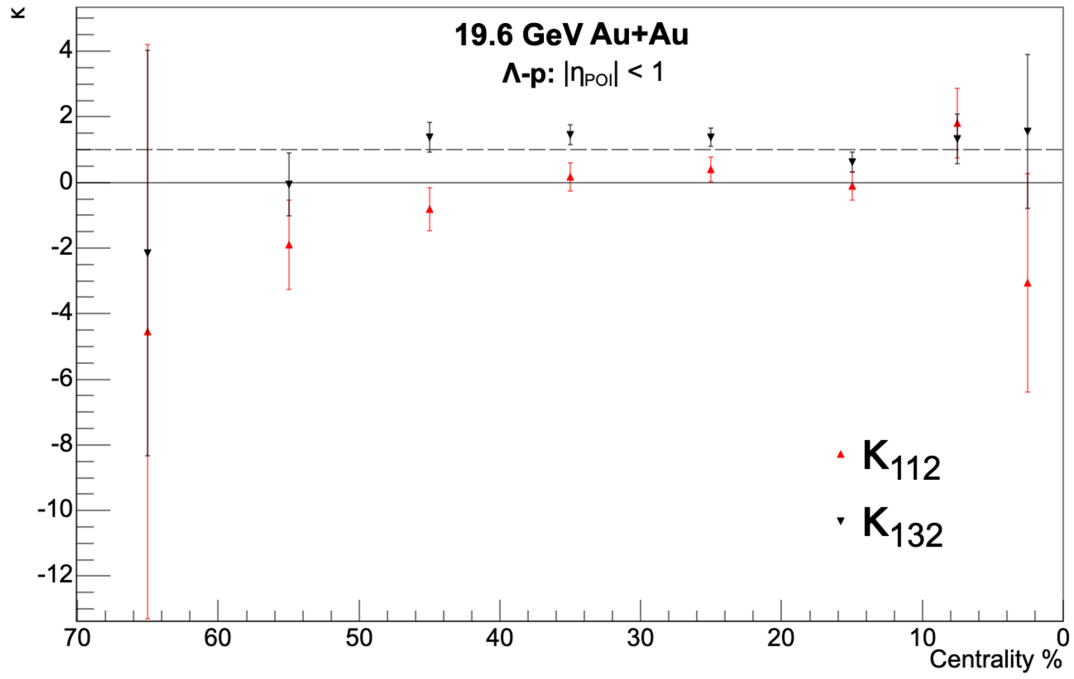


Figure 5.14: Ensemble results for  $\kappa$  using  $\Lambda$ - $p$  pairs.

(a) AMPT 19.6 GeV Au+Au Collisions  $\kappa$



(b) AMPT 27 GeV Au+Au Collisions  $\kappa$

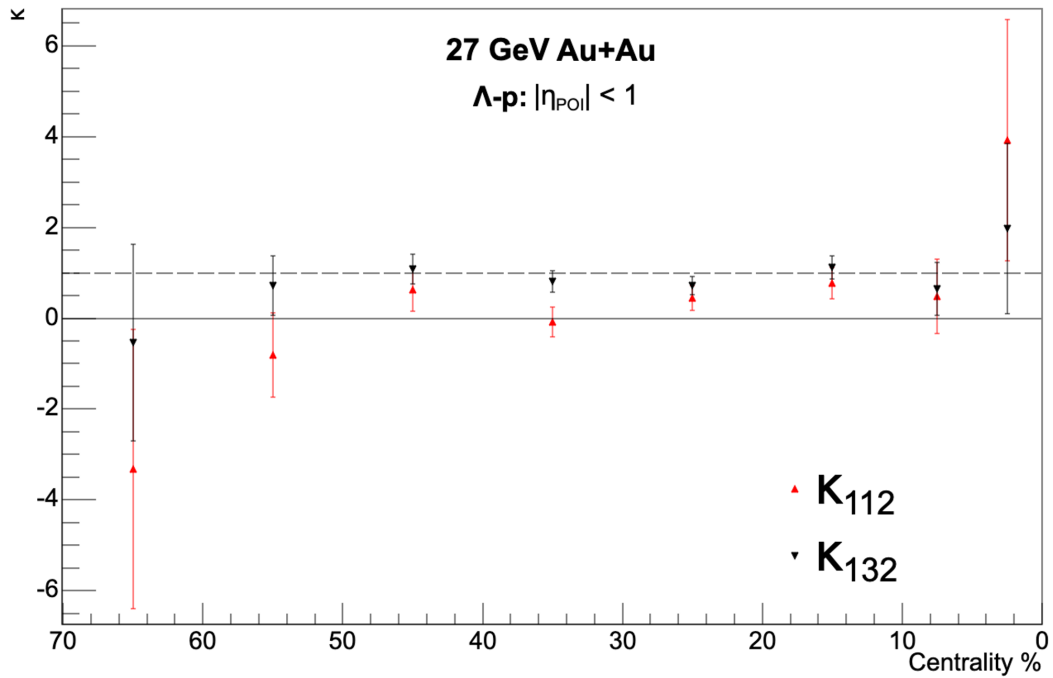


Figure 5.15: AMPT results for  $\kappa$  using  $\Lambda$ - $p$  pairs.

From the above results, there are a few points to note: First, for the data from heavy-ion collisions, it seems that for most of the results that  $\Delta\gamma^{112}$  and  $\Delta\gamma^{132}$  are equivalent to each other, and both are essentially consistent with zero; Second, for the AMPT results, it is clear that there is significant difference between  $\Delta\gamma^{112}$  and  $\Delta\gamma^{132}$  results, and while  $\kappa_{132}$  is as we would predict mathematically consistent with 1 - the case with only background described by  $v_2 \cdot \delta$ ,  $\kappa_{112}$  is actually less than  $\kappa_{132}$  in magnitude and consistent with 0 instead. These seem to suggest that  $\Delta\gamma^{112}$  is not purely equivalent to the background that  $\Delta\gamma^{132}$  represents, but the effects seem to lower their values; and that there might be some interesting physics leading to the two results being equivalent to each other in heavy-ion collisions, a qualitatively different result than that from AMPT.

## 5.4 Event Shape Selection Method

As previously discussed when introducing the  $\gamma^{112}$  correlator, the background contributions are intended to be removed by ensuring that  $B_{IN}$  and  $B_{OUT}$  are roughly similar. However, even after subtracting same sign results from opposite sign results, the directed flow contributions are not entirely canceled out, indicating some contamination from background effects. One possible source of this contamination is elliptic flow,  $v_2$ .

For example, due to elliptic flow, there may be a higher number of clusters flying along the reaction plane compared to those flying out of it, unrelated to the CME or CVE. As an extreme example, say we consider two  $\rho$  mesons traveling in opposite directions, but both within the reaction plane, and that would give us an elliptic flow of  $v_2 = 1$ . Now if the daughter pions of these mesons are highly boosted, potentially because of the high transverse momentum of the parents, and they essentially follow the exact directions of their parents, then there would be no out-of-plane charge separation, and yet  $\Delta\gamma^{112}$  of this event would still equal to 1, signaling to us that there is CME. Therefore, in the scenario of this analysis, we can see that if there is general elliptic flow, then these clusters of  $\Lambda$ - $p$  can in a sense decay into particles of opposite charges, they will move in opposite directions relative to the reaction plane, leading to charge separation across it. This spurious effect can contribute

to the measured signal, making it challenging to isolate the genuine CME/CVE signal from flow-related backgrounds [139].

To address this issue, various scenarios have been considered where elliptic flow is coupled with transverse momentum conservation (TMC) or local charge conservation (LCC) [140][135][141].

To mitigate flow-related backgrounds, the event-shape-selection (ESS) approach was developed. This method involves selecting spherical events, where the particles of interest carry no elliptic flow [139]. The authors of Ref. [139] outlined three key components for a valid ESE approach:

1. The need for a direct handle on the event shape that accurately reflects the ellipticity of the particles of interest in each event.
2. When this handle is turned to zero-flow mode, the flow background must vanish. To check this requirement, the AMPT model is utilized, which contains only backgrounds and no signals.
3. The alteration of this handle should not introduce additional artificial background beyond our control. To validate this, a simple Monte Carlo simulation is employed.

By adhering to these requirements, the ESE approach offers a promising avenue to address and potentially remove the influence of elliptic flow-related backgrounds from CME measurements in heavy-ion collisions.

First we will discuss the choosing of the handle that will properly reflect the ellipticity of the particles of interest. A straightforward idea would be to project to strictly spherical events, which means having no eccentricity, with  $v_2$  being on average 0 for all particles, regardless of them being primordial, decay products or parent particles. However, since the particle emission pattern may have event-by-event fluctuations, it is possible to have on average an almost-zero  $v_2$  despite the individual events having finite eccentricity. Such an effect is demonstrated by Figure 5.16.

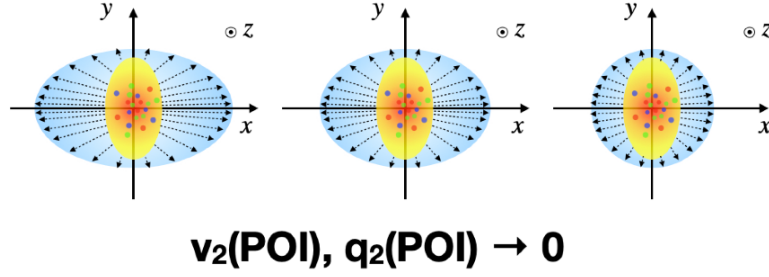


Figure 5.16: A schematic diagram of the event shape selection that attempts to project the entire event to spherical events. We see that this method is based on the particle emission pattern in the transverse plane, and therefore it could be possible that both  $v_2$  and  $q_2$  of the particles of interest fluctuate towards zero and yet there is a finite eccentricity in the overlapping region.

An early method that was used categorized events directly using “observed  $v_2$ ” [142]. What this “observed  $v_2$ ” would entail is to define an event-by-event  $v_2$  variable that describes the ellipticity of the event. By requiring it to be zero, it seems like we would be able to choose the spherical events with zero flow effects.

$$v_{2,ebye}^{observe} \equiv \langle \cos [2(\phi_A - \Psi_{EP}^B)] \rangle \quad (5.35)$$

We first have to eliminate self-correlation, and we do so by splitting the events into two sub-events, which we denote by A and B, as seen in the equation above. However, the problem with this is that zero “observed  $v_2$ ” doesn’t necessarily mean that particles in A have zero  $v_2$ . We see that in Figure 5.17, where an interesting, non-monotonic relationship between “observed  $v_2$ ” and  $v_2$  of particles in A was found, and the minimum of  $v_2$  of particles in A was strictly above zero. This means that using “observed  $v_2$ ” as the handle seems to have failed at actually projecting the particles in A to a spherical event. Another troubling correlation we see here is that the true event plane resolution  $R^B$  strongly depends on the “observed  $v_2$ ” and could even become negative. This means that we would not even be able to correct “observed  $v_2$ ” with the true event plane resolution to retrieve the true  $v_2$  values of the particles in A.

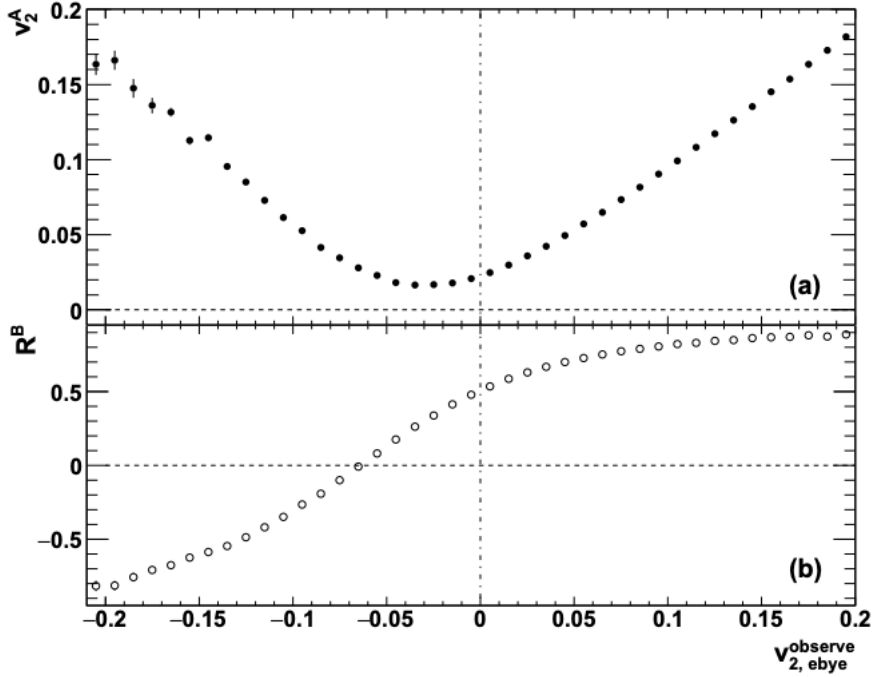


Figure 5.17: Top Panel: True  $v_2$  of particles of interest in sub-event A. Bottom Panel: Reaction plane calculated from sub-event B, used to correct results from sub-event A, to avoid self-correlation.  $x$ -axis is the variable proposed,  $v_{2,ebye}^{observe}$  that describes the ellipticity of the event. As seen in this figure, unfortunately such an event does not truly describe the ellipticity of the particles of interest, and especially even when it is required to be 0, it does not coincide with the particles of interest exhibiting a spherical nature. The correlation between  $R^B$  and the event handle is also troubling. This plot is taken from [139].

So instead, the magnitude of the flow vector, denoted as  $q$ , reconstructed from a sub-event, seems to be a better candidate for the handle on event shape, because by definition it has no explicit contributions from the other sub-event or the reaction plane. The definition of  $q$  can be found as follows:

$$\vec{q}_2 = (q_{2,x}, q_{2,y}) \quad (5.36)$$

$$q_{2,x} \equiv \frac{1}{\sqrt{N}} \sum_i^N \cos(2\phi_i) \quad (5.37)$$

$$q_{2,y} \equiv \frac{1}{\sqrt{N}} \sum_i^N \sin(2\phi_i) \quad (5.38)$$

There are different ideas with regards to how to construct  $q_2$ . One was to construct it from a sub-event that does not include the particles of interest (POI) - the particles used in computations for the observables that we are trying to reduce the background in. However, there are issues with such definitions because the correlation between  $q_2$  and  $v_2^{POI}$  is typically weak, which leads to the scenario of a sizable positive  $v_2^{POI}$  even when  $q_2 = 0$ . Then we have to extrapolate over a significant region of unmeasured  $v_2^{POI}$  that introduces substantial statistical and systematic uncertainties - for example, fitting the data with a linear fit versus a quadratic fit yields fits that fit the data substantially well, but with drastically different conclusions about what the value is after using the Event Shape Selection method, also with significantly different statistical errors [143] [144]. Taking into account the potential of longitudinal flow-plane decorrelations, we see the importance of maintaining that the POI and the sub-event used for constructing  $q_2$  to be within the same rapidity region [145, 146, 147, 148, 149]. So if we construct flow vector  $q$  with the POI, it seems to model the true ellipticity, as it was shown in the paper that as  $v_2$  values approach zero, so did  $q$ , as shown in Fig. 5.18.

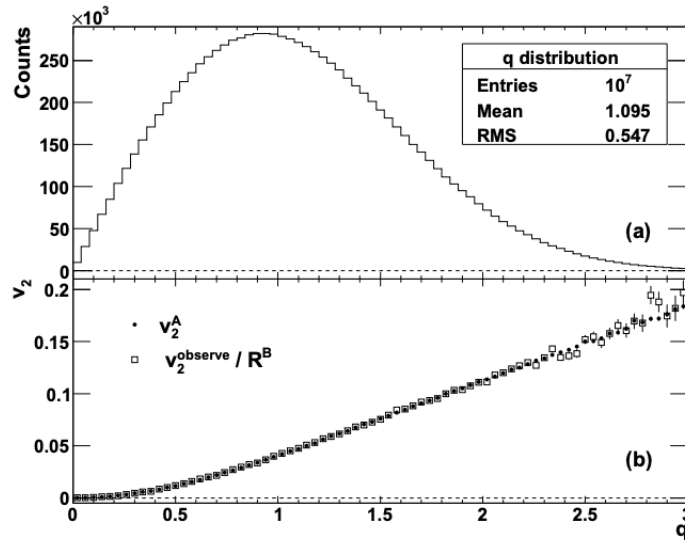


Figure 5.18: In the bottom panel, it is clear that the true elliptic flow  $v_2^A$  and the corrected elliptic flow  $v_2^{observe}$  as functions of  $q$  are in a higher level of agreement. This plot is taken from Ref. [139].

Now, the other candidate is  $q^2$  and that is an even better candidate. First,  $q^2 = 0$  is equivalent to  $q = 0$ , so they have the same capability of selecting spherical sub-events in terms of the second harmonic. Then  $q^2$  is a better handle than  $q$  because of the following two reasons and is depicted in Fig. 5.19: The first reason is that the relationship between the elliptic flow variables  $v_2$  and  $q^2$  at low  $q^2$  values is close to being a linear relationship, which means that we can more reliably project our  $\gamma$  correlators to zero  $q^2$  in order to remove  $v_2$ -related backgrounds; the second reason for  $q^2$  being a better handle lies in the distributions of these respective variables shown in the top panels of Fig. 5.18 and 5.19. The distribution for  $q$  has lower statistics towards lower  $q$ , as it peaks around unity, and so the projection of  $\gamma$  correlators towards  $q = 0$  would become unstable. This is however not the case for  $q^2$ , as the distribution is shifted in phase space towards zero. Therefore,  $q^2$  would be the handle for us to use in order to reflect the ellipticity of the particles of interest in the events.

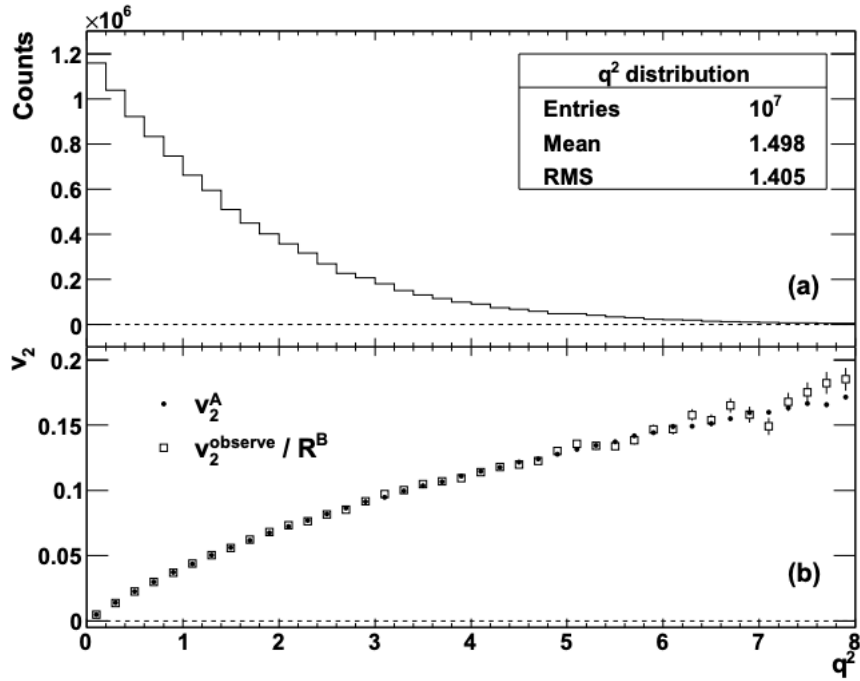


Figure 5.19: In the bottom panel, it is clear that the true elliptic flow  $v_2^A$  and the corrected elliptic flow  $v_2^{\text{observe}}$  as functions of  $q$  are in a higher level of agreement. This plot is taken from Ref. [139].

Now that we've discussed the handle to use for properly reflecting the ellipticity of the particle of interest, we need to check and see that when this handle is turned to zero-flow mode, that the flow background actually vanishes. In order to check this, we turn to the AMPT model mentioned previously, because this model contains only background and no CME signals. So using the handle  $q^2$ , the authors of the paper looked at our  $\gamma^{112}$  correlator and found that the background contributions were eliminated when the correlator was projected to zero  $q^2$ , see Fig. 5.20. This demonstrates the second key factor for a good event shape selection method. However, one caveat is that in extreme scenarios, this can still be invalidated. Suppose we have an in-plane-going resonance decaying into a positive and negative particle, one travelling at  $45^\circ$  and another at  $-45^\circ$ , then this would be a charge separation event that contributes to  $\Delta\gamma$  while having no contribution to  $q$ , and so its effect will not be eliminated even as we extrapolate our results to  $q^2 = 0$ . This means that the background from such flowing resonance will not completely vanish [150]. Despite this, given the performance of such a method in AMPT, we conclude that such an effect from extreme scenarios is negligible.

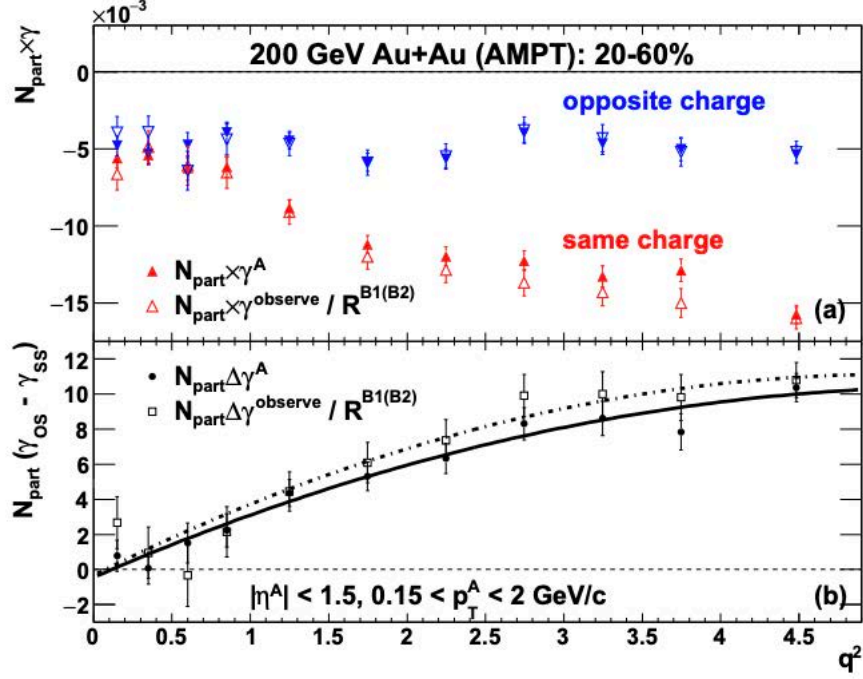


Figure 5.20: This figure shows in (a)  $N_{\text{part}} \times \gamma^{112}$  and (b)  $N_{\text{part}} \Delta \gamma^{112}$  as a function of  $q^2$ . The full symbols represent results obtained with the true reaction plane, whereas the open symbols are for the reconstructed event plane corrected for the event plane resolution. In the lower panel, the solid line is a second-order polynomial fit of the full data points, and the dashed line is for the open data points. This plot is taken from Ref. [139].

The last key factor to have a good event shape selection method is that when we alter the handle, it would not introduce artificial background in a way that we cannot model or control. This is something that warrants further study, in order to truly understand how the adjustment of the event shape handler might potentially introduce artificial background, or if it truly restores the ensemble average of the signal. The final piece to this event shape handler that we have to take into account is this: if we look at the expansion of  $q_2^2$ ,

$$\begin{aligned}
 q_2^2 &= \frac{1}{N} \left[ \left( \sum_{i=1}^N \sin 2\varphi_i \right)^2 + \left( \sum_{i=1}^N \cos 2\varphi_i \right)^2 \right] \\
 &= 1 + \frac{1}{N} \sum_{i \neq j} \cos[2(\varphi_i - \varphi_j)],
 \end{aligned} \tag{5.39}$$

we can estimate the event average of  $q_2^2$  to be:

$$\langle q_2^2 \rangle \approx 1 + Nv_2^2\{2\}. \quad (5.40)$$

where  $v_2\{2\}$  is the ensemble average of elliptic flow obtained from two-particle correlations. Eq 5.39 and 5.40 show that there is a connection between the event shape handler and  $v_2\{2\}$  that warrants a correction to normalization for  $q_2^2$ . Therefore, we will redefine  $q_2^2$  as:

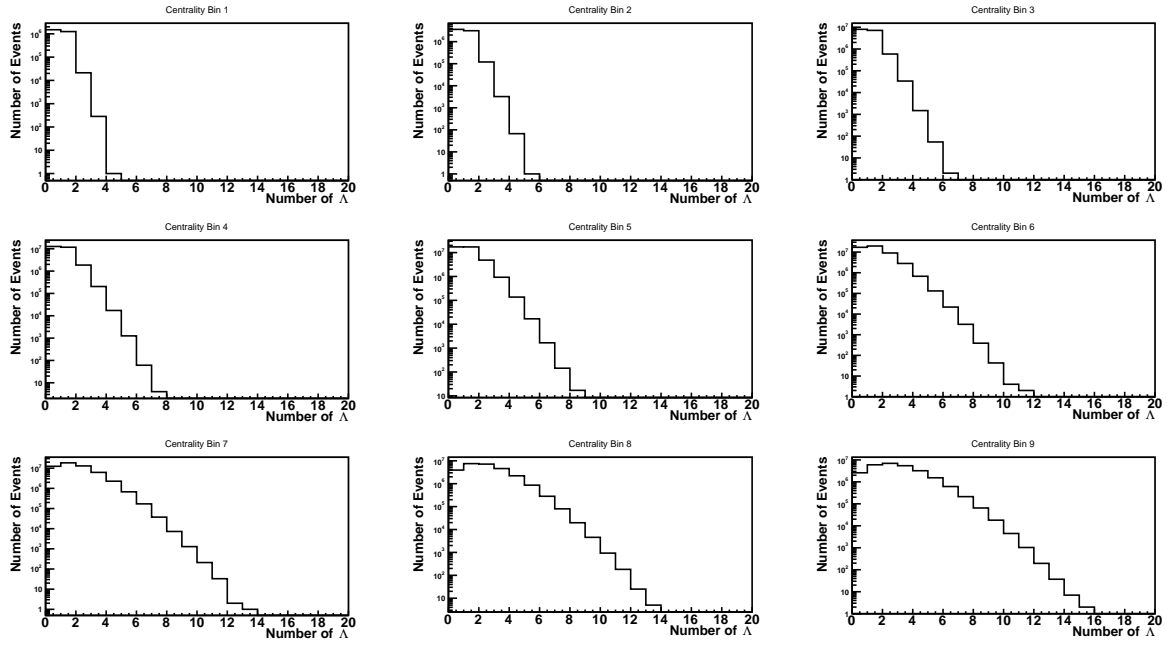
$$q_2^2 = \frac{(\sum_{i=1}^N \sin 2\varphi_i)^2 + (\sum_{i=1}^N \cos 2\varphi_i)^2}{N(1 + Nv_2^2\{2\})}. \quad (5.41)$$

This will be the event shape handler definition that is used in the rest of this analysis.

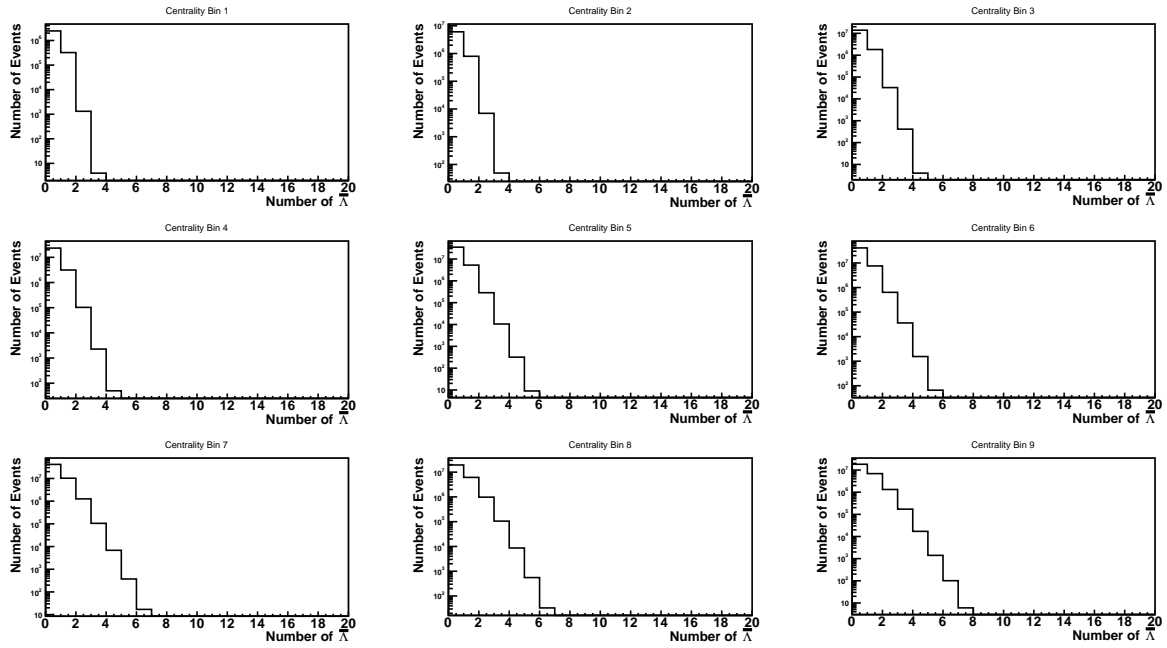
#### 5.4.1 Application of ESE on $\Lambda$ - $p$ CVE Observables

For this specific analysis, the POI are pairs of  $\Lambda$ - $p$ , which are not abundant in the products of the heavy-ion collisions in this study, especially in peripheral events.

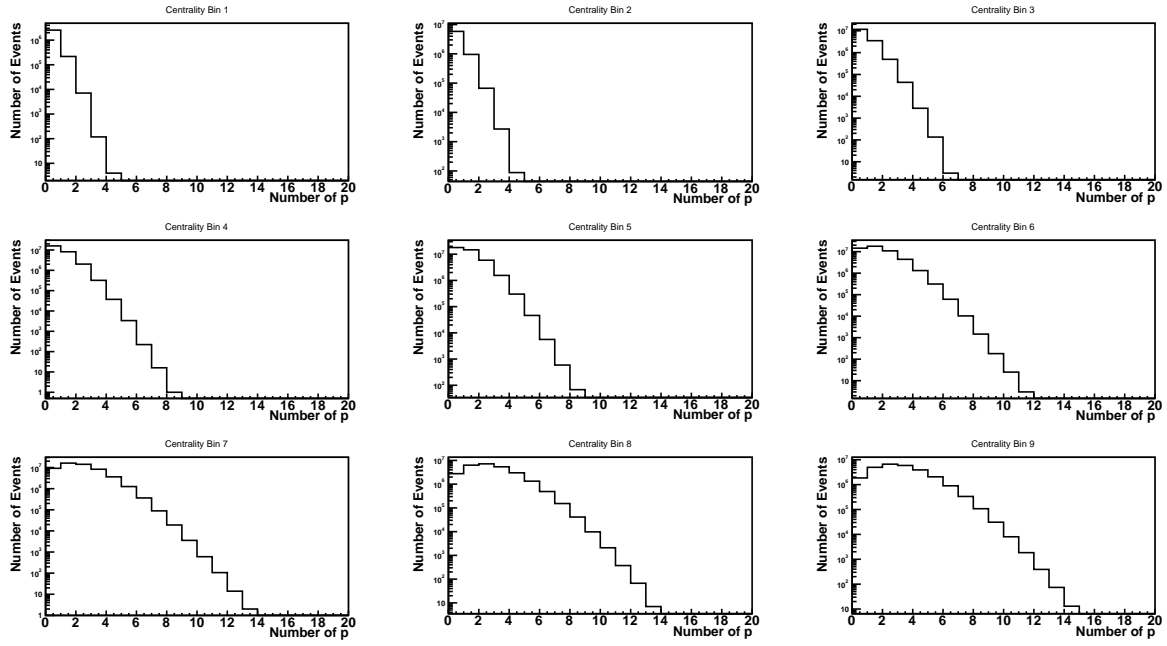
(a) Distribution of  $\Lambda$  Multiplicity



(b) Distribution of  $\bar{\Lambda}$  Multiplicity



(c) Distribution of  $p$  Multiplicity



(d) Distribution of  $\bar{p}$  Multiplicity

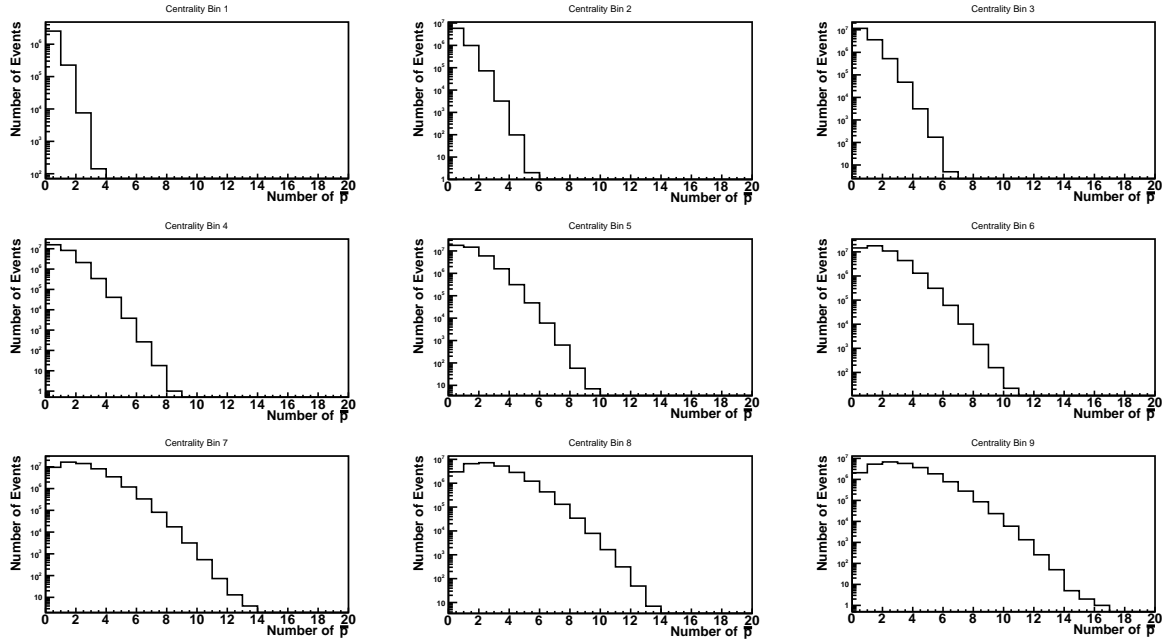
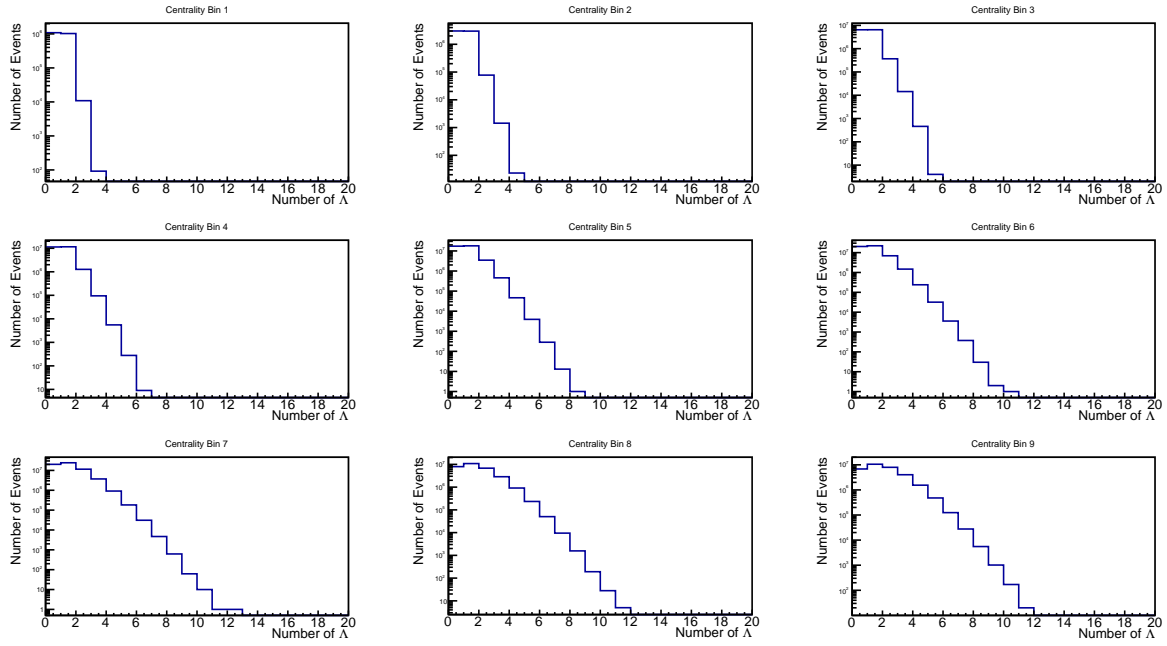
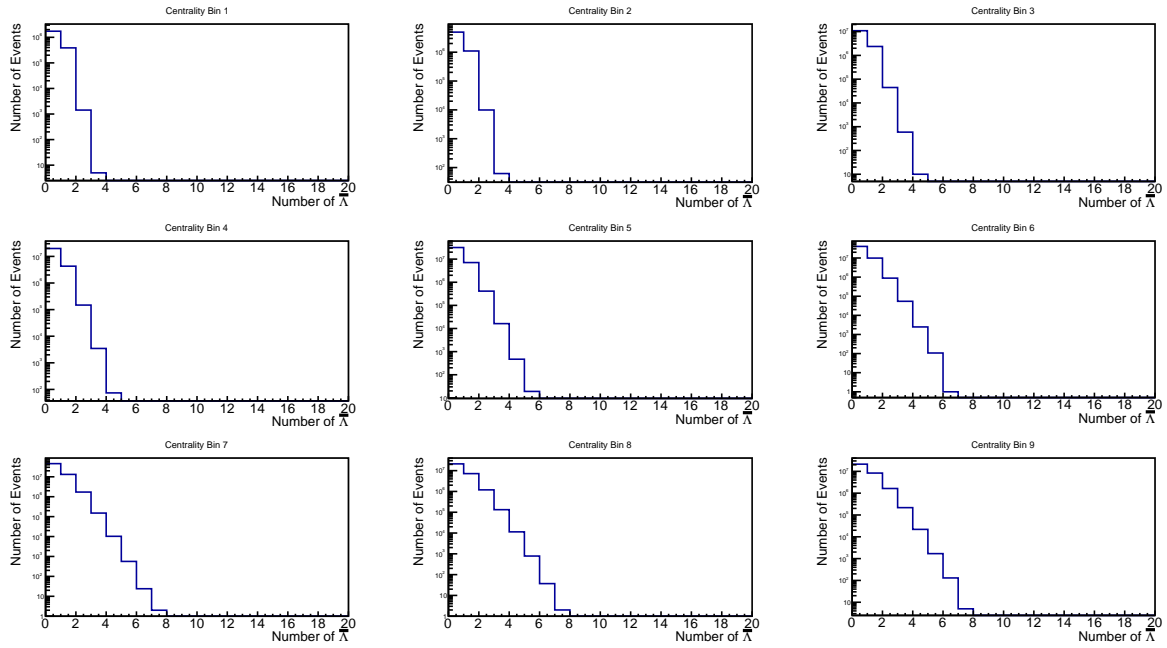


Figure 5.21: Distribution of  $\Lambda/p$  Multiplicities for Au+Au 19.6 GeV.

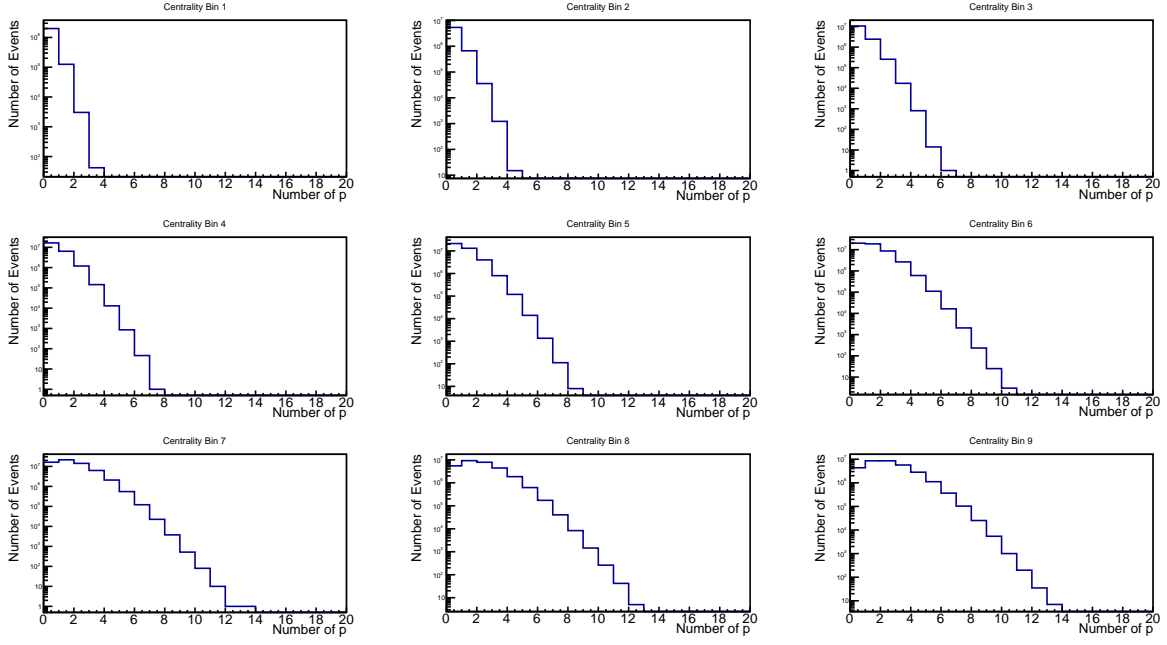
(a) Distribution of  $\Lambda$  Multiplicity



(b) Distribution of  $\bar{\Lambda}$  Multiplicity



(c) Distribution of  $p$  Multiplicity



(d) Distribution of  $\bar{p}$  Multiplicity

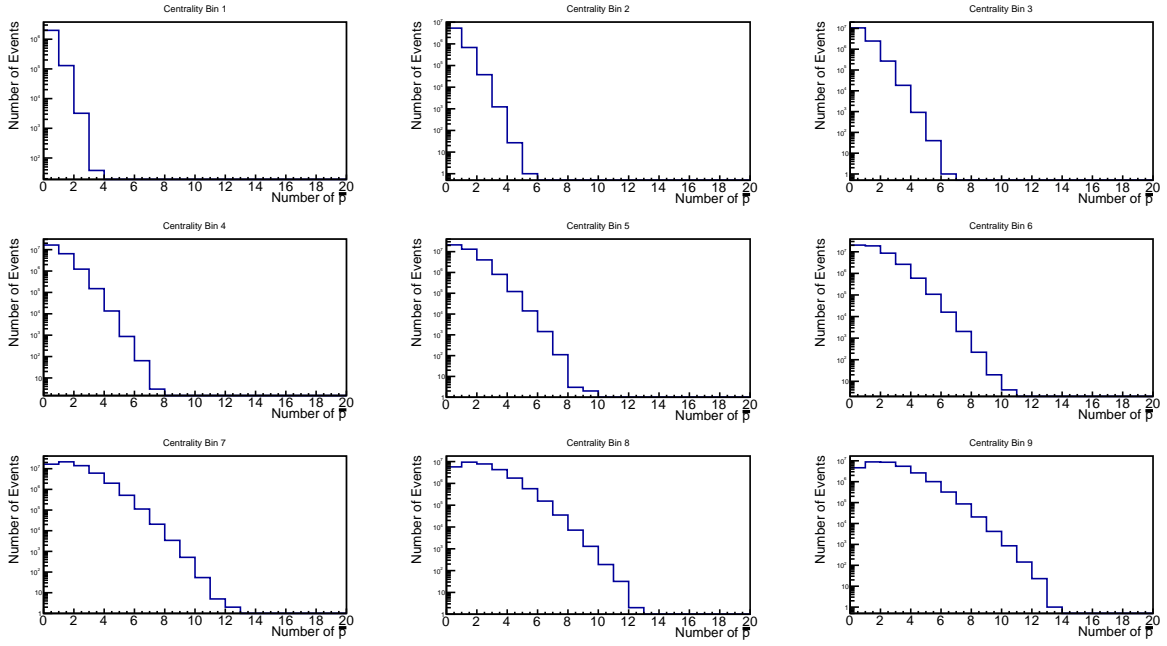


Figure 5.22: Distribution of  $\Lambda/p$  Multiplicities for Au+Au 27 GeV.

Therefore, it introduces serious uncertainties in constructing the event shape handler  $q_2^2$  as well as when extrapolating to zero elliptic flow of the POI. In order to address this, we keep

in mind that we need to, as mentioned above, for the sake of taking into account potential longitudinal flow-plane decorrelations, maintain the POI and particles used to construct the event shape handler to be within the same rapidity region, in a similar kinematics region. Thus we have chosen to use pions to model the event shape for the POIs in this study.

#### 5.4.2 4 Approaches of ESE

The idea behind constructing  $q_2$  with POI was that hopefully it, as well as  $v_2$ , would reflect the initial geometry of the collision system. However, upon further examination, we realized that the anisotropy of pairs of particles might be more relevant to the background in our correlators, because these observables are correlations of pairs of particles and not quantities based on single particles. Also, the background caused by local charge conservations would mean that the primordial particles that contribute to the background would really contribute as if they had hypothetical parent particles that they were decay products of.

Therefore, instead of simply relying on the single POI to construct  $q_2$  and  $v_2$ , we also construct them based on pairs of them as follows:

$$v_{2,\text{pair}} = \langle \cos(2\varphi^{\text{pair}} - 2\Psi_{\text{RP}}) \rangle, \quad (5.42)$$

$$q_{2,\text{pair}}^2 = \frac{(\sum_{i=1}^{N_{\text{pair}}} \sin 2\varphi_i^{\text{pair}})^2 + (\sum_{i=1}^{N_{\text{pair}}} \cos 2\varphi_i^{\text{pair}})^2}{N_{\text{pair}}(1 + N_{\text{pair}}v_{2,\text{pair}}^2\{2\})}, \quad (5.43)$$

where  $\varphi^{\text{pair}}$  is the azimuthal of the pairs of POI, which originate from the sum of their momentum.

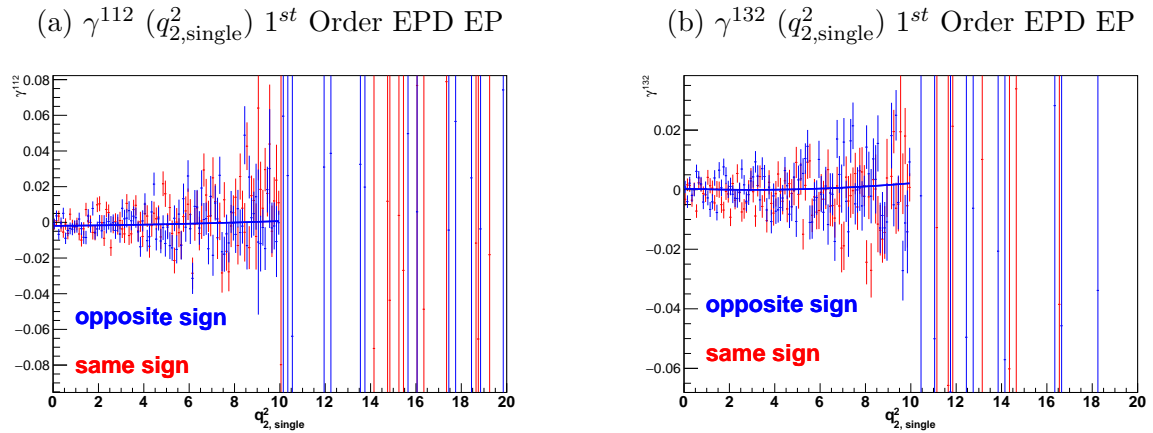
In our paper [151], we performed model studies with a toy model [152] based on Pythia6 [153], as well as the EBE-AVFD model [154, 155, 156] that has both the dynamical CME transport for light quarks, and the capability to effectively handle background mechanisms like flowing resonances, and TMC and LCC effects that were described earlier. These model studies were performed based on the decay of  $\rho$  mesons into pairs of pions, and they showed the varying levels of effectiveness of these recipes. This gives reason to look into the different recipes for this analysis as well, and see if their performances would differ based on the different combinations of particles used for the construction of the event shape handler and elliptic flow observable.

With the full exploration of the event shape handlers used for ESE, now we are ready to discuss the procedure of the analysis using ESE. First, we group all our events according to the event shape handler and compute  $\Delta\gamma^{112}$  and  $\Delta\gamma^{132}$  for all the  $\Lambda$ - $p$  pairs, as well as the elliptic flow variable for all for pion pairs, for each of the groups of events. Then we use that information to reveal the dependence of  $\Delta\gamma^{112}$  on the elliptic flow computed, and project it to the zero-flow limit. This will be done for all four combinations of single and pair POI constructed  $q_2^2$  and  $v_2$ .

### 5.4.3 Methodology

In this section, we will outline the key steps to implementing the ESE approach to reduce the background for this analysis. All the figures used to depict the methodology used in this section are from the 19.6 GeV Au+Au collision, Centrality Bin 5, 30-40%.

First, we bin the correlators of interest,  $\gamma^{112}$  and  $\gamma^{132}$ , by the event shape handler:



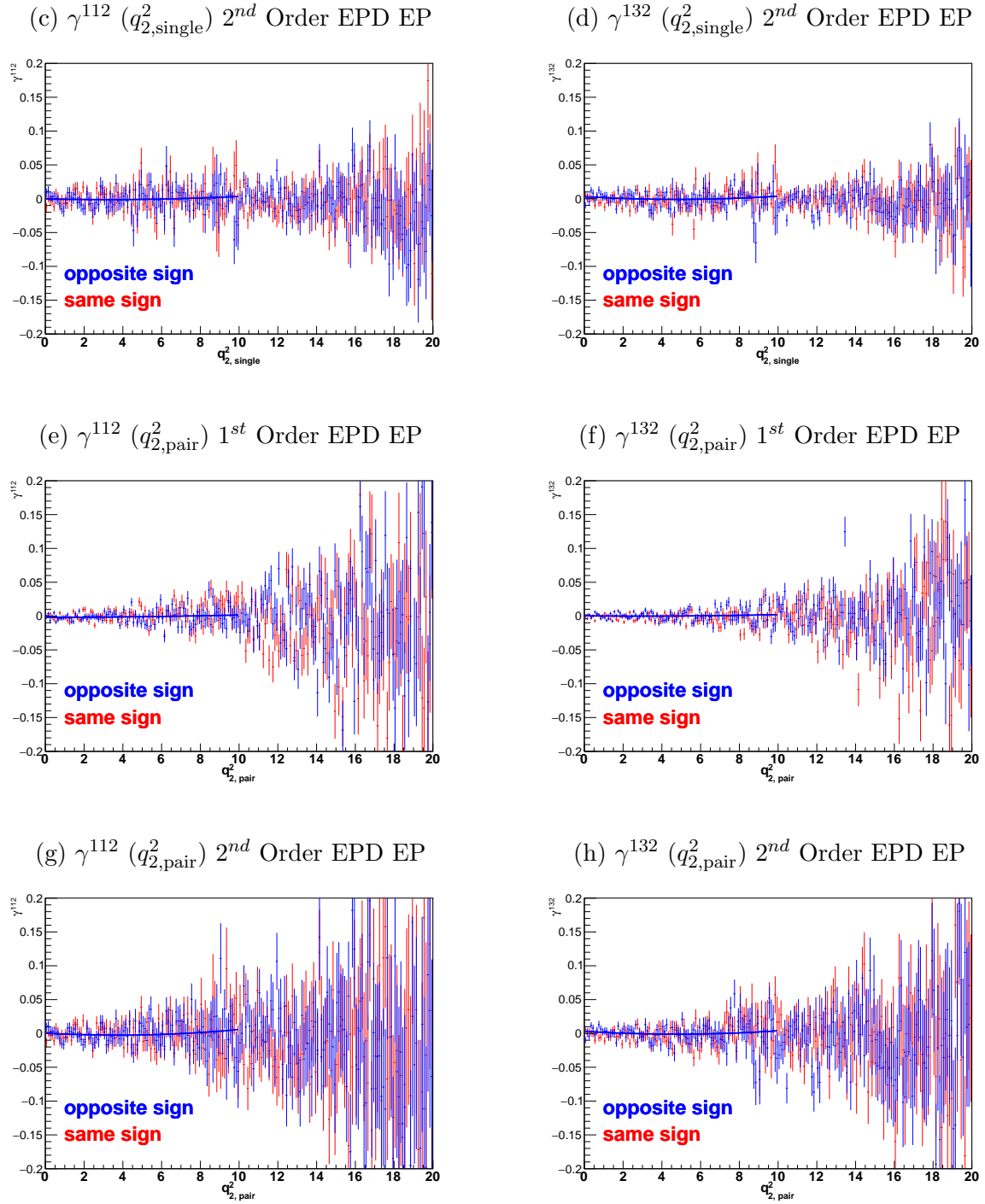
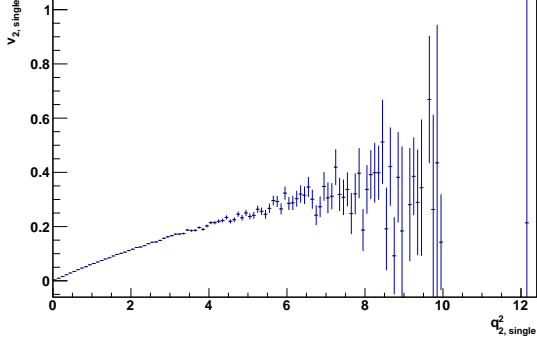


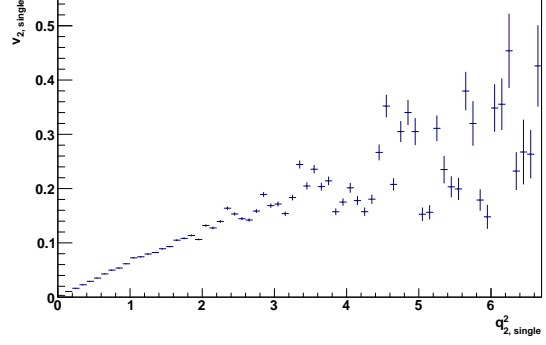
Figure 5.23: Correlators of interest,  $\gamma^{112}$  and  $\gamma^{132}$ , binned by the event shape handlers used to control the flow background.

Then, we bin the elliptic flow by the event shape handler as well:

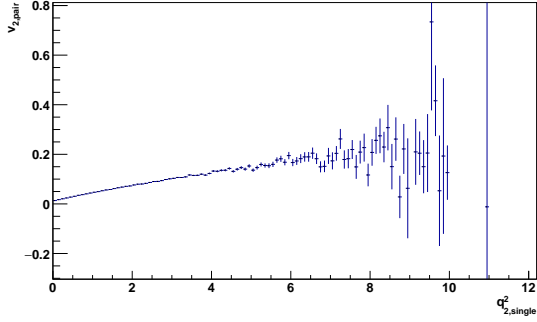
(a)  $v_{2,\text{single}}(q_{2,\text{single}}^2)$  1<sup>st</sup> Order EPD EP



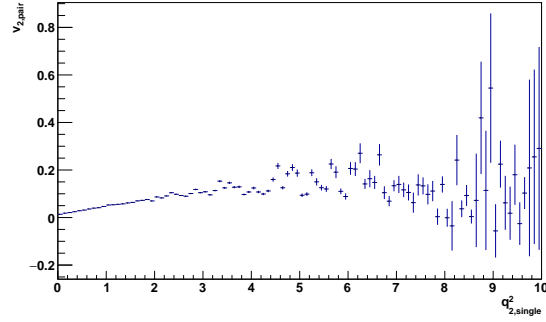
(b)  $v_{2,\text{single}}(q_{2,\text{single}}^2)$  2<sup>nd</sup> Order EPD EP



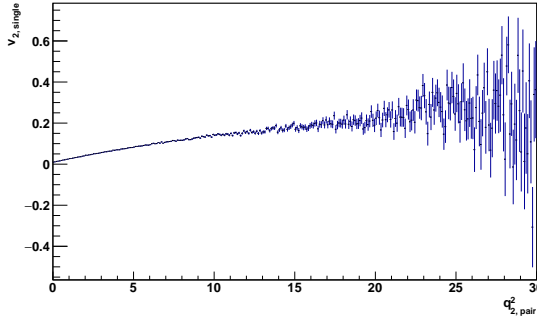
(c)  $v_{2,\text{pair}}(q_{2,\text{single}}^2)$  1<sup>st</sup> Order EPD EP



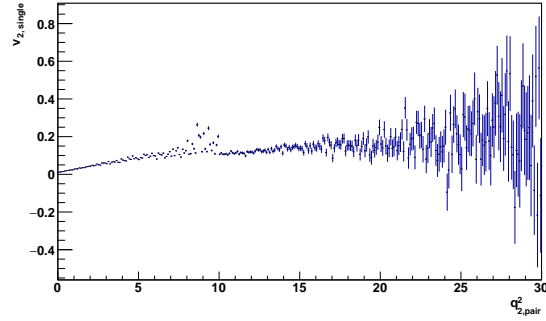
(d)  $v_{2,\text{pair}}(q_{2,\text{single}}^2)$  2<sup>nd</sup> Order EPD EP



(e)  $v_{2,\text{single}}(q_{2,\text{pair}}^2)$  1<sup>st</sup> Order EPD EP



(f)  $v_{2,\text{single}}(q_{2,\text{pair}}^2)$  2<sup>nd</sup> Order EPD EP



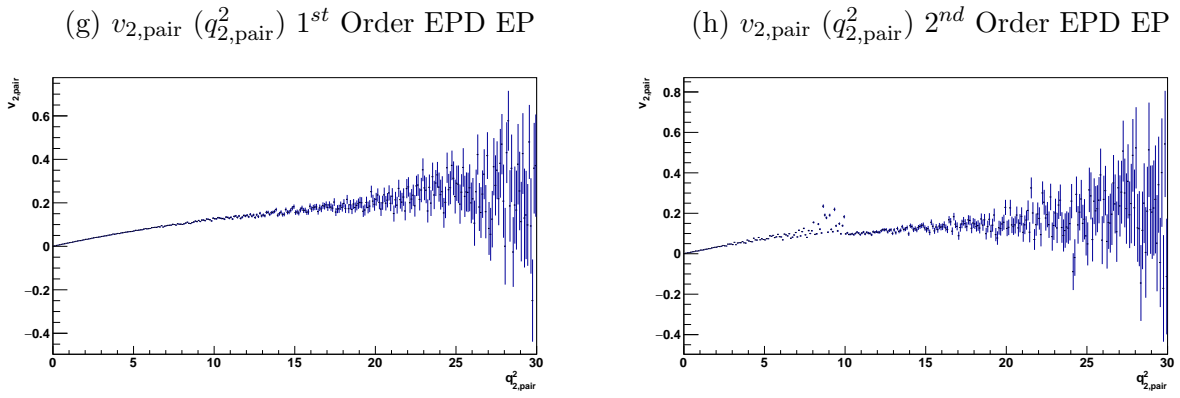


Figure 5.24:  $v_2$  binned by the event shape handlers.

With these values, we then correct them by the resolution of the 1<sup>st</sup> and 2<sup>nd</sup> order EPD event planes, which are also binned by the event shape handlers:

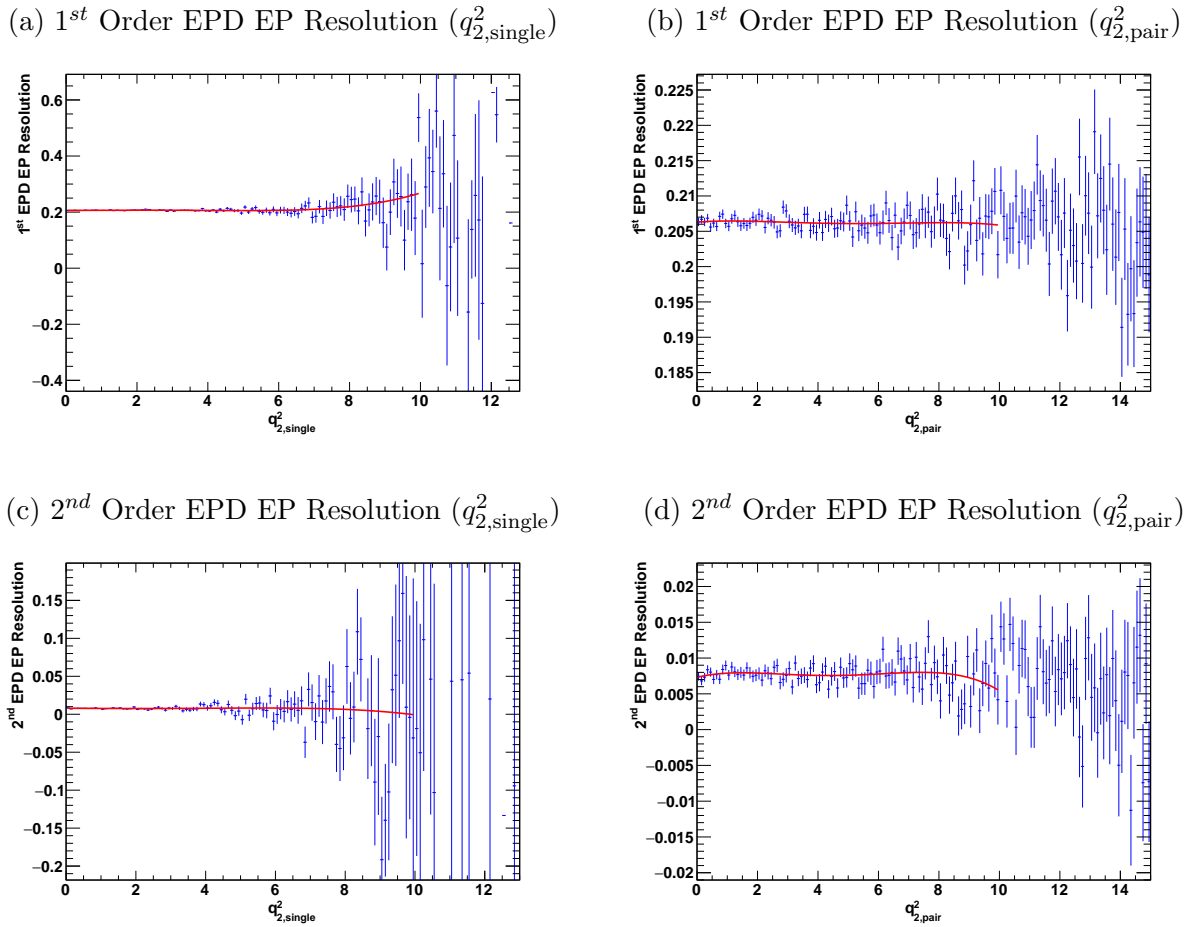
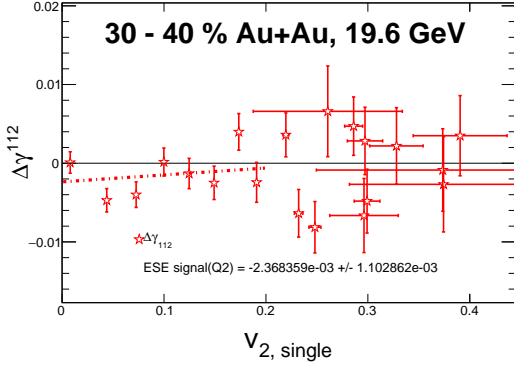


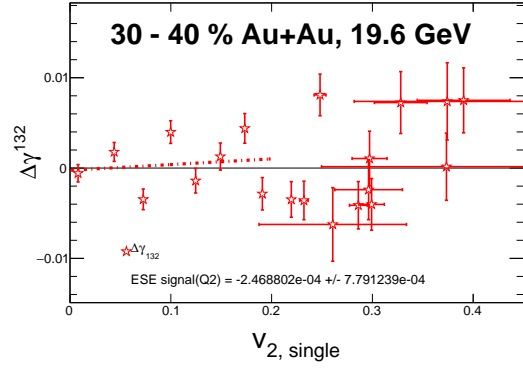
Figure 5.25: Event Plane resolutions binned by event shape handler. The red line depicts the range of the event shape handler considered in the ESE approach, but the fit values were not used. The specific binned values were used in the event plane resolution correction.

After correcting by the resolution, we find the relationship between the correlators of interest on the elliptic flow observables based on the event shape handlers:

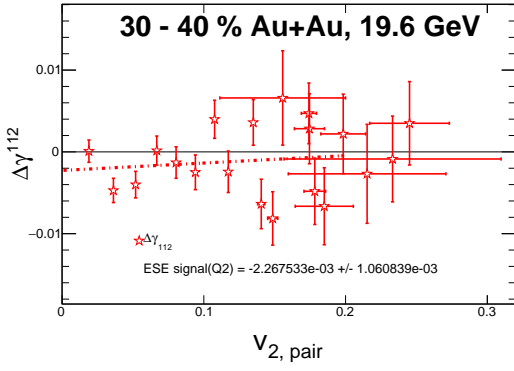
(a)  $\Delta\gamma^{112}\{v_{2,\text{single}}, q_{2,\text{single}}^2\}$  1<sup>st</sup> Order EPD EP



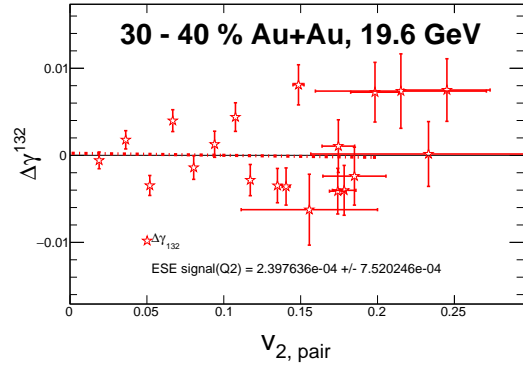
(b)  $\Delta\gamma^{132}\{v_{2,\text{single}}, q_{2,\text{single}}^2\}$  1<sup>st</sup> Order EPD EP



(c)  $\Delta\gamma^{112}\{v_{2,\text{pair}}, q_{2,\text{single}}^2\}$  1<sup>st</sup> Order EPD EP



(d)  $\Delta\gamma^{132}\{v_{2,\text{pair}}, q_{2,\text{single}}^2\}$  1<sup>st</sup> Order EPD EP



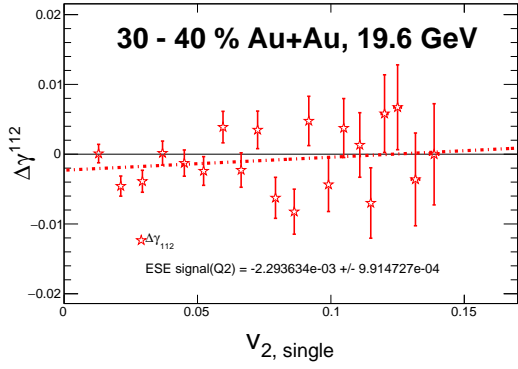
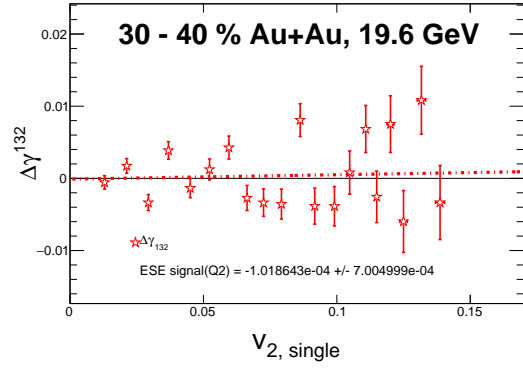
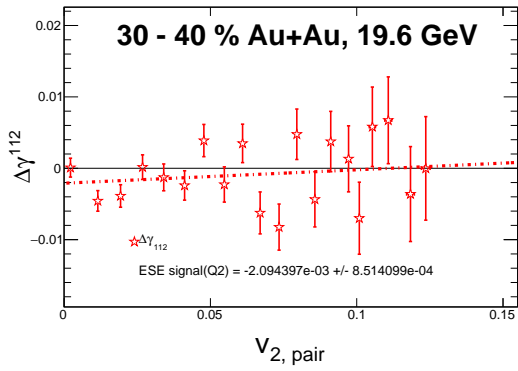
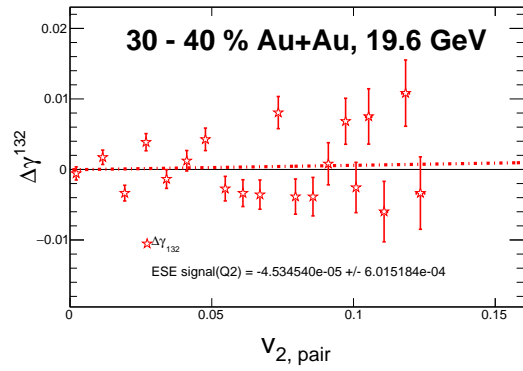
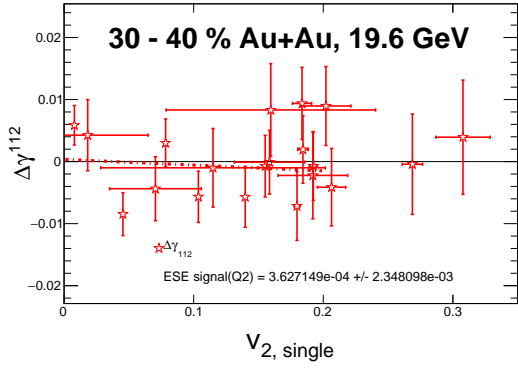
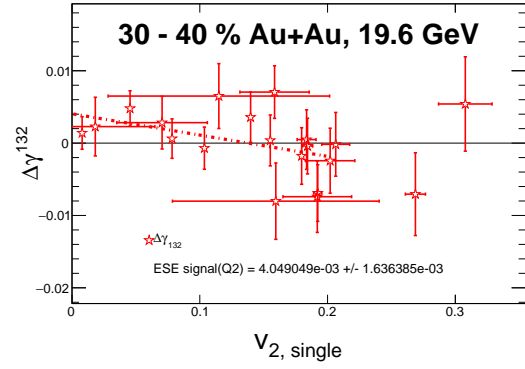
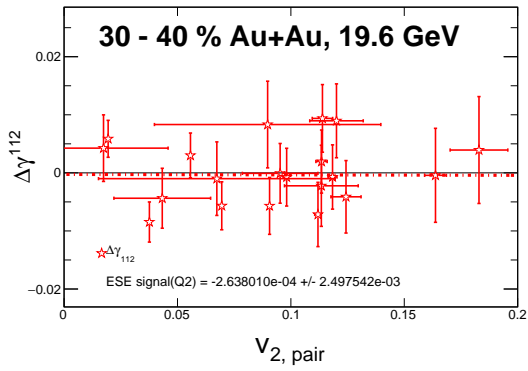
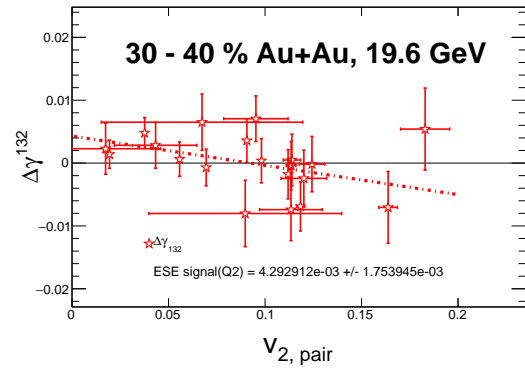
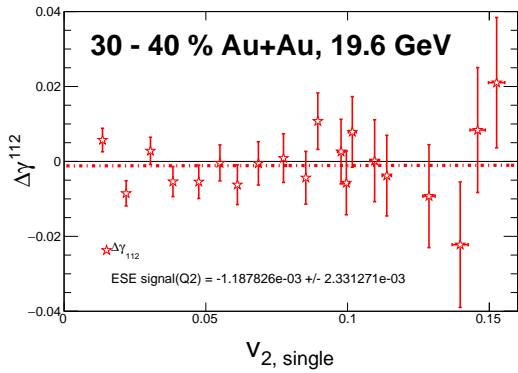
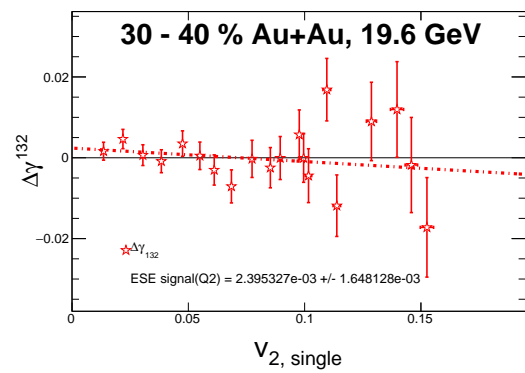
(e)  $\Delta\gamma^{112}\{v_{2,\text{single}}, q_{2,\text{pair}}^2\}$  1<sup>st</sup> Order EPD EP(f)  $\Delta\gamma^{132}\{v_{2,\text{single}}, q_{2,\text{pair}}^2\}$  1<sup>st</sup> Order EPD EP(g)  $\Delta\gamma^{112}\{v_{2,\text{pair}}, q_{2,\text{pair}}^2\}$  1<sup>st</sup> Order EPD EP(h)  $\Delta\gamma^{132}\{v_{2,\text{pair}}, q_{2,\text{pair}}^2\}$  1<sup>st</sup> Order EPD EP

Figure 5.26:  $\Delta\gamma^{112}$  and  $\gamma^{132}$  event shape selection method for the 4 recipes, projecting to zero flow, based on the first order EPD event plane.

(a)  $\Delta\gamma^{112}\{v_{2,\text{single}}, q_{2,\text{single}}^2\}$  2<sup>nd</sup> Order EPD EP(b)  $\Delta\gamma^{132}\{v_{2,\text{single}}, q_{2,\text{single}}^2\}$  2<sup>nd</sup> Order EPD EP(c)  $\Delta\gamma^{112}\{v_{2,\text{pair}}, q_{2,\text{single}}^2\}$  2<sup>nd</sup> Order EPD EP(d)  $\Delta\gamma^{132}\{v_{2,\text{pair}}, q_{2,\text{single}}^2\}$  2<sup>nd</sup> Order EPD EP(e)  $\Delta\gamma^{112}\{v_{2,\text{single}}, q_{2,\text{pair}}^2\}$  2<sup>nd</sup> Order EPD EP(f)  $\Delta\gamma^{132}\{v_{2,\text{single}}, q_{2,\text{pair}}^2\}$  2<sup>nd</sup> Order EPD EP

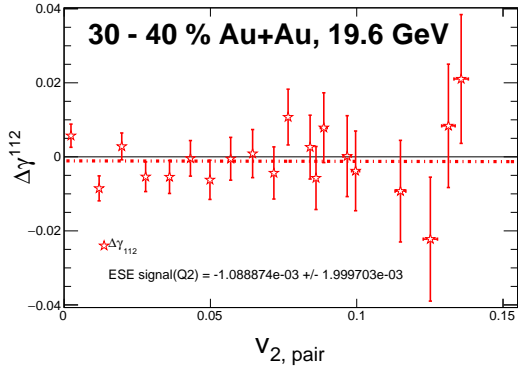
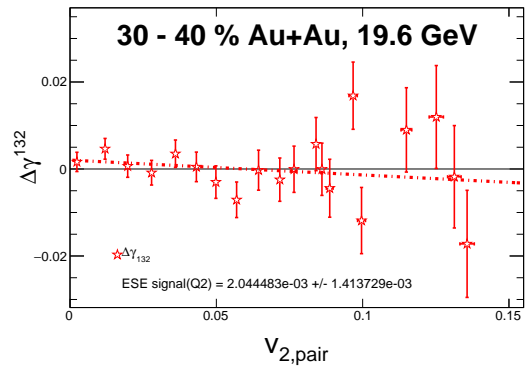
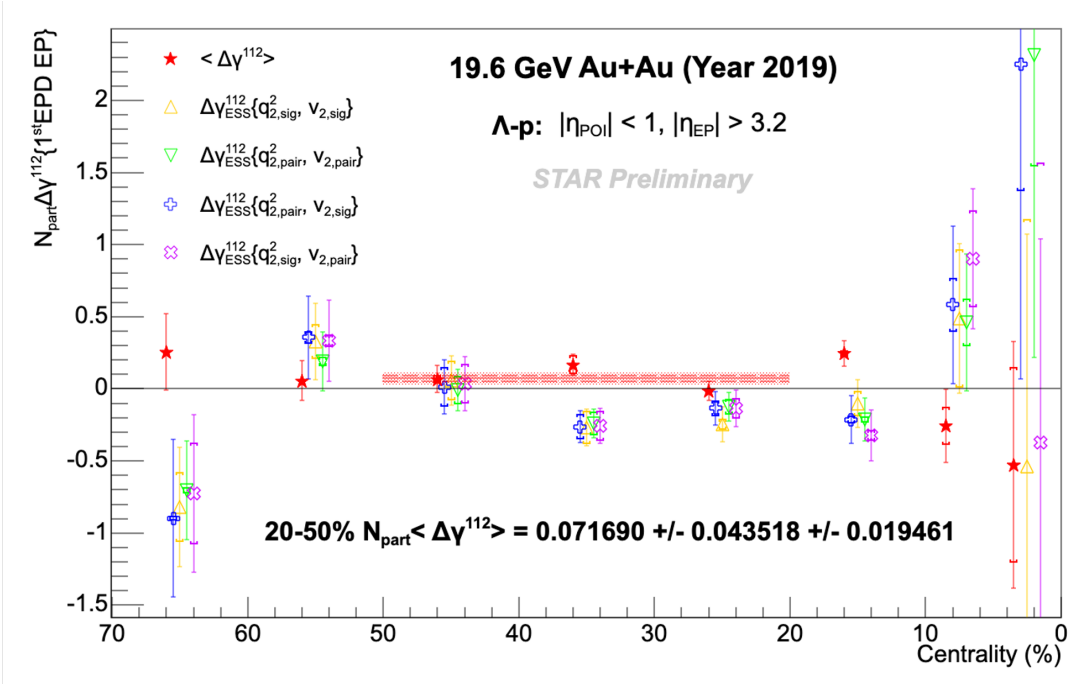
(g)  $\Delta\gamma^{112}\{v_{2,\text{pair}}, q_{2,\text{pair}}^2\}$  2<sup>nd</sup> Order EPD EP(h)  $\Delta\gamma^{132}\{v_{2,\text{pair}}, q_{2,\text{pair}}^2\}$  2<sup>nd</sup> Order EPD EP

Figure 5.27:  $\Delta\gamma^{112}$  and  $\Delta\gamma^{132}$  event shape selection method for the 4 recipes, projecting to zero flow, based on the second order EPD event plane.

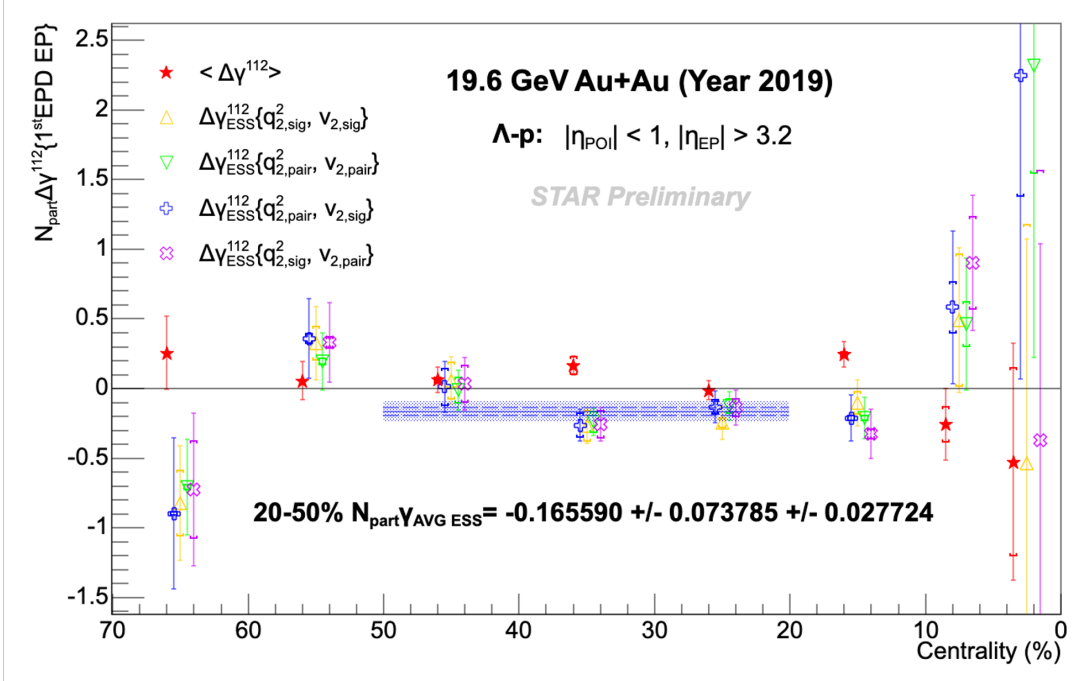
With the event shape selection method, we attempted to suppress the flow background to our CVE measurements. The next section will discuss those results.

## 5.5 Summary of Results for the Search for the CVE

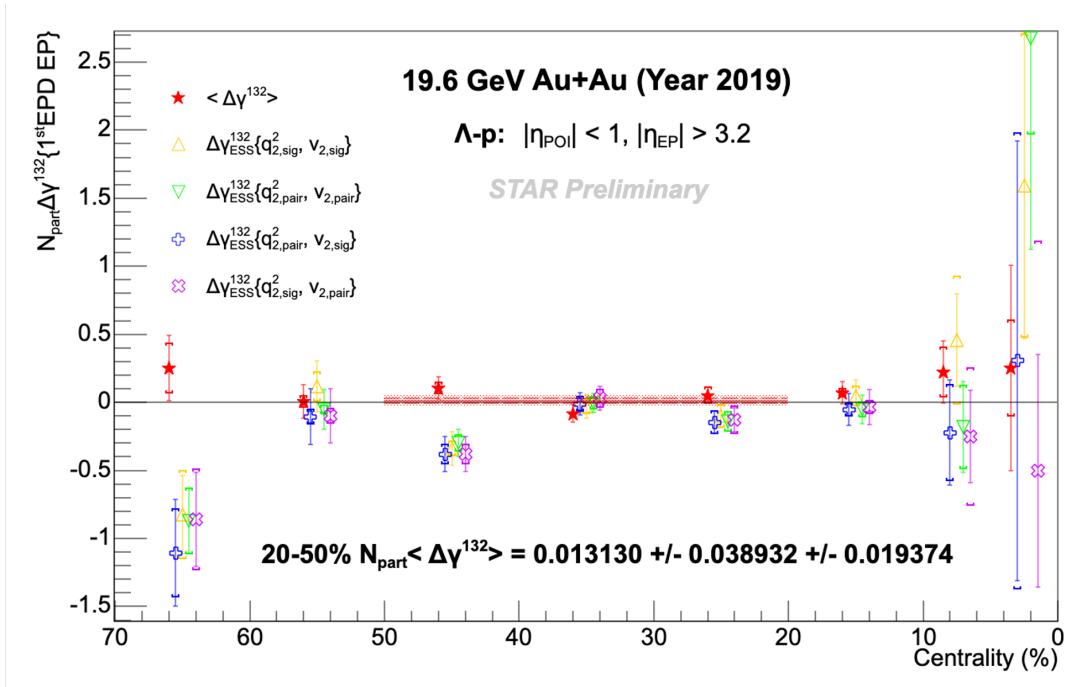
In the following figures, the final results of this analysis will be portrayed. They will include figures of the  $\Delta\gamma^{112}$  and  $\Delta\gamma^{132}$ , both the ensemble average and the 4 recipes of event shape selection, as a function of Centrality, for both first and second order EPD event planes, for both data sets of interest. There is also a fit for the results at Centrality 20-50%, which will be used as our final result for the search of the CVE.



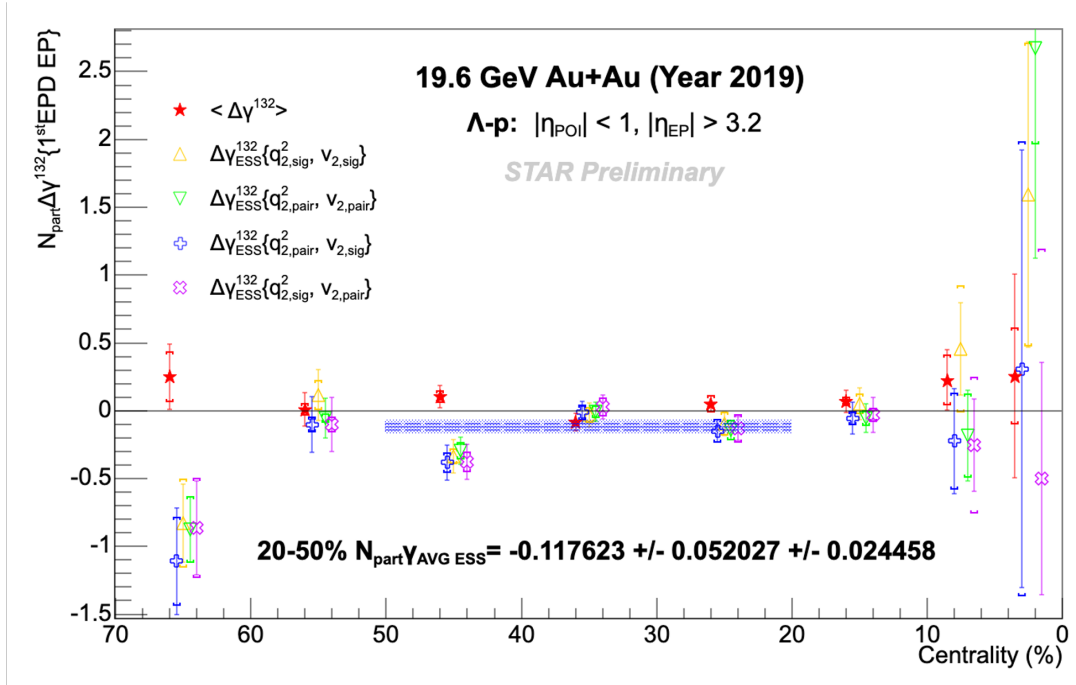
(a)  $\Delta\gamma^{112}$  with 1<sup>st</sup> Order EPD EP with fit for ensemble results.



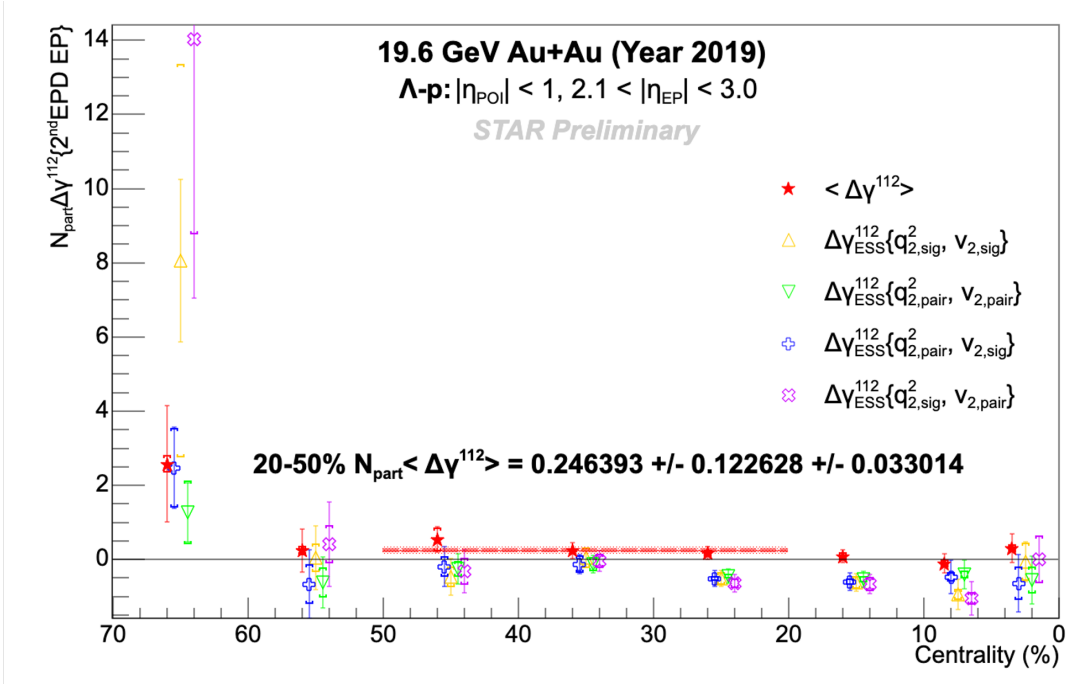
(b)  $\Delta\gamma^{112}$  with 1<sup>st</sup> Order EPD EP with fit for ESS results.



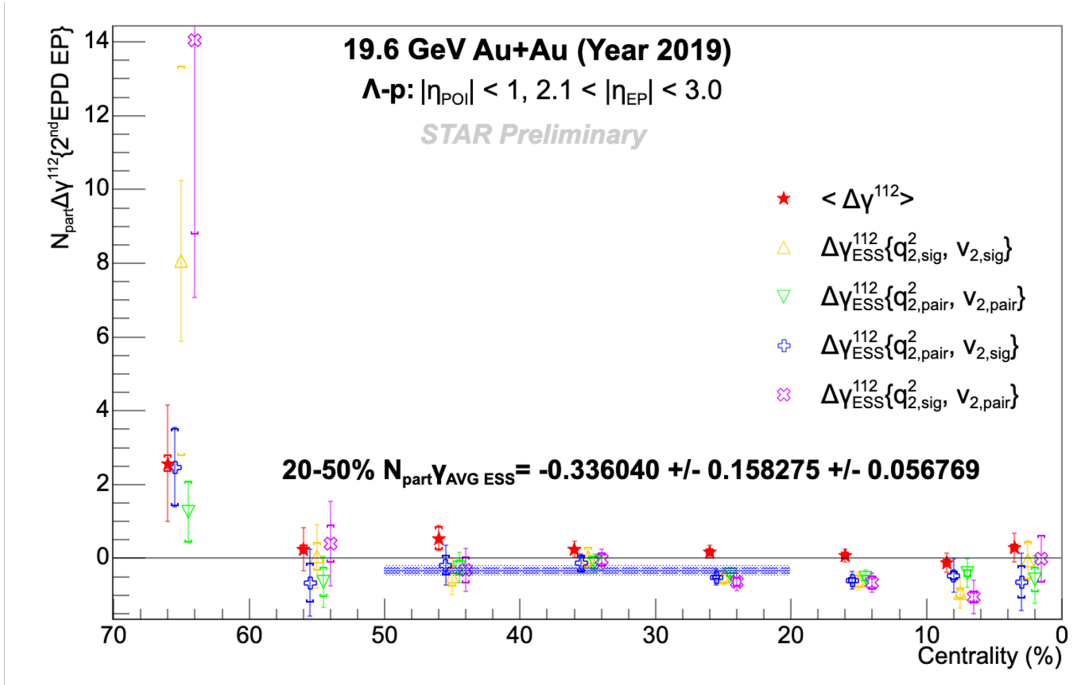
(c)  $\Delta\gamma^{132}$  with 1<sup>st</sup> Order EPD EP with fit for ensemble results.



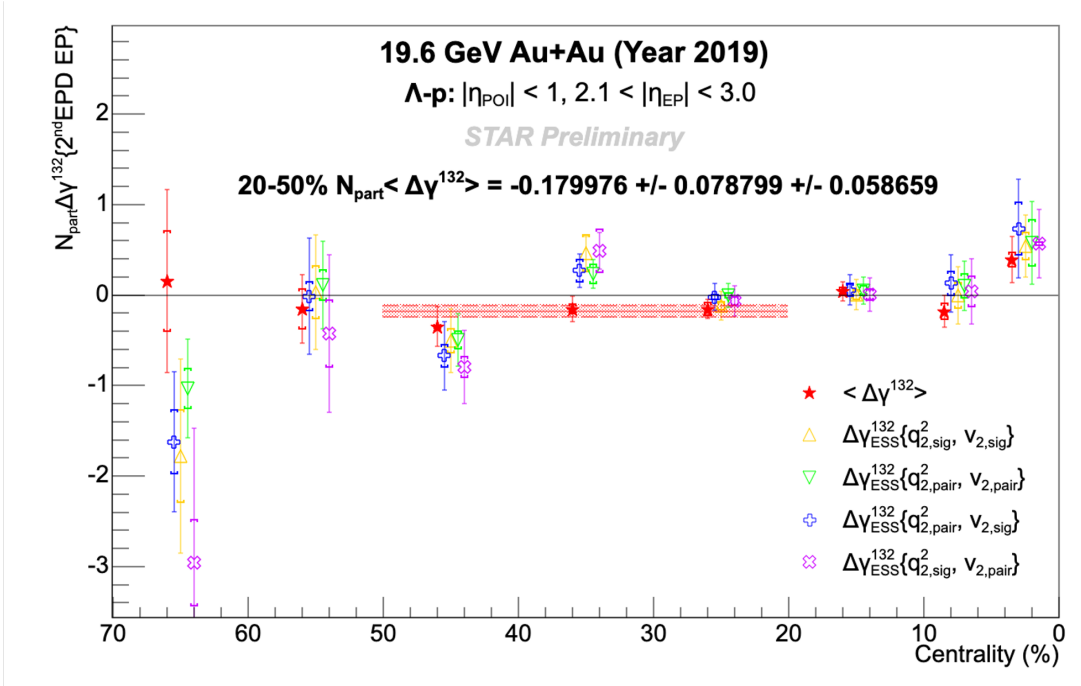
(d)  $\Delta\gamma^{132}$  with 1<sup>st</sup> Order EPD EP with fit for ESS results.



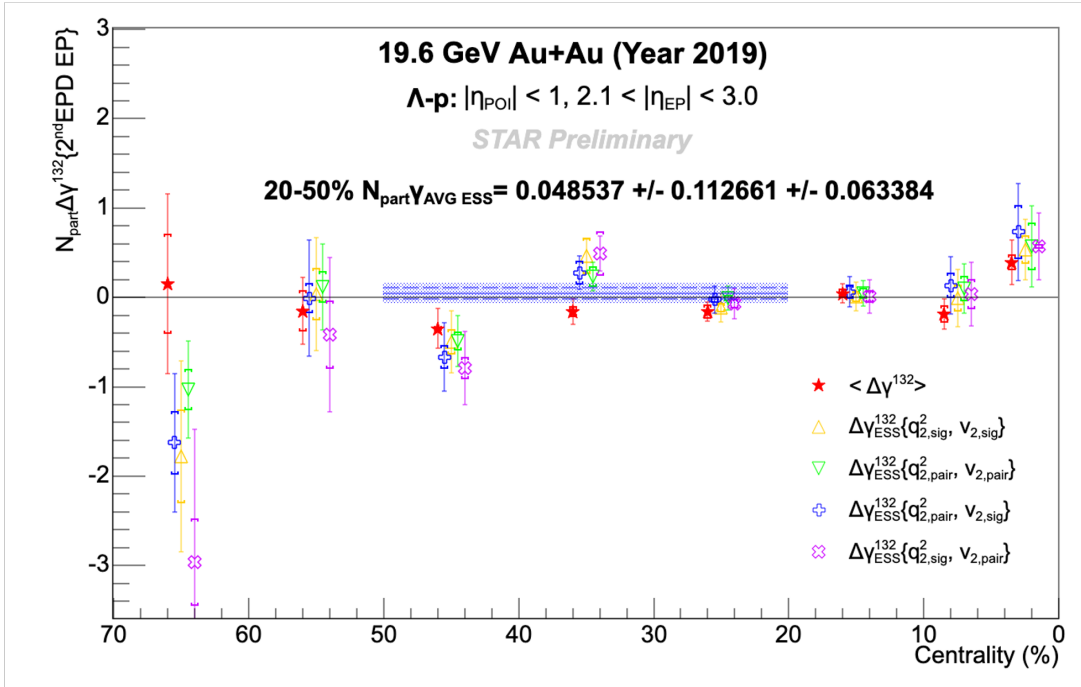
(e)  $\Delta\gamma^{112}$  with  $2^{\text{nd}}$  Order EPD EP with fit for ensemble results.



(f)  $\Delta\gamma^{112}$  with  $2^{\text{nd}}$  Order EPD EP with fit for ESS results.

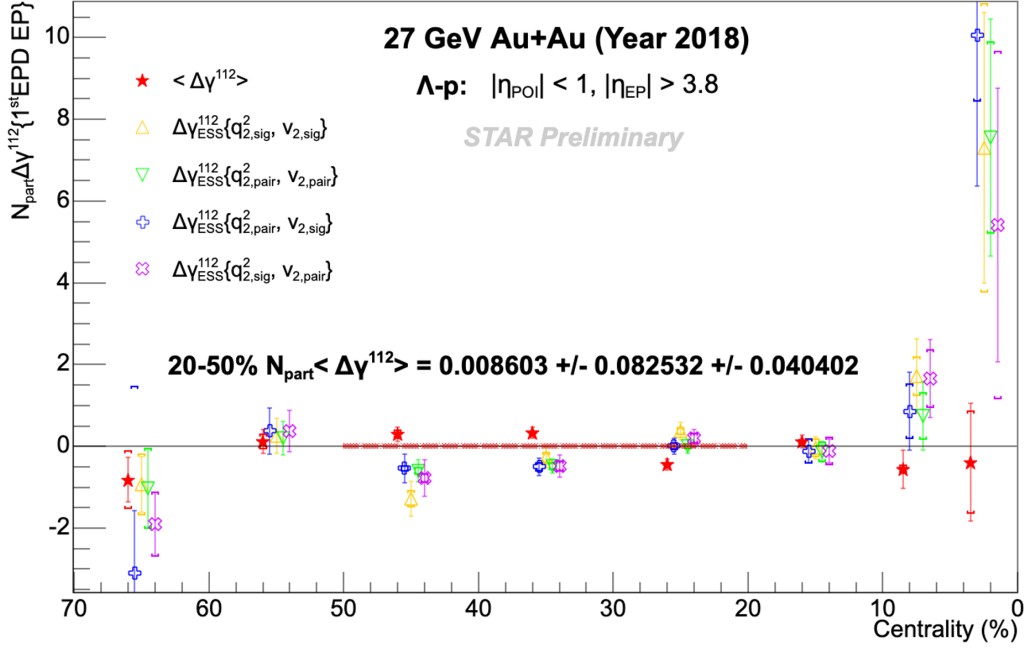


(g)  $\Delta\gamma^{132}$  with  $2^{\text{nd}}$  Order EPD EP with fit for ensemble results.

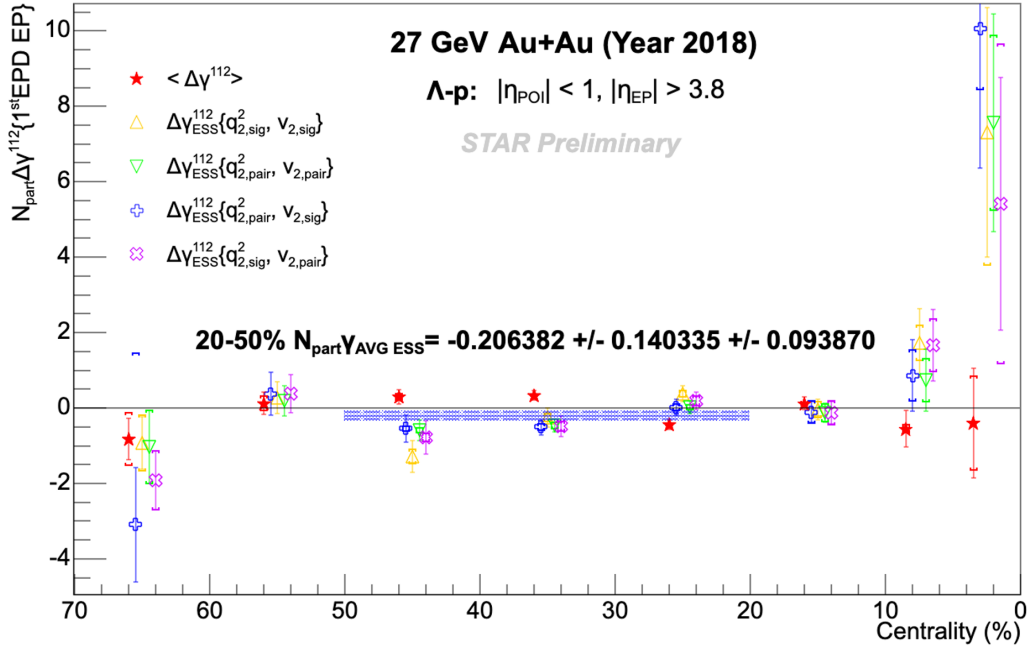


(h)  $\Delta\gamma^{132}$  with  $2^{\text{nd}}$  Order EPD EP with fit for ESS results.

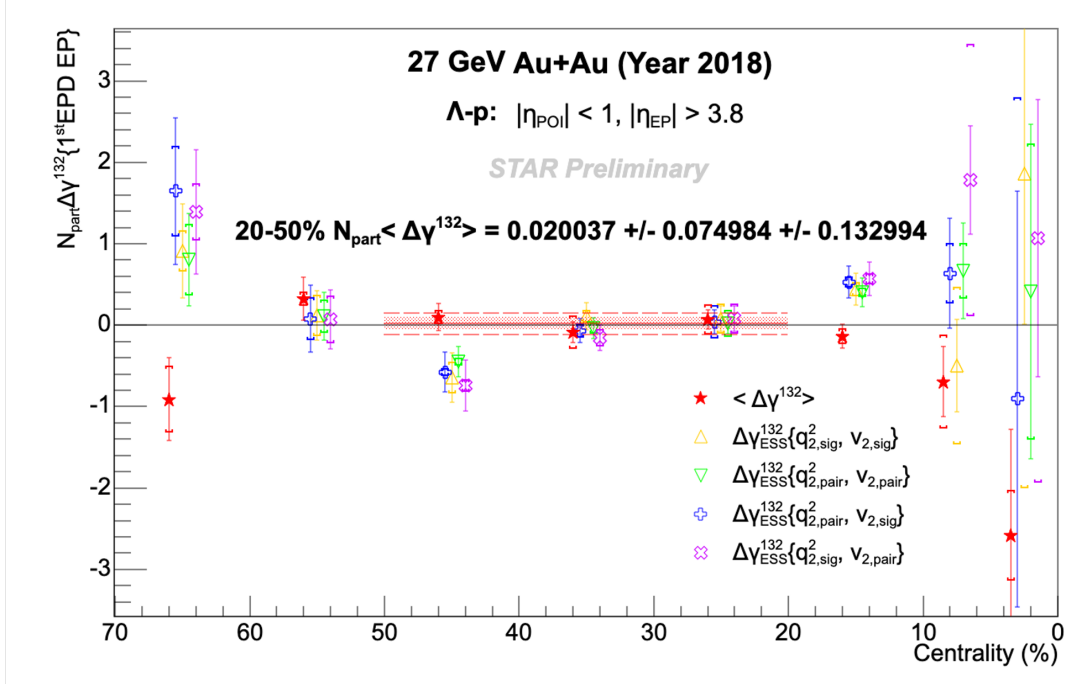
Figure 5.28:  $\Delta\gamma^{112}$  and  $\Delta\gamma^{132}$  for  $\Lambda$ -p Correlations for Au+Au 19.6 GeV collisions.



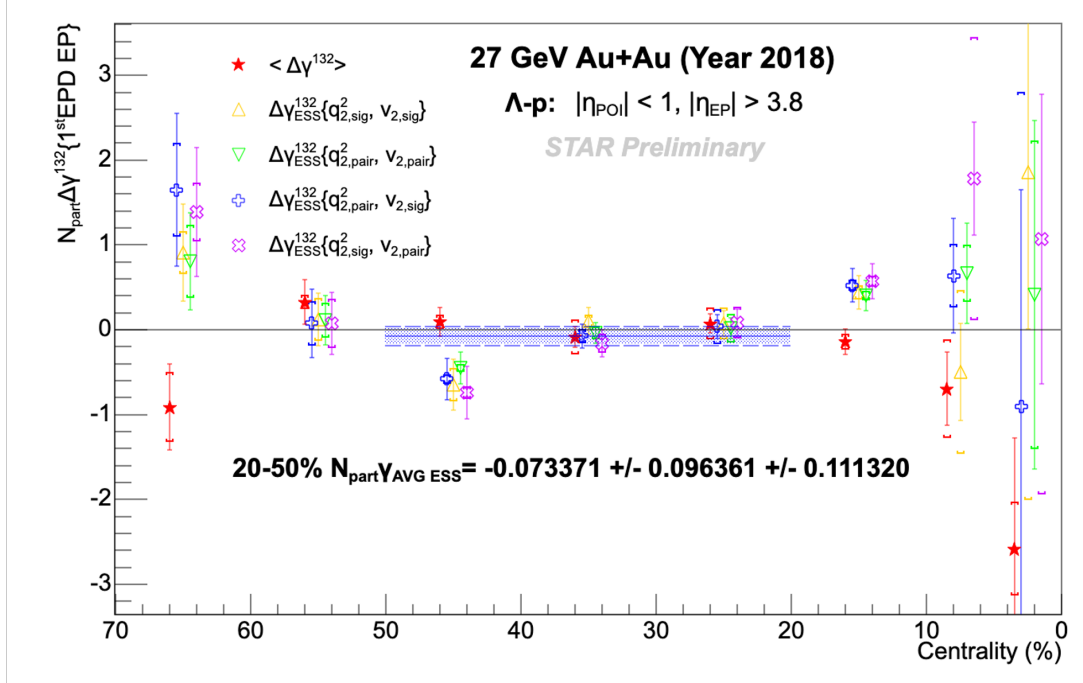
(a)  $\Delta \gamma^{112}$  with 1<sup>st</sup> Order EPD EP with fit for ensemble results.



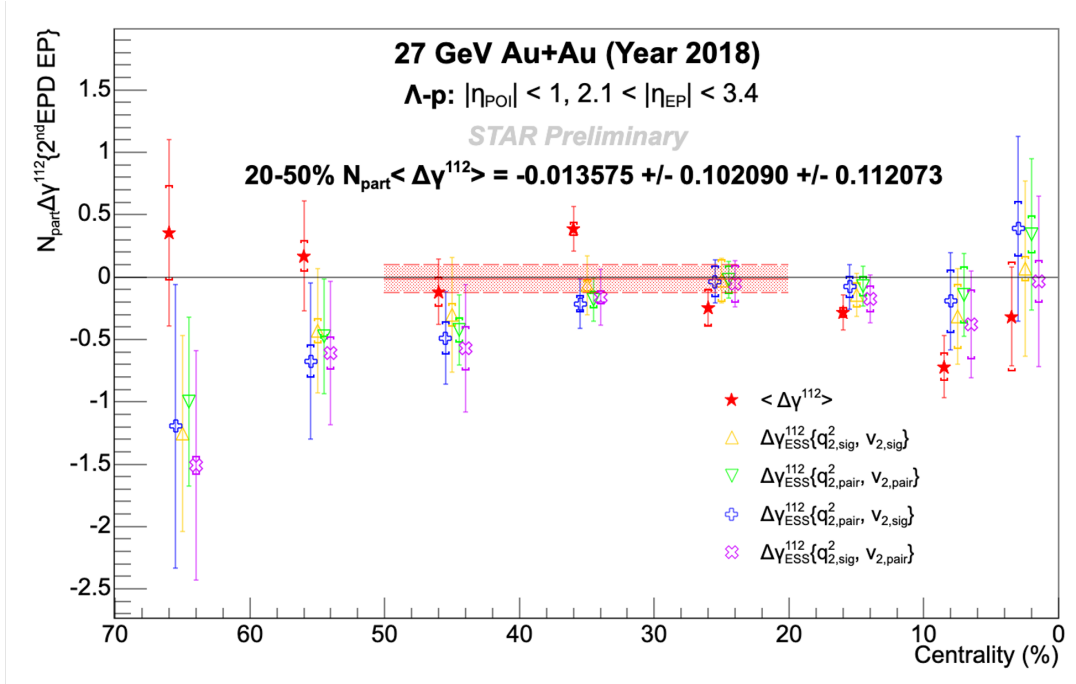
(b)  $\Delta \gamma^{112}$  with 1<sup>st</sup> Order EPD EP with fit for ESS results.



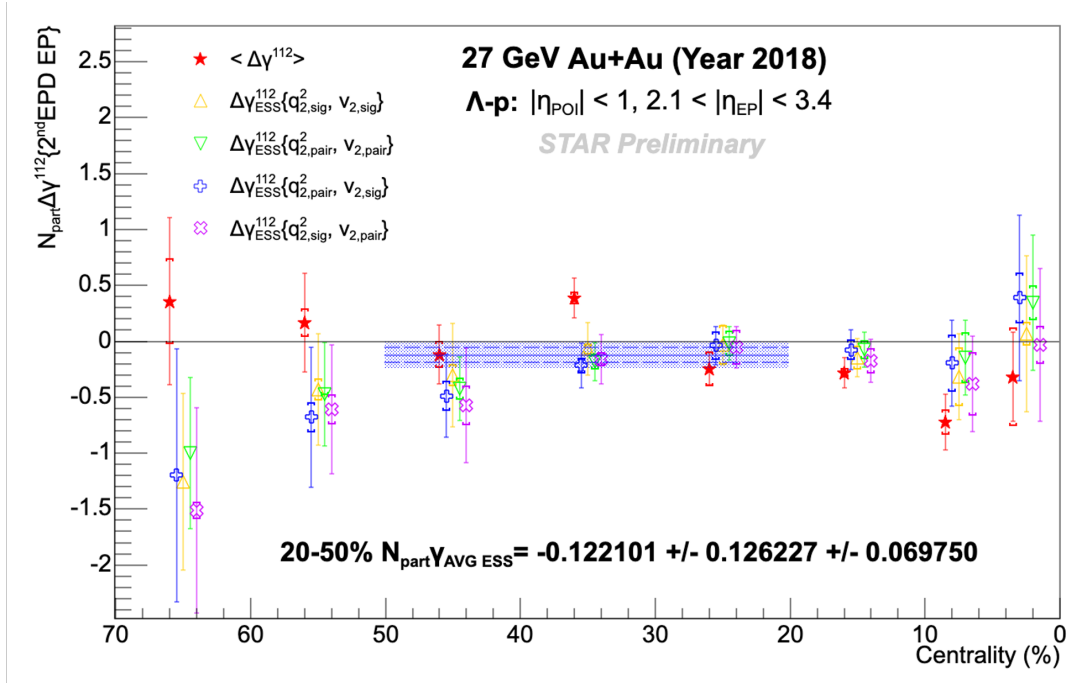
(c)  $\Delta\gamma^{132}$  with 1<sup>st</sup> Order EPD EP with fit for ensemble results.



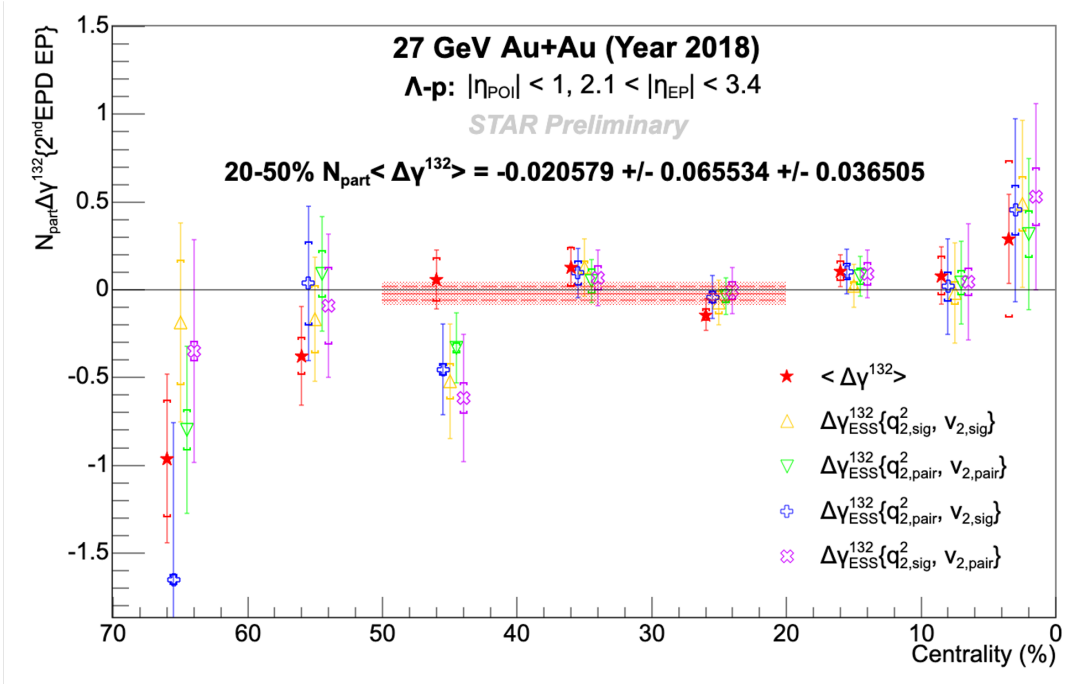
(d)  $\Delta\gamma^{132}$  with 1<sup>st</sup> Order EPD EP with fit for ESS results.



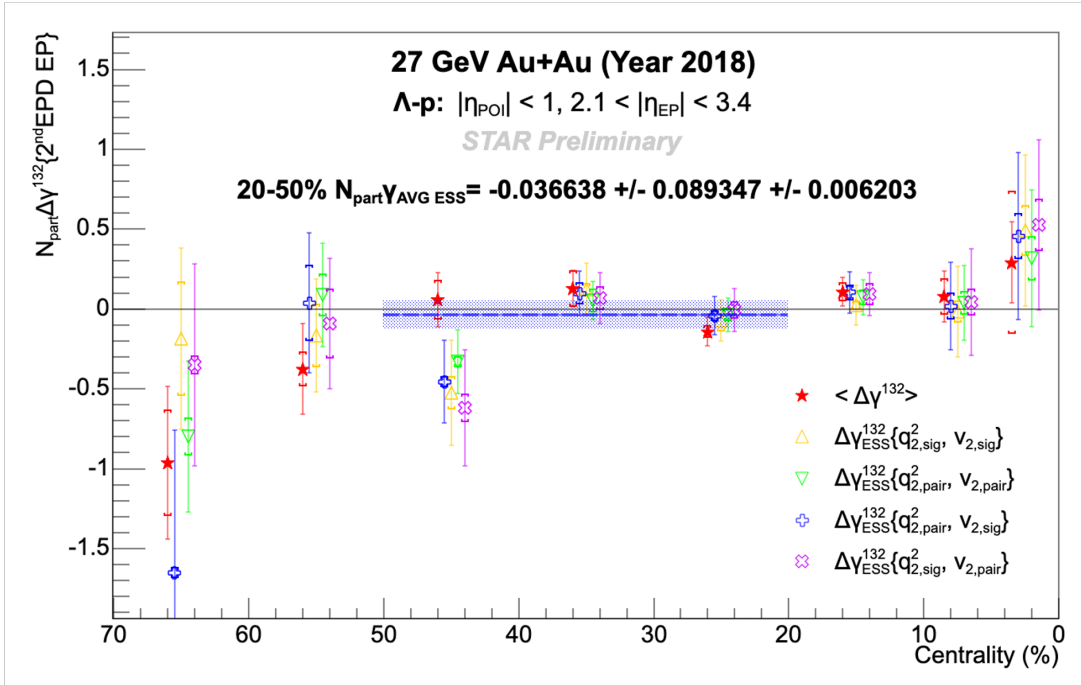
(e)  $\Delta\gamma^{112}$  with  $2^{\text{nd}}$  Order EPD EP with fit for ensemble results.



(f)  $\Delta\gamma^{112}$  with  $2^{\text{nd}}$  Order EPD EP with fit for ESS results.



(g)  $\Delta\gamma^{132}$  with  $2^{\text{nd}}$  Order EPD EP with fit for ensemble results.



(h)  $\Delta\gamma^{132}$  with  $2^{\text{nd}}$  Order EPD EP with fit for ESS results.

Figure 5.29:  $\Delta\gamma^{112}$  and  $\Delta\gamma^{132}$  for  $\Lambda$ -p Correlations for Au+Au 27 GeV collisions.

Summarizing all the results for the search of the CVE in the QGP, we get Figure 5.30, including the results for Centrality 20-50% for all the different combinations covered in this thesis, as well as Table 5.2, which summarizes the upper bound on the CVE signal that we've found in this analysis (computed as the central value  $+1.96 \times \sigma$ ):

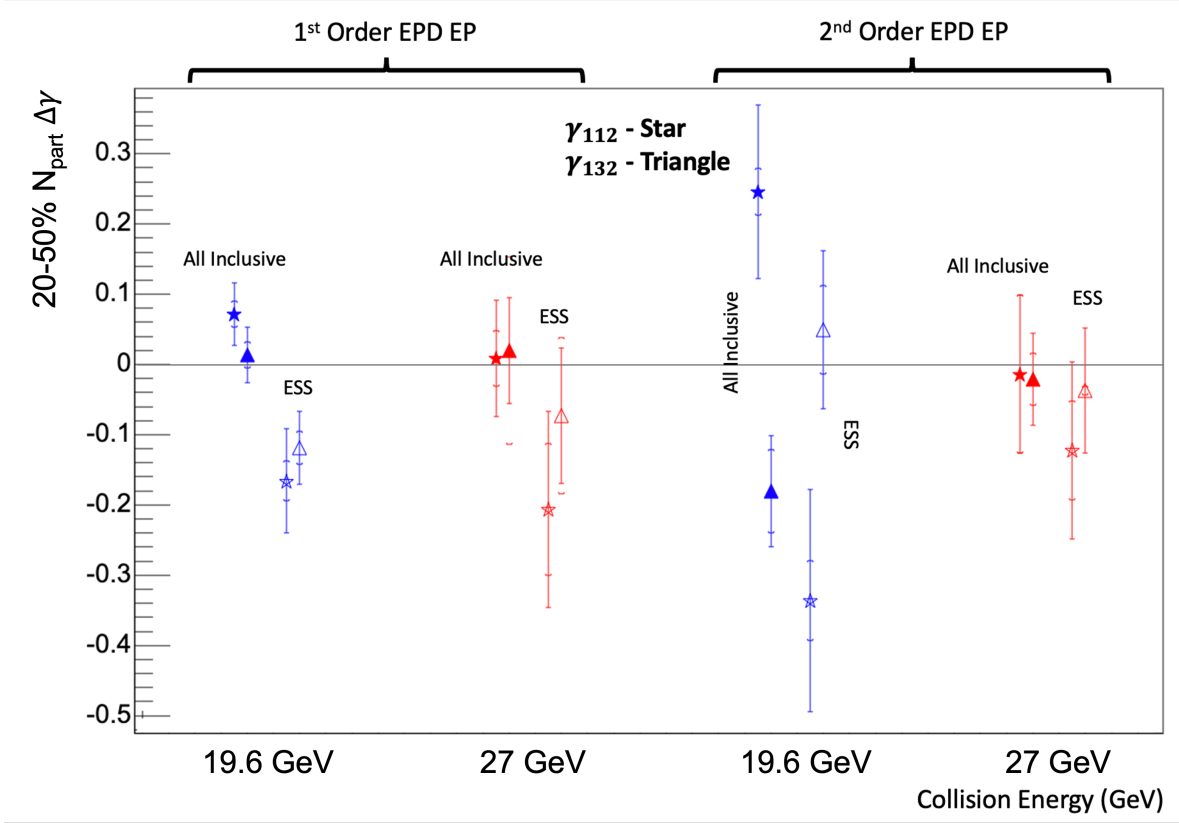


Figure 5.30: Summary results for  $\Delta\gamma^{112}$  and  $\Delta\gamma^{132}$  for  $\sqrt{s_{\text{NN}}} = 19.6$  GeV and 27 GeV for  $1^{\text{st}}$  and  $2^{\text{nd}}$  order EPD event plane.

Table 5.2: Upper Bound of CVE Signal As Represented By  $N_{\text{part}}\Delta\gamma^{112}$

Event Plane Option	19.6 GeV	27 GeV
$1^{\text{st}}$ Order EPD EP	0.195	0.551
$2^{\text{nd}}$ Order EPD EP	0.250	0.406

As we can see from these results, the all inclusive data points are mostly consistent with 0 results, whereas the event shape selection method seems to bring the values closer to negative

values. Despite that, it is probably the most reasonable conclusion to make that these values are all mostly consistent with zero, and the error bars are too large, meaning the statistics are too low, for us to make any definitive conclusion on the search for the CVE in the QGP with  $\Lambda$ - $p$  azimuthal correlations.

## CHAPTER 6

### Conclusion and Future Perspectives

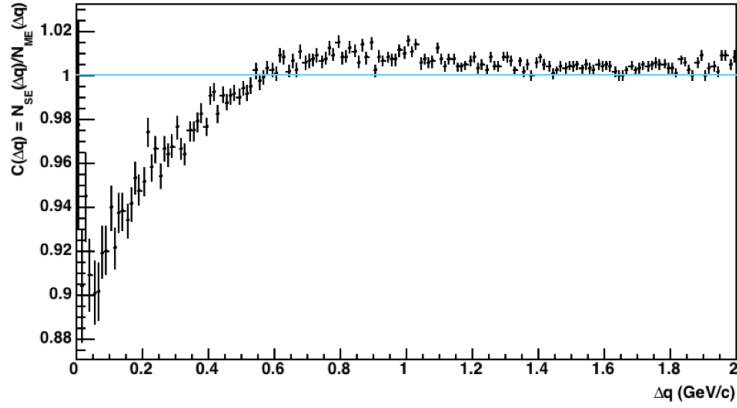
In this thesis, we carried out a search for the Chiral Vortical Effect (CVE) in the Quark Gluon Plasma (QGP) created in the heavy-ion collisions at the Relativistic Heavy-Ion Collider (RHIC) at the Brookhaven National Laboratory (BNL) located in New York, United States. Specifically, we looked at the azimuthal correlations between the same-sign baryon number ( $\Lambda$ - $p$  and  $\bar{\Lambda}$ - $\bar{p}$ ) and the opposite-sign baryon number ( $\bar{\Lambda}$ - $p$  and  $\Lambda$ - $\bar{p}$ ) pairs to calculate the observables  $\Delta\gamma_{112}$  and  $\Delta\gamma_{132}$  that gave insight into the existence of the CVE. With the limited statistics of the data sets that we have analyzed, we have not observed a definitive reaction plane dependent baryon number separation signal  $\Delta\gamma_{112}$  that were predicted to arise from the CVE. We presented an upper bound on the possible CVE signal as represented by  $N_{\text{part}}\Delta\gamma_{112}$ . In this thesis, we have established an analysis approach in heavy-ion collisions to search for the CVE and also explored the Event Shape Selection method to suppress background. Because of the yield of  $\Lambda$  hyperons and the detection efficiency, a significantly large data set will be critical for future definitive search of the CVE in heavy-ion collisions. In addition, the current research also points to an important baryon annihilation effect which could bias the opposite-sign - same-sign pair subtraction scheme used for background subtraction. We will briefly discuss the observed feature of baryon annihilations in the next section.

#### 6.1 Baryon Annihilation Effect on $\Delta\gamma$ Correlation

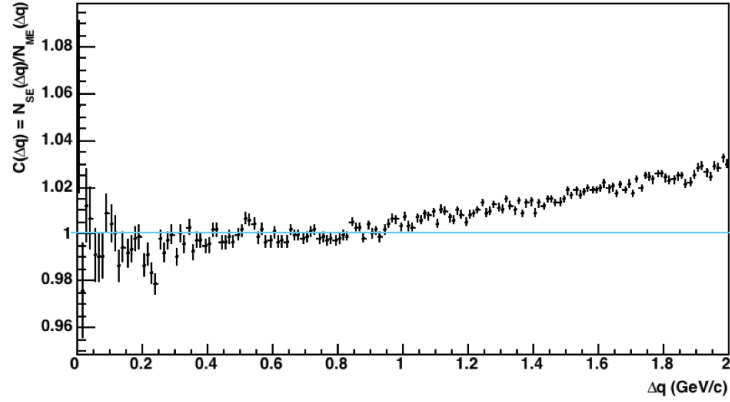
One interesting phenomenon that has been observed is that Au+Au collisions at the RHIC energies of the BES yield a baryon-rich environment, and the baryons that are created within

the reaction plane get absorbed more than the ones that travel perpendicular to it. This would mean that the elliptic flow background, described previously, that we predicted to create fake signals, actually potentially because of the absorption, could lead to a depletion of signal instead.

The following figure is an example of looking at pairs of  $\Lambda$ - $p$  and taking the ratio of them versus mixed events, and seeing the depletion in the number of pairs nearer the region where they are kinematically similar in phase space:



(a)  $\Lambda\bar{p}$  and  $\bar{\Lambda}p$



(b)  $\Lambda p$  and  $\bar{\Lambda}\bar{p}$

Figure 6.1: Distribution of the ratio of number of  $\Lambda$ - $p$  pairs in same event data to mixed event data as a function of  $\Delta q$ , the invariant vector used here to measure how close these tracks are in the kinematic phase space. This is data from the 2018 27 GeV Au+Au data set.

In this figure, we use  $\Delta q$  as our kinematic observable to look at how close the  $\Lambda$ - $p$  tracks are to each other in the kinematic phase space, with the following definition of  $\Delta q$ :

$$\Delta q \equiv \sqrt{|\vec{p}_{\Lambda/\bar{\Lambda}} - \vec{p}_{p/\bar{p}}|^2 - (E_{\Lambda/\bar{\Lambda}} - E_{p/\bar{p}})^2} \quad (6.1)$$

We see in Figure 6.1a, in the region where the two baryons are of opposite charge, that there is a significant depletion of those pairs of particles compared with the mixed event data. We also see in Figure 6.1b that this effect does not exist. This seems to be evidence for the Baryon annihilation effect proposed here. Suppose that were true, then we see from the AMPT results, Figure 5.15, that while  $\kappa_{132}$  is as expected to be around 1, given that  $\gamma_{132}$  simply models the background from elliptic flow,  $\kappa_{112}$  is actually consistently lower than  $\kappa_{132}$ . Comparing that with the ensemble results from heavy-ion collision data, Figure 5.14, we see that in collision data  $\kappa_{112}$  and  $\kappa_{132}$  are actually more or less equivalent, and both are 0.

Suppose this hypothesis of the baryon annihilation is true. Could it be that it serves as a negative background for both correlators, which is why  $\kappa_{132}$  is brought down to zero, but while  $\kappa_{112}$  should have been brought down to negative values, because CVE exists,  $\kappa_{112}$  has the CVE added on top of the background, and therefore is equivalent to zero?

One way to test this hypothesis would be to isolate the correlators based on the phase space, and compare the different regions to further understand the baryon annihilation effect, and devise a scheme to minimize it. Unfortunately, with the data that we have now, isolating such a phase space will not yield any significant result, but simply have error bars too large to make any conclusion from it.

## 6.2 Conclusion

In summary, we have measured upper limits for the Chiral Vortical Effect (CVE) using  $\Lambda$ - $p$  pairs from heavy-ion collisions at the Relativistic Heavy-Ion Collider (RHIC) detected by the Solenoid Tracker at RHIC (STAR) detector. We found the upper limit values to be the following table:

Table 6.1: Upper Bound of CVE Signal As Represented By  $N_{\text{part}}\Delta\gamma_{112}$

Event Plane Option	19.6 GeV	27 GeV
1 <sup>st</sup> Order EPD EP	0.195	0.551
2 <sup>nd</sup> Order EPD EP	0.250	0.406

According to simulations done [157], we see that even though theoretically the CVE would be stronger than the CME, they are in the same order of magnitude. Analyses from STAR data have set limits on the CME in the  $10^{-4}$  range, and given  $N_{\text{part}}$  is around 110, the limit we are setting here is still around  $10^{-3}$ . This implies potentially that we would need to reduce the error bars 10-fold, thus requiring 100 times the statistics, before we would be able to see a signal for the CVE. Thus the main limitation of further pursuing this analysis is on the statistics that we were able to get. Also, as briefly discussed above, the Baryon Annihilation Effect would also benefit greatly with more statistics, allowing us to look at different regions in the kinematic phase space to try to address the effect's impact on the measurement of the CVE.

Because of that, we look forward to future experiments when we would be able to collect significantly more data, and resume this analysis and reach a more conclusive statement on the existence of the CVE in the QGP. And there is hope in the horizon! As we move into the next two years, STAR will be collecting data from the  $\sqrt{s_{\text{NN}}} = 200$  GeV system that would potentially yield the amount of statistics that we need for furthering this analysis, and we look forward to the new data that will be collected.

# APPENDIX A

## List of Bad Runs

19.6GeV Au+Au 2018 Production:

20057007, 20057025, 20057026, 20057050, 20058001, 20058002, 20058003, 20058004, 20058005,  
20060012, 20060022, 20060025, 20060060, 20060061, 20060062, 20062010, 20062011, 20062012,  
20062036, 20063011, 20063034, 20063035, 20063036, 20063039, 20064008, 20064009, 20064011,  
20064012, 20064040, 20065018, 20067014, 20067023, 20067024, 20067029, 20067030, 20067045,  
20067046, 20069030, 20069032, 20069054, 20070042, 20070043, 20070044, 20070047, 20071001,  
20071004, 20071005, 20071006, 20071027, 20071037, 20072034, 20072035, 20072036, 20072039,  
20072041, 20072045, 20072047, 20073071, 20073072, 20073076, 20074001, 20074003, 20074004,  
20074005, 20074007, 20074008, 20074009, 20074012, 20074014, 20074017, 20074018, 20074020,  
20074021, 20074026, 20074027, 20074029, 20074032, 20074033, 20074034, 20074044, 20074045,  
20075001, 20075002, 20075006, 20075007, 20075009, 20075011, 20075013, 20081002, 20081014,  
20082060, 20082065, 20083024, 20086012, 20087007, 20089008, 20090024, 20091011, 20092054,  
20062007, 20062009, 20065017, 20065056, 20065060, 20066001, 20066008, 20066015, 20066019,  
20066023, 20066026, 20066066, 20066067, 20066068, 20066073, 20066078, 20067001, 20067004,  
20067009, 20067012, 20067015, 20067016, 20067019, 20067028, 20067038, 20067041, 20067047,  
20068001, 20068004, 20068008, 20068012, 20068019, 20068026, 20068034, 20068051, 20068055,  
20068058, 20068060, 20068064, 20069001, 20069004, 20069007, 20069010, 20069020, 20069023,  
20069026, 20069031, 20069033, 20069042, 20069050, 20069053, 20069057, 20069060, 20070002,  
20070005, 20070010, 20070013, 20070016, 20070019, 20070041, 20070045, 20071003, 20071007,  
20071010, 20071013, 20071016, 20071019, 20071024, 20071029, 20071036, 20071041, 20071044,  
20071047, 20071050, 20071053, 20071056, 20071059, 20071063, 20072002, 20072005, 20072009,  
20072012, 20072016, 20072037, 20072038, 20072046, 20072050, 20072055, 20073002, 20073006,

20073013, 20073017, 20073022, 20073025, 20073074, 20074002, 20074006, 20074010, 20074011, 20074016, 20074019, 20074023, 20074030, 20074043, 20074046, 20075004, 20075008, 20075014, 20075010, 20075015, 20075020, 20075025, 20075031, 20075035, 20075039, 20075043, 20075048, 20075054, 20075057, 20075060, 20075066, 20076001, 20076004, 20076007, 20076010, 20076013, 20076017, 20076021, 20076025, 20076028, 20076031, 20076034, 20076037, 20076040, 20076045, 20076048, 20076051, 20076054, 20076059, 20077002, 20077005, 20077008, 20077011, 20077014, 20077017, 20077018, 20078001, 20078007, 20078013, 20078016, 20078019, 20078022, 20078028, 20078032, 20078035, 20078040, 20078043, 20078046, 20078051, 20078054, 20078057, 20078060, 20078063, 20078067, 20079006, 20079009, 20079013, 20079017, 20079020, 20079023, 20079044, 20080006, 20080009, 20080012, 20080016, 20080020, 20081001, 20081004, 20081007, 20081012, 20081015, 20081018, 20081025, 20082002, 20082005, 20082010, 20082013, 20082016, 20082019, 20082024, 20082029, 20082034, 20082038, 20082047, 20082050, 20082053, 20082056, 20082059, 20082063, 20082066, 20083001, 20083004, 20083019, 20083022, 20083025, 20083029, 20083032, 20083074, 20083077, 20083079, 20084001, 20084002, 20084005, 20084009, 20084013, 20084016, 20084022, 20085006, 20085009, 20085017, 20086002, 20086005, 20086056, 20086011, 20086015, 20087008, 20087012, 20087021, 20088005, 20088009, 20088012, 20088030, 20088033, 20088037, 20089003, 20089006, 20089009, 20089012, 20089015, 20089018, 20089028, 20090002, 20090005, 20090008, 20090011, 20090014, 20090017, 20090021, 20090031, 20090048, 20091003, 20091006, 20091009, 20091012, 20091016, 20091019, 20091020, 20092005, 20092012, 20092015, 20092018, 20092021, 20092024, 20092027, 20092030, 20092033, 20092038, 20092053, 20092057, 20093001, 20093005, 20093010, 20093016, 20093025, 20093035

27GeV Au+Au 2018 Production:

19130085, 19131009, 19131010, 19131012, 19132063, 19133009, 19133010, 19133012, 19133013, 19133014, 19133018, 19134010, 19134011, 19135011, 19135013, 19135014, 19136016, 19137003, 19137022, 19137047, 19137050, 19137051, 19137052, 19137053, 19137056, 19137057, 19138008, 19138009, 19138014, 19139022, 19139023, 19139024, 19139026, 19139027, 19139028, 19139032, 19139033, 19139034, 19139037, 19140009, 19140014, 19141008, 19142005, 19142048, 19143008, 19143009, 19143010, 19143011, 19143012, 19143013, 19143014, 19143015, 19143016, 19143017,

19146016, 19147007, 19147008, 19147009, 19147010, 19147014, 19147015, 19147016, 19156002,  
19156032, 19156044, 19156045, 19156046, 19157013, 19158003, 19158007, 19158009, 19158010,  
19158011, 19158013, 19158014, 19158015, 19158017, 19158018, 19158019, 19160018, 19162002,  
19162005, 19165015, 19165020, 19165021, 19167042

## Bibliography

- [1] T. D. Lee and G. C. Wick. “Vacuum stability and vacuum excitation in a spin-0 field theory”. In: *Phys. Rev. D* 9 (8 Apr. 1974), pp. 2291–2316. DOI: 10.1103/PhysRevD.9.2291. URL: <https://link.aps.org/doi/10.1103/PhysRevD.9.2291>.
- [2] Judy Goldhaber. *BEVALAC had 40-year record of historic discoveries*. Oct. 1992. URL: <https://www2.lbl.gov/Science-Articles/Archive/Bevalac-nine-lives.html>.
- [3] *The physics of RHIC*. URL: <https://www.bnl.gov/rhic/physics.php>.
- [4] Eckhard Elsen and Frédérick Bordry. *A successful conclusion to run 2*. Dec. 2018. URL: <https://www.home.cern/news/opinion/accelerators/successful-conclusion-run-2>.
- [5] Jerzy Bartke. *Introduction to relativistic heavy ion physics*. 2009.
- [6] Reinhard Stock. “7 Relativistic Nucleus-Nucleus Collisions and the QCD Matter Phase Diagram”. In: *Landolt-Börnstein - Group I Elementary Particles, Nuclei and Atoms* (2008), pp. 225–315. ISSN: 1616-9522. DOI: 10.1007/978-3-540-74203-6\_7. URL: [http://dx.doi.org/10.1007/978-3-540-74203-6\\_7](http://dx.doi.org/10.1007/978-3-540-74203-6_7).
- [7] J. Adams et al. “Experimental and theoretical challenges in the search for the quark–gluon plasma: The STAR Collaboration’s critical assessment of the evidence from RHIC collisions”. In: *Nuclear Physics A* 757.1-2 (Aug. 2005), pp. 102–183. ISSN: 0375-9474. DOI: 10.1016/j.nuclphysa.2005.03.085. URL: <http://dx.doi.org/10.1016/j.nuclphysa.2005.03.085>.
- [8] F. Karsch. “Lattice QCD at high temperature and density”. In: *Lect. Notes Phys.* 583 (2002). Ed. by Willibald Plessas and L. Mathelitsch, pp. 209–249. DOI: 10.1007/3-540-45792-5\_6. arXiv: hep-lat/0106019.
- [9] J. Cerny et al. “Physics through the 1990s: Nuclear physics”. In: (1986).

- [10] Dirk H. Rischke. “The Quark gluon plasma in equilibrium”. In: *Prog. Part. Nucl. Phys.* 52 (2004), pp. 197–296. DOI: 10.1016/j.pnpnp.2003.09.002. arXiv: nucl-th/0305030.
- [11] Grazyna Odyniec. “The RHIC Beam Energy Scan program in STAR and what’s next ...” In: *Journal of Physics: Conference Series* 455 (Aug. 2013), p. 012037. DOI: 10.1088/1742-6596/455/1/012037. URL: <https://doi.org/10.1088/1742-6596/455/1/012037>.
- [12] Olaf Kaczmarek et al. “Heavy quark potentials in quenched QCD at high temperature”. In: *Phys. Rev. D* 62 (2000), p. 034021. DOI: 10.1103/PhysRevD.62.034021. arXiv: hep-lat/9908010.
- [13] A. M. Poskanzer and S. A. Voloshin. “Methods for analyzing anisotropic flow in relativistic nuclear collisions”. In: *Physical Review C* 58.3 (Sept. 1998), pp. 1671–1678. ISSN: 1089-490X. DOI: 10.1103/physrevc.58.1671. URL: <http://dx.doi.org/10.1103/PhysRevC.58.1671>.
- [14] H. Sorge. “Soft transverse expansion in Pb (158-A-GeV) on Pb collisions: Preequilibrium motion or first order phase transition?” In: *Phys. Lett. B* 402 (1997), pp. 251–256. DOI: 10.1016/S0370-2693(97)00474-7. arXiv: nucl-th/9701012.
- [15] H. Sorge. “Highly sensitive centrality dependence of elliptic flow: A novel signature of the phase transition in QCD”. In: *Phys. Rev. Lett.* 82 (1999), pp. 2048–2051. DOI: 10.1103/PhysRevLett.82.2048. arXiv: nucl-th/9812057.
- [16] Peter F. Kolb and Ulrich W. Heinz. “Hydrodynamic description of ultrarelativistic heavy ion collisions”. In: (May 2003). Ed. by Rudolph C. Hwa and Xin-Nian Wang, pp. 634–714. arXiv: nucl-th/0305084.
- [17] Peter F. Kolb, Josef Sollfrank, and Ulrich W. Heinz. “Anisotropic transverse flow and the quark hadron phase transition”. In: *Phys. Rev. C* 62 (2000), p. 054909. DOI: 10.1103/PhysRevC.62.054909. arXiv: hep-ph/0006129.

- [18] Miklos Gyulassy et al. “Jet quenching and radiative energy loss in dense nuclear matter”. In: (2004). Ed. by R. C. Hwa and X. N. Wang, pp. 123–191. DOI: 10.1142/9789812795533\_0003. arXiv: nucl-th/0302077.
- [19] R. G. Roberts, Rudolph C. Hwa, and Satoshi Matsuda. “PARTON RECOMBINATION MODEL INCLUDING RESONANCE PRODUCTION”. In: *J. Phys. G* 5 (1979), p. 1043. DOI: 10.1088/0305-4616/5/8/009.
- [20] T. S. Biro, P. Levai, and J. Zimanyi. “Quark coalescence in the mid-rapidity region at RHIC”. In: *J. Phys. G* 28 (2002). Ed. by J. Tennant, pp. 1561–1566. DOI: 10.1088/0954-3899/28/7/306. arXiv: hep-ph/0112137.
- [21] Berndt Muller. “Hadronic signals of deconfinement at RHIC”. In: *Nucl. Phys. A* 750 (2005). Ed. by D. Rischke and G. Levin, pp. 84–97. DOI: 10.1016/j.nuclphysa.2004.12.067. arXiv: nucl-th/0404015.
- [22] Olga Yu. Barannikova. “Probing collision dynamics at RHIC”. In: *17th International Conference on Ultra Relativistic Nucleus-Nucleus Collisions (Quark Matter 2004)*. Mar. 2004. arXiv: nucl-ex/0403014.
- [23] John Adams et al. “Particle type dependence of azimuthal anisotropy and nuclear modification of particle production in Au + Au collisions at  $s(\text{NN})^{1/2} = 200$ -GeV”. In: *Phys. Rev. Lett.* 92 (2004), p. 052302. DOI: 10.1103/PhysRevLett.92.052302. arXiv: nucl-ex/0306007.
- [24] P. Huovinen et al. “Radial and elliptic flow at RHIC: Further predictions”. In: *Phys. Lett. B* 503 (2001), pp. 58–64. DOI: 10.1016/S0370-2693(01)00219-2. arXiv: hep-ph/0101136.
- [25] C. Adler et al. “Identified particle elliptic flow in Au + Au collisions at  $s(\text{NN})^{1/2} = 130$ -GeV”. In: *Phys. Rev. Lett.* 87 (2001), p. 182301. DOI: 10.1103/PhysRevLett.87.182301. arXiv: nucl-ex/0107003.
- [26] Edward Shuryak. “Why does the quark gluon plasma at RHIC behave as a nearly ideal fluid?” In: *Prog. Part. Nucl. Phys.* 53 (2004). Ed. by A. Faessler, pp. 273–303. DOI: 10.1016/j.pnnp.2004.02.025. arXiv: hep-ph/0312227.

- [27] C. Adler et al. “Centrality dependence of high  $p_T$  hadron suppression in Au+Au collisions at  $\sqrt{s_{NN}} = 130\text{-GeV}$ ”. In: *Phys. Rev. Lett.* 89 (2002), p. 202301. DOI: 10.1103/PhysRevLett.89.202301. arXiv: nucl-ex/0206011.
- [28] I. Arsene et al. “Transverse momentum spectra in Au+Au and d+Au collisions at  $s^{*(1/2)} = 200\text{-GeV}$  and the pseudorapidity dependence of high p(T) suppression”. In: *Phys. Rev. Lett.* 91 (2003), p. 072305. DOI: 10.1103/PhysRevLett.91.072305. arXiv: nucl-ex/0307003.
- [29] S. S. Adler et al. “Absence of suppression in particle production at large transverse momentum in  $S(NN)^{*(1/2)} = 200\text{-GeV}$  d + Au collisions”. In: *Phys. Rev. Lett.* 91 (2003), p. 072303. DOI: 10.1103/PhysRevLett.91.072303. arXiv: nucl-ex/0306021.
- [30] B. B. Back et al. “Centrality dependence of charged hadron transverse momentum spectra in d + Au collisions at  $S(NN)^{*(1/2)} = 200\text{ GeV}$ ”. In: *Phys. Rev. Lett.* 91 (2003), p. 072302. DOI: 10.1103/PhysRevLett.91.072302. arXiv: nucl-ex/0306025.
- [31] J. Adams et al. “Evidence from d + Au measurements for final state suppression of high p(T) hadrons in Au+Au collisions at RHIC”. In: *Phys. Rev. Lett.* 91 (2003), p. 072304. DOI: 10.1103/PhysRevLett.91.072304. arXiv: nucl-ex/0306024.
- [32] Ivan Vitev and Miklos Gyulassy. “High  $p_T$  tomography of d + Au and Au+Au at SPS, RHIC, and LHC”. In: *Phys. Rev. Lett.* 89 (2002), p. 252301. DOI: 10.1103/PhysRevLett.89.252301. arXiv: hep-ph/0209161.
- [33] K. J. Eskola et al. “The Fragility of high-p(T) hadron spectra as a hard probe”. In: *Nucl. Phys. A* 747 (2005), pp. 511–529. DOI: 10.1016/j.nuclphysa.2004.09.070. arXiv: hep-ph/0406319.
- [34] J. Adams et al. “Transverse momentum and collision energy dependence of high p(T) hadron suppression in Au+Au collisions at ultrarelativistic energies”. In: *Phys. Rev. Lett.* 91 (2003), p. 172302. DOI: 10.1103/PhysRevLett.91.172302. arXiv: nucl-ex/0305015.
- [35] Brookhaven National Laboratory. *RHIC*. URL: <https://www.bnl.gov/rhic/> (visited on 07/02/2021).

- [36] M. Harrison, T. Ludlam, and S. Ozaki. “RHIC project overview”. In: *Nucl. Instrum. Meth. A* 499 (2003), pp. 235–244. DOI: 10.1016/S0168-9002(02)01937-X.
- [37] J Alessi et al. “The Brookhaven National Laboratory electron beam ion source for RHIC”. In: *The Review of scientific instruments* 81 (Feb. 2010), 02A509. DOI: 10.1063/1.3292937.
- [38] B. B Back et al. “The PHOBOS detector at RHIC”. In: *Nucl. Instrum. Meth. A* 499 (2003), pp. 603–623. DOI: 10.1016/S0168-9002(02)01959-9.
- [39] M Adamczyk et al. “The BRAHMS experiment at RHIC”. In: *Nucl. Instrum. Meth. A* 499 (2003), pp. 437–468. DOI: 10.1016/S0168-9002(02)01949-6.
- [40] K. Adcox et al. “PHENIX detector overview”. In: *Nucl. Instrum. Meth. A* 499 (2003), pp. 469–479. DOI: 10.1016/S0168-9002(02)01950-2.
- [41] K. H. Ackermann et al. “STAR detector overview”. In: *Nucl. Instrum. Meth. A* 499 (2003), pp. 624–632. DOI: 10.1016/S0168-9002(02)01960-5.
- [42] Brookhaven National Laboratory. *STAR*. URL: <https://www.star.bnl.gov/> (visited on 07/20/2021).
- [43] M. Anderson et al. “The STAR time projection chamber: a unique tool for studying high multiplicity events at RHIC”. In: *Nuclear Instruments and Methods in Physics Research Section A: Accelerators, Spectrometers, Detectors and Associated Equipment* 499.2-3 (Mar. 2003), pp. 659–678. ISSN: 0168-9002. DOI: 10.1016/S0168-9002(02)01964-2. URL: [http://dx.doi.org/10.1016/S0168-9002\(02\)01964-2](http://dx.doi.org/10.1016/S0168-9002(02)01964-2).
- [44] Howard Matis. *STAR Coordinate System*. 1993. URL: <https://drupal.star.bnl.gov/STAR/starnotes/public/csn0121> (visited on 11/08/2021).
- [45] W.J Llope et al. “The TOFP/pVPD time-of-flight system for STAR”. In: *Nuclear Instruments and Methods in Physics Research Section A: Accelerators, Spectrometers, Detectors and Associated Equipment* 522.3 (Apr. 2004), pp. 252–273. ISSN: 0168-9002. DOI: 10.1016/j.nima.2003.11.414. URL: <http://dx.doi.org/10.1016/j.nima.2003.11.414>.

- [46] M Beddo et al. “The STAR Barrel Electromagnetic Calorimeter”. In: *Nuclear Instruments and Methods A* 499 (Apr. 2002). URL: <https://www.osti.gov/biblio/816369>.
- [47] C. E. Allgower et al. “The STAR endcap electromagnetic calorimeter”. In: *Nuclear Instruments and Methods in Physics Research A* 499 (Mar. 2003), pp. 740–750. DOI: 10.1016/S0168-9002(02)01971-X.
- [48] F. Bergsma et al. “The STAR detector magnet subsystem”. In: *Nuclear Instruments and Methods in Physics Research Section A: Accelerators, Spectrometers, Detectors and Associated Equipment* 499 (Mar. 2003), pp. 633–639. DOI: 10.1016/S0168-9002(02)01961-7.
- [49] J. Kiryluk. “Local polarimetry for proton beams with the STAR beam beam counters”. In: *16th International Spin Physics Symposium (SPIN 2004)*. Jan. 2005, pp. 718–721. DOI: 10.1142/9789812701909\_0152. arXiv: hep-ex/0501072.
- [50] C. Adler et al. “The STAR level-3 trigger system”. In: *Nucl. Instrum. Meth. A* 499 (2003), pp. 778–791. DOI: 10.1016/S0168-9002(02)01975-7.
- [51] Joseph Adams et al. “The STAR Event Plane Detector”. In: *Nucl. Instrum. Meth. A* 968 (2020), p. 163970. DOI: 10.1016/j.nima.2020.163970. arXiv: 1912.05243 [physics.ins-det].
- [52] J. Lin et al. “Hardware controls for the STAR experiment at RHIC”. In: *1999 IEEE Conference on Real-Time Computer Applications in Nuclear Particle and Plasma Physics. 11th IEEE NPSS Real Time Conference. Conference Record (Cat. No.99EX295)*. 1999, pp. 246–249. DOI: 10.1109/RTCON.1999.842612.
- [53] M. Anderson et al. “The STAR time projection chamber: a unique tool for studying high multiplicity events at RHIC”. In: *Nuclear Instruments and Methods in Physics Research Section A: Accelerators, Spectrometers, Detectors and Associated Equipment* 499.2-3 (Mar. 2003), pp. 659–678. ISSN: 0168-9002. DOI: 10.1016/S0168-9002(02)01964-2. URL: [http://dx.doi.org/10.1016/S0168-9002\(02\)01964-2](http://dx.doi.org/10.1016/S0168-9002(02)01964-2).

- [54] Fuwang Shen et al. “MWPC prototyping and performance test for the STAR inner TPC upgrade”. In: *Nucl. Instrum. Meth. A* 896 (2018), pp. 90–95. DOI: 10.1016/j.nima.2018.04.019. arXiv: 1805.03938 [physics.ins-det].
- [55] The STAR Collaboration. *Technical Design Report for the iTPC Upgrade*. Dec. 2015.
- [56] Roli Esha. “Exploring the critical phenomenon in the QCD phase diagram at STAR”. PhD thesis. Los Angeles CA, 2019.
- [57] Hans Bichsel. “A method to improve tracking and particle identification in TPCs and silicon detectors”. In: *Nuclear Instruments and Methods in Physics Research Section A: Accelerators, Spectrometers, Detectors and Associated Equipment* 562.1 (2006), pp. 154–197. ISSN: 0168-9002. DOI: <https://doi.org/10.1016/j.nima.2006.03.009>. URL: <https://www.sciencedirect.com/science/article/pii/S0168900206005353>.
- [58] B Bonner et al. “A single Time-of-Flight tray based on multigap resistive plate chambers for the STAR experiment at RHIC”. In: *Nuclear Instruments and Methods in Physics Research Section A: Accelerators, Spectrometers, Detectors and Associated Equipment* 508.1 (2003). Proceedings of the Sixth International Workshop on Resistive Plate Chambers and Related Detectors, pp. 181–184. ISSN: 0168-9002. DOI: [https://doi.org/10.1016/S0168-9002\(03\)01347-0](https://doi.org/10.1016/S0168-9002(03)01347-0). URL: <https://www.sciencedirect.com/science/article/pii/S0168900203013470>.
- [59] M Shao et al. “Beam test results of two kinds of multi-gap resistive plate chambers”. In: *Nuclear Instruments and Methods in Physics Research Section A: Accelerators, Spectrometers, Detectors and Associated Equipment* 492.3 (2002), pp. 344–350. ISSN: 0168-9002. DOI: [https://doi.org/10.1016/S0168-9002\(02\)01355-4](https://doi.org/10.1016/S0168-9002(02)01355-4). URL: <https://www.sciencedirect.com/science/article/pii/S0168900202013554>.
- [60] L. Adamczyk et al. “Bulk Properties of the Medium Produced in Relativistic Heavy-Ion Collisions from the Beam Energy Scan Program”. In: *Phys. Rev. C* 96.4 (2017), p. 044904. DOI: 10.1103/PhysRevC.96.044904. arXiv: 1701.07065 [nucl-ex].

- [61] J. M. Landgraf et al. “An overview of the STAR DAQ system”. In: *Nucl. Instrum. Meth. A* 499 (2003), pp. 762–765. DOI: 10.1016/S0168-9002(02)01973-3.
- [62] A. Vilenkin. “EQUILIBRIUM PARITY VIOLATING CURRENT IN A MAGNETIC FIELD”. In: *Phys. Rev. D* 22 (1980), pp. 3080–3084. DOI: 10.1103/PhysRevD.22.3080.
- [63] Dmitri E. Kharzeev, Larry D. McLerran, and Harmen J. Warringa. “The Effects of topological charge change in heavy ion collisions: ‘Event by event P and CP violation’”. In: *Nucl. Phys. A* 803 (2008), pp. 227–253. DOI: 10.1016/j.nuclphysa.2008.02.298. arXiv: 0711.0950 [hep-ph].
- [64] Shiin-Shen Chern and James Simons. “Characteristic forms and geometric invariants”. In: *Annals Math.* 99 (1974), pp. 48–69. DOI: 10.2307/1971013.
- [65] Dmitri Diakonov. “Instantons at work”. In: *Prog. Part. Nucl. Phys.* 51 (2003), pp. 173–222. DOI: 10.1016/S0146-6410(03)90014-7. arXiv: hep-ph/0212026.
- [66] Dmitri E. Kharzeev. “The Chiral Magnetic Effect and Anomaly-Induced Transport”. In: *Prog. Part. Nucl. Phys.* 75 (2014), pp. 133–151. DOI: 10.1016/j.ppnp.2014.01.002. arXiv: 1312.3348 [hep-ph].
- [67] D. E. Kharzeev et al. “Chiral magnetic and vortical effects in high-energy nuclear collisions—A status report”. In: *Prog. Part. Nucl. Phys.* 88 (2016), pp. 1–28. DOI: 10.1016/j.ppnp.2016.01.001. arXiv: 1511.04050 [hep-ph].
- [68] Zuo-Tang Liang and Xin-Nian Wang. “Globally polarized quark-gluon plasma in non-central A+A collisions”. In: *Phys. Rev. Lett.* 94 (2005). [Erratum: *Phys.Rev.Lett.* 96, 039901 (2006)], p. 102301. DOI: 10.1103/PhysRevLett.94.102301. arXiv: nucl-th/0410079.
- [69] Mircea I. Baznat et al. “Femto-vortex sheets and hyperon polarization in heavy-ion collisions”. In: *Phys. Rev. C* 93.3 (2016), p. 031902. DOI: 10.1103/PhysRevC.93.031902. arXiv: 1507.04652 [nucl-th].

- [70] Sergei A. Voloshin. “Parity violation in hot QCD: How to detect it”. In: *Physical Review C* 70.5 (Nov. 2004). ISSN: 1089-490X. DOI: 10.1103/physrevc.70.057901. URL: <http://dx.doi.org/10.1103/PhysRevC.70.057901>.
- [71] L. Adamczyk et al. “Fluctuations of charge separation perpendicular to the event plane and local parity violation in  $\sqrt{s_{NN}} = 200$  GeV Au+Au collisions at the BNL Relativistic Heavy Ion Collider”. In: *Phys. Rev. C* 88.6 (2013), p. 064911. DOI: 10.1103/PhysRevC.88.064911. arXiv: 1302.3802 [nucl-ex].
- [72] L. Adamczyk et al. “Global  $\Lambda$  hyperon polarization in nuclear collisions: evidence for the most vortical fluid”. In: *Nature* 548 (2017), pp. 62–65. DOI: 10.1038/nature23004. arXiv: 1701.06657 [nucl-ex].
- [73] Michael L. Miller et al. “Glauber modeling in high energy nuclear collisions”. In: *Ann. Rev. Nucl. Part. Sci.* 57 (2007), pp. 205–243. DOI: 10.1146/annurev.nucl.57.090506.123020. arXiv: nucl-ex/0701025.
- [74] M. Tanabashi et al. “Review of Particle Physics”. In: *Phys. Rev. D* 98 (3 Aug. 2018), p. 030001. DOI: 10.1103/PhysRevD.98.030001. URL: <https://link.aps.org/doi/10.1103/PhysRevD.98.030001>.
- [75] J. Barrette et al. “Proton and pion production relative to the reaction plane in Au + Au collisions at AGS energies”. In: *Phys. Rev. C* 56 (1997), pp. 3254–3264. DOI: 10.1103/PhysRevC.56.3254. arXiv: nucl-ex/9707002.
- [76] R. Fruhwirth. “Application of Kalman filtering to track and vertex fitting”. In: *Nucl. Instrum. Meth. A* 262 (1987), pp. 444–450. DOI: 10.1016/0168-9002(87)90887-4.
- [77] Wolfgang Waltenberger. “RAVE—A Detector-Independent Toolkit to Reconstruct Vertices”. In: *Nuclear Science, IEEE Transactions on* 58 (May 2011), pp. 434–444. DOI: 10.1109/TNS.2011.2119492.
- [78] Sergey Gorbunov and Ivan Kisel. “Reconstruction of decayed particles based on the Kalman filter”. In: 2007.

- [79] Sergey Gorbunov. “On-line reconstruction algorithms for the CBM and ALICE experiments”. In: 2013.
- [80] Maksym Zyzak. “Online selection of short-lived particles on many-core computer architectures in the CBM experiment at FAIR”. PhD thesis. 2016, p. 165.
- [81] Volker Friese and Christian Sturm, eds. *CBM Progress Report 2012*. Darmstadt: GSI, 2013, 120p. ISBN: 978-3-9815227-0-9. URL: <https://repository.gsi.de/record/54078>.
- [82] L. Adamczyk et al. “Centrality dependence of identified particle elliptic flow in relativistic heavy ion collisions at  $\sqrt{s_{NN}}=7.7\text{--}62.4$  GeV”. In: *Phys. Rev. C* 93.1 (2016), p. 014907. DOI: 10.1103/PhysRevC.93.014907. arXiv: 1509.08397 [nucl-ex].
- [83] P. Braun-Munzinger et al. “Thermal equilibration and expansion in nucleus-nucleus collisions at the AGS”. In: *Phys. Lett. B* 344 (1995), pp. 43–48. DOI: 10.1016/0370-2693(94)01534-J. arXiv: nucl-th/9410026.
- [84] J. Cleymans and K. Redlich. “Unified description of freezeout parameters in relativistic heavy ion collisions”. In: *Phys. Rev. Lett.* 81 (1998), pp. 5284–5286. DOI: 10.1103/PhysRevLett.81.5284. arXiv: nucl-th/9808030.
- [85] P. Braun-Munzinger, I. Heppe, and J. Stachel. “Chemical equilibration in Pb + Pb collisions at the SPS”. In: *Phys. Lett. B* 465 (1999), pp. 15–20. DOI: 10.1016/S0370-2693(99)01076-X. arXiv: nucl-th/9903010.
- [86] F. Becattini et al. “Features of particle multiplicities and strangeness production in central heavy ion collisions between 1.7A-GeV/c and 158A-GeV/c”. In: *Phys. Rev. C* 64 (2001), p. 024901. DOI: 10.1103/PhysRevC.64.024901. arXiv: hep-ph/0002267.
- [87] C. M. Hung and Edward V. Shuryak. “Hydrodynamics near the QCD phase transition: Looking for the longest lived fireball”. In: *Phys. Rev. Lett.* 75 (1995), pp. 4003–4006. DOI: 10.1103/PhysRevLett.75.4003. arXiv: hep-ph/9412360.

- [88] Dirk H. Rischke, Stefan Bernard, and Joachim A. Maruhn. “Relativistic hydrodynamics for heavy ion collisions. 1. General aspects and expansion into vacuum”. In: *Nucl. Phys. A* 595 (1995), pp. 346–382. DOI: 10.1016/0375-9474(95)00355-1. arXiv: nucl-th/9504018.
- [89] Dirk H. Rischke, Yaris Pursun, and Joachim A. Maruhn. “Relativistic hydrodynamics for heavy ion collisions. 2. Compression of nuclear matter and the phase transition to the quark - gluon plasma”. In: *Nucl. Phys. A* 595 (1995). [Erratum: *Nucl.Phys.A* 596, 717–717 (1996)], pp. 383–408. DOI: 10.1016/0375-9474(95)00356-3. arXiv: nucl-th/9504021.
- [90] P. F. Kolb et al. “Elliptic flow at SPS and RHIC: From kinetic transport to hydrodynamics”. In: *Phys. Lett. B* 500 (2001), pp. 232–240. DOI: 10.1016/S0370-2693(01)00079-X. arXiv: hep-ph/0012137.
- [91] P. F. Kolb et al. “Centrality dependence of multiplicity, transverse energy, and elliptic flow from hydrodynamics”. In: *Nucl. Phys. A* 696 (2001), pp. 197–215. DOI: 10.1016/S0375-9474(01)01114-9. arXiv: hep-ph/0103234.
- [92] D. Teaney, J. Lauret, and E. V. Shuryak. “A Hydrodynamic Description of Heavy Ion Collisions at the SPS and RHIC”. In: (Oct. 2001). arXiv: nucl-th/0110037.
- [93] R. Mattiello et al. “Multistrangeness production in heavy ion collisions”. In: *Nucl. Phys. B Proc. Suppl.* 24 (1991), pp. 221–233. DOI: 10.1016/0920-5632(91)90328-C.
- [94] Y. Pang, T. J. Schlagel, and S. H. Kahana. “Cascade for relativistic nucleus collisions”. In: *Phys. Rev. Lett.* 68 (1992), pp. 2743–2746. DOI: 10.1103/PhysRevLett.68.2743.
- [95] H. Sorge. “Elliptical flow: A Signature for early pressure in ultrarelativistic nucleus-nucleus collisions”. In: *Phys. Rev. Lett.* 78 (1997), pp. 2309–2312. DOI: 10.1103/PhysRevLett.78.2309. arXiv: nucl-th/9610026.
- [96] Bin Zhang. “ZPC 1.0.1: A Parton cascade for ultrarelativistic heavy ion collisions”. In: *Comput. Phys. Commun.* 109 (1998), pp. 193–206. DOI: 10.1016/S0010-4655(98)00010-1. arXiv: nucl-th/9709009.

- [97] S. A. Bass et al. “Microscopic models for ultrarelativistic heavy ion collisions”. In: *Prog. Part. Nucl. Phys.* 41 (1998), pp. 255–369. DOI: 10.1016/S0146-6410(98)00058-1. arXiv: nucl-th/9803035.
- [98] T. J. Humanic. “Constraining a simple hadronization model of relativistic heavy ion collisions using hadronic observables”. In: *Phys. Rev. C* 57 (1998), pp. 866–876. DOI: 10.1103/PhysRevC.57.866.
- [99] D. E. Kahana and S. H. Kahana. “J / psi suppression in heavy ion collisions at the CERN SPS”. In: *Prog. Part. Nucl. Phys.* 42 (1999). Ed. by A. Faessler, pp. 269–278. DOI: 10.1016/S0146-6410(99)00082-4. arXiv: nucl-th/9808025.
- [100] Li and Ko. “Formation of superdense hadronic matter in high energy heavy-ion collisions.” In: *Physical review. C, Nuclear physics* 52 4 (1995), pp. 2037–2063.
- [101] BAO-AN LI et al. “STUDIES OF SUPERDENSE HADRONIC MATTER IN A RELATIVISTIC TRANSPORT MODEL”. In: *International Journal of Modern Physics E* 10.04n05 (2001), pp. 267–352. DOI: 10.1142/S0218301301000575. eprint: <https://doi.org/10.1142/S0218301301000575>. URL: <https://doi.org/10.1142/S0218301301000575>.
- [102] Yuri L. Dokshitzer et al. *Basics of perturbative QCD*. 1991.
- [103] Xin-Nian Wang. “pQCD based approach to parton production and equilibration in high-energy nuclear collisions”. In: *Phys. Rept.* 280 (1997), pp. 287–371. DOI: 10.1016/S0370-1573(96)00022-1. arXiv: hep-ph/9605214.
- [104] Larry D. McLerran and Raju Venugopalan. “Computing quark and gluon distribution functions for very large nuclei”. In: *Phys. Rev. D* 49 (1994), pp. 2233–2241. DOI: 10.1103/PhysRevD.49.2233. arXiv: hep-ph/9309289.
- [105] Larry D. McLerran and Raju Venugopalan. “Gluon distribution functions for very large nuclei at small transverse momentum”. In: *Phys. Rev. D* 49 (1994), pp. 3352–3355. DOI: 10.1103/PhysRevD.49.3352. arXiv: hep-ph/9311205.

- [106] Yuri V. Kovchegov and Dirk H. Rischke. “Classical gluon radiation in ultrarelativistic nucleus-nucleus collisions”. In: *Phys. Rev. C* 56 (1997), pp. 1084–1094. DOI: 10.1103/PhysRevC.56.1084. arXiv: hep-ph/9704201.
- [107] Dmitri Kharzeev and Eugene Levin. “Manifestations of high density QCD in the first RHIC data”. In: *Phys. Lett. B* 523 (2001), pp. 79–87. DOI: 10.1016/S0370-2693(01)01309-0. arXiv: nucl-th/0108006.
- [108] Dmitri Kharzeev, Eugene Levin, and Marzia Nardi. “QCD saturation and deuteron nucleus collisions”. In: *Nucl. Phys. A* 730 (2004). [Erratum: Nucl.Phys.A 743, 329–331 (2004)], pp. 448–459. DOI: 10.1016/j.nuclphysa.2004.06.022. arXiv: hep-ph/0212316.
- [109] Dmitri Kharzeev and Marzia Nardi. “Hadron production in nuclear collisions at RHIC and high density QCD”. In: *Phys. Lett. B* 507 (2001), pp. 121–128. DOI: 10.1016/S0370-2693(01)00457-9. arXiv: nucl-th/0012025.
- [110] K. J. Eskola et al. “Scaling of transverse energies and multiplicities with atomic number and energy in ultrarelativistic nuclear collisions”. In: *Nucl. Phys. B* 570 (2000), pp. 379–389. DOI: 10.1016/S0550-3213(99)00720-8. arXiv: hep-ph/9909456.
- [111] K. J. Eskola, K. Kajantie, and Kimmo Tuominen. “Centrality dependence of multiplicities in ultrarelativistic nuclear collisions”. In: *Phys. Lett. B* 497 (2001), pp. 39–43. DOI: 10.1016/S0370-2693(00)01341-1. arXiv: hep-ph/0009246.
- [112] K. J. Eskola et al. “Rapidity dependence of particle production in ultrarelativistic nuclear collisions”. In: *Phys. Lett. B* 543 (2002), pp. 208–216. DOI: 10.1016/S0370-2693(02)02457-7. arXiv: hep-ph/0204034.
- [113] R. Baier et al. “‘Bottom up’ thermalization in heavy ion collisions”. In: *Phys. Lett. B* 502 (2001), pp. 51–58. DOI: 10.1016/S0370-2693(01)00191-5. arXiv: hep-ph/0009237.
- [114] Zi-Wei Lin et al. “A Multi-phase transport model for relativistic heavy ion collisions”. In: *Phys. Rev. C* 72 (2005), p. 064901. DOI: 10.1103/PhysRevC.72.064901. arXiv: nucl-th/0411110.

- [115] Bin Zhang et al. “A Transport model for heavy ion collisions at RHIC”. In: *Centennial Celebration and Meeting of the American Physical Society (Combining Annual APS General Meeting and the Joint Meeting of the APS and the AAPT)*. Mar. 1999, pp. 146–150. arXiv: nucl-th/9904075.
- [116] Bin Zhang et al. “A multiphase transport model for nuclear collisions at RHIC”. In: *Phys. Rev. C* 61 (2000), p. 067901. DOI: 10.1103/PhysRevC.61.067901. arXiv: nucl-th/9907017.
- [117] Zi-wei Lin et al. “Charged particle rapidity distributions at relativistic energies”. In: *Phys. Rev. C* 64 (2001), p. 011902. DOI: 10.1103/PhysRevC.64.011902. arXiv: nucl-th/0011059.
- [118] Zi-Wei Lin et al. “Multiphase transport model for relativistic heavy ion collisions”. In: *Phys. Rev. C* 72 (Dec. 2005). DOI: 10.1103/PhysRevC.72.064901.
- [119] Rohini Sharma and Ramni Gupta. “Scaling Properties of Multiplicity Fluctuations in the AMPT Model”. In: (June 2018).
- [120] Zi-wei Lin and C. M. Ko. “Partonic effects on the elliptic flow at RHIC”. In: *Phys. Rev. C* 65 (2002), p. 034904. DOI: 10.1103/PhysRevC.65.034904. arXiv: nucl-th/0108039.
- [121] Zi-wei Lin, C. M. Ko, and Subrata Pal. “Partonic effects on pion interferometry at RHIC”. In: *Phys. Rev. Lett.* 89 (2002), p. 152301. DOI: 10.1103/PhysRevLett.89.152301. arXiv: nucl-th/0204054.
- [122] Bin Zhang, Lie-Wen Chen, and Che-Ming Ko. “Charm elliptic flow in Au+Au collisions at RHIC”. In: *Nucl. Phys. A* 774 (2006). Ed. by T. Csorgo et al., pp. 665–668. DOI: 10.1016/j.nuclphysa.2006.06.110. arXiv: nucl-th/0509095.
- [123] Zi-wei Lin and C. M. Ko. “Kaon interferometry at RHIC from AMPT model”. In: *J. Phys. G* 30 (2004). Ed. by S. A. Bass et al., S263–S270. DOI: 10.1088/0954-3899/30/1/031. arXiv: nucl-th/0305069.

- [124] Xin-Nian Wang. “Role of multiple mini - jets in high-energy hadronic reactions”. In: *Phys. Rev. D* 43 (1991), pp. 104–112. DOI: 10.1103/PhysRevD.43.104.
- [125] Xin-Nian Wang and Miklos Gyulassy. “HIJING: A Monte Carlo model for multiple jet production in p p, p A and A A collisions”. In: *Phys. Rev. D* 44 (1991), pp. 3501–3516. DOI: 10.1103/PhysRevD.44.3501.
- [126] Xin-Nian Wang and Miklos Gyulassy. “A Systematic study of particle production in  $p + p$  (anti-p) collisions via the HIJING model”. In: *Phys. Rev. D* 45 (1992), pp. 844–856. DOI: 10.1103/PhysRevD.45.844.
- [127] Miklos Gyulassy and Xin-Nian Wang. “HIJING 1.0: A Monte Carlo program for parton and particle production in high-energy hadronic and nuclear collisions”. In: *Comput. Phys. Commun.* 83 (1994), p. 307. DOI: 10.1016/0010-4655(94)90057-4. arXiv: nucl-th/9502021.
- [128] J. D. Bjorken. “Highly Relativistic Nucleus-Nucleus Collisions: The Central Rapidity Region”. In: *Phys. Rev. D* 27 (1983), pp. 140–151. DOI: 10.1103/PhysRevD.27.140.
- [129] Bo Andersson, G. Gustafson, and B. Soderberg. “A General Model for Jet Fragmentation”. In: *Z. Phys. C* 20 (1983), p. 317. DOI: 10.1007/BF01407824.
- [130] Bo Andersson et al. “Parton Fragmentation and String Dynamics”. In: *Phys. Rept.* 97 (1983), pp. 31–145. DOI: 10.1016/0370-1573(83)90080-7.
- [131] Torbjorn Sjostrand et al. “High-energy physics event generation with PYTHIA 6.1”. In: *Comput. Phys. Commun.* 135 (2001), pp. 238–259. DOI: 10.1016/S0010-4655(00)00236-8. arXiv: hep-ph/0010017.
- [132] J. Zimanyi et al. “Quark liberation and coalescence at CERN SPS”. In: *Phys. Lett. B* 472 (2000), pp. 243–246. DOI: 10.1016/S0370-2693(99)01461-6. arXiv: hep-ph/9904501.
- [133] Bao-An Li, Che Ming Ko, and Wolfgang Bauer. “Isospin physics in heavy ion collisions at intermediate-energies”. In: *Int. J. Mod. Phys. E* 7 (1998), pp. 147–230. DOI: 10.1142/S0218301398000087. arXiv: nucl-th/9707014.

- [134] Subikash Choudhury et al. “Background evaluations for the chiral magnetic effect with normalized correlators using a multiphase transport model”. In: *Eur. Phys. J. C* 80.5 (2020), p. 383. DOI: 10.1140/epjc/s10052-020-7928-4. arXiv: 1909.04083 [hep-ph].
- [135] Adam Bzdak, Volker Koch, and Jinfeng Liao. “Charge-Dependent Correlations in Relativistic Heavy Ion Collisions and the Chiral Magnetic Effect”. In: *Lect. Notes Phys.* 871 (2013), pp. 503–536. DOI: 10.1007/978-3-642-37305-3\_19. arXiv: 1207.7327 [nucl-th].
- [136] Jean-Yves Ollitrault. “Anisotropy as a signature of transverse collective flow”. In: *Phys. Rev. D* 46 (1 July 1992), pp. 229–245. DOI: 10.1103/PhysRevD.46.229. URL: <https://link.aps.org/doi/10.1103/PhysRevD.46.229>.
- [137] S. Voloshin and Y. Zhang. “Flow study in relativistic nuclear collisions by Fourier expansion of Azimuthal particle distributions”. In: *Z. Phys. C* 70 (1996), pp. 665–672. DOI: 10.1007/s002880050141. arXiv: hep-ph/9407282.
- [138] Gang Wang. “Correlations relative to the reaction plane at the relativistic heavy ion collider based on transverse deflection of spectator neutrons”. PhD thesis. Kent State University, 2006, pp. 0–122. URL: <https://drupal.star.bnl.gov/STAR/theses/ph-d/gang-wang>.
- [139] Fufang Wen et al. “Event-shape-engineering study of charge separation in heavy-ion collisions”. In: *Chin. Phys. C* 42.1 (2018), p. 014001. DOI: 10.1088/1674-1137/42/1/014001. arXiv: 1608.03205 [nucl-th].
- [140] Scott Pratt, Soeren Schlichting, and Sean Gavin. “Effects of Momentum Conservation and Flow on Angular Correlations at RHIC”. In: *Phys. Rev. C* 84 (2011), p. 024909. DOI: 10.1103/PhysRevC.84.024909. arXiv: 1011.6053 [nucl-th].
- [141] Sören Schlichting and Scott Pratt. “Charge conservation at energies available at the BNL Relativistic Heavy Ion Collider and contributions to local parity violation observables”. In: *Phys. Rev. C* 83 (1 Jan. 2011), p. 014913. DOI: 10.1103/PhysRevC.83.014913. URL: <https://link.aps.org/doi/10.1103/PhysRevC.83.014913>.

- [142] L. Adamczyk et al. “Measurement of charge multiplicity asymmetry correlations in high-energy nucleus-nucleus collisions at  $\sqrt{s_{NN}} = 200$  GeV”. In: *Phys. Rev. C* 89 (4 Apr. 2014), p. 044908. DOI: 10.1103/PhysRevC.89.044908. URL: <https://link.aps.org/doi/10.1103/PhysRevC.89.044908>.
- [143] Shreyasi Acharya et al. “Constraining the magnitude of the Chiral Magnetic Effect with Event Shape Engineering in Pb-Pb collisions at  $\sqrt{s_{NN}} = 2.76$  TeV”. In: *Phys. Lett. B* 777 (2018), pp. 151–162. DOI: 10.1016/j.physletb.2017.12.021. arXiv: 1709.04723 [nucl-ex].
- [144] Albert M Sirunyan et al. “Constraints on the chiral magnetic effect using charge-dependent azimuthal correlations in  $p$ Pb and PbPb collisions at the CERN Large Hadron Collider”. In: *Phys. Rev. C* 97.4 (2018), p. 044912. DOI: 10.1103/PhysRevC.97.044912. arXiv: 1708.01602 [nucl-ex].
- [145] Piotr Bozek, Wojciech Broniowski, and Joao Moreira. “Torqued fireballs in relativistic heavy-ion collisions”. In: *Phys. Rev. C* 83 (2011), p. 034911. DOI: 10.1103/PhysRevC.83.034911. arXiv: 1011.3354 [nucl-th].
- [146] Long-Gang Pang et al. “Longitudinal decorrelation of anisotropic flows in heavy-ion collisions at the CERN Large Hadron Collider”. In: *Phys. Rev. C* 91.4 (2015), p. 044904. DOI: 10.1103/PhysRevC.91.044904. arXiv: 1410.8690 [nucl-th].
- [147] Bjoern Schenke and Soeren Schlichting. “3D glasma initial state for relativistic heavy ion collisions”. In: *Phys. Rev. C* 94.4 (2016), p. 044907. DOI: 10.1103/PhysRevC.94.044907. arXiv: 1605.07158 [hep-ph].
- [148] Chun Shen and Björn Schenke. “Dynamical initial state model for relativistic heavy-ion collisions”. In: *Phys. Rev. C* 97.2 (2018), p. 024907. DOI: 10.1103/PhysRevC.97.024907. arXiv: 1710.00881 [nucl-th].
- [149] Arabinda Behera, Maowu Nie, and Jiangyong Jia. “Longitudinal eccentricity decorrelations in heavy ion collisions”. In: *Phys. Rev. Res.* 2.2 (2020), p. 023362. DOI: 10.1103/PhysRevResearch.2.023362. arXiv: 2003.04340 [nucl-th].

- [150] Fuqiang Wang and Jie Zhao. “Challenges in flow background removal in search for the chiral magnetic effect”. In: *Phys. Rev. C* 95 (5 May 2017), p. 051901. DOI: 10.1103/PhysRevC.95.051901. URL: <https://link.aps.org/doi/10.1103/PhysRevC.95.051901>.
- [151] Zhiwan Xu et al. “Event Shape Selection Method in Search of the Chiral Magnetic Effect in Heavy-ion Collisions”. In: (July 2023). arXiv: 2307.14997 [nucl-th].
- [152] A. H. Tang. “Probe chiral magnetic effect with signed balance function”. In: *Chin. Phys. C* 44.5 (2020), p. 054101. DOI: 10.1088/1674-1137/44/5/054101. arXiv: 1903.04622 [nucl-ex].
- [153] Torbjorn Sjostrand, Stephen Mrenna, and Peter Z. Skands. “PYTHIA 6.4 Physics and Manual”. In: *JHEP* 05 (2006), p. 026. DOI: 10.1088/1126-6708/2006/05/026. arXiv: hep-ph/0603175.
- [154] Shuzhe Shi et al. “Anomalous Chiral Transport in Heavy Ion Collisions from Anomalous-Viscous Fluid Dynamics”. In: *Annals Phys.* 394 (2018), pp. 50–72. DOI: 10.1016/j.aop.2018.04.026. arXiv: 1711.02496 [nucl-th].
- [155] Yin Jiang et al. “Quantifying the chiral magnetic effect from anomalous-viscous fluid dynamics”. In: *Chin. Phys. C* 42.1 (2018), p. 011001. DOI: 10.1088/1674-1137/42/1/011001. arXiv: 1611.04586 [nucl-th].
- [156] Shuzhe Shi et al. “Signatures of Chiral Magnetic Effect in the Collisions of Isobars”. In: *Phys. Rev. Lett.* 125 (24 Dec. 2020), p. 242301. DOI: 10.1103/PhysRevLett.125.242301. URL: <https://link.aps.org/doi/10.1103/PhysRevLett.125.242301>.
- [157] Xingyu Guo et al. “Chiral Vortical and Magnetic Effects in Anomalous Hydrodynamics”. In: *Nuclear Physics A* 967 (Nov. 2017), pp. 776–779. DOI: 10.1016/j.nuclphysa.2017.06.039. URL: <https://doi.org/10.1016%2Fj.nuclphysa.2017.06.039>.